Universidad Carlos III de Madrid

TESIS DOCTORAL

Synthesis, structure and scalability of macroscopic carbon nanotube fibre.

Autor:

Víctor Javier Reguero Sanz

Director:

Dr. Juan José Vilatela Garcia

DEPARTAMENTO DE CIENCIA E INGENIERÍA DE MATERIALES E INGENIERÍA QUÍMICA

UNIVERSIDAD CARLOS III DE MADRID

Leganés, Marzo 2017

Universidad Carlos III de Madrid
www.uc3m.es

TESIS DOCTORAL

SYNTHESIS, STRUCTURE AND SCALABILITY OF MACROSCOPIC CARBON NANOTUBE FIBRE

Autor: Víctor Javier Reguero Sanz

Director: Dr. Juan José Vilatela Garcia

Firma del Tribunal Calificador:

Firma:

Presidente:

Vocal:

Secretario:

Calificación:

Leganés, 31 de marzo de 2017

A mis padres

"Now this is not the end.
It is not even the beginning of the end.
But it is, perhaps, the end of the beginning"

Winston Churchill

Acknowledgements

I am grateful to my supervisor Dr. Juan José Vilatela Garcia, for his help during my PhD. This work would not have been possible without his academic advice and guidance.

I would like to extend my gratitude to the Multifunctional Nanocomposite Group for helping me in my work with rewarding advice from the first day. It has been pleasure to share this time together. Double acknowledgements for who were supporting me in the bad moments.

I am thankful to the external participants: IMDEA Energy & Nanoscience, Centro Nacional de Microscopía (CNM), Centro de Apoyo a la Investigación (CAI) and Science and Materials Institute (ICMM).

I am indebted to the technician members of IMDEA Materials, all of you; receiving a technical work and important advices, even in the most desperate moments.

So many people had been important during these years, so many names who support me personally. I do not want to forget anyone. Thus, if you took the trouble to read these, you are one of them: Thank you! (Or a curious person ;))

I do not want to forget and also thanks those to trip me up, you make me stronger.

Finally, I would like to thanks to all of my friends and family for their unconditional support and understanding.

Preface

The research described in this work is submitted for the degree of Doctor of Philosophy to the University of Carlos III. The work was carried out during the period from February 2013 to February 2017 in Multifunctional Nanocomposites Group, IMDEA Materials, under the supervision of Dr Juan José Vilatela García. Unless indicated, the results, discussions and conclusions drawn by this dissertation are to the best of my knowledge original.

Víctor Javier Reguero Sanz,

March 2017.

Abstract

Carbon nanotube fibre is one of the most promising new materials due to the excellent combination of macroscopic properties (mechanical, electrical and thermal) and its particular hierarchical structure. Individual CNT is defined as a basic structural block, thus, CNT fibre combines the properties of a solid monolithic material but coexists with mesoporous structure, providing a high surface area (260m^2/g). Kilometres of continuous macroscopic fibre of control number of layers are synthesised, tailored by the addition of sulphur as a catalyst promoter during chemical vapour deposition (CVD) in the direct spinning process. Further chirality distribution is obtained in SWCNT sample, showing the predominance of arm-chair and metallic behaviour. Distribution of chirality angles matches with the theoretical predictions for CNTs produced by a molten catalyst. Polymer fibre spinning principles are inspired the highly oriented CNT fibre by reducing the entanglements in gas phase through CNT dilution. Increasing the friction during its furnace extraction until ratios over 17 times, compare to the carrier gas. The resulting fibre obtains mechanical properties similar to commercial fibre as Kevlar. Specific strength and Young´s modulus are in overall 1.1 GPa and 60GPa, respectively, tuning the strain from 23% to 8% with toughness over 80J/g. Moreover, electrical conductivity reached until 3.5 x 10^5 S/m. Internal porous structures and the building block interactions are analysed in detail by BET, BJH and XRD techniques, illustrating the links presented at different scales. Finally, it is studied whether different critical parameters of the synthesis are reproducible scaling-up the process, permitting the development of macroscopic devices for different applications.

Resumen

Debido a la combinación de propiedades macroscópicas (mecánicas, eléctricas y térmicas) y su estructura jerarquizada, la fibra de nanotubos de carbono es uno de los materiales más prometedores. Los nanotubos de carbono actúan como bloques básicos en la fibra, de este modo, la fibra puede combinar las propiedades de un sólido monolítico, junto con la de una estructura mesoporosa, alcanzando una elevada área superficial (260m^2/g). Mediante el método de hilado directo es posible la producción de kilómetros de fibra macroscópica continua, controlando el número de capas añadiendo azufre, que actúa como promotor del catalizador en la reacción de deposición química en fase vapor (CVD). Se ha determinado también la distribución de quiralidades en fibra de CNTs de una sola capa, siendo *arm-chair* la predominante, proporcionando a la fibra de un comportamiento metálico. Esta distribución de quiralidades encaja con las predicciones teóricas para tubos sintetizados por un catalizador en estado fundido. Se ha utilizado el conocimiento ya existente de las fibras poliméricas para conseguir la síntesis de fibras orientadas, reduciendo el número de entrecruzamientos mediante la dilución de la muestra en el aerogel. En estas condiciones de reacción es posible extraer la fibra hasta 17 veces más rápido que la velocidad del gas en el interior del reactor, incrementando la fricción que permite la orientación. Las propiedades mecánicas obtenidas son similares a las de fibras comerciales como el Kevlar, obteniendo valores de fuerza específica y módulo de 1.1 GPa y 60 GPa, respectivamente, pudiendo modificar la elongación entre el 23% y el 8%, con tenacidades del orden de 80J/g. Además, se logró obtener una conductividad de 3.5 x 10^5 S/m. A través de técnicas como el BET, BJH y XRD es posible conocer las conexiones que existen en el interior de la fibra a diferentes escalas. Finalmente, parámetros críticos de la reacción han sido escalados, facilitando su aplicación en la industria, permitiendo el desarrollo de dispositivos macroscópicos para diferentes aplicaciones.

List of Abbreviation and Symbols

AFM	Atomic force microscopy
ALO	Agricultural land occupation
BCC	Body centred cubic
BET	Brunauer-Emmett-Teller gas adsorption
BJH	Barret Joyner Halenda
BWF	Breit-Wigner-Fano
Bφ	Orientation distribution
CAI	Centro de apoyo a la investigación
CCI	Catalyst co-injection
CNT	Carbon nanotube
CPD	Catalyst pre-deposition
CVD	Chemical vapour deposition
Ds	Fractal dimension
DW	Double wall
EDLC	Electric double layer capacitor
EDS	Energy dispersive x-ray spectroscopy
FCC	Face centred cubic
FD	Fossil depletion
FE	Freshwater eutrophication
FE	Freshwater ecotoxicity
FHH	Frenkel Halsey Hill
FIB	Focused ion beam
FWHM	Full width at half maximum
GC	Gas chromatography
Gr	Grashof number
GWP	Global warming potential
HRTEM	High resolution TEM
HT	Human toxicity potential
iPP	Isostatic polypropylene
IR	Ionising radiation
IUPAC	International union of pure and applied chemistry
Kp	Porod constant
L3	Average length of structural units along fibre axis
LCA	Life cycle assessment
LCIA	Life cycle impact assessment
Lp	Average lateral size of the pore
MDP	Metal depletion
ME	Marine eutrophication
ME	Marine ecotoxicity
MW	Multi wall
NCD	Non crystalline diffraction
NLDFT	Nonlocal density functional theory
OD	Ozone depletion
OEA	Organic elemental analysis
PBO	Polybenzoaxozole
PE	Polyethylene
PMF	Particulate matter formation potential
POF	Photo oxidation formation
Pr	Prandtl number
Q	The invariant/Scattering power
q	Scattering vector
RBM	Radial breathing mode
Re	Reynolds number
Rg	Radius of gyration
SAED	Selected area electron diffraction
SAXS	Small angle x-ray scattering
SEM	Scanning electron microscope
SG	Specific gravity
SW	Single wall
TA	Terrestrial acidification
TC	Transcrystalline
TE	Terrestrial ecotoxicity
TEM	Transmission electron microscope
TGA	Thermogravimetric analysis
ULT	Urban land transformation
WAXS	Wide angle x-ray scattering
WDEPL	Water depletion
XPS	X-ray photoelectron spectroscopy
XRD	X-ray diffraction

Table of contents

1 Introduction

During this work, we are going to be immersed in the exciting world of the carbon nanotube materials. Particularly, which are synthesized by direct spinning method from chemical vapour deposition (CVD) reactor. Multifunctional nanocomposite group, enrolled in IMDEA Materials institute, is focused in the synthesis of carbon nanotubes (CNT) in macroscopic architectures for real applications. This promising method has critical questions that it has to be answered for obtaining the real potential, including: how can we control the CNT type? In terms of number of layers, chirality; how can we control the alignment of the CNT bundles? Which leads to the next question: is it possible to tune the macroscopic properties of the fibre? And finally, how scalable is the production process from lab-scale to the industrial factory? Along the chapters, this dissertation offers the opportunity to advance in this specific subjects along the chapters.

Literature review is presented in chapter 2, focusing on the synthesis of CNT by CVD reactor and the particular parameters related to the direct spinning method as well as the properties and application obtained.

CVD reactor and the experimental techniques are shown in chapter 3.

Understanding the chemistry of the reaction is the first step for controlling the synthesis of macroscopic. It is evaluated the importance of the main elements as sulphur, iron and carbon, as well as its interaction. Role of sulphur is described in detail, being responsible for controlling the type of tubes in terms of number of layers. Controlling type of CNTs permits us to produce SWCNT fibre for studying the distribution of CNT chiralities, showing the predominance of armchair-metallic. Sulphur is associated directly to the metal catalyst, studying its structure and composition, defining the position in the isothermal section of C-Fe-S ternary diagram and the role of interfacial energies. Finally, the presence of impurities in the fibre has been reported, emphasising in the iron catalyst particles stick or trapped into the fibre, carbonaceous impurities and silicon-based compounds. Synthesis information is presented in chapter 4.

In chapter 5, it is presented a method to spin highly oriented continuous fibre of adjustable CNT type, with mechanical properties in the high-performance range by lowering the concentration of nanotubes in the gas phase, up to 55m/min. Applying these principles then, high-performance fibre are produced under dilute conditions and high draw ratios, obtaining mechanical properties in the range of 60 GPa/SG and 1.1GPa/SG in tensile modulus and strength.

Chapter 6 presents the CNT fibres as nanostructure building blocks, forming a hierarchical structure. CNT fibre combines the properties of a solid monolithic material, such as high strength and stiffness, but coexists with a large porosity, similar to that of an activated carbon. Hierarchical structure covers different scales, therefore, the fibre is characterised by BET, BJH and XRD (WAXS and SAXS), confirming by SEM and TEM. Particular emphasis has been placed on orientation and densification imparted during assembly. Finally, optical properties from CNT films are discussed.

Direct spinning from CVD reaction is one of the most promising process for a large-scale production of CNT materials. It is possible to produce a large amount of materials and in different architectures. Along chapter 7, there are evaluated different industrial issues as; controlling the nanostructure and the microstructure of the fibre at different precursor feed rates, its environmental impact through the LCA analysis and the applications performed in the multifunctional nanocomposites group (energy storage devices, sensor, composites, etc.…).

Final conclusions and the future work are presented in chapter 8.

2 Literature review

2.1. Carbon nanotubes

2.1.1. Structure

CNTs can be visualised as graphene sheets rolled up forming a hollow tube with cylindrical structure. CNT were first related to fullerenes by Iijima in 1991[1]. In CNTs, carbon atoms are strongly bonded by sp^2 hybridisation (σ-bonds), establishing a hexagonal lattice with 120º angle. In term of number of layers, CNT are mainly classified in two categories: single[2] [3] and multi-wall[1] (SWCNT and MWCNT, respectively). The different layers are separated by ≈ 0.344nm[4], related to the distance between turbostratic graphitic planes and more precise by according to the empirical equation; $d_{002} = 0.344 + 0.1.e^{(-D/2)}$ [5]. Where D is the local diameter.

The diameters of CNTs are in the range from 0.7 to tens of nanometres. It is worth mentioning that the low ratio between number of layer/ diameter promoted the self-collapse of CNTs[6]. E.g. SWCNTs are collapsed over 5nm [7]. It is also observing that the SWCNT with diameter over 10nm can self-fold and remain stable with this addition layer[8], same architecture is described bending a single graphene layer[9].

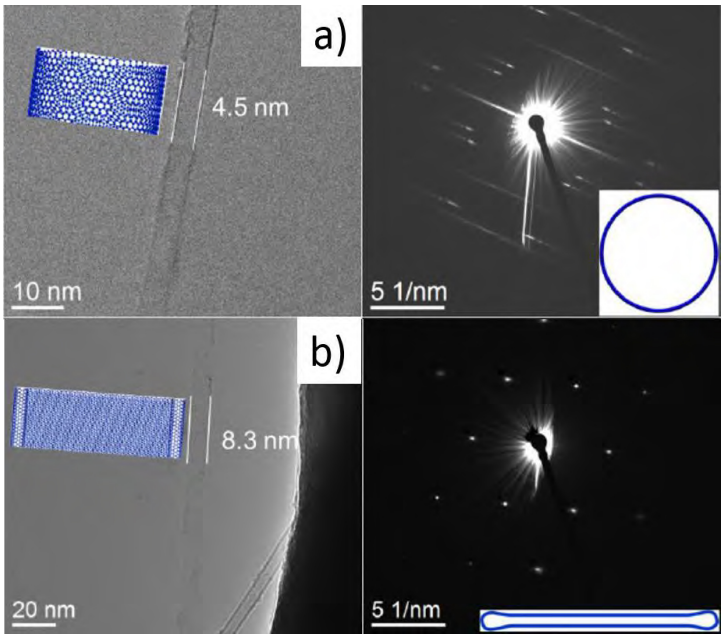

Figure 2.1. TEM images and ED patterns of a (a) round compare to a (b) collapse CNT[7].

This effect is a balance between the surface energy, van der Waals interaction between the adhering layers and the elastic energy, associated to the curvature energy[7]. Figure 2.1 shows TEM micrographs and electron diffraction patterns compared a circular and a collapse CNT.

One of the main characteristics of CNTs is the diameter/length ratio, then CNT length is between 1 and 7 orders of magnitude longer than the diameter[10].

Another important parameter for the CNT structure is the chiral angle. Which structure relates geometrically it to a graphene sheet by the chiral vector[11], $C_n = na_1 + ma_2$. This equation defines the direction of rolling of a sheet relative to the origin (0,0). Figure 2.2.a shows schematic representation. Depending on the chiral angles, SWCNT structure belongs to one of these three groups: zig-zag (θ = 0º; m = 0), armchair (θ = 30º; m = n) or chiral (0º< θ < 30º) (figure 2.2.b).

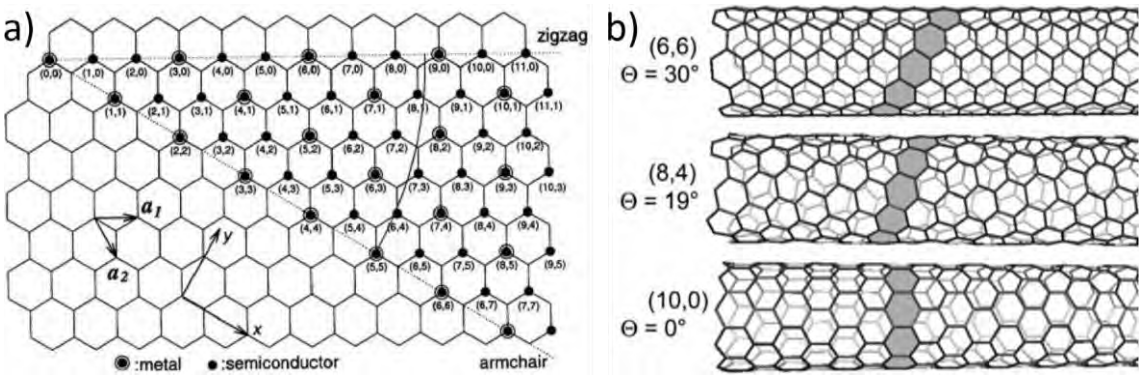

Figure 2.2. (a) Schematic of a graphene sheet with unitary vectors a_1 and a_2, showing the rolling possibilities from the origin to a point (n,m) in the lattice[12].(b) Three typical CNTs with different chiral angles: 30º, 19º and 0º, armchair, chiral and zig-zag respectively[13].

Chiral angles are defined through its (n,m) indices by:

$$\theta = \arctan\left(-\frac{\sqrt{3m}}{2n+m}\right) \quad Equation\ (2.1)$$

Furthermore, it is possible to extract the diameter of the CNT by the following equation. Where a = 1.42 x √3 Å.

$$\Phi = \frac{a\sqrt{(m^2 + mn + n^2)}}{\pi} \quad Equation\ (2.2)$$

CNT typically have some defects in the carbon lattice[14], such as vacancies, 5-7 defect, functional groups and topological defects[15] (figure 2.3.a-b). The

presence of defects, affects significantly the properties of individual CNTs. For example, one vacancy can decrease 30% CNT tensile strength values, and 50% with 3 vacancies[16].

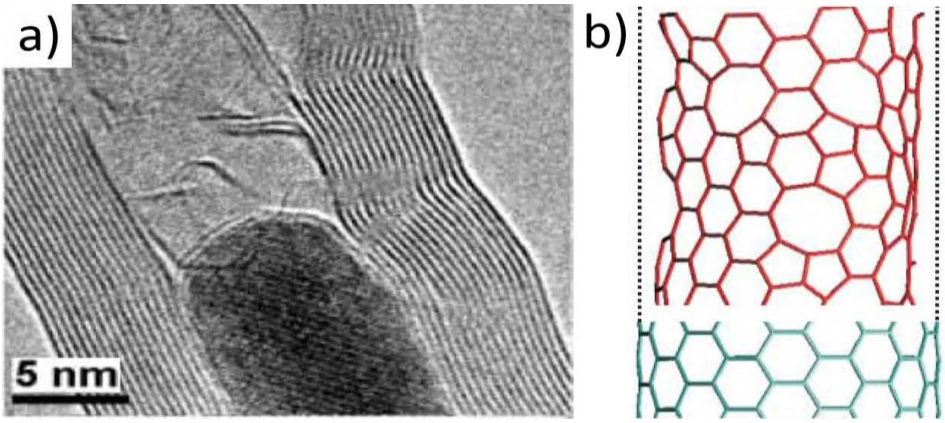

Figure 2.3. (a) TEM image shows the change in direction of the lattice planes in a MWCNT. (b) Atomic carbon networks of an armchair CNT with (in red) and without defects (in green)[14].

2.1.2. Properties

Mechanical properties: Early theoretical studies predicted a young modulus in range from 0.40 to 1 TPa[17]. Experimental measure results give SWCNTs tensile strength in the range from 13 to 52GPa and Young´s modulus between 320 and ≈1TPa[18] [19] [20]. MWCNTs have tensile strength in the range from 63GPa to 110 GPa and Young´s modulus also ≈ 1TPa[21] [22]. Measurements on 10 cm long triple-WCNTs are in agreement with these values. Theoretical and experimental results are in the same order of magnitude to the single graphene sheets [23] [24].

The wide range of values for young modulus and tensile strength arise because of differences in sample composition, but also because the difficulties to précising determine, the diameter (10^{-9} m) and the length (10^{-3} -10^{-1} m) of the CNTs , as well as in assigning a cross-section.

Electrical properties: Theory predicts that the electrons can flow ballistically through SWCNTs and the conductance is quantised, since the conduction occurs through discrete electron states. Quantised conductance results from the electronic wave guide properties of extremely small wire diameters and constrictions[25]. However, on the length scale of the sample used in this work this effect is not observable.

SWCNT chirality is an important characteristic for electrical properties. The molecular structure is directly related to their (n,m) indices. All armchair SWCNTs have a metallic behaviour whereas zig-zag SWCNTs have to fulfil the condition (2n + m) / 3 = integer. The ratio between semiconductor and metallic is 2:1 in zig-zag SWCNTs. In view of the different electronic properties of SWCNTs, depending on their chiral angle, there has been a continuous effort for many years to grow SWCNTs of specific chiralities. Relating the properties of MWCNT to those of SWCNT is difficult since the electrical properties depend not only on the chiral angle of the various layers but also their separation[26], but for ~ > 5 layers, they are metallic.

The electrical conductivity of SWCNTs have been estimated theoretically to be 10^8 S/m[27] [28], similar results were reported experimentally[29], while for individual MWCNTs, the value obtained was 10^6 S/m[28]. For an ideal graphene sheets, the conductivity has been estimated theoretically as 10^8 S/m [30]. MWCNT could be potentially limited by the electron transfer between layers, same effect could be detected in macroscopic architectures, between the CNT crystals or links.

CNT properties are summarised in the table 2.1. The results are compared to related materials as graphene or graphite and references as high-performance commercial fibre, copper or steel.

Table 2.1. Properties of the CNT, compared to relate and references materials.

Material	Strength (GPa/SG)	Stiffness Modulus (GPa/SG)	Electrical cond. (10^6 S/m)	Thermal cond. (W/mK)
SWCNT bundle	52[18]	1000[18]	100[29]	120[31] - 5800[32]
MWCNT	63[22]-100[21]	1000[21]	1[33]	700 [34]– 3000 [35]
Graphene	130[24]	1000[24]	100[30]	5000[36]
S2 Glass[a]	4.9	87	-	-
Aramid[b]	3	112	-	-
Steel 371	0.4[37]	210[37]	-	-
Copper	-	-	58[38]	-
Graphite (parallel)	-	-	-	3000 - 4000[39]
Graphite (perpend.)	-	-	-	100[39]

[a] Hex Tow®AS4 [b] Kevlar®49(K49)

2.1.3. Synthesis of CNTs by Chemical Vapour Deposition (CVD)

Owing to its higher degree of control and its scalability, CVD is now the predominant method for growth of CNTs. CVD involves the decomposition of gaseous or volatile carbon compounds in the presence of catalyst nanoparticles to form CNTs[40]. Furthermore, it is economically attractive and under special synthesis parameters can be used to produce macroscopic CNT-architectures with large quantity of CNTs. For these reasons, there has been wide research on the growth of CNTs by CVD. In order to improve the quality or the amount of CNT, there have been several modifications of this process including oxygen[41], plasma[42], vapour[43] or radio-frequency[44]. Figure 2.4 shows a typical CVD set-up.

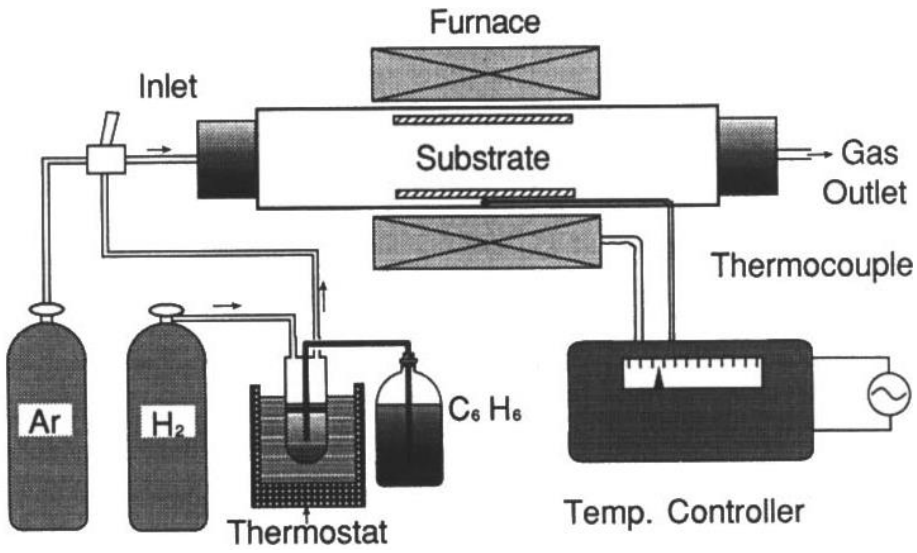

Figure 2.4. (a) Set-up for CNT production by CVD[40].

2.1.3.1. Carbon source

A wide range of carbon sources has been to grow CNTs, including hydrocarbons, aliphatic carbons or aromatic compounds. The main differences between the different sources to produce CNTs are the thermodynamic decomposition route.

Figure 2.5.a reports the standard Gibbs energy of formation for different possible carbon sources at different temperatures. Thermodynamic stability is a critical parameters to analyse the decomposition route of the carbon precursors. For example, methane requires temperature over 700ºC to be less stable than graphite. The decomposition products are mainly carbon and hydrogen[45]. The presence of secondary elements in the carbon sources are mainly hydrogen and

oxygen. Which can play and important role to tune the CNTs in the reaction; improving the graphitisation[46] or the kinetic in the CNT growth[47]. Carbon sources are carried through the reactor by a carrier gas as inert gases; helium or argon; nitrogen or hydrogen.

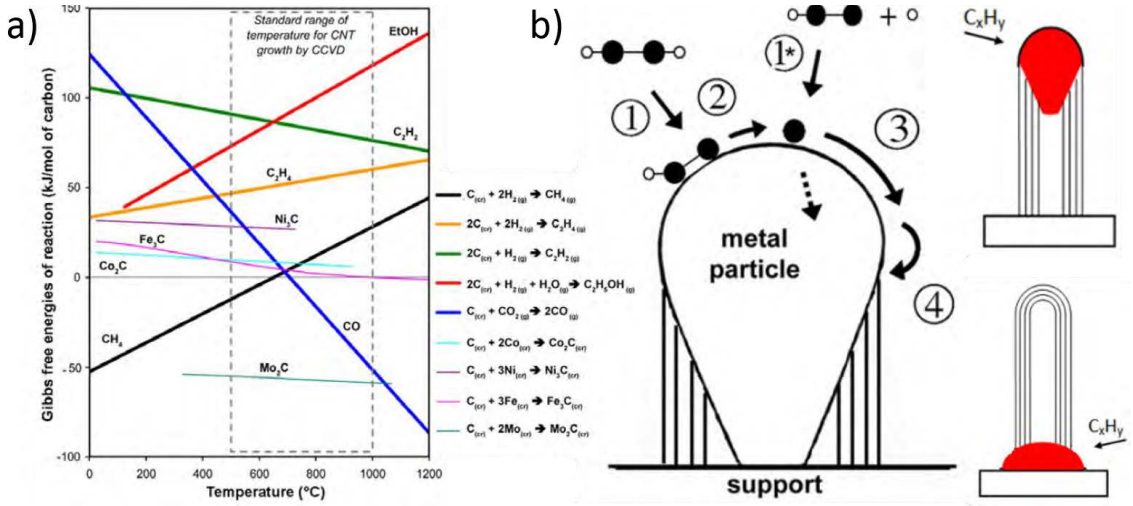

Figure 2.5. (a) Gibbs free energy of reaction per mole of carbon against the temperature of different carbon sources[45]. (b) Schematic growth model with the different stages[48] and the tip-growth model and base-growth model adapted from[49].

2.1.3.2. Catalyst

Catalyst is critical to break the carbon source bonds, diffuses the carbon, creates a template to stabilise the nascent CNT and being active during long time. Figure 2.5.b shows the different stages for growing a CNT.

Carbon dissociation: Carbon source in contact to the catalyst particle decreases the activation barrier for its dissociation. This barrier is related to the nature of the catalyst. The carbon source is dissociated in intermediate hydrocarbon or isolate atoms depending on the reaction temperature[50].

Carbon solubility and diffusion: The affinity between metal catalyst and carbon is critical to grow CNTs and it is related to the vacancies in d-orbitals. Low vacancies lead to low affinity (Zn or Cu). While, high unfilled orbitals as Ti, Co are established strong bonds with carbon. Intermediate states are provided by transition metals as Fe[51], Ni[48] and Co[45], which are the most widely used catalyst[52]. The affinity is directly related to the solubility and it was reported the critical importance of the solubility to growth CNTs[53]; Cu shows a carbon solubility ≈ 0.01%at, compared with iron, which can increase until 4%at at 800ºC

for FCC Fe. However, the solubility in nanoparticles is not well established, finding a dramatic increases in solubility in nanometre particles[54].

One of the most controversial aspect in the synthesis of CNTs is to understand the carbon diffusion in the catalyst. The diffusion mechanism during the CNT growth is divided in mainly two theories; surface and bulk diffusion.

Carbon bulk diffusion depends on the crystal phase, increasing in more open structure. E.g. FCC iron diffuse more the carbon compare to BCC. The bulk diffusion of carbon atoms (interstitial diffusion) is much faster than metal diffusion (substitutional diffusion)[55]. Moreover, melting point is inversely related to diffusion (higher melting point, lower the diffusion).

Surface diffusion has the activation barriers lower than bulk diffusion[48], predicting its predominance in diffusion through the catalyst. Experimentally, it was found the important dependence between the surface diffusion and the catalyst size[56]. Although, the diffusion through the surface is not already very well-known. In future work, it will be important to describe in detail to control the synthesis of CNTs.

Due to the wide range of temperature from 450ºC to 1250ºC, the physical state of the catalyst is critical. Thus, it can modify catalyst solubility or diffusion of carbon. Many aspects have to be considered; nanoparticles size and that the presence of other elements decrease sharply the melting point[57] [58]. Carbon solubility is 0.8wt% in FCC Fe at 723ºC and 4.3wt% in liquid Fe at 1148ºC, these values are directly extracted from the binary Fe-C diagram phases.

CNT growth: Catalyst particles are provided the template to the CNT to be extruded. In many reports, it was found directly correlation between the CNT diameter and catalyst size[59] [60]. It is unusual to find an active catalyst particle with a round shape[61], instead being elongated in the direction of CNT extrusion saturation of carbon in the catalyst can fixed the iron structure, preventing iron deformation[62]. The interaction between carbon and catalyst depends on carbon architecture. Interaction between individual carbon atom and metal is strong, allowing carbon diffusion in the catalyst, although the interaction between a graphene layer and the metal is very weak, repelling the layers during the CNT extrusion.

Contrary effects was reported modifying the reaction temperature. Which leads to bigger [63] and smaller CNTs[64], this effect can be related to the shape and not directly related to the size.

Not all the catalyst particles are extruded a CNT, the inactive catalyst particles are encapsulated by a graphitic layer. Thus, it was explained by the supersaturation of the catalyst with carbon[65]. Moreover, It was reported that the catalyst size is not directly related to inactive particles[66]. The proportion of active particles is varying in a wide range from 0.5% to 20%[67]. Which are relatively low values. This implies that controlling the carbon concentration in the catalyst can lead to increase the efficiency in the reaction.

CNT length is another important parameter that can vary from several nm (10^{-9} m) to cm (10^{-2} m). Similarly, growth rate varies sharply from nm/min to μm/s. The length is usually directly linked to the lifetime of the catalyst. Thus, the growth rate decreases with CVD reaction time[68]. It is also studied the directly relationship between the growth rate and the chiral angle under identical conditions, being favourable the synthesis of armchair CNT[69].

Limiting step control is a controversial subject. In temperature ranges from 150 to 650ºC, there are two hypothesis. First hypothesis supports the idea that diffusion through catalyst is the determining step[70]. While other analysis concluded that the carbon source decomposition is the limiting step[71]. It is worth mentioning that these effects tend to disappear increasing the temperature in the CVD reactor upper 800ºC [72]. There is no conclusion related to the influence of the catalyst size in the growth rate [73] [74].

Catalyst lifetime is mainly affected by two parameters; temperature and the concentration of the carbon source. In principle, there is a critical temperature, in which the tendency of increasing the temperature decrease the lifetime changes ≈ 850ºC[75]. Concentration of carbon source affects decreasing the lifetime as it was reported by Futaba, in this work lifetime was increased adding water as an oxygen source [76].

Floating catalyst can lead to synthesised ultralong CNTs. Almost all the works reported long CNTs are produced by direct spinning from CVD, and it is further explain in details in next section. Temperature and appearance of a promoter are

the main distinction between the conventional growth methods. The differences between mechanism is due to the catalyst size and the interaction between the substrate and the catalyst particle (figure 2.5.b)

Numbers of walls: It is also linked to the catalyst size, larger diameter and tubes with more layers are synthesised using bigger catalyst[77]. Very interesting results were analysed. It was reported that is possible to tune the number of layers in the CNT decreasing the precursor feed rate, suggesting that the increase in the concentration of carbon in the catalyst particles leads to decrease the number of the layers[78] [45]. Moreover, In situ growth observations concluded that the number of layers extruded by a particular catalyst can decrease along its growth[66]. This fluctuation in the number of walls can be related to the saturation of carbon in the catalyst, affecting in turn to the catalyst shape. Concluding the fact that the control of carbon concentration in the catalyst is the critical parameter.

The CNT growth processes by CVD can be divided in two main groups in terms of location of the catalyst. Firstly, the addition of the catalyst is mixed with the carbon source, which is named as *catalyst co-injection* (CCI), temperature range is between 1000ºC – 1250ºC [79] [80], and *catalyst pre-deposition* (CPD) with catalyst pre-deposition on a substrate, which is exposed to the carbon source with temperature in the reactor between 300ºC- 800ºC [81].

2.2. Direct Spinning from CVD reactor.

The CNTs grow very fast in the gas-phase and form an aerogel that can be continuously withdrawn from the reactor as a fibre[80]. Some of the parameters that affect the growth of CNTs in this fibre spinning process are the carbon source, the catalyst, the promoter (sulphur, selenium and tellurium), furnace temperature, injection position and gas as the most important.

The scheme in figure 2.6 shows the schematic of the direct spinning process, collection CNT fibre over a substrate.

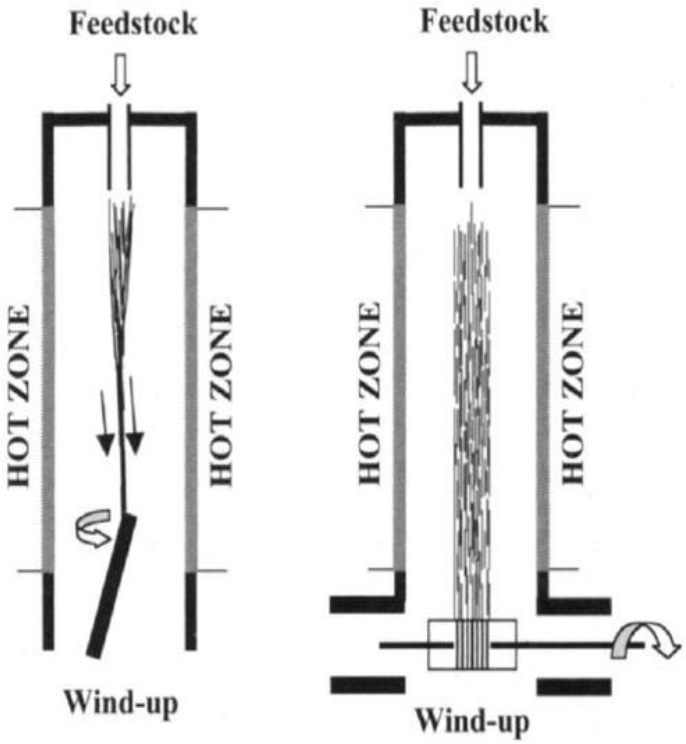

Figure 2.6. Schematic of direct spinning process, collecting CNT fibre over a winder[80].

Mainly CVD publication are related to grow at low temperature with reaction times from minutes to hours. In this work the reaction described, correspond to synthesis at high temperature, which lead to instantaneous reaction (seconds). Catalyst particles are melted and it is possible to spin fibre continuously. The synthesis and structure of CNTs are made by this method and it is the main subject of this report. This method provides the ability to synthesise nanotubes with certain control of their number of walls, dimensions, and introduced dopants, among other parameters.

Table 2.2 summarises the differences between the reaction at low and high temperature. Therefore, it is a big challenge to understand and control the synthesis at high temperature. During this work, the synthesis and structure of CNTs are made by this method and it is the main subject of this report.

Table 2.2. Summarises the main differences between CVD reaction at low and high temperature.

	High Temperature	Low Temperature
Temperature (ºC)	1100 - 1300	450 - 850
Reaction time	Few seconds	From min to hours
Catalyst Activity	0.05%	~ 20%
Catalyst State	Molten	Solid
Substrate	No	Yes
Promotor	Yes (group 16)	Without
Continuous Spun	Yes	No
Growth Rate	1µm/s	1nm/s

2.2.1. Molecular control: Current understanding

2.2.1.1. Carbon source

CNT fibres synthesised from ethanol[80] [82] [83] [84] [46], methane[85] [86] [87] [88] [89] acetone [90] [91], hexane[46], toluene[92] [89] and butanol [89] have been reported. These carbon sources have different decomposition routes. Aliphatic carbons start the decomposition route around ≈ 400ºC[93] [94], while the aromatic ring is broken over 900ºC [95] in carbon sources as toluene. The main products of the decomposition at reaction temperature are mainly atomic carbon, hydrogen, and secondary elements as oxygens, which are also present in some carbon source stoichiometry[96]. The decomposition temperature indicates the availability of carbon in the reactor, allowing to determine the decomposition sequence in comparison with the catalyst and promotor source. Consequently, decomposition sequence affects to the CNT synthesis , modifying the carbon diffusion into or over the catalyst particles[97] to extrude the CNTs for producing the fibre [90] [98].

Not only decomposition route affects to the reaction but also its concentration. Carbon atom concentration in the reactor is an important factor; high level of carbon concentration entails catalyst deactivation due to carbon encapsulation or producing amorphous carbonaceous material. On the other hand, low levels of concentration implicates low possibilities of collision with the catalyst[99].

Carbon and hydrogen are present in all the carbon sources, moreover secondary elements are depending on the compound, as oxygen. Which, in appropriate

quantities, is also observed to increase catalyst lifetime and result in faster growth rate and longer CNTs[45].

2.2.1.2. Catalyst particle

2.2.1.2.1 Catalyst structure

Several variety of metal transition have been used in CNT synthesis by CVD at low temperature as Fe[59], Co[100], Ni[101]. Nevertheless, Fe is the only one in that has been successfully used for the direct spinning. In all cases the source of Fe is ferrocene, which itself contributes with carbon to the reactor.

The synthesis of specific CNT requires careful study of the catalyst particle. There is comparatively much more well-established in low temperature CNT synthesis by CVD[45] but it is difficult to relate to the direct spinning method; at low temperature, catalyst surface is not in molten state[102] as it was presented in the table 2.2. Experimental evidences situated the transition between solid and molten state between 850 and 1100ºC, temperature can vary depending on the catalyst size[58], evidencing a significantly decrease in nucleation density and the lifetime[103]. Some experimental observation are discussed in the literature. Catalyst size is directly related with the CNT diameter[84] [90]. Moreover, modifying catalyst formation adding a promoter, is possible to promote the selective growth of CNTs: single or multi wall[104] and control their chirality[105].

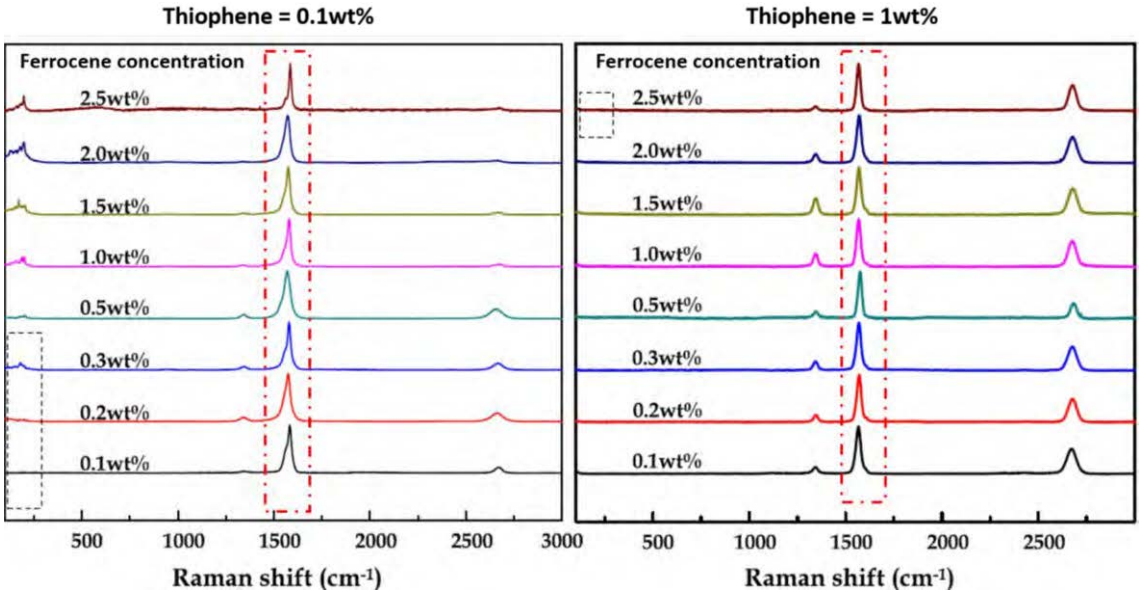

Figure 2.7. Raman spectra of CNT fibre produced with different amount of ferrocene, establishing the thiophene concentration at 0.1%wt and 1%wt, respectively. Adapted from Jung et al.[82]

Because of the observed correspondence between catalyst particle size and catalyst diameter in traditional CVD, various reports assumed that a greater availability of Fe would lead to the particle coarsening in the gas phase and to the formation of larger diameter CNTs in the direct spinning process. Jung et al for example claimed that synthesis of SW was affected mainly by the concentration of ferrocene, modifying also the ratio of raman intensities I_D/I_G.[82] However, figure 2.7 shows a negligible change in raman spectra increasing ferrocene concentration more than one order of magnitude. It is remarked the absence of RBM when the amount of ferrocene increase (RBM is measured with 514nm laser, which is the less favourable in promoting radial vibrations [85]); nevertheless, peak G is not analysed in detail, which is clearly similar in all the ferrocene concentration (emphasised by red dash line).

The presence of more ferrocene itself, it produces a negligible change in the type of carbon nanotube. Consequently, catalyst particle is closely linked with the promoter, affecting to the intrinsic catalyst properties.

2.2.1.2.2 Promoter

The main characteristic of direct spinning method, it is the capacity of the reaction to enable a continuous spinning. This is possible by adding a small amount of promoter, which increases the growth rate and length of the CNTs. Typical promoter is sulphur, through different sources as thiophene [82][92], carbon disulphide [85] or sulphur[73], but the same effect is found synthesising in presence of selenium and tellurium[8]. Different promoter sources lead to different decomposition routes and availability along the reactor, affecting directly to the CNT growth.

The promoter together with iron forms a sulphur-rich phase in the catalyst surface, allowing to limit surface diffusion of carbon in the particle. Iron sulphide is in the catalyst surface[104] producing different types of CNTs, modifying the CNT chirality. Average catalyst size decreases with reduction in the promoter content [106]. Therefore, At higher concentration of thiophene in the feedstock, bigger CNTs and with more layers are produced[90]. This shows that although particle size affects CNT diameter, the size effective particles is dictated by the concentration of promoter. Furthermore, according to the literature preferential

chirality are obtained using different sulphur sources; armchair and metallic CNTs are promoted with CS_2; whereas employing S or H_2S, CNT fibre contains metallic and semiconducting CNTs[85].

Schematic CNT growth model is presented in the figure 2.8.a, carbon atoms are diffused through a molten Fe-S shell and extrude a CNT.

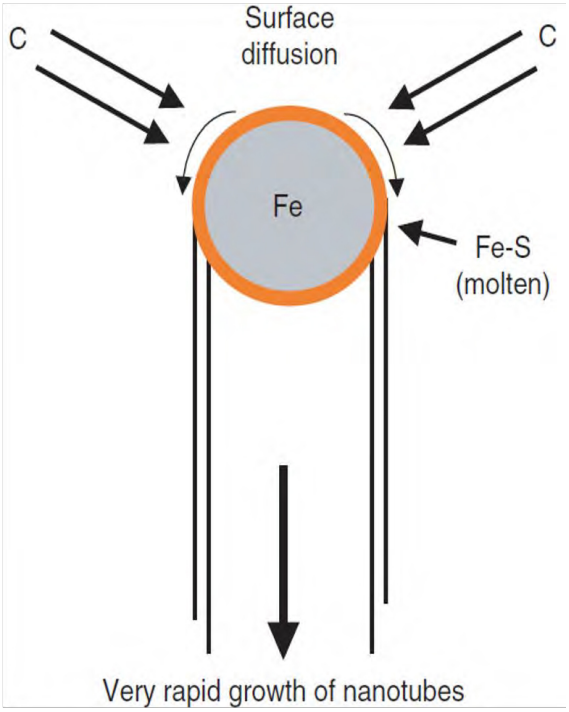

Figure 2.8. (a) Schematic representation of the CNT growth model in the presence of sulphur in the surface[104].

The understanding of the direct spinning process before this work emphasised the important role of sulphur but fail to associate the type of the tubes in terms of number of layer with the ratio Fe/C.

2.2.1.3. Secondary reactants: Hydrogen, oxygen and silicon.

Hydrogen is used as the main carrier gas in the direct spinning reaction, controlling the residence time and the flow rate along the tube.

Hydrogen flow affects to the CNT graphitisation; Motta et al. reported that increasing the hydrogen flow leads to more quality CNTs, while at low flow, the CNTs are thick and poor graphitised[46]. Hydrogen can be helped to control the carbon concentration in the reaction area or reacting with S producing H_2S [92], affecting to the CNT growth. Furthermore, hydrogen is creating a reducing

atmosphere, being the most abundant atom in the reaction area, H_2 ratio is between 60 and 95 at%.

Recent works are trying to replace hydrogen with inert gases as nitrogen[107] and argon[108] [109].However, the quality of the fibre and its reproducibility is already questioned, observing the aerogels and the fibres in the micrographs. Therefore, it is important to understand the interaction between carrier gas atoms and the other reactant, to describe in detail the role in the reaction, which is not well established.

Increasing moderate the hydrogen flow rate leads to displace the reaction deeper in the reactor, where the parameters of the reaction are maintained. Thus, same CNT type are synthesised[110], with the exception of the reactant concentration. Increasing hydrogen dilutes the particles, affecting to the CNT concentration in the reaction area.

Oxygen is present in carbon sources as aliphatic carbon or aromatic compounds, therefore, oxygen atoms are located in the reaction area.

The effect of oxygen has been studied in lower temperature and promoter free CNT growth. The different conclusion are extracted; finding better selectivity in graphitic carbon[10]; promoting the removal of metallic SWCNTs[111] or oxidising the graphitic carbon surrounded the catalytic to revive its activity[43]. However, at high temperature, it is possible to spin long CNTs using oxygen free carbon sources as toluene and methane.

Silicon is the main element of the reactor tube, which is made of mullite or quartz in all the literature. Observing in detail the results, the presence of silicon in the CNT fibre is a constant, being observing mainly by X-ray or EDS [112] [113] [114] [115]. According to the literature, it is possible that the presence of oxide, acting as a substrate, can affect to the synthesis of the CNTs, producing an interface between the oxide and the catalyst [116] and increasing the catalyst lifetime[117].

This work shows the presence of residual Si-based particles in CNT fibres, as observed in sample reported elsewhere. It is originates from the reactor tube, which is made of mullite (62.5% Al_2O_3; 35.2% SiO_2 + impurities)

Tso et al. presented a complete studied comparing the reduction of SiO_2 in different materials in presence of hydrogen atmosphere. The silicon amounts are quite significantly compare with the other elements in the reaction area (figure 2.9).

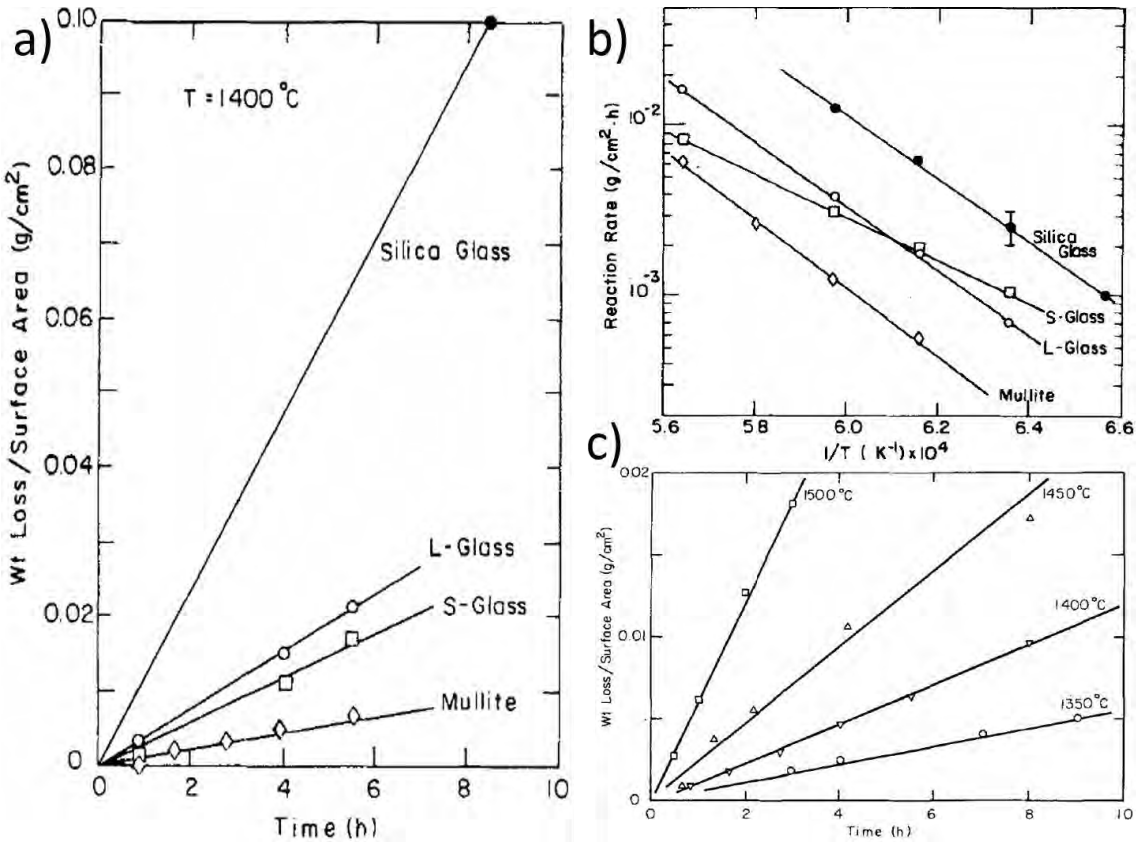

Figure 2.9. (a) Mass loss per area of flowing H_2, (b) reaction rate against the inverse of temperature and (c) mass loss per area at different temperature and exposure times. Plots are made for SiO_2, L/S-Glass and mullite[118].

The reduction reactions are:

$$SiO_2(s) + H_2(g) \rightarrow SiO(g) + H_2O(g)$$

$$SiO(g) + H_2(g) \rightarrow Si(g) + H_2O(g)$$

It worth mentioning that during these work, alumina tube (Al_2O_3) was used in order to produce CNT fibre, being impossible to spin continuously CNT fibre at same conditions than mullite.

2.3. Other methods for CNT fibre spinning.

Synthesis of CNT fibre has mainly other 3 different methods. *Polymer/CNT coagulation route* and *Liquid-crystalline spinning*, which are catalogued as wet

spinning and *Spinning from arrays of aligned CNTs*, together with the previous mention, *Direct spinning from CVD reaction*, which are included in dry spinning methods.

Polymer/CNT coagulation route: It is a simple method to produce continuous polymer/CNT composite. This process consists of a dispersion of nanotubes in surfactant solution into the stream of a polymer, which acts as a coagulation bath[119] (figure 2.10.a). Excess of solvent is subsequently removed. Typical CNT/polymer fibre composition obtained is 60wt.% nanotubes. The different properties of the polymer/CNT fibres are related to the formation of semi-crystalline polymer. When the polymer is mainly amorphous, the fibre shows outstanding values of toughness in tension because of the combination between the nanotubes strength and the tensile elongation of the amorphous polymer domain[120]. For many semi crystalline rather than amorphous polymer, the fibre formed, has higher strength and stiffness although reduced toughness[121].

Liquid-crystalline spinning: Dispersions with superacids[122] or ethylene glycol are mixed together with CNT, obtaining a lyotropic liquid crystalline solution. CNTs are producing in a coagulation bath and continuously spun[123] (figure 2.10.b), similarly to the process to produce poly-phenylene benzo-bisthiazole (PBO) fibres. CNT fibres are flexible and easily manipulated. It also retained any imparted twist and could be knotted. Properties are important for the weaving and knitting. Fibre can be oriented easily due to the short length of CNT (1-100 μm), obtaining promising properties; tensile strength ≈ 1 GPa/SG, stiffness ≈ 120 GPa/SG, electrical conductivity ≈ $3x10^6$ S/m and thermal conductivity ≈ 380 W/mK in specimens of 1.5mm length [124].

Spinning from arrays of aligned CNTs: Aligned CNTs are grown on a substrate. Drawing is possible due to the small separation between CNT fibres and the Van der Waals forces between them[125].To increase the fibre density and improve the interaction between the CNTs, the fibre is twisted at the drawing stage. Typical fibre diameter range is between 1 to 10μm. Figure 2.10.c shows a SEM micrograph reporting a fibre being collected from a CNT array and twisted. The type of CNT is critical to obtain different properties of the fibre. CNTs with fewer layers and longer diameters are reported to result in the fibres with higher

values of strength and stiffness[126]. MWCNT and DWCNT fibres with the same length but comprised of different type of CNT, show different properties. Strength and stiffness values are in the range of 0.8 GPa and 275GPa for MWCNT[127] to 2.6GPa and 263GPa for DWCNT probably collapsed[126]. Electrical and thermal conductivity are also obtained good results, the values reported was $5x10^4$ S/m[47], and 50W/mK [128],respectively.

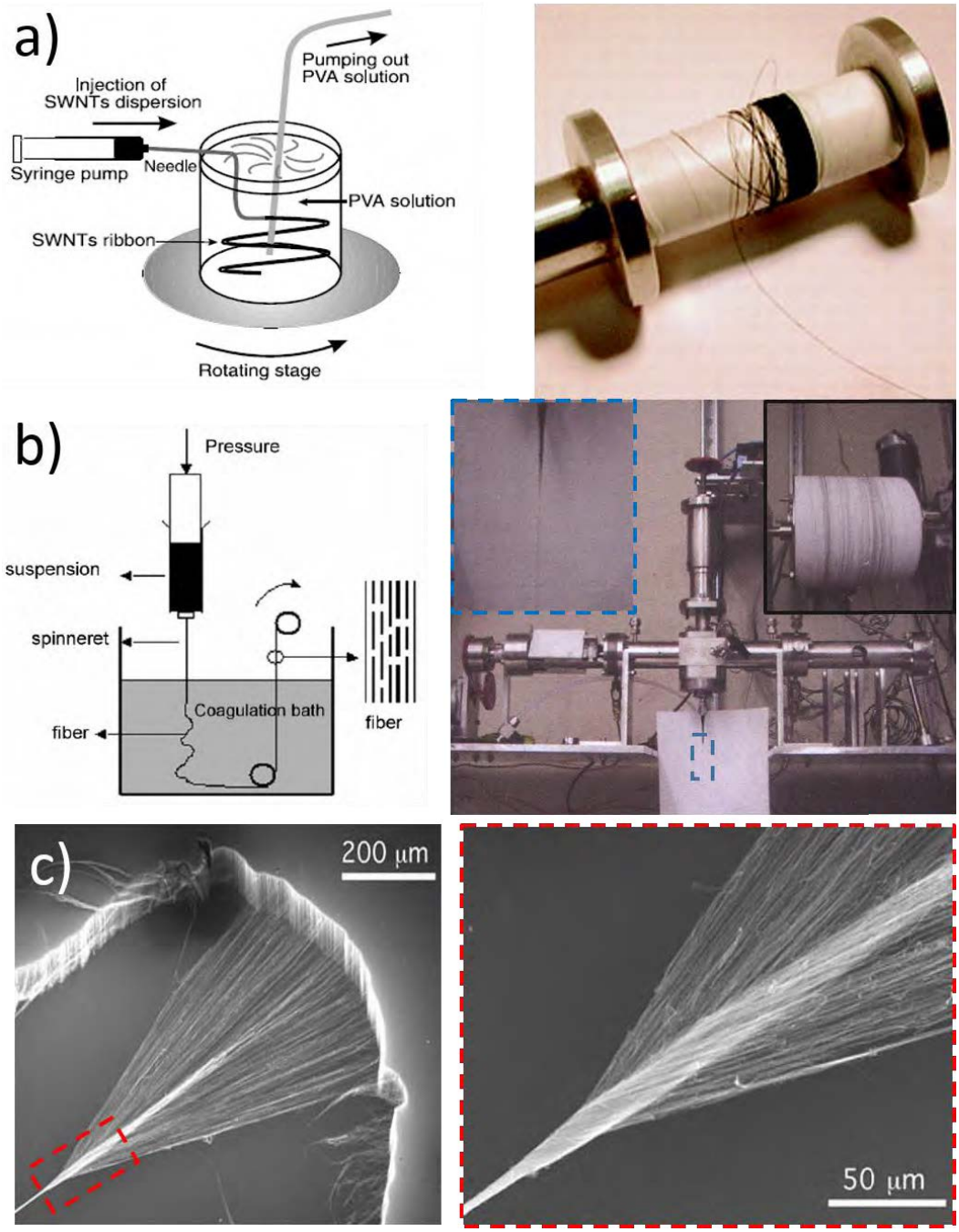

Figure 2.10. (a) Set-up of polymer/CNT coagulation route[119] and the fibre synthesised[121] (b) schematic of liquid-crystalline spinning[129] and the set-up producing fibre[123].(c) SEM micrograph reporting a fibre being collected from CNT array and twisted [125].

2.4. Mesoscopic structure: Drawing inspiration from polymer fibre.

One of the most important challenge associated with the CNTs, it is the exploitation of the exceptional properties on a macroscopic length. The individual nanotube, due to the dimension, is not feasible to use in envisaged applications. Therefore, macroscopic architecture are synthesised, assembling a large number of CNTs.

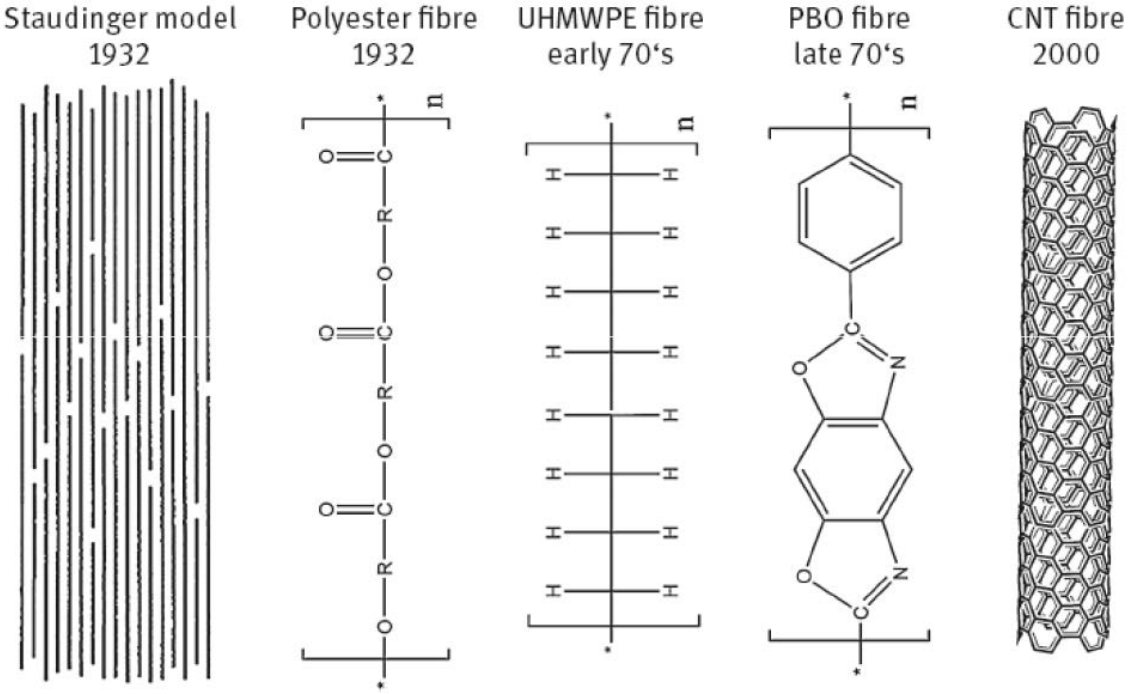

Figure 2.11. Basic structural block of high performance fibre, which is inspiring the CNT fibre production[130].

The ideal high-performance fibre requires alignment of the CNTs parallel to each other along the fibre axis, in an architecture that thus efficiently exploits their axial properties. This arrangement is in the line with Staudinger´s[131] and Carother´s[132] models for producing strong fibres from extended highly oriented molecules, which were proposed more than 80 years ago. These models have been the inspiration for a wide range of high-performance polymer fibre. Figure 2.11 shows the basic structural block of some high-performance polymer fibre (polyester, dyneema or PBO), including CNT [130]. CNTs are indeed similar to polymer chains and can be spun as continuous macroscopic fibres, in a process very similar to polymer fibre wet spinning.

According to the literature, it is proven the effect of the spinning speed increasing the alignment of the CNT along the fibre axis. Though the enhancement in the orientation, it is possible to improve the macroscopic properties (mechanical, electrical and thermal)[133].

In this work, it is demonstrated that the polymer analogy can be extended to CNT fibres produced directly from the gas-phase during CVD. By controlling the dilution of CNTs in the gas phase, it is possible to reduce the number of entanglements in the aerogel, similar to the dilution applied in wet spinning of gel polymer fibres, thus enabling the drawing of the in-forming fibre and alignment of its building blocks.

2.5. Structural studies of CNT fibre

In the macroscopic ensemble the spatial distribution and the interaction between building blocks play a critical part in determining the bulk properties of the CNT fibre. The confluence of multiple length scale also implies that these macroscopic assembles of nanobuilding blocks have a complex hierarchical structure that is in both cases difficult to probe experimentally and to characterise precisely.

Similar 3D structure can be synthesised and studied; bucky papers are produced by vacuum CNT filtration[134] and CNT fibre spun by different methods[135]. Direct spinning from CVD reactor structure is interesting for different reasons, building block can be tuned from SW to MW and bundles can be oriented along the fibre axis producing high-performance fibre in the reaction process.

2.5.1. Gas-adsorption (isotropic analysis)

It is possible to define CNT fibre as a mesoporous structure (after densification). Pore size distribution is calculated in the range from 5 to 60nm in CNT fibre produced by direct spinning[136]. This range is more spread than the values from CNT fibres spun by polymer coagulation spinning, which are distributed from 1.5 to 20 nm[137].

This singular structure allows to infiltrate with liquid[136] or polymer[138] for producing devices for different applications as electrodes or composites. Which is composed by two main phases: CNT bundles and pores. It is observed a

correlation between diameters in both phases, which correspond to ≈50% of porosity[136].

In several applications, the main specification to select the material is the amount of surface area available to interact. Nitrogen adsorption measurement is one of the best technique to obtain the surface area of CNT fibre. It was reported 76 m^2/g [136], 195 m^2/g[139] and 250m^2/g [138] in CNT fibre synthesised by direct spinning from CVD method. Different values can be explained due to the different type of CNT in terms of number of the layers and diameter of the CNTs in the sample, affecting also the packing and dimension of CNT bundles.

2.5.2. X-Ray Diffraction (anisotropic analysis)

2.5.2.1. SAXS analysis

Several structure of high-performance fibres are characterised by SAXS, including carbon fibre[140], Kevlar[141] or PBO[142] (figure 2.12.a-c). As it is mentioned in the previous section, CNT is compared with a polymer chain as a basic structure of the CNT fibre. SAXS scatter is principally depended on the electron density difference between the CNTs and the pores and its volume fraction. SAXS patterns cover distances from ≈ 4 to 100nm.

Figure 2.12 shows typical SAXS patterns from different oriented fibre. Along this axis is extended streak reflection, related to the oriented component, increasing the distance from the beam stop, the intensity decreases sharply.

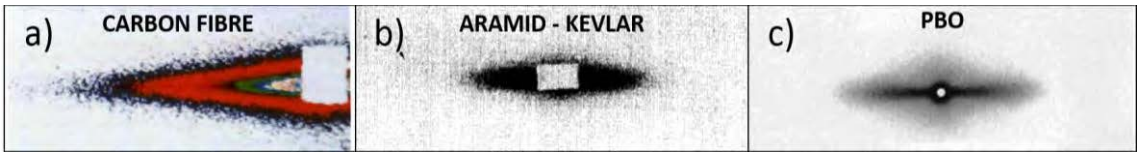

Figure 2.12. 2D pattern of various high-performance fibre (a)carbon fibre[140], (b)Aramid-Kevlar[141] and (c)PBO[142].

For CNTs fibre, unlike WAXS, SAXS interpretation is complicated. Related to the sample; CNTs are not scattered individually, most of them are packed forming bundles, which are not even homogeneous. Thus, this effect can interfered in the results interpretation[143], since the scattering intensity is mainly related to the sequences of different electron density materials. Related to the technique, objects with different structures can produce similar scattering at small

angle[144]. Still, it is possible to extract important structural information from the 2D SAXS pattern of CNT fibre. Qiu et al. could extract from the CNT fibre structural parameters as: the invariant *Q*, radius of gyration R_g, average length of structural units along fibre axis L_3, ,orientation distribution B_ϕ, and surface fractal dimension D_s [136].

Invariant or scattering power *(Q)* quantifies the ability of the CNT fibre to scatter x-rays and it is dependence on the electron density difference and the volume fraction of the two phases. It can be calculated integrating the scattering intensity *I(q)* against the scattering vector *(q)*.

Figure 2.13.a shows a scheme of the CNT fibre, CNTs are extended along the fibre axis and connected with others forming bundles. The bundle orientation are creating elongated pores[130]. Through SAXS information is possible to obtain information from the structural unit predominant in the fibre. A schematic model is reported, defining the L_3 and B_ϕ parameters (figure2.13.b)[145].

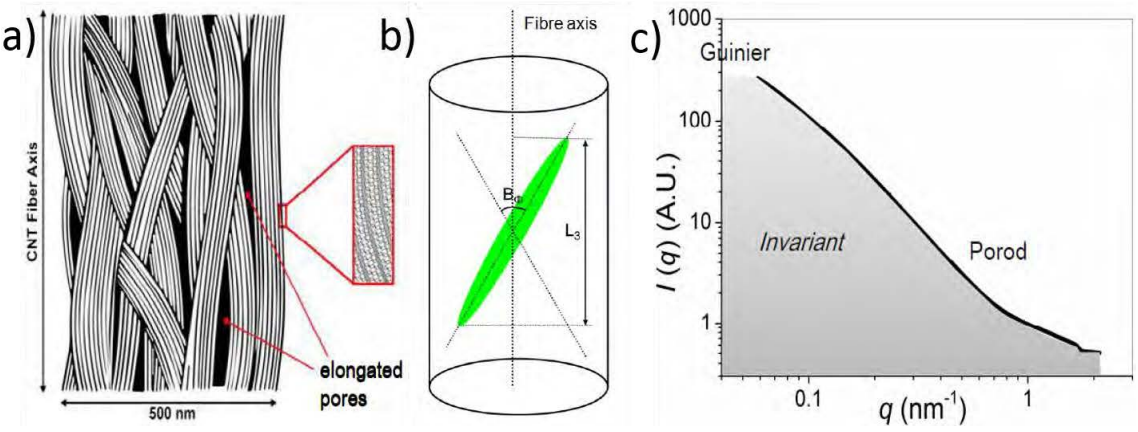

Figure 2.13. (a) Schematic structural model of a CNT fibre, showing the alternation pore/bundle[130]. (b) Scheme of the physical meaning of L_3 and B_ϕ[145]. (c) Radial integration of a typical SAXS pattern with the different regions[130].

Surface fractal dimension is extracted directly from the porod slope (linear intensity decrease region), representing *I(q)* against scattering vector *q;* being $I(q) \propto q^{-(6-D_S)}$[144]. In fractal 3D structures D_s= 2 is related to smooth and D_s= 3 to irregular surfaces [146] . Firstly, it was studied in rocks and coals [147] and it was extended to other CNT structures, produced by different methods as filtration of CNTs dispersed from aqueous solution [148]. It is also included CNT fibre synthesised by direct spinning from CVD reactor. In oriented fibre

Ds≈3[136], comparing to non-oriented fibre obtaining Ds≈2.5[130]. Different values are explained by the wide range of porous distribution due to the different degree of alignment along the fibre.

At higher angles, related to distances between 4 and 11 nm, a shoulder appears in the SAXS integration (figure 2.14.a), being more accused in the oriented CNT fibres. Figure 2.14.b shows two SAXS patterns with different streak intensity perpendicular to the fibre axis, evidencing different degree of orientation. FIB-SEM micrographs are confirming the SAXS observation (figure 2.14.c). This effect is found in different CNT synthesis methods, it is always more evidence in sample, which improves the CNT alignment [149] [150].

Through a simple SAXS analysis, it is possible to obtain a global overview of CNT fibre structure, pore/bundle interaction and CNT orientation along the fibre.

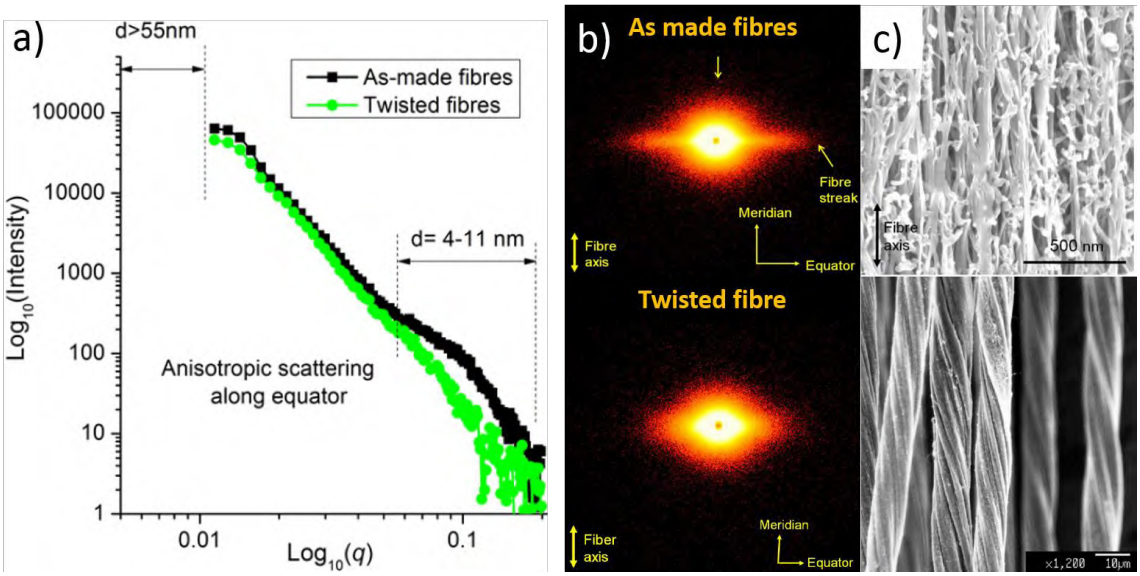

Figure 2.14. (a) SAXS integration for as made and twisted fibre in logarithmic scale. (b) Radial integration is performed, using SAXS patterns, observing different shape in the streak intensity, related to the orientation. (c) FIB-SEM micrographs of as made and twisted fibre. Adapter from [145].

2.5.2.2. WAXS analysis

WAXS technique was used in CNT fibre to measure the fibre orientation of the CNT[114], moreover catalyst [113] and residues[112] structures. In WAXS, the pattern reflects scattering from coherent crystal structures present in the sample.

Davies et al. carried out a WAXS study of fibre structure (figure2.15.a). The assigned the equatorial component to oriented CNTs and the circular halo from non-oriented graphitic particulates in the fibre. Figure 2.15.b shows that the 002 reflection extends to >0.344 nm. It is possible to extract information related to the CNT alignment, performing an azimuthal integration of the 002. The full width half maximum (FWHM) values are extracted from the fitting, which indicates the orientation spread in degrees. Figure 2.15.c shows the azimuthal integration from the 002 reflection in a CNT fibre. Because the fitting of experimental data with Gaussian functions required the superposition of three peaks where assigned to distinguish three population: unoriented, poorly oriented and highly oriented[113].

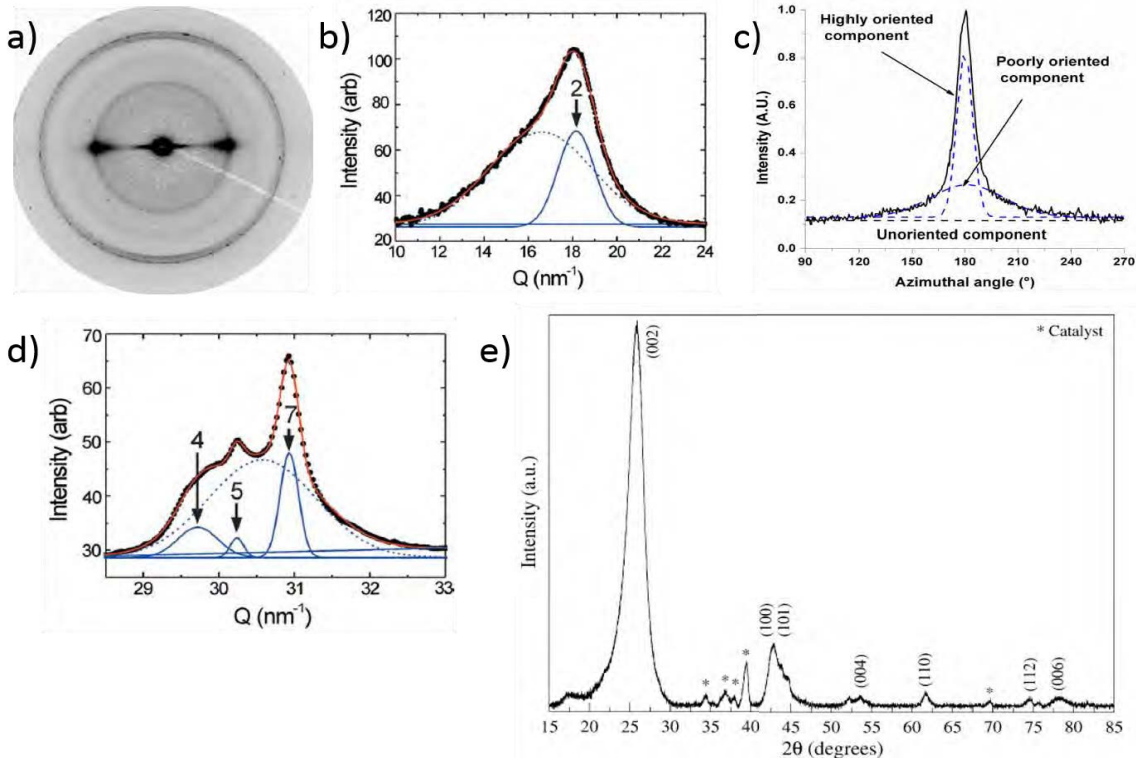

Figure 2.15. WAXS pattern, showing the CNT streak reflection of 002 perpendicular to the fibre axis and the circle reflection related to the iron catalyst and the 100 from CNTs. Radial integration in the range of (b) 002 reflection adapted from Davies et al[114] and (c) the 002 azimuthal integration[113] and (d)100 and iron reflection[114]. (e) XRD pattern of MWCNT in powder (λ = 0.154nm), showing the CNT peaks at higher angles as (004), (110), (112) and (006)[151].

Increasing the angles, other circular reflection are studied, alternating intense spots with shadow line, corresponding mainly to the isotropic contribution from catalyst and the 100 reflection in the CNTs. Figure 2.15.d shows the 100 reflection (≈ 0.21 nm) and the iron peaks, matched with distances of 0.208 and 0.203nm respectively.

At higher angles ($q > 33nm^{-1}$), it is possible to observe more reflections from CNT 110, 004, 112 and 006, which correspond to distances between 0.1 - 0.17nm, moreover other reflections related to catalyst particles and impurities (figure 2.15.e) [151].

2.6. Properties

It is an important challenge to make an aligned CNT fibre yarn without defects. Improving nanoscale and microscales properties lead to enhance the results in macroscopic architectures. Synthesis is one of the most important factor to produce specific CNTs and therefore obtain the desired fibre properties without applying aggressive post-treatments.

It is worth mentioning that due to the difficulties of choosing the effective cross section area and for making comparisons between different experiments and materials are more straightforward when tensile properties are normalised with respect to the mass per unit length in the materials. Consequently, the measurement belongs independent of the effective section, which is very difficult to measure accurately, ever more in macroscopic architectures. In this work, the mechanical properties are normalised by specific gravity (SG).

2.6.1. Mechanical properties

The mechanical properties of CNT fibre by direct spinning were very promising[152], obtaining results of Young´s modulus 80GPa[92] [153] tensile stress ≈ 1.5-2 GPa/SG for fibres with gauge length of 20mm[154] [115]. Decreasing the length less detects are testing, therefore better mechanical properties were obtain even though the spread is considerable at low gauge distance[133] in tensile test. Furthermore, as a unique high-performance fibre, mechanical properties of CNT fibre are not affected when it is knotted or bended. This effect is consequence of the semi-continuous structure[154].

To evaluate the high-performance properties, it is necessary to consider the CNT fibre as a hierarchical structure, assembly by building block at different scales, CNTs, bundles and filaments. The relation between the blocks is critical to determine the mechanical behaviour[155].

Firstly, covalent carbon bonds (C-C) are strong and capable to store tensile energy of 85nN[156], therefore individual CNT obtains amazing properties[17]. Tens of nanotubes are formed a CNT bundle, in this scale the properties are dictated by the degree of alignment, packing and the type of CNTs. Collapse CNTs tend to have a higher contact surface with neighbouring CNTs and therefore result in better mechanical properties. The fibrous fracture surface of the fibre indicates that its strength is related to the overlapping contact area of load-bearing elements and the friction between them. In this contest being able to make fibre of different types of CNTs would enable a comparative study of mechanical properties with identical length and alignment but different number of layers.

Surprisingly, the sp^3 carbon presents on the surface of the CNTs is working as an interbundle connection, improving the stress transfer into the CNT fibre[157]. Furthermore, CNT fibre is comparable to commercial high-performed fibre in terms of toughness, which is the combination between the high tensile stress and the strain. A model of the failure of CNT fibre during a tensile fracture is shown in figure 2.16.a. Figure 2.16.b show a TEM micrograph of a typical CNT bundle and its simulation[158].

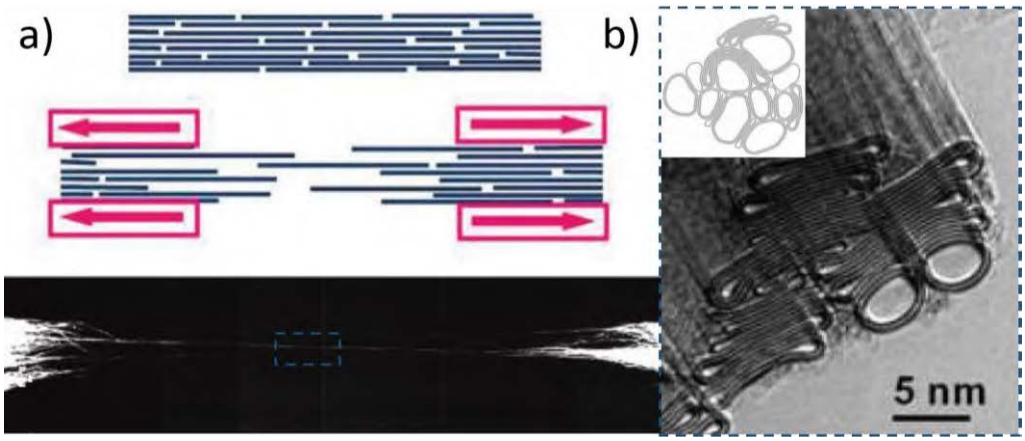

Figure 2.16. (a) A model of the failure between CNT bundle in a tensile test and (b) TEM micrograph of a typical CNT bundle and its simulation. Adapted from [158].

2.6.2. Electrical properties

Electrical behaviour of CNT fibre has to be treat as well as mechanical properties. Not only, it is necessary to take into account the character of an individual CNT; e.g. metallic or semiconductor, circular or collapse, but also the assembly

between CNTs and bundles; e.g. alignment or packing, producing changes in links and contact areas.

The electrical conductivity of SWCNTs has been estimated theoretically to be 10^8 S/m[28]. The highest electrical conductivity reported in CNT fibre with direct spinning is $8.3x10^5$ S/m[80], which is far away than the individual CNT. Although, electrical conductivity of CNT fibre has been reported in $3.6x10^6$ S/m[124], which was synthetized by liquid crystalline spinning. The fibre was produced with short tubes together with a good alignment.

As it was mentioned in a previous section the knowledge of an electrical behaviour of an individual CNT is very well-known through the chirality control (section 2.1.2). Therefore, big efforts are focused in synthesising fibres with metallic SWCNTs. The role of the promoter source plays an important role in synthesis of CNTs with different electrical properties. Different sulphur source might be leads to delay CNT extrusion, appearing CNTs with a dominant chirality[159]. Moreover, it is possible to characterise the CNT ratio between metallic/semiconductor, analysing the resistance against the temperature (figure 2.17.a). Semiconductor behaviour leads to decrease the resistance with temperature, in contrast to metallic character that increases the resistance with the temperature. Upshift temperature point (T_o) determines the limit point over the metallic CNTs are predominant[160].

Building block character of the CNT fibre can provide to the CNT fibre several configuration. It is possible to control the porosity in the fibre and therefore the number of contacts between the CNTs or bundles. Figure 2.17.b shows that highly compact fibre leads to better conductivity, promoting contacts and decreasing intertube space [161] [162]. It is worth mentioning that the effect of the atmosphere condition can control in the electrical measurement. Changes in the humidity affect largely to the conductivity of the fibre[163].

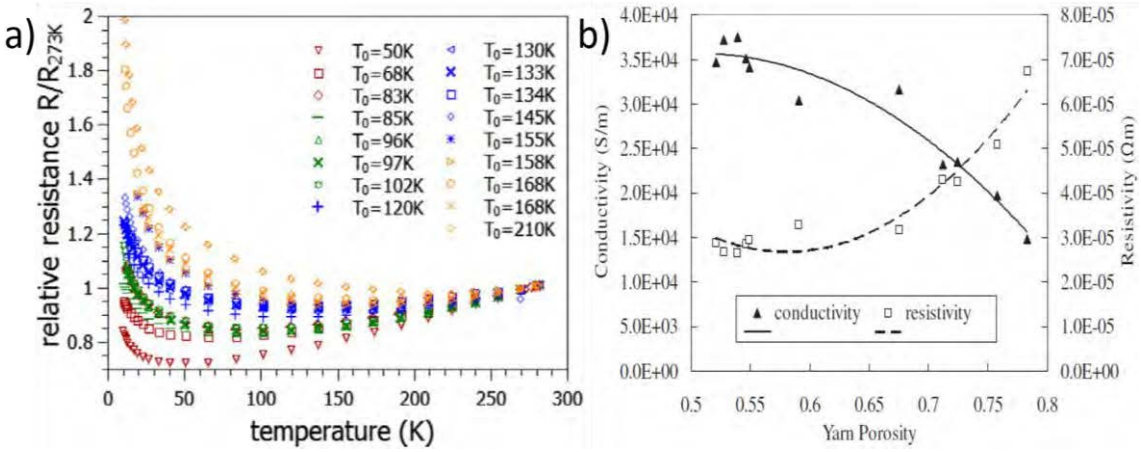

Figure 2.17. (a) Effect of temperature and spinning conditions against the relative resistance[160]. (b) Conductivity and resistivity change as a function of fibre porosity[161].

Nowadays, the CNT links or bundle interaction formation are not well established in direct spinning method. Structural characterisation and the influence in the properties is an important objective of this work, and it is presented along the chapter 5 and 6.

2.6.3. Fibre properties table

Table 2.3 summarises all the data extracted from the literature, related to direct spinning method. The data are organised by research groups. Furthermore, the results more relevant from other methods are shown to compare the fibre performance.

There are wide range of distribution in the values, mainly because an important part of the results are extracted in different condition and with other tested parameters. This would suggest that the experiments has to be standardised to compare the fibre under the same conditions as sample length, tested device, diameter normalisation or units.

Another important observation is the lack of information, mainly which is related with the microstructural studies, bundle orientation and specific surface area. The material necessary to obtain these values is extracted during hours. Showing the big challenge of controlling the synthesis condition (type of CNT, bundle orientation and properties) to be reproducible along the time, producing kilometres of fibre.

Table 2.3 Properties of the CNT fibre produced by different spinning method

Synthesis method	Modulus (GPa/SG)	Specific Strength (GPa/SG)	Toughness J/g	Conductivity (S/m)	CNT type	FWHM	Post-treatments	Surface area (m^2/g)
CNT Carpets (Q. Li) [127] [126]	275	0.85	Estimated 15	1.7×10^4	MWCNT	-	As- Spun[127]	-
	263	2.64	198	-	DWCNT	-	Twisting [126]	-
Coagulation (PVA/Water bath) [119]	15	0.15	Estimated ≈ 2.5	10^3	Mainly SWCNT	-	As- Spun	-
Coagulation (PVA/Water bath) [121]	45	1.4 – 1.8	40 - 60	10^4 [164]	SWCNT & MWCNTs	As spun - 27° stretched 4°	Hot stretched	-
Liquid crystalline CNT/H_2SO_4[165]	120	0.12	-	5×10^3	SWCNT	31°	As- spun	-
Liquid crystalline CNT/HSO_4Cl [124]	120	1	Estimated ≈ 18	3×10^6	Mainly DWCNT	9.4°	As- spun	-
Direct spinning (H. Espinosa) [153]	80	1	40	-	DWCNT	≈25° Assuming Lorentzian distribution	Fibre coated (polymer) Stretched and twisted.	-
Direct spinning (Y.Jeong)[110] [91]	19	0.53	Estimated ≈ 40[91]	3.2×10^5	SWCNT	-	As-spun[110] /Surfactant[91]	-
	8	0.31	-	1.1×10^5	MWCNT	-	As-spun[110]	-
Direct spinning (Y.L Li)[139]	25	1.25	Estimated ≈ 85	5×10^5	DWCNT	Estimated 28 °	As-spun	194

Direct spinning (J.N. Wang)[107]	4	0.35	Estimated ≈ 40	$1.3x10^5$	MWCNT	Estimated 27°	As-spun	-
Direct spinning (A.Windle) [80] [166] [115] [167] [154] [92] [168] [89]	-	1	-	$8.3 x10^5$	SWCNT	11°	As-spun[80]	-
	30	1.5	-	-	SWCNT	-	As-spun[166]	-
	60-142	1.1-2.1	42	-	Collapse SW & MWCNT (few layers)	-	As-spun[115]	-
	50	1.1	Estimated ≈ 10	-	Collapse SW&DW	Estimated ≈ 5-10°	As-spun[167] [154]	-
	70	1.6	Estimated ≈ 40	-	Collapse SW	-	As-spun[92]	76[136]
	40	0.85	Estimated ≈ 20	Calculated $3 x10^5$	Mainly SW & DWCNT	10-20°	As-spun [168]	-
	78	1.7	-	$\approx 2 x10^5$	SW & MWCNT Depending on C precursor	Calculated ≈ 25-32°	As-spun [89]	-
Direct spinning (K.Koziol) [157] [169] [86] [170] [171] [172]	80	2.3	63	-	Collapse SW&DW[167]	-	Hexadiene bath & UV irradiation [157]	-
	-	-	-	$\approx 3- 6 x10^3$	MWCNT (poorly graphitised)	-	As-spun[169] [86] [170]	-
	-	-	-	$\approx 2- 5 x10^4$	-	-	As-spun [171]	-
	-	-	-	$\approx 1- 2.5 x10^5$	-	-	As-spun and coated with sealant [172]	-

2.7. Industrial scale

One of the most important issues for a laboratory reactor is to scale-up for producing industrially. However, particularly in CNT fibre synthesised by direct spinning method only a few works are discussing valuable information for improving the industrial scalability. Some parameters have been identified as important[84]. More specific parameters related directly with the CNT fibre reaction at different injection rates are included in this work (chapter 7), providing valuable information to scale-up the process and produce the desirable fibre with its specific properties.

2.7.1. Scaled-up facilities and materials

Some companies are scaling up the process all over the world to produce kilograms of fibre by direct spinning from CVD floating catalyst reactor. *Tortech nanofiber* from *Plasan group* scaled up the process in collaboration with Cambridge University. Figure 2.18. shows the fibre directly spun on a metallic winder, producing CNT sheets[173].

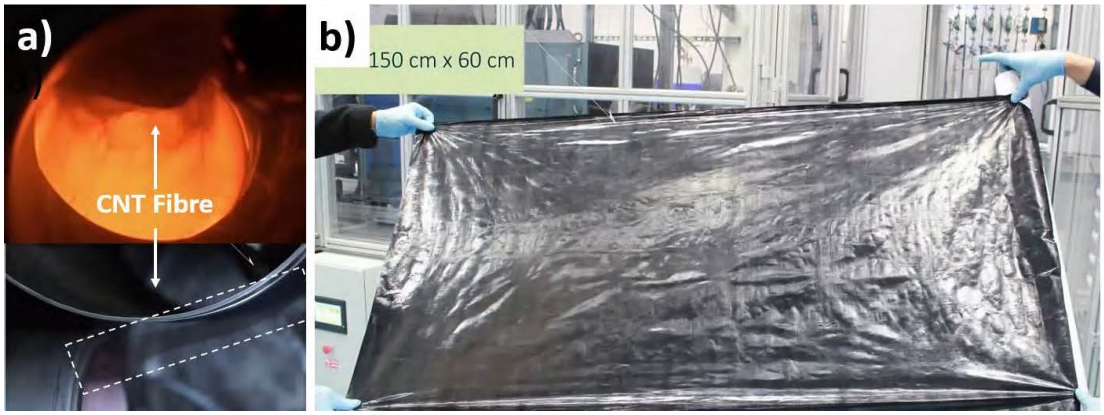

Figure 2.18. (a) Optical micrograph of the aerogel and being spun on a metallic winder and (b) 150 x 60cm film synthesised in the industrial reactor [173].

Nanocomp Technologies in the USA is producing CNT in industrial scale in different architectures as films or fibre (figure 2.19.a-c)[174].

Figure 2.19. (a) Pictures of the different CNT architectures (a) film (b) fibre and (c) powder[174].

Finally, Infra technologies are synthesised CNT fibres in a factory in Russia.

Thank to these companies, it was possible to analyse material synthesised by *tortech*, *nanocomp* and *infra*. Figure 2.20 shows raman spectra normalised by G peak intensity and TGA measurements from CNT fibre provided by Tortech, Infra and Nanocomp.

By raman spectra (figure 2.20.a), it is possible to extract information related to the CNT graphitisation and the type of tubes in terms of number of layers. The absence of noise in the spectra, concluding that the graphitisation of the layers in CNTs is satisfactory. Analysing peak shapes and positions, it is possible to observe differences. Nanocomp and Tortech fibres are mainly composed by MWCNT. Even, it could be extracted that the Tortech CNTs has more layers. Thus, Infra spectrum presented evidences that in the CNT population some proportion are SWCNTs, which leads to decrease ratio between D and G peaks.

TGA results show differences in all the sample (figure 2.20.b). Infra and Tortech fibres decompose approximately at the same temperature and the difference in the catalyst ratio can be related to the number of layers in the CNT. However, Nanocomp sample contains around 40 wt% of catalyst, which is promoting the fibre decomposition at lower temperature.

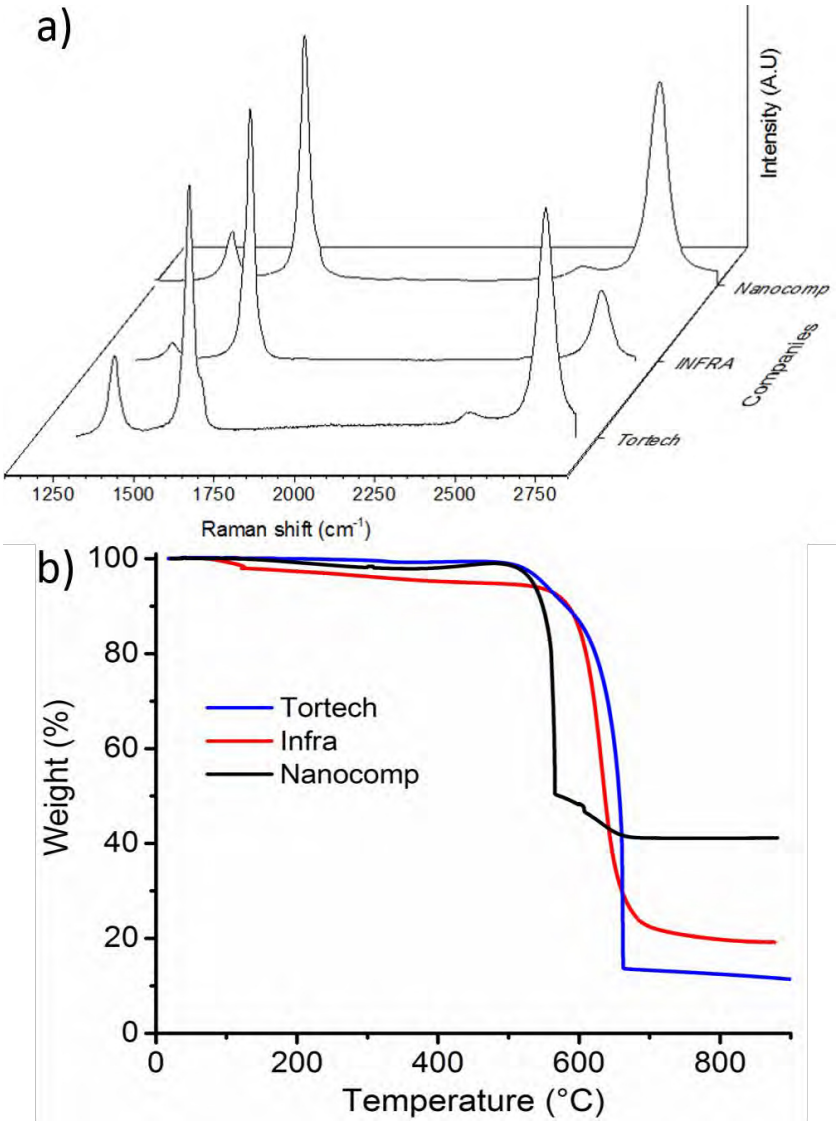

Figure 2.20. (a) Raman spectra normalised by G peak intensity and (b) TGA measurements from CNT fibre provided by Tortech, Infra and Nanocomp.

2.7.2. Sustainability (Life cycle assessment)

Life-Cycle Assessment (LCA) is a standardized (ISO 14040/44) and established for the assessment of the sustainability. LCA is a comprehensive framework that quantifies ecological and human health impact of a product or system over its complete life cycle.

LCA is recommended as powerful tool to assess the environmental sustainability of nanomaterials. Nowadays, LCA studies are still starting on nanomaterials area. The main reason is the lack of information on the side of inventory data. Thus, the LCA studies on nanomaterials are limited and mainly based on literature and patents data[175]. Despite the uncertainty intrinsically related to the assessment

of this new type of material, there is the urgency to establish their sustainability. This work is trying to promote *the first baseline evaluation* for emerging material and technology. The main purpose of LCA is to evaluate the environmental performance of the production of CNT fibre at lab-scale by accounting different scenario which considered different carbon sources and different feeding rate. Then, the assessment of the environmental performance has been also conducted by upscaling the production route to an industrial plan level.

2.7.3. Applications

The combination of CNT fibres properties are very promising to compete with other high-performance fibres or metals. Table 2.4 presents a comparison with carbon fibre (AS4), Kevlar 49 and copper.

Table 2.4 Properties of the CNT fibre and high - performance commercial fibre.

	CNT fibre	Carbon fibre (AS4)[a]	Kevlar 49[b]	Copper[38]
Tensile Strength (GPa/SG)	1.5-2[154]	2.4	2.1	0.22
Tensile Modulus (GPa/SG)	80[92]	129	78	0.12
Electrical Conductivity (S/m)	$8.3x10^{5}$ [80]	$6x10^{4}$	-	$5.8x10^{7}$
Thermal Conductivity (W/mK)	750[176]	6.8	0,3	400[177]
Specific Surface (m^2/g)	270[178]	0.2	0.2	-
Density (g/cm^3)	0.8 - 1[133]	1.8	1,5	8.9

[a] Hex Tow®AS4 [b] Kevlar®49(K49)

Supercapacitor and batteries using CNT arrays are attractive materials for charge storage due to the high electrochemically accessible surface combined with their high electronic conductivity, mechanical properties and long cycle life[179]. In supercapacitors the change are maintained in the electrolyte-electrode interface. The electrode in supercapacitor is typical made by activated carbon in powder, with a high surface area 1500-2000m^2/g, obtaining capacitances around 100-150 F/g[180].

Figure 2.21.a shows the CNT structure, around 50% is pore and its size distribution (figure 2.21.b). Figure 2.21.c presents a plot of surface area vs toughness for different carbon materials, related to CNT fibre. The values of surface area are similar to other methods for synthesising CNT fibre, the only exceptions are the activated carbon and activated carbon fibre, which is induced structural defects by chemical activation[181]. However, mechanical properties

of these structures are very low. In comparison, the CNT fibres present a combination of high surface area and toughness. According to the literature, depend on the treatment, hybridisation or spinning method the capacitance can vary between 15 and 200 F/g [182].

It is worth mentioning that several CNT fibre studies did not report surface area, because, it is necessary to collect at least 70mg to obtain a trustable value by BET, which reflects the difficulty in spinning 1 - 10km of homogeneous fibre.

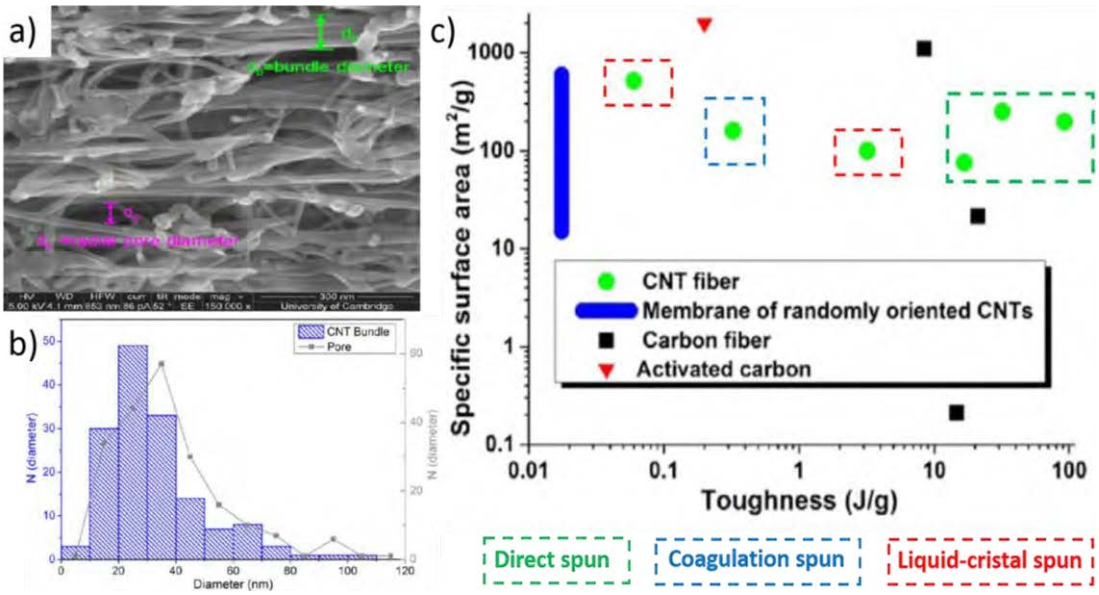

Figure 2.21. (a) FIB-SEM micrograph shows a longitudinal section of CNT fibre, emphasising pore and bundle diameters. (b) Histogram of bundle and pore diameters along the fibre[136]. (c) Comparison of surface area and toughness of different materials, related to CNT fibre as activated carbon, carbon fibre or other CNT structures, adapted from[181].

The CNT supercapacitor prospect is replaced structural panels, exploiting the combination of electronic and mechanical properties. This device can be bend, stretch or wove.

Sensors is one of the most promising application for CNT fibre. In contrast with the traditional high-performance fibre, compose by a monolithic structure, CNT structure is composed by a distribution of porous and bundles. Furthermore, it has the ability to be knitted, knotted and woven as a textile fibre[154]. Fibre encompass high electrical conductivity, large surface area and piezoresistive behaviour to be a precise sensor, detecting gases, particles or liquid though the intrinsically variation of properties[183].

Hybrids can exploit the combination of mechanical properties, high thermal stability-conductivity and very high carrier mobility from CNT fibre, allowing to use in solar cells, photo-electrochemical cells and change transfer applications[184].

The combination of CNTs and inorganic semiconductors can lead to new hybrid material with improved properties, such as a piezoelectric properties and higher photocatalytic activity. This improvement is associated with charge transfer processes at the CNT/semiconductor interface and therefore it is dependent on CNTs by its properties as chirality, diameter and number of walls[135].

The CNT/semiconductor interface can be exploited in small devices. Mesoporous structure of CNT together with the high surface area can act as a large-area scaffold for the semiconductor, obtaining piezoelectric properties together with a semiconductor as ZnO. Moreover, CNTs hybridised with one of the most used semiconductor TiO_2 can create a mesoporous network highly crystalline to improve the oxide photoactivity, reaching the hydrogen production[185].

Composites is probably the most reported application related to CNTs. A wide range of polymers and liquid are infiltrated or added to improve different matrix properties. CNTs are mainly used for reinforcing polymers[186]. Various semicrystalline polymers are accelerated the process and forming a transcrystalline (TC) layer perpendicular to the fibre axis. This especial nucleation change the interaction between CNT/polymer and thus bulk properties of the composite system[138]. Moreover, according to the continuous structure of CNT fibre can increase the electrical properties dramatically [187]

Finally, CNT fibre have been combined with different metals as copper. Cu/CNT Cables are produced by electrodeposition, where Cu is filled the voids in the fibre with the objective of increasing the current carrying capacity and decrease the weight[188].

3 Experimental techniques

All the samples studied and characterised in this work, were performed in IMDEA Materials institute, using a homemade reactor by direct spinning from CVD[80]. The fibre are produced by continuous drawing of the aerogel from the gas phase into a winder. Vertical tubular reactor is used at mainly 1250ºC in hydrogen atmosphere.

The sample was introduced in a pressure reservoir in liquid state, mass flow controller was installed for controlling the injection from 1ml/h until 7ml/h. The liquid injection is vaporised by a CEM around 200ºC to homogenise the feed rate entrance in the reactor. Furthermore, the vapour is helped, using a small amount of hydrogen as a carrier gas from 5ml/min to 10ml/min, which is controlled by a gas flow. In this work, it was performed a lot of different fibres with different type of CNT and orientation. Therefore, a wide range of precursor were used. Firstly, butanol was the main carbon source, but toluene and benzyl alcohol was used, from 97.7 to 99.2%wt. Thus, ferrocene and thiophene were used in different proportion from 0.02 to 1.5wt% to tune the CNT fibre.

Injection streams is mixed in the upper part of the reactor with a hydrogen flow. Hydrogen flow rate can vary from 0.6 to 2.8l/min. The appearance of the aerogels are situated in the first third of the reaction, when the temperature is over 1100ºC and depending on the aerogel characteristics the winding rate are between 7 m/min to 55 m/min. Depending on the application the CNT fibre can be supported in paper, aluminium, Teflon, quartz, glass or even in a hollow space. It is worth mentioning that all the fibres presented in this work can be spun continuously during hours, obtaining homogeneous results along the time.

Figure 3.1 shows the picture of the vertical tubular reactor for producing CNT fibre by a continuously spinning.

Figure 3.1. Picture of the reactor for producing CNT fibre by direct spinning.

3.1. Brunauer-Emmett-Teller gas adsorption (BET)

3.1.1. Surface area and pore volume

Surface area and pore volume information are one of the most important characterisation to understand the fibre structure. The Brunauer-Emmett-Teller (BET) gas adsorption method is performed to obtain the total surface area and pore volume of porous materials (V_P). BET method is based on physical adsorption of gas molecules on a solid surface, the amount of gas molecules is obtained[189]. BET adapt the Langmuir theory for monolayer molecular adsorption to multilayer. The surface is covered by all the adsorbed molecules for monolayer. In multilayer adsorption, there is only one layer in contact with the solid surface. The surface area (A_{BET}) and the specific surface area (A_{SBET}) are calculated by the following equations:

$$(A_{BET}) = n_m^a \, L \, a_m \quad \text{Equation (3.1)}$$

$$(A_{SBET}) = \frac{A_{BET}}{m} \quad \text{Equation}(3.2)$$

Where L is the Avogadro constant, 6.023_x10^{23} mol^{-1}, m is the mass of the sample, a_m is the area effectively occupied by each adsorbed molecule (N_2 is the most common gas) in the complete monolayer and n_m^a can be calculated by the BET equation:

$$\frac{P}{n^a\,(P_0 - P)} = \frac{1}{n_m^a\,C} + \frac{(C-1)}{n_m^a\,C}\frac{P}{P_0} \quad \text{Equation}(3.3)$$

Where n_a is the amount of N_2 adsorbed at the relative pressure (P/P_0), C is a constant, which is depended on the isotherm shape. This equation can be expressed as, relating directly to the weight of gas adsorbed (W) and the weight, which correspond with a monolayer (W_m):

$$\frac{1}{W\,[(P_0 - P) - 1]} = \frac{1}{W_m C} + \frac{(C-1)}{W_m C}\frac{P}{P_0} \quad \text{Equation (3.4)}$$

W_m is calculated from a linear regression of the BET plot. It is worth mentioning that the plot is restricted, in the range of $0.05 < P/P_0 < 0.35$ due to the capillary densification[189].

3.1.2. Pore size distribution

Pore size distribution are obtained by Barret-Joyner-Halenda (BJH), based on nitrogen isotherms by defining the relationship between volumes of capillary densified against the relative pressure[190]. Considering the pores as cylindrical, open and desorption mechanism are filled with liquid adsorbate, then the thinning of the physically adsorbed layer is followed over the pressure decrement. The nitrogen vapour adsorbed determine the total pore volume.

In the CNT fibre the pores are generally elongated and preferentially oriented parallel to the fibre axis. IUPAC classify pores depending on their size; 1.- pores with widths exceeding about 50 nm are macropores; 2.- between 2nm and 50nm are called mesopores and 3.- pores under 2nm are called micropores[191]. It is worth mentioning that the weight of the sample were over 70mg per sample, optimizing the equipment error. Consequently, fibre densification is mandatory.

It is worth mentioning that the fibre was measured after densification, further information between densified and as-spun fibre structure is provided in chapter 6.

Nitrogen adsorption measurements were accomplished with N_2 at 77 K after degassing the samples at 300 ºC under vacuum for 3 hours using a Quantachrome Quadrasorb SI porosimeter. The adsorption/desorption isotherms were obtained at 77K by allowing 4 min for equilibration between each successive point. The surface area was calculated by applying the the Brunauer–Emmett–Teller (BET) model to the isotherm data points of the adsorption branch in the relative pressure range $P/P_0 < 0.3$. The pore size distribution was determined from the desorption branch of the isotherms using the nonlocal density functional theory (NLDFT) equilibrium model method for slit pores provided by Quantachrome data reduction software QuadraWin Version 5.05.

3.1.3. Linear density

Draw ratio and the bundle distribution affect to the linear density and volumetric density, respectively. Figure 3.2.a presents the plots of fibre linear against draw ratio. The linear density decreases with increasing winding rate following the expected inverse relation $y = -0.004 + 0.32x$ (figure 3.2.b). As the winding rate approaches the gas-flow rate in the reactor.

CNT fibre in terms of mass production is constant and independent of draw ratio. Therefore, linear density has inverse relation with draw ratio.

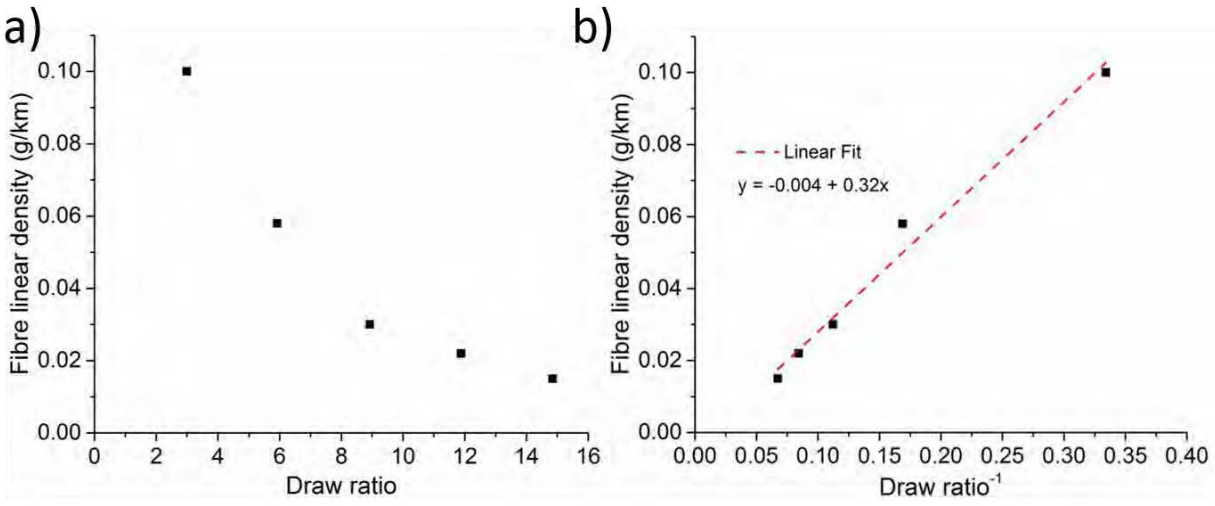

Figure 3.2. (a) Influence of draw ratio on the fibre linear density, (b) showing linear dependence as expected.

3.2. X-ray diffraction (XRD)

XRD is based in the interaction of light of wavelength λ, which is in the range of the size of the atoms, the incident x-ray are diffracted with the crystal, which are located in a regular array of atoms, in some specific crystallographic planes of the material are in agreement with the Bragg´s law:

$$n\lambda = 2d \sin\theta \quad \text{Equation (3.5)}$$

Where n is an integer, d the spacing between the planes in the atomic lattice and θ the scattering vector. The scattered intensity is presented as a function of scattering vector q:

$$q = \frac{4\pi \sin(\theta)}{\lambda} \quad \text{Equation (3.6)}$$

SAXS is an analytical method to determine structure in terms of shape and size between 1 and 90 nm due to the different electron density in the material. X-ray penetrate inside the sample and every element CNT or bundles in contact with the beam emit its signal. Therefore, it is possible to study the average structure of all the irradiated surface composed by millions of CNTs. It is possible to obtain information, related with different SAXS parameters.

CNT fibre is two-phase system composed by CNTs and air. It is possible to calculate the invariant, which is well-defined for two component, following the expression:

$$Q = \int_0^\infty q^2 \, I\,(q)\, dq = 2\pi^2 \varphi_1 \, \varphi_2 \, V\,(\Delta\rho)^2 \quad \text{Equation (3.7)}$$

Where φ_1 and φ_2 are the volume fraction of each phase, V Is the volume of the sample and $\Delta\rho$ is the difference in electro density between the two-phases, and it is possible to calculate:

$$\rho_e = \frac{N_A \rho_m n_e}{M} \quad \text{Equation (3.8)}$$

Where N_A is Avogadro constant (6.023 x10^{23} mol^{-1}), M the molar mass (g/mol), n_e the number of electron per molecule ρ_m the mass density (g/cm^3). CNT fibre has an electro density ≈ 6.45 x10^{23} e/cm^3[130].

It is necessary to apply an approximation, extending the peak intensity until 0, related to the lack of information due to the beam stop, called Guinier´s

approximation[136]. Fibre orientation is obtained through the calculation of FWHM in the azimuthal integration SAXS reflection by fitting experimental data with a Lorentzian distribution.

WAXS pattern are related to the distance repetitions between the interatomic planes, the distances are in the range of angstroms. WAXS provides information related to the graphitic reflection originating from 002, 100 and 101 planes. As well as obtaining information from the catalyst or impurities. Fibre orientation is obtained through the calculation of FWHM in the azimuthal integration of the 002 reflection ≈ 0.34.

3.2.1. Synchrotron X-ray

Almost all the X-ray diffraction pattern presented in this work were performed at Non crystalline diffraction (NCD) in ALBA Synchrotron light facility. It is possible to obtain SAXS and WAXS patterns simultaneously, providing structural information of the CNT fibre from 1 angstrom until 100nm. WAXS and SAXS detectors are Rayonix (LX255-HS) and imXPAD-S70 with an active area of 255x85mm^2 ; 152x149.6mm^2 and 5760x1920 pixels ; 1200x1120 pixels, respectively. Beam dimension are 100x50µm using a wavelength of 0.1nm. The distance from the sample to the detector was 174 and 2618mm. CNT fibre were collected as a 100 filaments fibre and densified with acetone. Sample were located in a hollow frame to modify fibre orientation against the beam. WAXS detector does not cover the whole pattern, sample has to be rotate to obtain a complete pattern. Figure 3.3 shows a scheme of the synchrotron configuration and sample frame.

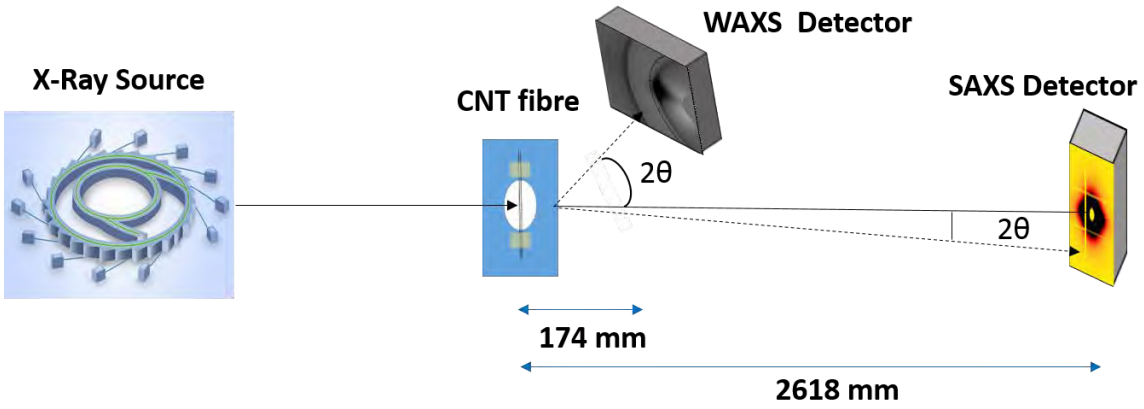

Figure 3.3. Schematic of a synchrotron set-up in the NCD line.

It is worth mentioning that these values of FWHM included misalignment of filaments in the sample and thus underestimate the intrinsic orientation in the material. In order to obtain more intense pattern, the sample is prepared, densifying 100 filaments.

3.2.2. WAXS in CAI

Wide angle 2-dimensional X-ray scattering (SAXS and WAXS) patterns were taken at room temperature with a Bruker-AXS SMART 1000 single crystal diffractometer using Mo Kα radiation and a CCD detector. The sample-detector distance was determined using silicon single crystal standard. The X-ray scattering patterns were integrated to obtain radial and azimuthal profiles. The samples used for WAXS measurements consisted of multiple parallel CNT fibres produced by winding individual filaments continuously for typically >20 min, corresponding to >1000 filaments.

3.3. Raman spectroscopy

Raman spectroscopy is a spectroscopic technique based on inelastic scattering of monochromatic light, related to vibrational modes in the material. Inelastic scattering means that the frequency of monochromatic light changes upon interaction with a sample. Raman is considered a surface characterisation technique, and it has been widely used in the characterisation of CNT.

Raman spectra were acquired with two different spectrometers: a Renishaw PLC and a Jasco NRS-5100. All the spectra were taken in the range from 120- 3000 cm^{-1} using a 100x objective lens and the exposition time was 15s. With the Renishaw spectrometer a 532 nm laser line (2.33 eV) was used as excitation source, taking three accumulations at 5% of the total power laser (≈ 1.68 mW) was used. A Jasco spectrometer was used to acquire the spectra with 633nm and 785 nm laser (1.57 eV), with a fixed power of 5.5 mW and a single accumulation. In order to maximize the Raman signal, the polarization of the excitation signal was kept parallel to the CNT fibre axis.

Radial Breathing Mode (RBM) peaks are observed in the range 70-400cm^{-1}. RBMs peaks are directly associated with the radial vibration of carbon atoms by the radial expansion and contraction of CNT. Its frequency is inversely

proportional to the CNTs diameter. Thus, the diameter of the CNT can be determined from the Raman shift of the RBM peak *(ω);* $\phi = a/(\omega - b)$. Where *a* and *b* are experimental parameters, which are depending on CNT chirality. Results obtaining in this work were best adjusted using the following parameters: $\phi = 248/\omega$. The RBM intensity peaks are associated with the excitation energies and the signal is more intense when the optical transition energies of the CNTs are in resonance with the excitation energy used. To obtain a complete overview of CNT diameters is important to use different laser, modifying the excitation energies.

D peak *(Disorder peak)* is around 1320 cm^{-1} and is associated with the sp^3 bonds implying that it has to be with the disorder peak (D) because the graphitic bonds are sp^2. The intensity of D peak is taken as a measure of defects or impurities (poor graphitisation) in the sample.

G peak is observed around 1580 cm^{-1}. G peak is associated with the tangential vibration of carbon atoms in a hexagonal lattice and is characteristic from sp^2 bonds (level of graphitisation). The peak structure has relationship with the type of CNT and diameter. MWCNTs generate a symmetric peak centred ≈ 1578 cm^{-1}. However SWCNTs can be divided in two peaks: G^+ is also ≈ 1582 cm^{-1}. On the other hand the G^- peak, which appears ≈ 1570cm^{-1}, shows a direct relationship with the metallic SWCNTs. Third peak appear in metallic predominance CNT sample at 1554 cm^{-1}. Due to a low frequency G band component arising from the coupling of lattice vibrations to free electrons. It can be accurately fitted by the corresponding Breit-Wigner-Fano (BWF) line shape.

In the literature the purity of a graphical material are measured using the ratio of the intensities of the peak D and G (I_D/I_G). However, it is necessary to obtain a good statistics; the presence of a few SWCNT can increase sharply G peak, making unappropriated conclusions from I_D/I_G values.

M peak is a minor peak, in the dimension point of view, because, it can provide information about how packed are the CNTs. It is concluded that M peak is strongly dependent on stacking order of graphene layers. Disappears for bilayer samples. It is observable in CNT samples with predominance of collapse CNTs, which are stacked as a sheets in the bundles and it can be obtained mechanical and electrical behaviour.

2D peak appear from 2650 to 2700cm^{-1}, which is an overtone of the D-band and it has a direct relationship with the diameter of CNTs and the excitation wavelength affected by the interaction between the amount of CNT layers and by the termination of this layers. In all nano-carbons and more clearly in graphene, the position and shape of the peak is directly related to the number of layers.

3.4. Electron microscopy

Electron microscopy generate images of materials microstructure at high magnification; Beam of electrons interact with the sample to form specimen images, obtaining information at micro and nanoscale and confirming evidences, which are studied through other techniques. The CNT structure characterisation has been obtained by scanning electron microscopy (SEM) and transmission electron microscopy (TEM).

In the SEM technique, the electron, beam interacts with the sample, losing and energy leading to the emission of secondary electrons, backscattered electrons and X-ray. Secondary electrons shows the topographical characterisation of the sample. Backscattered samples determine the compositional characterisation of the sample, the shine intensity of the electrons are proportional to the atomic weight. Furthermore, elemental analysis are carried out using energy-dispersive X-Ray spectroscopy (EDS). EDS is an analytical technique used for the elemental analysis or chemical characterization of a sample. The energy of photons emitted after the electron beam interaction, is characteristic of the elements present in the sample, representing the atoms energy transition in the material. The SEM images and the EDS analysis were performing with EVO MA15, Zeiss model.

TEM uses a high energy electron beam (200 or 300 keV), which is between 10 to 100 times higher than SEM. Thin specimen is essential due to the electrons are transmitted through the specimen. The electron beam is magnified and focused to provide an image of the structure of the material. JEOL JEM 2100, JEOL JEM 3000F and Talos F200X FEI have been used to provide all the information.

3.5. Optical microscopy

Optical microscope (OM) were carried out with OLYPUES BX51 with the camera OLYMPUS ColorView, the images were capture in reflection at different magnifications.

3.6. Atomic force microscopy (AFM)

AFM is a high resolution microscopy, with a resolution on the order of nanometres. It is very useful for creating 3D images and studied the topography of the sample. A silicon cantilever with a sharply tip shape, which is scanning the surface of the sample. Depending on the application and the material, it is possible to apply two different modes: contact mode and non-contact mode.

In contact mode, the tip is in touch directly with the sample, forces between the sample and the cantilever produce a deflection in the cantilever. The amount of forces that the cantilever can distinguish are van der Waals, chemical, electrostatic or magnetic forces. In non-contact mode the cantilever is under vibration or oscillated, producing a frequency. The different force in the surface decrease the resonance frequency of the cantilever, using a scanning software, it is possible to reconstruct a topographic image of the surface. In this mode the surface of the sample is not affected by the cantilever, which is optimal for measuring roughness in CNT surface or analysed the thickness of a CNT film in the nanometre scale.

Atomic force microscopy (AFM) analysis of the surface thickness was performed using a Park XE-150 AFM Instrument (Park Systems Corp., Suwon, Korea) in non-contact mode.

3.7. Thermogravimetric analysis (TGA)

Thermogravimetric analysis (TGA) is an analytical technique used to determine a material's thermal stability and its fraction of volatile components by monitoring the weight change that occurs as a specimen is heated. The measurements are performed in air atmosphere, so as to identify the different carbonaceous species and the catalyst in the sample by recording the mass-loss associated with the temperature .The protocol is increasing the temperature 10ºC/min from 25ºC to 900ºC. The mass of CNT is in the range from 1 to 5mg.

It is possible to obtain information about the composition of the CNT fibre. Thus, the amount of sp^3 are determined calculating the loss weight until the onset around 500ºC. Sp^2 carbon species are degraded between 500ºC to 650ºC, appearing a sharply decrease in the mass. The remnant of weight at the end of the experiment is related with the catalyst, which is oxidised during the temperature slope to Fe_2O_3. TGA analysis was carried out using a TAQ800 model.

Iron catalyst is oxidising during TGA experiment to Fe_2O_3. Therefore, total catalyst in the fibre is approximately 70% of the total TGA residue. This value is calculated by using the oxygen and iron molar mass.

$$\boldsymbol{Iron\ (wt\%) = \frac{2xM_{Fe}}{3xM_O + 2xM_{Fe}}\ x\ 100} \qquad Equation\ (3.11)$$

Raman measurement was performed in order to confirm the presence of Fe_2O_3 as the catalyst residue after oxidation. The raman peaks in the figure 3.4 evidence clearly the modes from the Fe_2O_3 oxide: (224-A_{1g}, 243-E_g, 290-E_g, 408-E_g, 496-E_g, 609-E_g, 659-E_u)[192]. It is worth mentioning that oxide peaks were not observed in CNT fibre raman spectra, confirming the metallic iron as a catalyst.

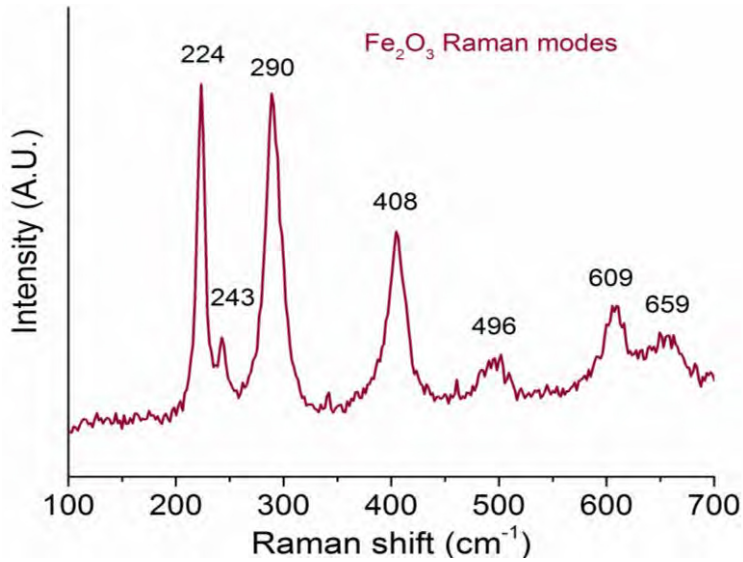

Figure 3.4. Raman spectra of catalyst residue, conforming the presence of Fe_2O_3.

3.8. X-ray photoelectron spectroscopy (XPS)

XPS is a semi-quantitative technique, using to estimate the stoichiometry, oxidation state or electronic state of the different elements present in the sample. The specimen is irradiated with X-rays and the detector determine the kinetic

energy and the number of electron that are escaping from the surface. This emitted electrons provide information related to the binding energy and consequently related to the emitter atom. The measurement has to be made under ultra-high vacuum. XPS are used in characterised CNT, providing information related with the catalyst structure, the nature of different impurities or CNT doping. In crystalline structures can also confirm XDR information.

XPS data were collected in a SPECS GmbH electron spectroscopy system provided with a PHOIBOS 150 9MCD analyzer. The deconvolution shown is fitted by Gaussian/Lorentzian peak shapes and Shirley background profile subtraction.

3.9. Organic elemental analysis

Organic elemental analysis is measured by combustion analysis. Sample is burned in a controlled atmosphere in excess of oxygen, trapping the combustion products as CO_2, H_2O and etc, and weighted. The main elements measured are carbon, hydrogen, nitrogen and sulphur.

3.10. Ellipsometry

Ellipsometry is an optical technique for obtaining the dielectric properties from a thin film structures, measuring the change of polarisation in reflection and transmission. One of the main advantage of this technique is that the ellipsometry is very accurate and robust, being reproducible.

The light incident in the sample is decomposed is s and p component, which represent the perpendicular and parallel oscillation, related to the surface, respectively. The amplitudes of both components are measured at different incident angle and named as r_s and r_p. Ellipsometry measures the reflectance ratio (ρ), which is the ratio of both component, being proportional to the amplitude (ψ) and the phase shift (Δ):

$$\rho = \frac{r_p}{r_s} = \tan(\psi)e^{i\Delta} \qquad Equation\ (3.12)$$

Ellipsometer SOPRA GES 5E were performed the reflectance measurement and calculated the refractive index with a Xe lamp. Different thickness were analysed using light reflection for p-polarization and s-polarization by modifying the incident angle from 55º-65º-75º the wavelength cover the range between 200 to 1500nm

3.11. Mechanical and electrical test

Mechanical properties related to individual filaments were performed by Textechno Favimat tensile tester with 2N induction load cell. Samples are tested in a vertical configuration, holding in the edges by two pair of rubber grips closed by an adjustable force spring. To situate the fibre completely vertical and no twisted, small weight is holding from the fibre. This weight is negligible avoiding densification, strain or alignment in the fibre structure. Test configuration was optimised during the duration of this work, small pretension of 0.002N/TEX is applied to avoid fibre relaxation. Continuous strain rate is configured in the experiments 1mm/min (5%/min). Fibre length in the samples are 20 mm.

Fibres are tested in two different configuration, as-spun and densified. Monofilaments are densified with acetone. 16 hours was waiting for drying to avoid the effect of the liquid in the inter-bundle connexions. The different section and volumetric density difficulty the comparison between different experiments. Therefore, tensile properties are normalised with respect to the mass per unit length in the materials, called specific gravity. Consequently, the measurement belongs independent of the effective section, ever more in as spun samples.

Nominal fibre linear density is determined by weighing a known length of fibre. The linear density of samples subjected to tensile tests was further refined using the vibroscopic method. No substantial discrepancies were observed between the two techniques. Results are shown in this work, it is represented by the average for more than 20 filaments (figure 3.4).

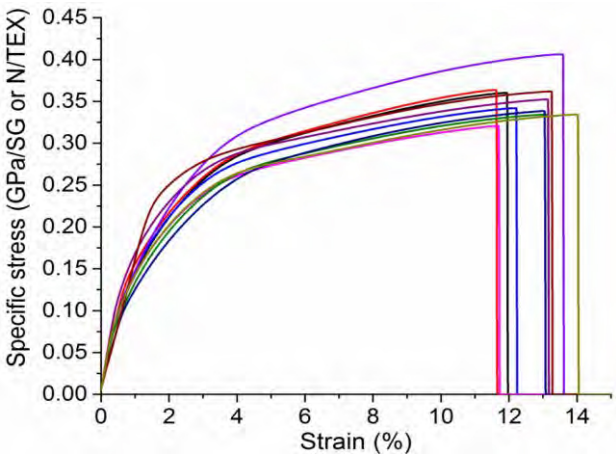

Figure 3.4. 10 typical stress-strain curve show the reproducibly of the measurements

Electrical measurements were performed with an Agilent 34410A 6-1/2 digit multimeter. The experimental set-up was built using copper tape electrodes, separate 30mm, connecting both electrodes with a CNT fibre, silver paint is spreading in the link between the electrode and fibre edge, letting the solvent evaporate for approximately two hours. Identical results of electrical resistance are obtained using two and four point's method.

4 Synthesis: Molecular control and catalyst studies

4.1. Introduction

Understanding the chemistry of the reaction is the first and most important step for controlling the synthesis of macroscopic fibres by direct spinning from floating catalyst CVD CNT growth. It is evaluated the importance of the main elements as sulphur iron and carbon, as well as its interaction. Furthermore, the reaction temperature, higher than 1100ºC, is also critical to reach the long CNT growth (>1mm).

Role of sulphur in the CVD reaction is the responsible for controlling the type of tubes in terms of number of layer, allowing to tune the CNT from SWCNT to MWCNTs. Changing the previous theories establishing models based on simple particle coarsening. Sulphur importance is presented in this chapter. Controlling type of CNTs, permit us to produce SWCNT fibre for studying the distribution of CNT chiralities, showing the predominance of armchair-metallic SWCNTs probed by Raman spectroscopy and electron diffraction pattern.

It is studied in detail the catalyst structure and composition, defining the position in the isothermal section of C-Fe-S ternary diagram and the role of interfacial energies. Allowing to explain; the low proportion of active catalyst particles in the direct spinning process (<0.1%) and stabilizing the edge of the emerging CNT and controlling the carbon diffusion in the iron catalyst particle, respectively.

Growth model is explained during this chapter, active and inactive catalyst are following different route that is analysed in detail. Furthermore, thermodynamic studies suggest a Fe FCC core surrounded by a liquid Fe-S shell, when temperature exceeded 1000ºC. The results presented here provide clue aspects in terms of CNT growth from liquid catalyst.

Finally, the presence of impurities in the fibre has been reported, emphasising in the iron catalyst particles stick or trapped into the fibre, carbonaceous impurities and silicon-based compounds.

4.2. Description of synthesis and spinning process

CNTs are synthesised by direct spinning from the gas phase with floating catalyst[80]. Precursors are decomposed in the upper part of the reactor. The reaction is carried out in hydrogen atmosphere at 1250ºC, using different precursor feed rate, carrier hydrogen flow and drawing winding rates.

Figure 4.1 summarises the direct CNT fibre process showing the aerogel formation.

Initially, precursors are introduced in the upper part of the reactor; ferrocene and thiophene as iron and sulphur sources, respectively. Precursor feed rate is mainly between 1.5 - 5ml/h. Different carbon source are used in this work, but butanol is the most common carbon source. The precursor injection point is situated at ≈ 300ºC, but the temperature profile rapidly increases up to 1250ºC. At this temperature, the different sources have been decomposed; while they are carried along by hydrogen flow. It is assumed that atomic collision form clusters of atoms which then coarsen into catalyst particle. Through the next step consists in the decomposition of the carbon source on the catalyst. Carbon diffusion and reconstruction into a graphitic arrangement, the carbon present in the catalytic surface forms a CNT

Millions of CNTs are synthesised simultaneously. Due to van der Waals forces, the CNTs are attracted to each other forming an aerogel that has enough mechanical stability to be directly drawn out of the reactor as a continuous fibre.

Hydrogen provides to the reaction the reducing atmosphere and it is also the main carrier gas, controlling the residence time and the concentration of the reactants along the tube.

During operation of the process, the fibre is mound on a spool, at rates from 1.5 until 55m/min, depending on the synthesis conditions.

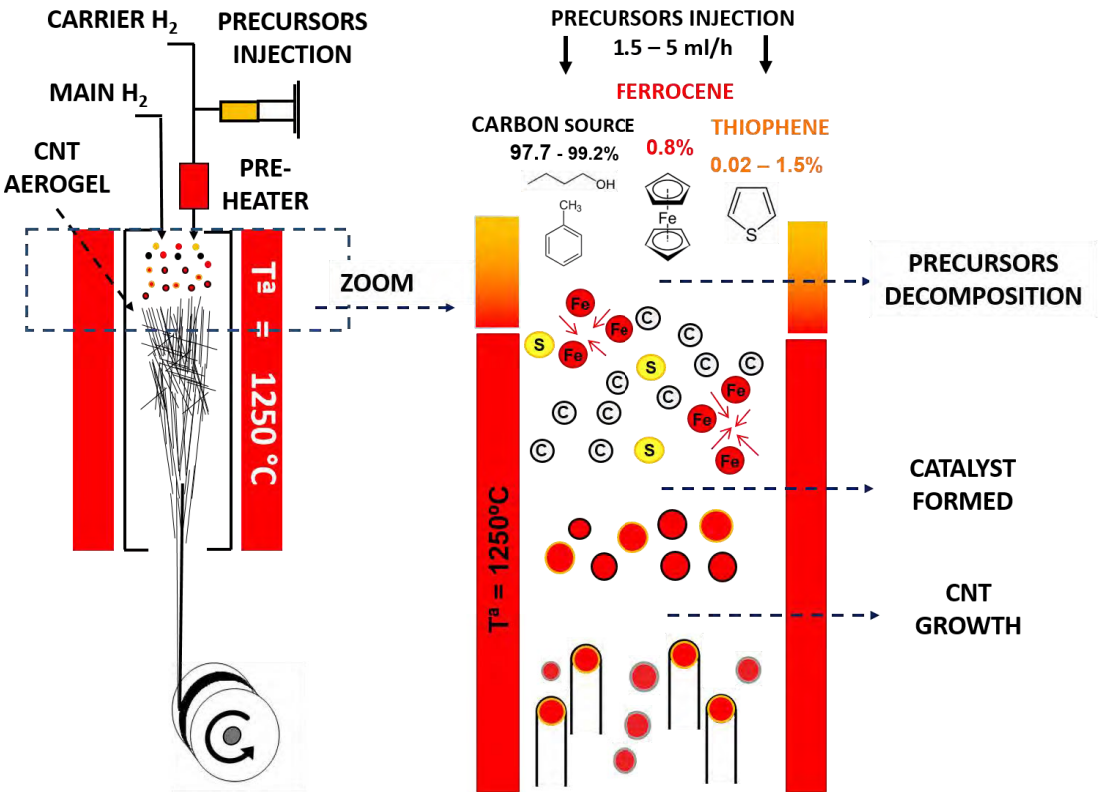

Figure 4.1. Schematic representation of the direct CNT fibre process showing the aerogel formation. On the right, it is focused in the reaction area; precursors are decomposed in the upper part of the reactor then coarsen and growth the CNTs, which are formed the aerogel.

4.3. Role of sulphur in the CVD reaction

Understand the role of sulphur is one of the most important achievement of this dissertation. Previous models predicted the tuning the type of tube from SWCNT to MWCNT by increasing the concentration of iron in the reactor, exclusively as a consequence of catalyst particle coarsening [46]. However, in this chapter is reported the clear evidence that varying the concentration of thiophene feedstock, it is possible to control the CNT that make up the fibre.

The fibre samples characterised in this chapter are synthesised with ferrocene and thiophene as a metal catalyst and promoter, respectively. Butanol is presented as carbon source in most experiments. Selected samples produced from toluene or benzyl-alcohol are also presented in order to confirm the trend found for butanol.

The experiments are performed by fixing the ferrocene (iron source) content in the precursor mixture and varying the ratio S/C in the range $3.3x10^{-3}$ to $2.2x10^{-4}$ %at. Table 4.1 summarises the synthesis parameters used.

Table 4.1 Process parameters used for producing the continuous a CNT fibres.

Parameter	Butanol	Toluene	Benzyl-Alcohol
Carbon source (wt%)	97.7 - 99.1	97.7 – 99.2	97.7 - 99.1
Ferrocene (wt%) $Fe(C_5H_5)_2$	0.8		
Thiophene (wt%) C_4H_4S	0.1 - 1.5	0.02 - 1.5	0.1 - 1.5
Furnace Temperature (°C)	1250		
Inlet Temperature (°C)	175		
H_2 flow rate (ml/min)	1200-1300		
Solution injection rate (ml/h)	5	1.3 - 2	1.3 - 2

4.3.1. Number of layers and diameter.

Raman spectroscopy is an ideal techniques for a rapid assessment of the composition of CNT samples. Figure 4.2.a presents the normalised raman spectra data showing the evolution from SWCNT to MWCNT by varying the amount of thiophene, at fixed Fe/C. Inlet plot shows the comparison of the spectra in absolute units shows a dramatic drop in the resonance as the number of CNT layers increase.

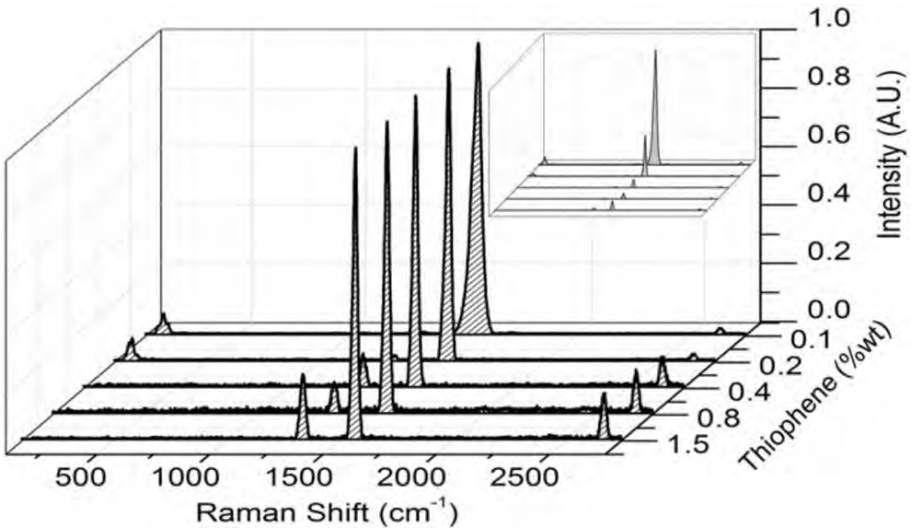

Figure 4.2. Normalised raman spectroscopy data presented the evolution from SW to MW with increasing thiophene during CNT synthesis.

The spectra are normalised to G peak in order to detect all the details in the difference between SW and MW. Intensity of G peak decreases in MWCNT, therefore I_D/I_G ratio increases. Note that this effect also makes I_D/I_G go from around 0.005 to 0.23, but without it necessarily implying a lower degree of graphitization.

RBM peaks are directly associated with the radial vibration of carbon atoms by the radial expansion and contraction of CNT. Its frequency is inversely proportional to the CNTs diameter, every peak correspond with a narrow number of SWCNTs (or layer of DWCNT). As thiophene is increased, RBMs gradually disappear. Further confirmation is extracted from the result using an additional excitation energy (785nm). RBM peaks frequency (ω) and diameter are directly related according with the equation: diameter = 248/ ω. There are several equations in the literature between diameter and frequency. Therefore, it was chosen, which was more adjusted to the obtained results. Typical RBM Raman spectra with different amount of thiophene are shown in the figure 4.3.a-b for 532 and 785nm, respectively. Figure 4.3.c represents a map of all observed SWCNT (further information in 3.3) shown as filled circle with grey scale intensity correspondence, superimposed on all the possible RBMs expected for the two laser energy (as crosses) up to the cut off filter frequency of the spectrometer used.

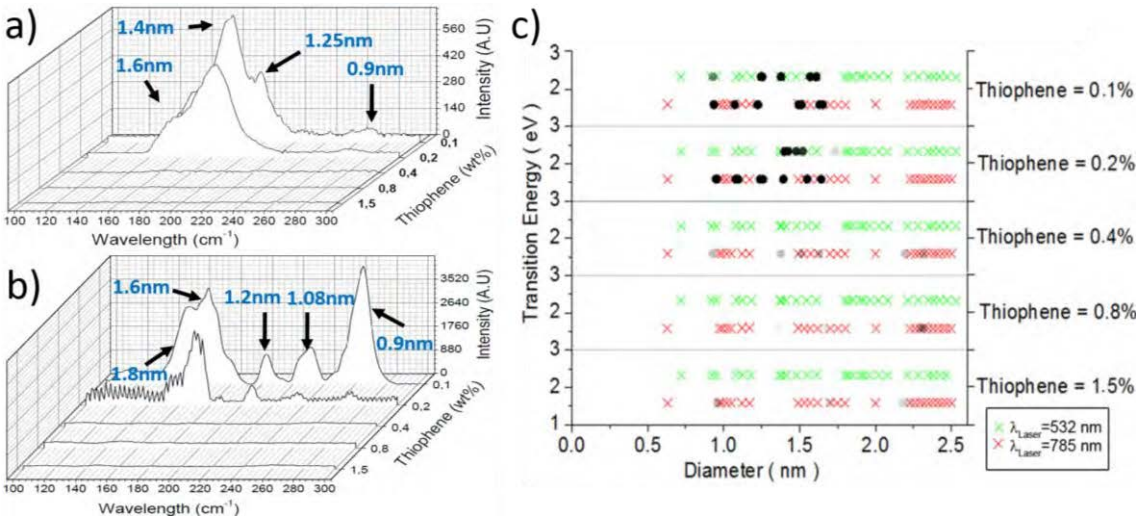

Figure 4.3. RBM Raman spectra with different amount of thiophene and related with the CNT diameter using the equation: diameter = 248/ ω with (a) green laser (532nm) and (b) red laser (785nm). (c) Map of all observed SWCNTs using 2.33eV and 1.58 eV excitation energies. Crosses represent possible SWCNTs detectable with 532 and 785 nm laser lines.

At low amount of thiophene is spilt G peak into G^+ and G^- components, and very low I_D/I_G ratio. Increasing sulphur G^- signal tends to disappear.

The upshift of 2D (2G`) band shows another clear evidence in the transition from SWCNT to MWCNT for increasing thiophene concentration. This shift is due to increase the number of layer in the CNTs, similar to the shift observed in graphene sheets[193]. Commercial SWCNT and MWCNT was measured, confirming the same range of shift in the 2D peak position (Figure 4.4).

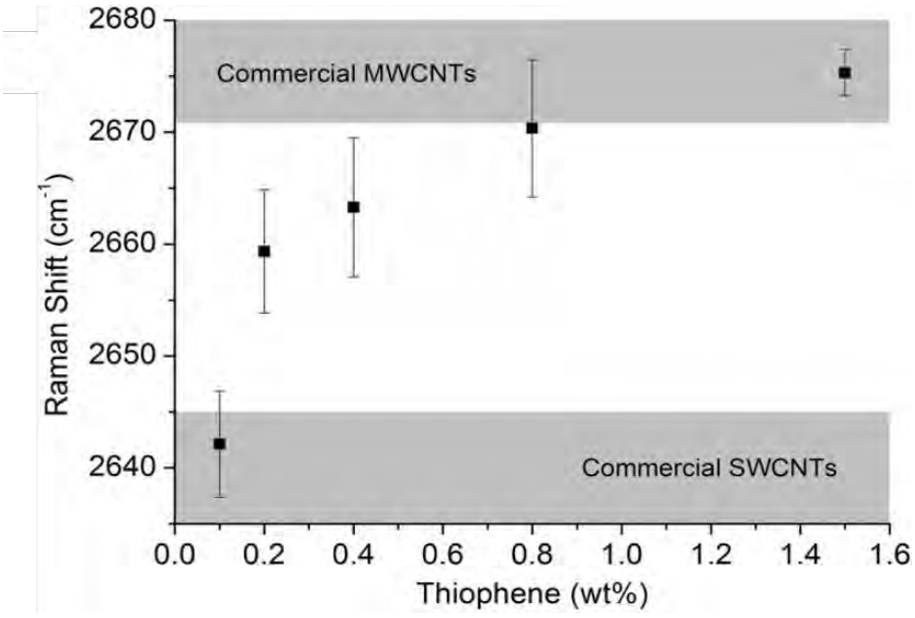

Figure 4.4. Plot of Raman 2D (G`) peak position for samples produced with different amount of thiophene precursor.

Further confirmation is observed changing the carbon source from butanol (aliphatic alcohol) to toluene and benzyl-alcohol, which are aromatic compounds. In order to compare different carbon sources, sample are synthesised under the same parameters, included the thiophene range from 1.5wt% to the minimum amount, that enable continuous spinning of a homogenous fibre. This highlights the ratio S/C as being the most relevant to control the reaction.

In the figures 4.5.a-b raman spectra at different amount of thiophene are shown. Again, the data shows gradual disappearance of SW features: RBM peaks, G-split, loss of resonance and an upshift in the 2D peak as the thiophene concentration increases. The raman shift in low sulphur is higher comparing aliphatic carbon with aromatic compounds, which seem to promote bigger bundles of SWCNT, this superposition of tubes is tuning the shift to higher values.

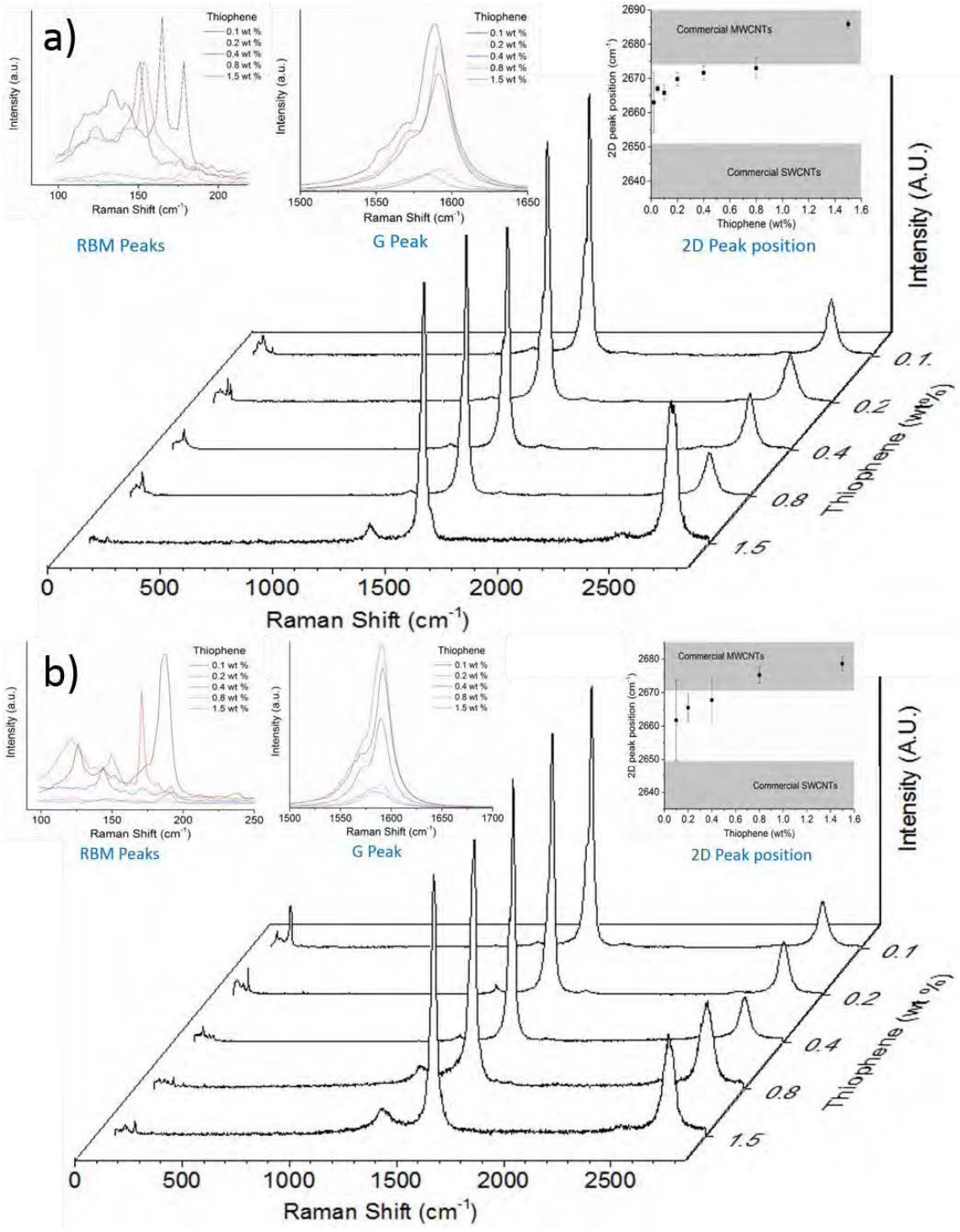

Figure 4.5. Raman spectroscopy data presented the evolution from SW to MW with increasing thiophene during CNT synthesis. RBM, G peaks and 2D peak position are shown by varying the amount of thiophene one order of magnitude using toluene and benzyl-alcohol.

HRTEM and SEM images confirm raman results and rule out the possibility of the strong SWCNT resonance masking other CNTs in low thiophene samples. Figures 4.6.a-f show representative images of samples produced using low (0.1wt%, figure 4.6.a-c-e)) and high (1.5wt% figure 4.6.b-d-f) thiophene

concentration, using butanol, toluene and benzyl-alcohol as a carbon source, respectively.

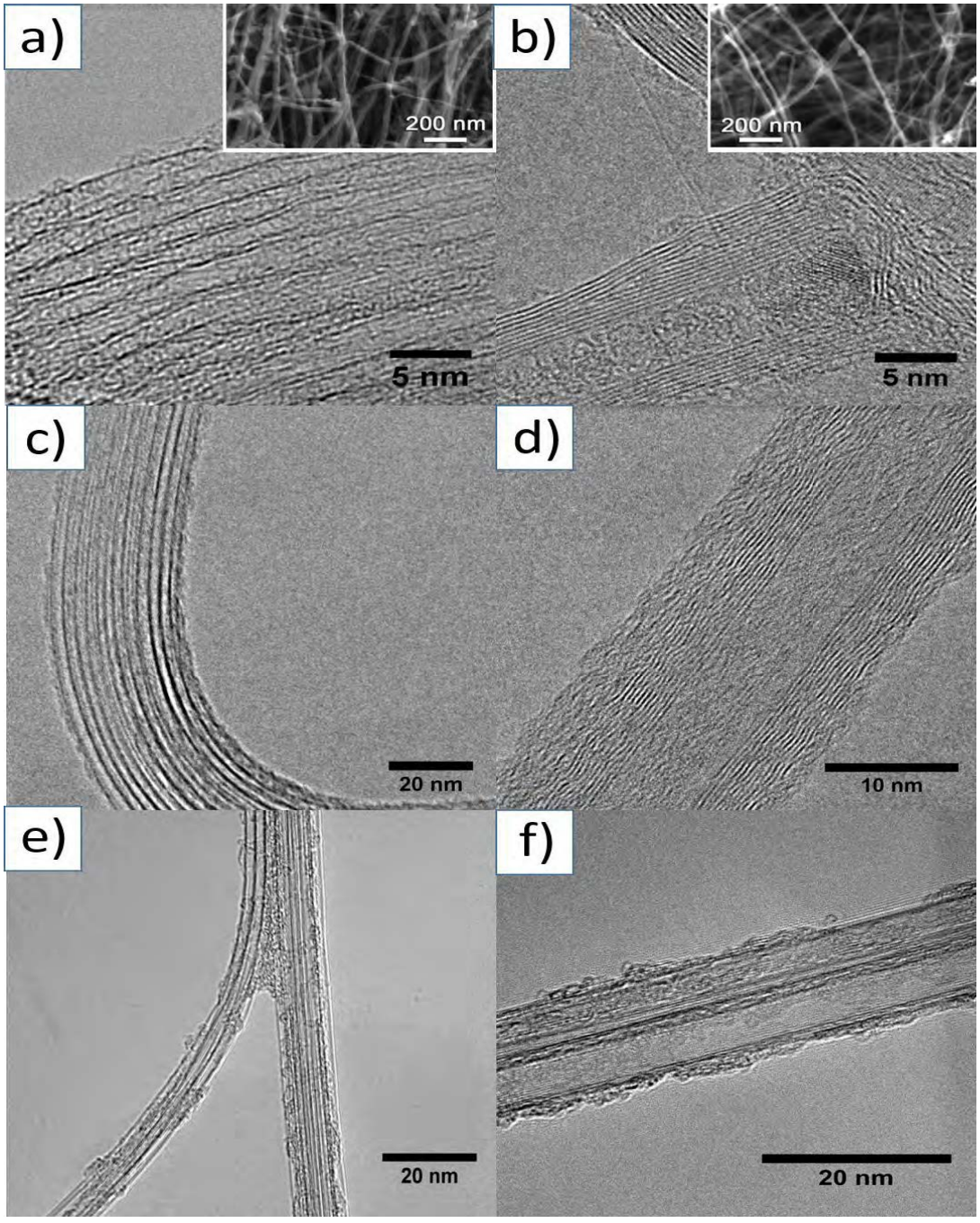

Figure 4.6. Electron micrograph of CNT fibres showing the effect of increasing sulphur precursor. TEM images shows the same evidence independent of the carbon source (a-c-d) SWCNTs are observed at low amount of sulphur. (b-d-f) MWCNT are observed at higher amount of sulphur.

S/C ratio importance contradicts the previous models, which presented the ratio Fe/C as critical to control the type of the CNTs in terms of number of the layers. To evidence the influence of Fe/C ratio, the concentration of iron was modifying one order of magnitude from 0.25 to 2.1wt%. It was observed that raman spectra

does not change, observing the typical SWCNT fingerprint of the fibre (figure 4.7.a). Increasing the amount of ferrocene does not affect significantly the type of CNT or the carbon conversion in the reaction. The catalyst included is mainly redundant that ends up trapped in the fibre. Increasing the concentration of iron more than one order of magnitude, the 2D peak is not affected (Figure 4.7.b).

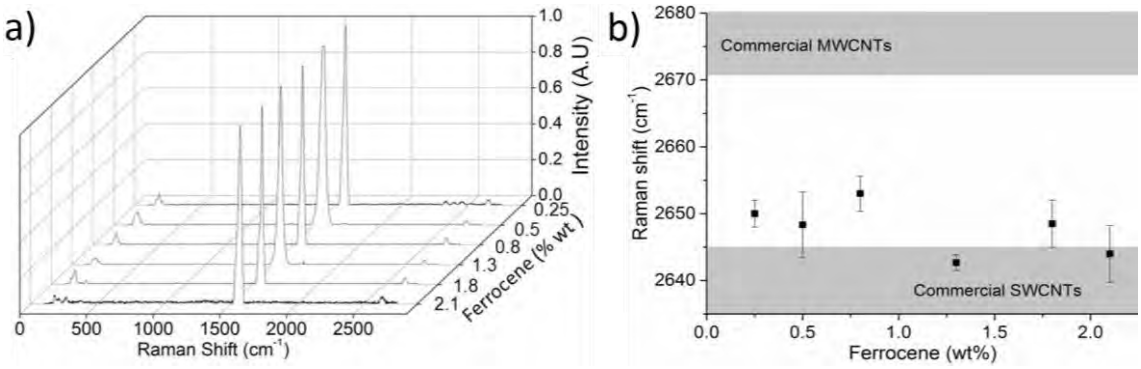

Figure 4.7. (a) Normalised raman spectroscopy data increasing the amount of ferrocene one order of magnitude. (b) Plot of raman 2D (G`) peak position for samples produced with different amount of ferrocene precursor.

An important observation during the spinning process is that increasing the amount of sulphur in the reaction area leads to a thicker fibre with higher linear density. Optical micrographs of densified filaments produced with different sulphur concentration are shown in the Figure 4.8. It is noted that from knowledge of the fibre linear density, winding rate 7m/min for these samples and precursors throughput, a reaction yield can be calculated. In terms of injected carbon/output carbon goes from around 0.7% to 9% for the data in figure 4.9.a (Yield (%) = linear density (g/km)*17.11 (km/g)). Using toluene the yield increases until 20%. A priori, this increase in yield could be due higher S/C, increasing the number of layers CNT and therefore their linear density.

Figure 4.9. Optical micrographs of fibres densified by interaction with acetone at their exit of the reactor. The use of higher precursor in the reaction produces larger diameter fibres.

It was performed the characterization of every sulphur concentration: inner and outer diameter, number of layers; more than 150 CNTs in total. Surprisingly the increase in the linear density, comparing the different amounts of sulphur, fits with the increase of CNT mass due to the fact that the CNT increase the inner diameter and the number of CNT layers (figure 4.9.b). Figure 4.9.a shows the mass increase of individual CNTs, for different thiophene concentration. Another conclusion is possible to extract from this interesting results, increasing the sulphur concentration does not increase the numbers of CNTs. Instead of increasing the nucleation density the effect of increasing sulphur concentration is making bigger catalyst due to the particles coarsening through collisions in the aerogel [194].

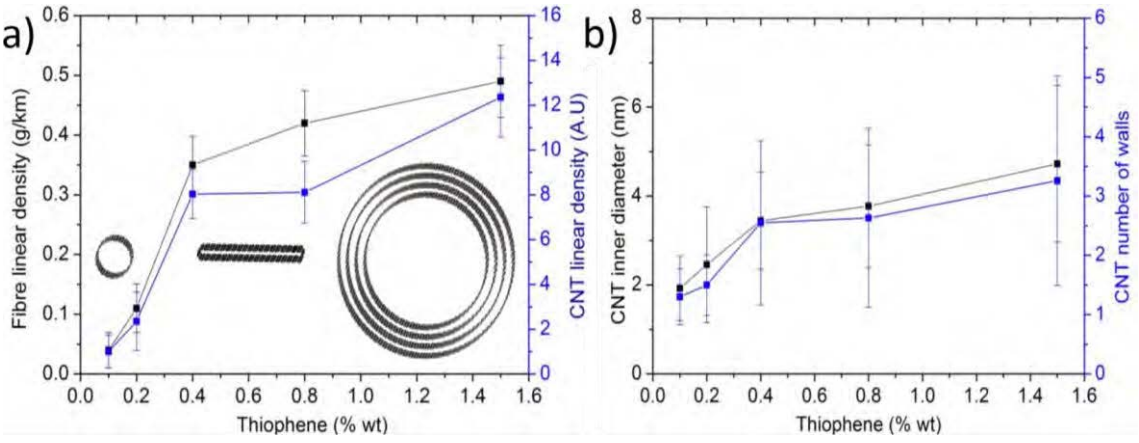

Figure 4.9. Plots of the effect of increasing sulphur precursor on fibre lineal density (a) and on the relative mass per unit length of individual CNTs (CNT linear density) determine from TEM. (b)

The close correspondence implies that fibre lineal density increase almost exclusively due to the increment in CNT number of layers and diameter but at an almost constant number of CNTs. Schematic representations of different CNTs, showing the evolution SWCNT to collapse CNT to MWCNT, are also included.

Samples synthesised in at 0.1% and 1.5% are analysed and extracted statistics, 20 CNTs in total, related to the number of walls and inner diameter using toluene and benzyl-alcohol as a carbon source (figure 4.10.a-b). At low amount of sulphur, homogeneous SWCNTs are synthesised with narrow distribution of layers and diameters, which are comparable with butanol results.

Although the increasing of sulphur has the same effect than butanol, fibres produced from toluene and benzyl-alcohol lead to multiwall with more layers and with higher inner diameter. This effect can be related to the route of decomposition of the aromatic compounds. Aromatic ring releases the carbon atoms ≈ 950ºC, at this temperature secondary reactive products are mainly isolated atoms, for its part, butanol decomposition route starts ≈ 400ºC, proving hydrocarbon with lower molecular weight in an early stage. However, it is evidenced that benzyl-alcohol leads to high number of collapse CNT 80%, compared to toluene with 20%. This effect might be related to the presence of oxygen in the reaction. However, it has to be study more in detail, recommending this direction in future experiments as it is discussed in section 4.7.2.

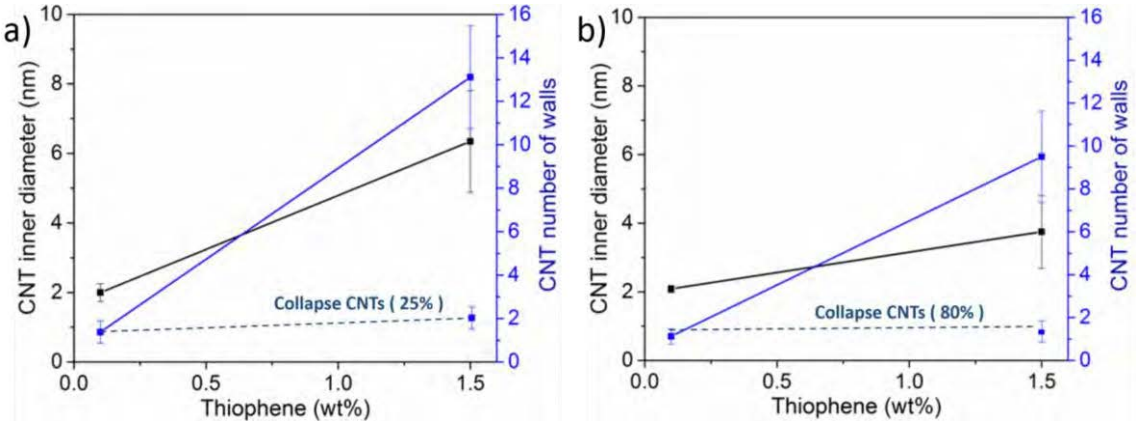

Figure 4.10. Plots are representing the response related to the inner diameter and number of the layers, when thiophene goes from 0.1% to 1.5% using (a) toluene and (b) benzyl alcohol as a carbon source.

4.3.2. Length of the CNTs

CNT length is very difficult to measure due to the exceptionally big ratio: diameter/ length ≈ $10^{(-5\ to-6)}$, which is evidenced by this synthesis method [104]. Using butanol as a carbon source the biggest CNTs diameter was in the range of 10-15nm. These CNTs are difficult to isolate because smaller CNT has more tendency to form CNT bundles, avoiding the observation the individual CNT using low magnification. Thus, thicker CNTs were synthesised using toluene as a carbon source around 20-30nm, which are easier to isolate, making possible to follow several individual CNT, measuring lengths over 0.1mm (Figure 4.11).

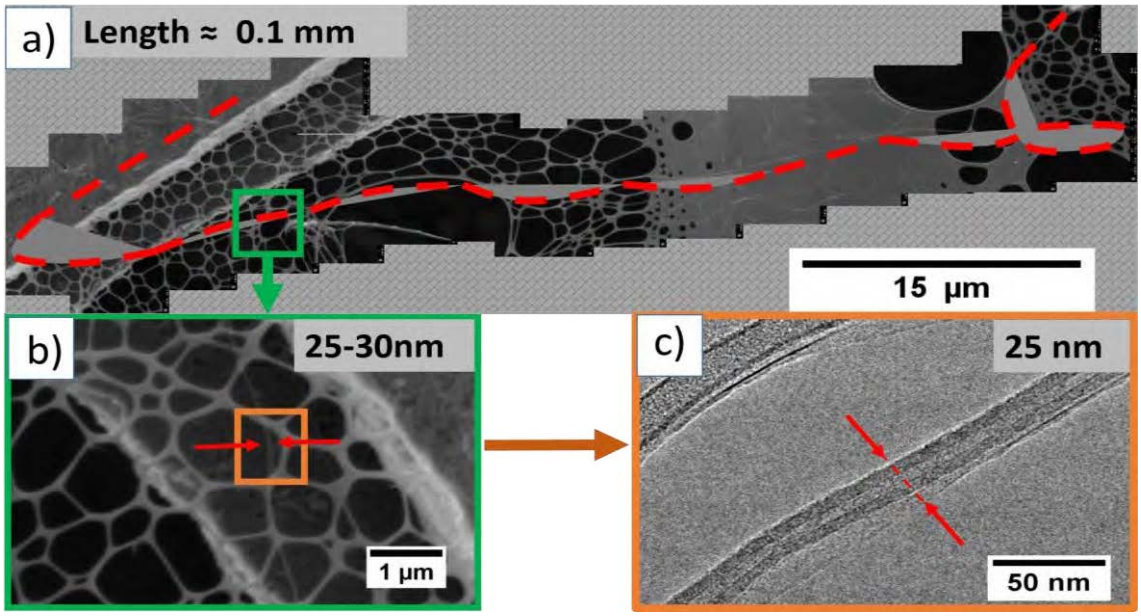

Figure 4.11. Electron micrograph of CNT fibres showing different magnifications. a) More than 40 images forming a puzzle showing both edges, length is around 0.1 mm. (b) One piece of the puzzle, showing the CNT diameter and confirming with (c) a TEM micrograph that it is following an individual CNT, comparing diameters.

4.3.3. Chiral angle distribution of SWCNTs.

As it is reported in the previous section, it is possible to tune the CNT fibre from SWCNT to MWCNT. Chiral angle of SWCNTs is studied electron diffraction.

Fibre samples of SWCNT were further analysed by Dr. Alemán, from SAED diffraction patterns, it was possible to determine directly the CNT chirality. Figure 4.12.a shows a typical armchair diffraction pattern from a SWCNT bundle. It shows the (100) located in a perpendicular direction to the 002, corresponding to a chiral angle of 30º, therefore with armchair chiral indices. The same procedure

applied to more than 20 bundles, including close to 400 CNTs. The distribution of chiralities is presented in the figure 4.12.b.

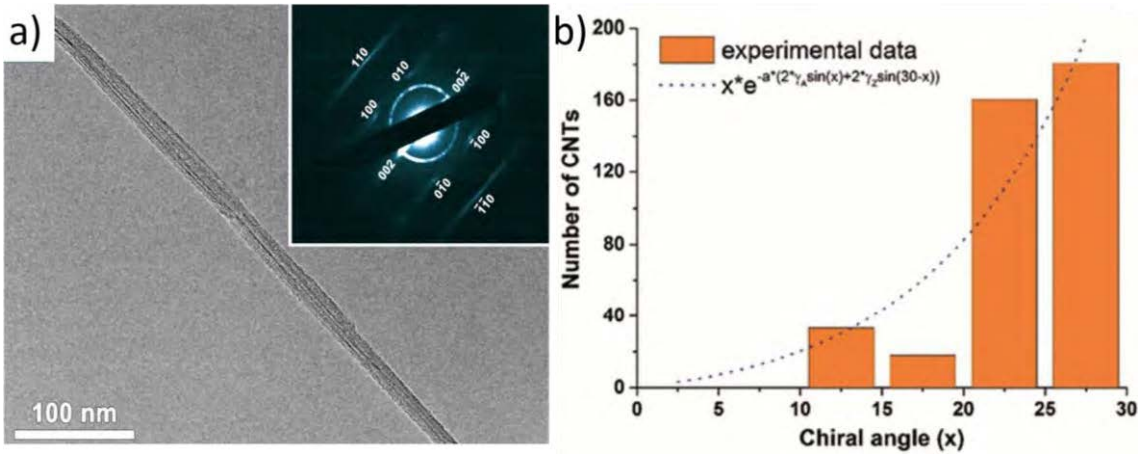

Figure 4.12. (a) SWCNT bundle with the SAED diffraction pattern from TEM and (b) chiral angle distribution related to 400CNTs.Dash line shows the theoretical prediction for molten catalyst particles[195].

The predominance of armchair CNTs is clear, with absence of zig-zag CNTs or chiral angle below 10º. Similar evidences are observed using toluene as a carbon source and selenium as a promoter, although for a smaller sample set[8].

More importantly for this work the distribution of chirality matches with the theoretical predictions for CNTs produced by a molten catalyst[195]. The molten state of the catalyst has implications for the solubility and diffusion of species, as well as other properties affecting CNT growth. These are discussed in more detail in section 4.5.

4.4. Catalyst study

4.4.1. Active Vs inactive catalyst particle

It is presented HRTEM images of a typical inactive particle and active particles, respectively. Overall, our post-reaction comparison has not exposed significant differences between them in the bulk part, other than their shape. Active particles have the typical elongated shape widely observed in CNT growth, whereas inactive ones are mainly spherical. Evidenced in the figures 4.13.a-b.

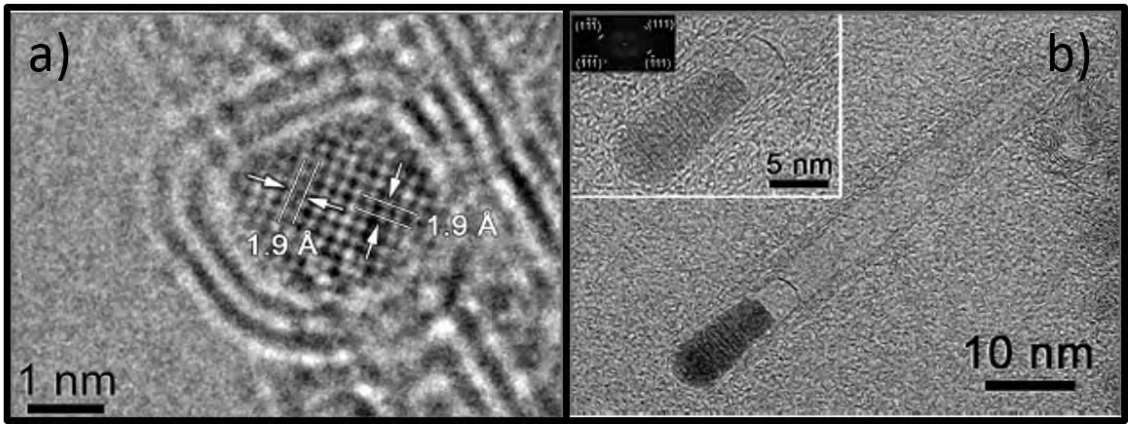

Figure 4.13. HRTEM micrographs of (a) an inactive catalyst particle encapsulated by a couple of graphitic layers and (b) an active particle that catalysed the growth of a MWCNT.

Hundreds of HRTEM micrographs were analysed in order to find active catalyst particles, evidencing the high fraction of inactive particles.

It is possible to estimate the ratio, between the catalyst particles involved in synthesising CNTs and the total catalyst particles present in the CNT fibre. The total amount of residual catalyst in the fibre is calculated by TGA measurement, analysing the iron residue after treatment at 900ºC.

The mass of inactive particles/carbon in the fibre is obtained from TGA as Fe_f/C_f. The mass of active catalyst particles/carbon in the fibre can be trivially calculated assuming that for each CNT there is a corresponding spherical particles of diameter equal to the CNTs inner diameter.

$$\frac{mass\ of\ catalyst}{mass\ of\ CNT} = \frac{\frac{\pi}{6}\phi^3\rho_{Fe}}{\pi\phi vnl} = 1.7 \times 10^9 \frac{\phi^2}{nl} \qquad Equation\ (4.1)$$

Where ρ_{Fe} is the volumetric density of iron, v is the areal density of graphene, n is the number of layers and l the CNT length. Taking, for example, n = 2, Φ = 5 nm and l = 1mm, this ratio comes out as 4.2 x 10^{-5} and the proportion of active over inactive particles 4.2 x 10^{-5}/0.08 = 5.2 x 10^{-4}.

Thus, The probability of finding an active catalyst particle in 2000 inactive or the end of a 1mm CNT in between the ≈ 10^7 CNT per fibre cross section is rather low. Hence the difficulty in direct observation of active catalyst particles by HRTEM. An implication of the small fraction of active particles is that some the bulk characterisation results might not apply to active particles.

The inactive catalyst particles due to the early encapsulation with graphitic carbon and attract with other inactive particle are forming clusters over CNT bundles (figure 4.14.a), comparing with the active catalyst encapsulated into the fibre (Figure 4.14.b-e).

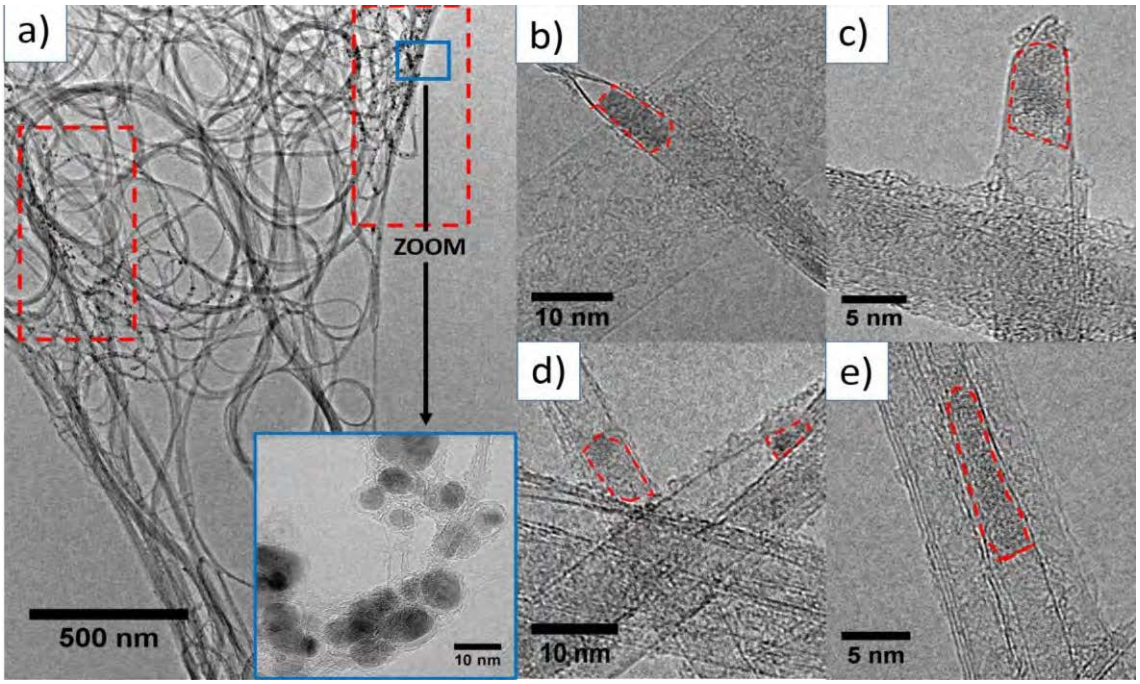

Figure 4.14. TEM micrograph of CNT fibres showing the different catalyst residue. (a) Catalyst surrounded by graphitic layers forming clusters over the bundle surface and (b-e) active catalyst particle trapped inside CNTs.

4.4.2. Growth model: Relation to bulk Fe-S-C ternary diagram

The concentration C/Fe estimated from TEM is then combined with the ratio of S/Fe (same in the fibre and in the catalyst), to calculate the complete elemental composition of the catalyst particles. The results for these inactive particles give an approximate atomic composition Fe:C:S of 68:26:6, only slightly dependent on reactant concentration (table 4.6).

Figure 4.15 shows the location of these inactive catalyst particles in the iron-rich corner of the isothermal 1400ºC section of the Fe-C-S ternary diagram[104]. Their composition is where the S-rich and C-rich liquids (L1, L2) coexist with solid carbon (i.e. graphite), towards the boundary with cementite.

Unlike most CNT substrate growth processes by low-temperature CVD where there is a large proportion of active particles (up to 20%[67] and 84% upon addition of water vapour[196]) easily accessible by inspection of the tip or root of

the array, in our method the proportion is to be around 0.05% as it is explain in section 4.4.1.

The emerging model is that all Fe particles saturated rapidly with C in their trajectory through the reactor. Most of them encounter S when their concentration of C is already very high, approaching the phase-diagram region that does not favour CNT growth because the two immiscible liquids (one s-rich and other c-rich) are in equilibrium with solid carbon. Therefore, encapsulation of particles is more likely than lifting off of the graphitic cap that starts CNT growth. Remnant C in the supersaturated particles precipitates upon cooling.

Following this argument, the very small proportion of active particles would be those in which S diffusion occurred at lower C concentrations corresponding to the regions of the ternary phase diagram in figure 4.15 where the liquid(s) is (are) not in equilibrium with C(S) and therefore the incoming carbon would upon saturation of the catalyst particle get extruded to form a CNT.

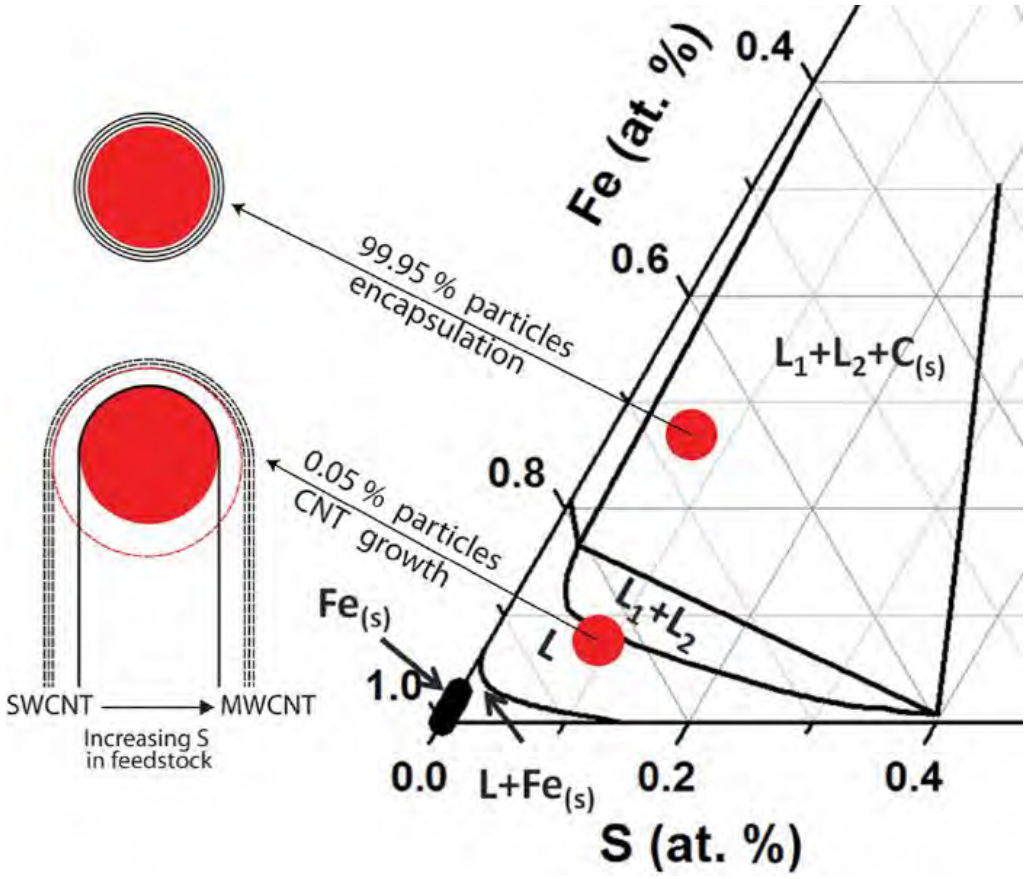

Figure 4.15: (a) Isothermal section of the Fe-C-S phase diagram at 1400ºC showing the location of inactive catalyst particles based on experimentally approximated composition and where active catalyst composition and CNT growth are expected.

This argument is in agreement with S limiting the diffusion of C in Fe, as observed both in CNT growth and in steel literature[104], and is also supported by our finding that the ratio S/C plays a far more central role in controlling CNT growth than Fe/C. The post-synthesis TEM analysis, by showing the similarity between active and inactive particles, highlights the subtle role of sulphur as a promoter, which even at small quantities (5 < at.%) plays a key role in controlling CNT growth not only by limiting C diffusion but also assisting C reconstruction and edge growth. The growth direction in the catalyst particles comes from the amount of sulphur in the particle.

4.4.3. Evidence of sulphur in the CNT fibre

The first evidence of the incorporation of sulphur in the iron catalyst comes from EDS measurements of the fibre. Figures 4.16.a-b present a typical EDS spectra confirming the presence of Fe and S in the fibre. Increasing the S in the feedstock, ratio S/Fe also increase. Other small peaks could be related to contaminant Al, O, Cu, Ca, Cl or Si.

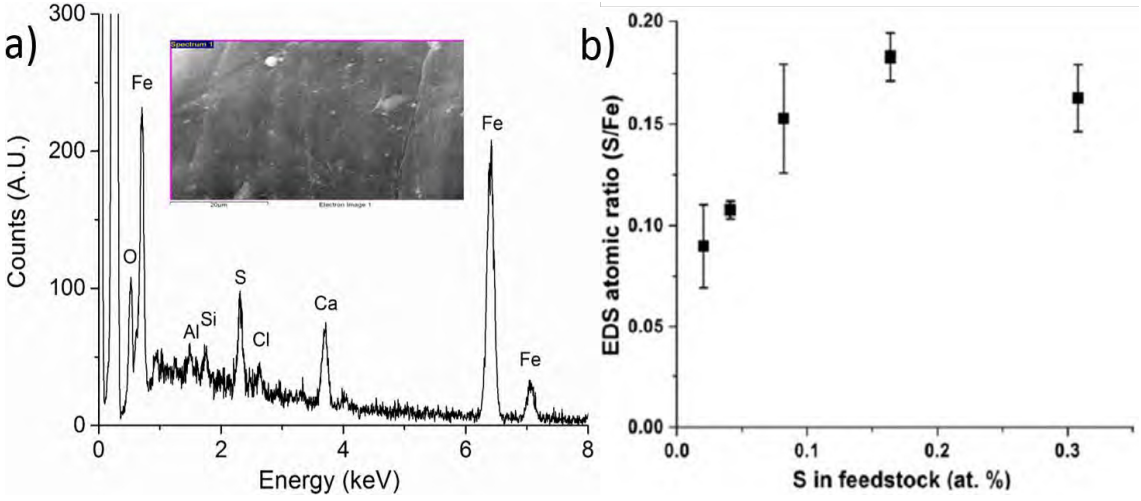

Figure 4.16. (a) EDS spectra showing the presence of sulphur and iron in the sample. (b) Increase in S/Fe ratio with increasing content of S precursor during synthesis.

Additional information about the presence of sulphur and in general the oxidation state of the catalyst obtained from XPS measurements. Figure 4.17 shows the Fe fingerprint in the XPS spectrum for a 0.2% thiophene fibre. The Fe 2p signal is evident, showing Fe peak splitting at 707.1 eV (Fe $2p_{3/2}$) and 720.3 eV (Fe $2p_{1/2}$) corresponding to the metallic iron. Increasing sulphur concentration leads

to the appearance of two emerging contribution to the spectra at 712 and 725 eV (inset) related with Fe-S compounds[197] in the catalyst particles.

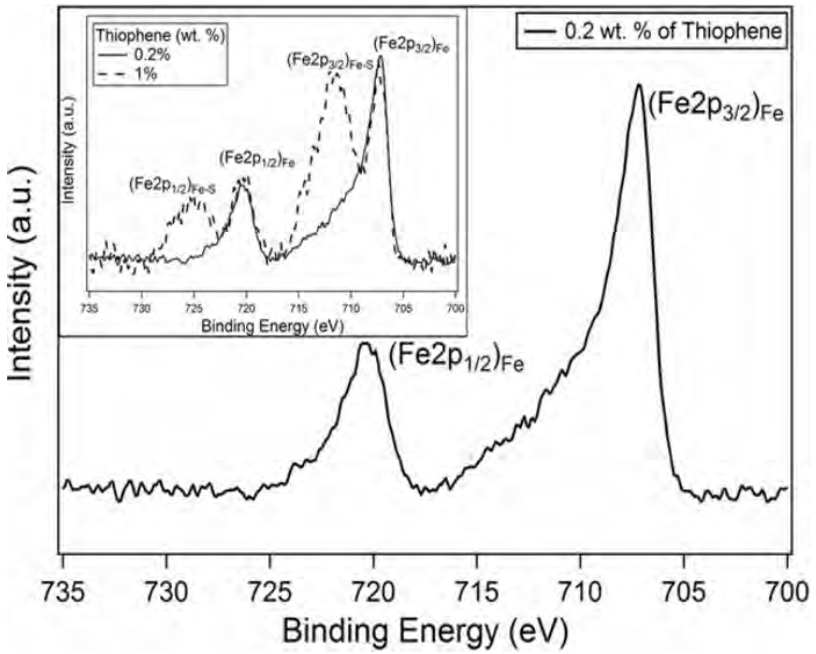

Figure 4.17. (a) Iron fingerprints in XPS spectrum for a 0.2 wt% thiophene fibre. (Inlet) Comparison between 0.2 wt% and 1 wt% thiophene fibre showing the increment in the peaks related with Fe-S compounds.

Figure 4.18 confirms the presence of sulphur compounds with the appearance of S2p peaks at 162.5eV and 169.5eV, related with sulphide and sulphate compounds, respectively. The observation of sulphur $2P_{3/2}$ fingerprint reveals another evidence of the sulphur presence in the catalyst particles .Furthermore, it is possible to study the different oxidations states of sulphur. The binding energies values of S $2P_{3/2}$ are located in function of the oxidation states, 162.1eV is related with oxidation state -1 and 168.7eV with oxidation state +6[197]. It is worth mentioning the lack of the evidences about the S +0 formation. The presence of the two peaks are related with Fe-S compounds and the ratio between them change when the amount of sulphur is increased in the synthesis of the fibre. Increasing the amount of sulphur leads to formation of sulphate formation, oxidation state +6, instead of sulphide, oxidation state -2. This could evidence the appearance of two different catalyst population. However, it is worth remarking that this analysis was made in the post-spinning particles, at 1250ºC these compounds are not stable.

Figure 4.18. Sulphur fingerprints in XPS spectrum comparing different amounts of thiophene for a 0.2 wt% and 2 wt% thiophene fibre. Showing the increment in the intensity peak ratio between sulphate/sulphide, related with Fe-S compounds.

It is obvious the presence of sulphur in the catalyst and its importance for CNT growing. Figure 4.19 presents a detail spectrum of C 1s core level showing a high intensity sharp peak at 284.5 eV from sp^2 C = C, a small shoulder at 285.7 eV related to low amount of sp^3 C – C carbon, and broad peak centred at 290.5 eV related to π-π* transitions attributed to the interaction between the CNTs in the bundles[198]. No changes in the peaks in the region 280-300eV are observed with an increasing amount of thiophene precursor. These measurements rule out the possibility of S doping by direct incorporation into CNTs and establish that all sulphur in the sample is associated with the catalyst.

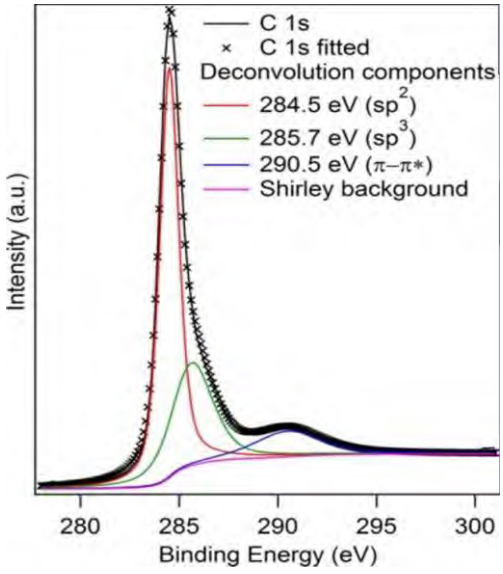

Figure 4.19. Deconvolution of C-related peaks showing the predominance of SP^2 C=C.

To summarise, the presence of sulphur in the CNT fibre is observed by EDS and XPS measurements, its presence is always associated to iron in catalyst.

4.4.4. Location of sulphur in catalyst

In the section 4.4.5, it is outlined the catalyst composition, the conclusion was clear, obtaining different catalyst composition and sizes, lead to different CNT synthesis.

Observing the electron micrographs (4.20.a) and its EDS maps (4.20.b), it is possible to conclude that active catalyst structure is not homogeneous, the amount of sulphur is higher in the CNT growth direction. Analysing several particles, which are grown CNTs, are shown the same evidence. On the other hand, the inactive catalyst particles are more homogenous or the amount of sulphur in the catalyst in negligible, confirming the sulphur role as a growing promoter not only being present in the catalyst but also increasing its presence in the growth direction. Which is observed without being emphasised in the literature[90].

Comparing the ratio S/Fe between the growth side of the particles and its opposite, in active catalyst particles, is ≈ 3 (4.20.b). Furthermore, in inactive catalyst particle the distribution of sulphur is more homogeneous and the ratio between the two sides in the particle is ≈ 1. Figure 4.20.c shows the representation of the signal from iron and sulphur, iron signal is semi-circular, according with the particle shape. However, the sulphur signal is more intense in the edges of the catalyst and especially in the growth direction of the CNT.

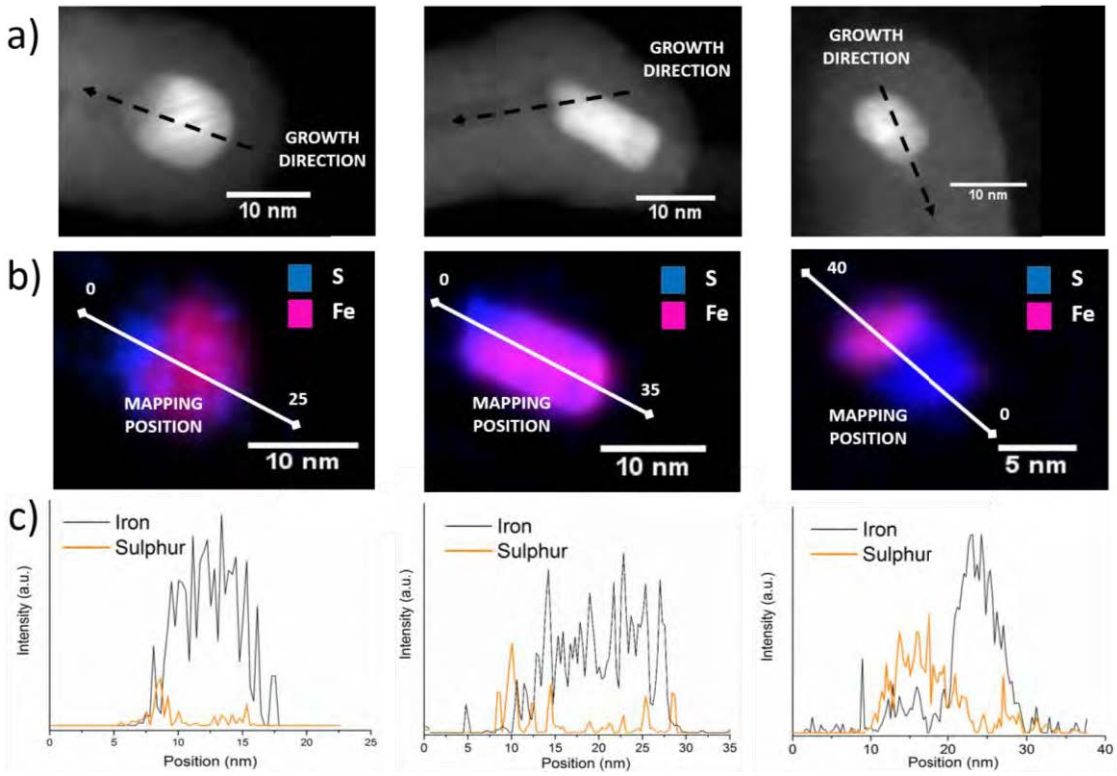

Figure 4.20. (a) Electron micrograph of active (1-2-3). (b) EDS maps are showing the mainly presence of sulphur in the growing size part of the catalyst in the active particle (c) Sulphur and iron concentration profile throw the catalyst particles by EDS.

4.4.5. Catalyst composition

In this section, the discussion moves on to the composition of the catalyst. Particles trapped in the CNT fibre were analysed by a combination of techniques: TGA, OEA and EDS. Reporting ratios between carbon, iron and sulphur, which are providing valuable information for quantitative results.

1. *Fe_f/C_f ratio:* TGA provides the mass of catalyst relative to the fibre (Fe/(S+C)) ≈ Fe/C. Amount of iron is between 3.5 wt% and 15 wt%, depending on synthesis conditions. At 700ºC in the TGA all iron has decomposed into iron oxide (Fe_2O_3) and therefore the iron content corresponds to ≈70% of the residual TGA mass. Assuming this path, it is possible to take the relative mass from TGA at 900ºC. Values are summarised in table 2.

Table 4.2. Values from TGA analysis.

% Thiophene	%Fe_2O_3	% Fe	% Amorphous Carbon	CNTs	Fe_f/C (%wt)	Fe_f/C (%at)
0.2	21.2	14.8	6.6	78.6	0.17	0.037
1.5	5.4	3.8	12.0	84.2	0.04	0.008

2. *Fe_f/C_f ratio:* Through the OEA results, it is possible to extract directly the S_f/C_f ratio. Table 4.3 shows the values obtained from the measurements.

Table 4.3. Values from OEA analysis.

Thiophene	C (%at.)	S (%at.)	S/C (%at.)
0.2	86.96	0.44	$5x10^{-3}$
1.5	94.83	0.11	$1.2x10^{-3}$

3. *S_f/Fe_f ratio:* EDS measurement provides the information about the ratio between S and Fe iron in the fibre. Furthermore, according to XPS, Fe and S are only present in the catalyst (S_f / Fe_f = S_c / Fe_c). Therefore, it is the overall ratio also in the catalyst. With respect to the catalyst, these techniques have thus provides the ratio S/Fe, yet, the previous section has demonstrated that the key parameter controlling the reaction is the ratio of S/C. Extracted values are in the table 4.4.

Table 4.4. Values from EDS analysis.

% Thiophene	Fe (% at.)	S (%at.)	S/Fe (%at.)
0.2	2.05	0.22	0.11
1.5	0.44	0.07	0.16

4. *C_c/Fe_c ratio:* It is assumed that the carbon of the layers to have diffused in the catalyst during CVD and then precipitated either at the point of reaction or upon cooling. Thus, the carbon fraction (in wt%) in these particles can be estimated from the number of encapsulated layers/particle diameter, which is approximated as: 3 Cs=$3n\ \nu\ /r\rho_{Fe}$ = $3a\ \nu\ /r\rho_{Fe}$. To calculate the catalyst composition, it is necessary to obtain statistic values from HRTEM micrographs (example figure 4.21).

HRTEM analysis gives values of α of 0.2-0.64nm^{-1}, higher than 0.2-0.3nm^{-1} reported for catalyst particles produced in low temperature CNT synthesis[199]. The mass of carbon in the catalyst is approximately $4nr^2\ \nu$. Where ν is the areal density of a graphene layer (0.75 x 10^{-6} kg/m^2).

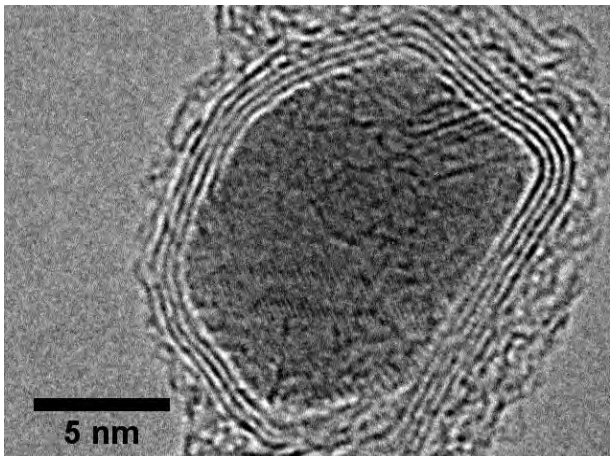

Figure 4.21. HRTEM micrographs of catalyst particle encapsulated by a couple of graphitic layers

The mass of catalyst is approximately $4/3\pi r^3\rho_{Fe}$. Where ρ_{Fe} = 7.87g/cm^3. The fraction of carbon in the catalyst, $C_c/(S_c + Fe_c) \approx C_c/Fe_c$;

To sum up the values are obtained in with the techniques represented in the Table 4.5 and the values in the Table 4.6.

Table 4.5. Determination of fibre and catalyst analysis.

Technique	Composition in fibre ($Fe_f + C_f + S_f = 1$)	Composition in catalyst ($Fe_c + C_c + S_c = 1$)
TGA	$Fe_f / (C_f + S_f) \approx Fe_f / C_f$	
OEA	S_f / C_f	
EDS	$S_f / Fe_f = S_c / Fe_c$	
TEM		C_c / Fe_c

The composition of two samples is listed in table 4.6, including concentrations in the fibre and in the catalyst but clearly the more relevant concentrations are those in the catalyst particles, not in the whole fibre.

Table 4.6. Determination of fibre and catalyst analysis.

	Fibre composition (at.%)			Catalyst composition (at.%)		
Concentration (wt. %)	**Fe**	**S**	**C**	**Fe**	**S**	**C**
Butanol 99, ferrocene 0.8, thiophene 0.2	3.7	0.4	96.1	68.2	5.8	26
Butanol 97.7, ferrocene 0.8, thiophene 1.5	0.7	0.1	99.2	63.2	10.8	26

This require knowing the amount of carbon in the catalyst, which it is possible to approximate by measuring the amount of carbon segregated by the catalyst particles using HRTEM and from knowledge of the catalyst crystallographic phase obtained by synchrotron XRD.

4.4.6. Crystal structure analysis.

Catalyst particle is divided in two main parts:

1. - Fe-S shell, which is surrounded the catalyst particles and its heterogeneous distribution over the surface.

2. -The iron bulk structure. Which is giving the structural conformation and accommodate inside all the carbon particles that are diffused into the catalyst particle.

The evolution of the catalyst during the CVD reaction has been studied by the research group by post-mortem examination of the catalyst and by thermodynamic calculations performed by collaborator[200].

The catalyst particles remain in liquid state at temperature over 1000ºC, during CNT growth[200]. Catalyst particles in the range of a few nanometres would decrease its melting point due to the Gibbs-Thomson effect [58].

Related to the iron bulk catalyst area, figure 4.22.a presents a typical XRD pattern, including lines in the critical angles in the range 25-55 nm^{-1}. In particular, this pattern was obtained from a catalyst structure of a sample produced with 1.5 wt% of thiophene, corresponding to MWCNT with 3.25±1.5 layers.

It is shown an intense reflections from the CNTs and evidence of the (111), (200) and (220) reflections from FCC Fe, but interestingly, closer inspection of the patterns shows the presence of martensite. In a detailed plot in the range 28-35 nm^{-1} (figure 4.22.b) the martensite (101), (110) reflections can now be clearly identified and distinguished from other intense contributions from FCC (111), CNT (100) and the expected positions for Fe_3C (031) (112). The slip of the martensite (002) and (200) peaks at 42.5 and 44.05nm^{-1} (figure 4.22.c). The data confirm the absence of BCC Fe or Fe oxide.

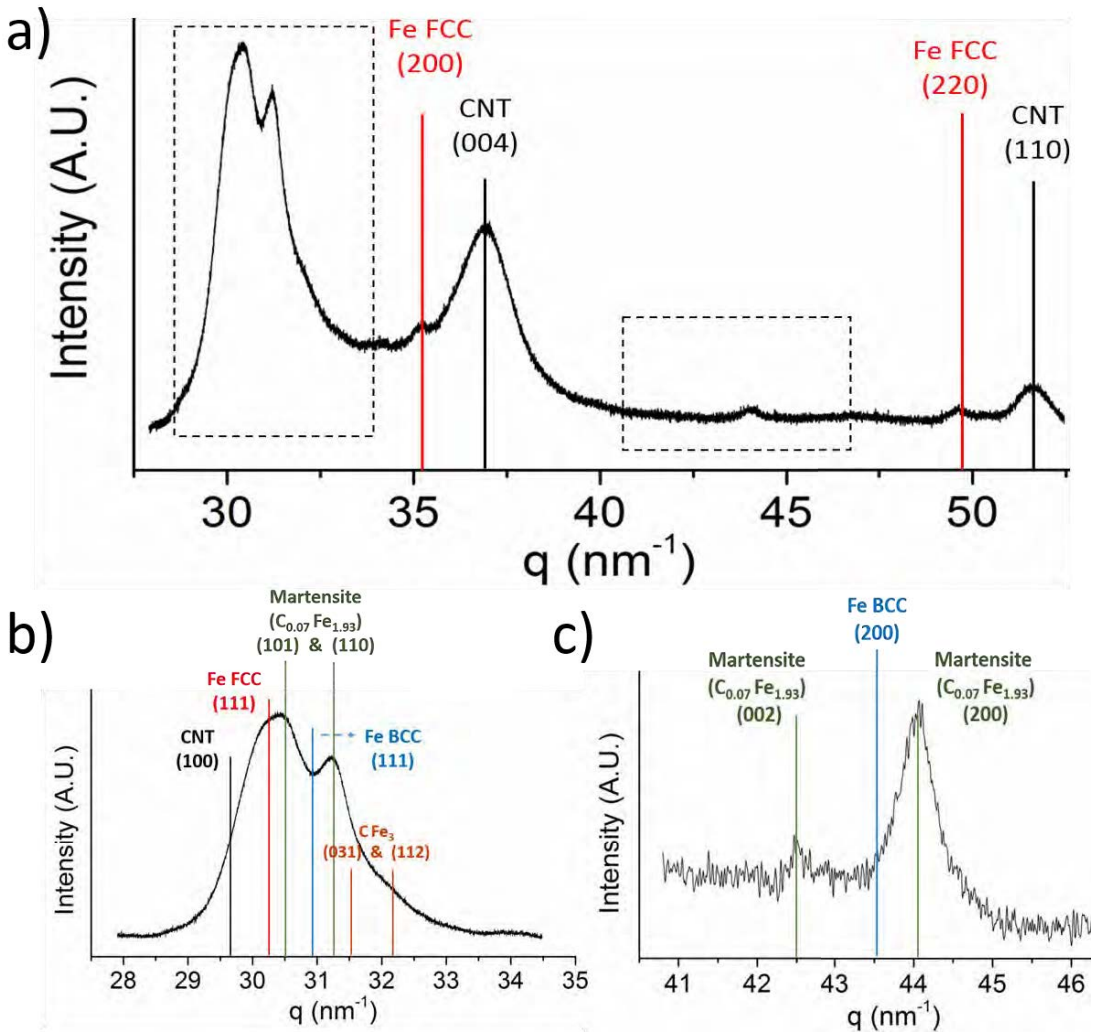

Figure 4.22. XRD pattern from a CNT fibre, (a) covering the typical catalyst range from 26 to 52nm^{-1}. It is possible to conclude clearly the presence of Fe FCC and the graphitic peaks related to CNTs. (b) and (c) are shown higher magnification from the dashed line. It is evident the presence of martensite and the absence of Fe BCC.

It is possible to calculate the amount of interstitial carbon dissolved analysing the shift of the peak due to the change of the lattice parameters, using the equation (1)

$$c/a = 1 + 0.045 \text{ wt\% C} \qquad Equation\ (4.2)[201]$$

Lattice parameters c and a are calculated using the distances related with the peaks positions from XRD, since the change in lattice parameters depends linearly on the carbon content. Equation is defined as Equation 4.3.

$$\frac{1}{d^2} = \frac{h^2}{a^2} + \frac{k^2}{b^2} + \frac{l^2}{c^2} \qquad Equation\ (4.3)$$

(002) and (200) are representing reflection from 1.48 and 1.43Å (figure 4.22.c), obtaining lattice parameters a = 2.86 and c = 2.96. Introducing lattice parameters in the equation 4.2, it is obtain a value for carbon content (wt% C) equal to 0.77%.

4.5. Catalyst evolution & the role of interfacial energies during CNT growth.

In the previous sections, it is explained the conditions under CNT is extruded. Thus, this section is focused in active catalyst particles, in order to explain the catalyst route and the importance of the different elements in CNT growth.

Due to the reaction conditions, the catalyst is evaluated in post-synthesis stage. However, as it is mentioned in section 4.4, there are strong evidences to conclude the liquid state of the catalyst particles at the reaction point. Catalyst size is in average between 3 and 10 nm and due to Gibbs-Thomson effect the melting point decrease significantly[57] [58]. The catalyst composition is calculated, allowing to predict the catalyst route from 1250ºC and throughout rapid cooling. Current understanding of the reaction is that upon the catalyst particle adopts a core-shell structure. Sulphur and other group 16 elements readily diffuse to the surface of transition metals with a low enthalpy of migration[8].

Cooling from molten state, the first expected transformation is the formation of a stable FCC Fe nucleus, upon which S is rejected to the surrounding liquid owing to the negligible solubility of S in FCC (< 0.1 at%). As FCC Fe core grows, liquid is increasingly enriched with S until an-intermetallic $Fe_{1-x}S$ forms. Although, the exact composition of the liquid in unknown, it is S-rich. Core-shell path could be confirmed by thermodynamic calculations of phase fraction of solid phases during fast cooling (quenching). Using *Thermocalc software* phase fraction evolution is calculated of Fe-9at%S binary mix. *Thermocalc* calculation were preform by *Computational alloy design group* in IMDEA materials institute.

Figure 4.23.a shows the thermodynamic path of the liquid around the FCC Fe nuclei along the liquidus line highlighted on the Fe-S binary diagram, whereas figure 4.23.b displays the corresponding phase fraction (solid line), predicting more than 15% fraction of liquid even at temperatures low as 1000ºC. Dashed blue and red line are the limits for the phase fraction evolution of the catalyst

during fast cooling. Dash lines are calculated by suspending/retarding the formation of FCC/Fe_{1-x}-S eutectics, yet preserving primary FCC.

The view that the catalyst is in liquid state on at least its surface, is consistent with the chiral angle distribution observed (figure 4.12), assuming the dislocation growth model proposed by Artyukhov et al.[195].

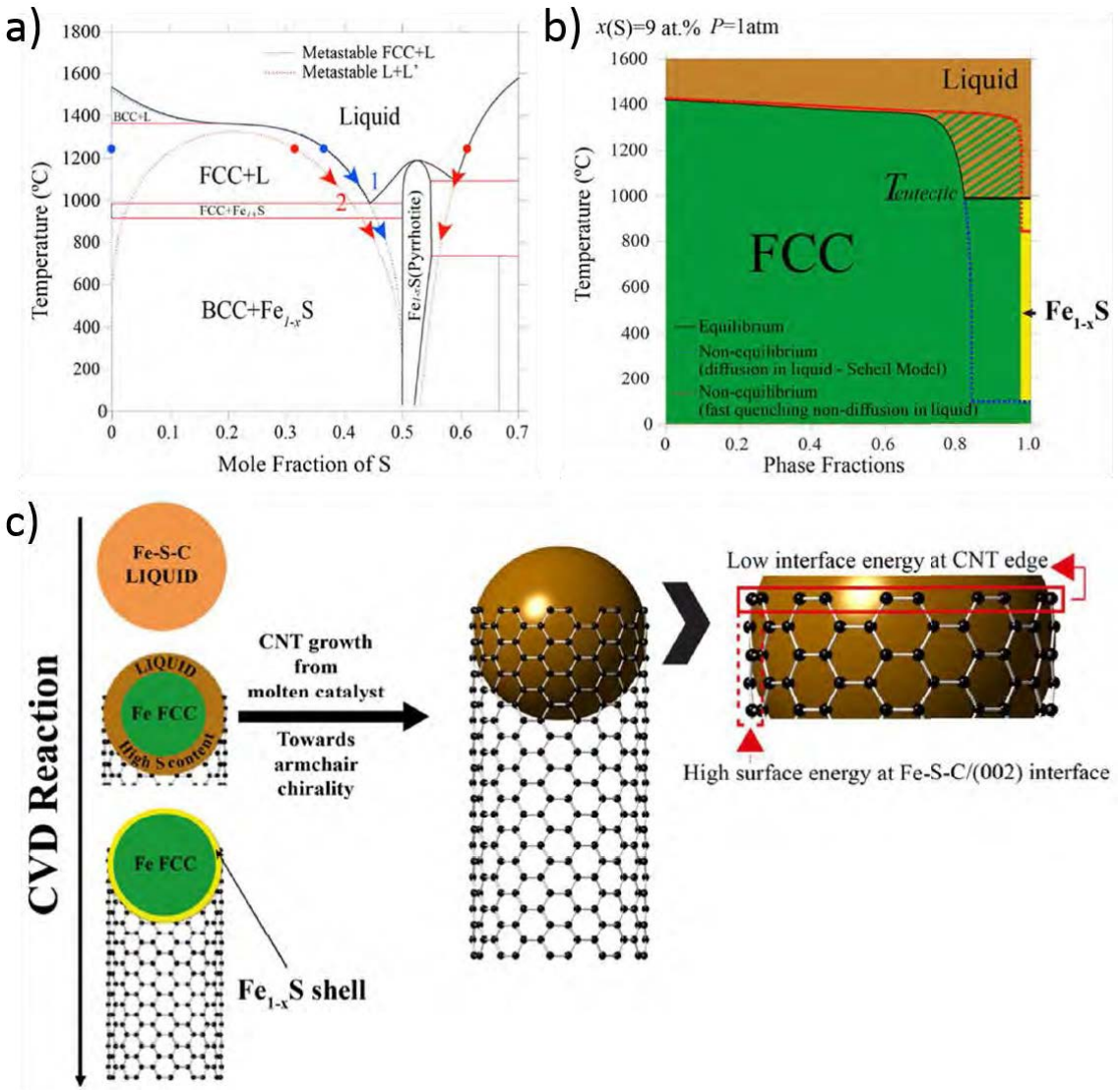

Figure 4.23. (a) Fe-S equilibrium phase diagram and calculation of fast cooling processes superimpose. (b) Phase fraction evolution showing the presence of a liquid shell down to least 1000ºC (c) Schematic showing the growth of the CNT from a core FCC Fe and Fe-S shell catalyst particle.

Figure 4.23.c shows the evolution of the most plausible stages of CNT growth. The formation of S-rich liquid at the surface limits the C diffusion into the bulk. It acts as a promoter in the catalytic decomposition of the incoming C-containing

molecules from the gas phase, having an important role than in methanation [202]. The formation of transient C-S bonds would stabilise the edge of a nascent CNT and lower interfacial energy between the graphite lattice edge and the Fe-S-C molten catalyst. However, once a graphitic ring or hemisphere is formed around the particle, an interfacial are between the graphite basal plane and the catalyst formed. Molten Fe-S-C is known not to wet graphite, even at small concentrations of S [203].This rejection of graphitic carbon probably plays an important role in the fast extrusion of the CNTs in the direct spinning process of the order of mm/s. Moreover, same evidences were found in metallurgy reports, growing fibrils of graphite in cast irons[202].

In order to control the CNT growth is clearly in a relationship with the catalyst diameter and shape. The amount incoming interacting of carbon the catalyst particle depends on the catalyst surface and its carbon solubility, following the expression: $(D^2 \cdot \pi/2) \cdot s$. Where D is the diameter of the catalyst and s the solubility. At the extrusion side the amount of graphitic carbon produced is related to the particle perimeter $(D \cdot \pi \cdot n)$, being n the number of layers in the CNT[8].

Therefore, the increase in number of layers and tube size can be partially explained by the increase in size. As the amount of available sulphur in the reactor is increased the probability of them coalescing increases as well and so does their size[194]. As it is shown in the figure 4.24 the trend supports the view that inactive particles, showing a similar diameter increase and therefore producing CNTs with larger inner diameters and higher number of layers.

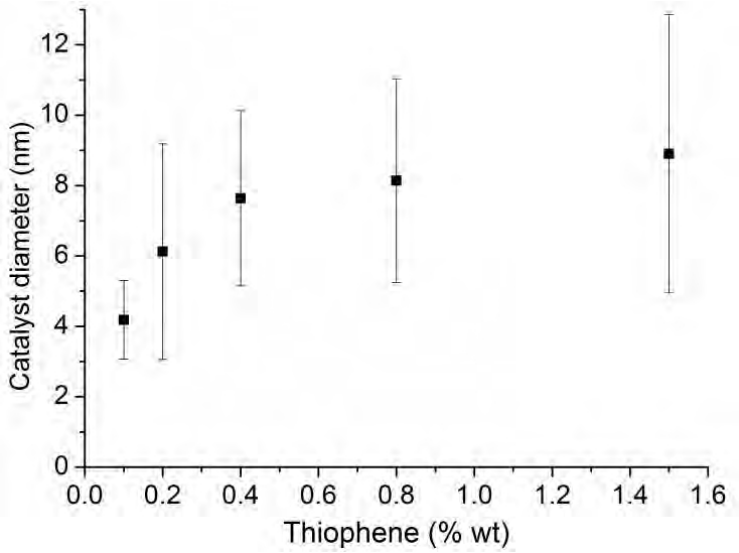

Figure 4.24. Plots of the effect of increasing sulphur precursor on catalyst size.

As implication of the model is that the kinetics of decomposition of the sulphur and carbon precursors in key to control the reaction yield and proportion of active catalyst, but the kinetics of particles collisions are also central for the control of CNT structure.

4.6. Impurities in the CNT fibre

4.6.1. Catalyst and carbonaceous materials

An important achieve is not only control the synthesis of macroscopic fibre producing CNTs with different amount of layers but also made it without increasing the amount of impurities and keeping constant the graphitization .

Thermogravimetric analysis (TGA) was performed in order to determine the mass fraction of iron catalyst trapped into CNT fibre, as well as carbon impurities. It is performed in air atmosphere

There is a range of composition of carbon based impurities, these include large molar weigh structures. Which are desorbed or decomposed at low temperature that 300ºC, up to amorphous temperature carbon which degrade at temperature close to the graphic carbon. Figure 4.25.a shows a CNT covering with non-graphitic carbon, mainly sp3. It is possible to quantify the amount of non-graphitic carbon by TGA. Which is degraded below 450ºC. The other carbon impurity is the graphic carbon, which is grown by an inactive catalyst particle. This carbon is graphitic, mainly sp2 (figure 4.25.b). It is difficult to detect this carbon impurities by TGA because the decomposition temperature is in the same range than the CNTs.

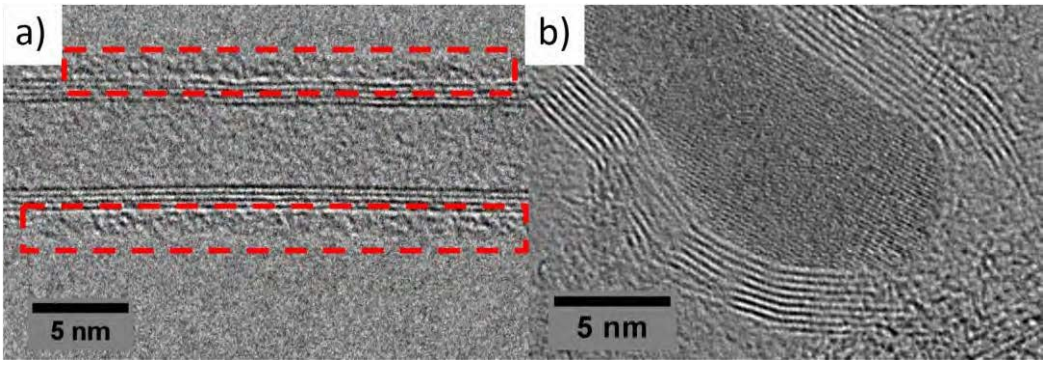

Figure 4.25. TEM micrograph of the two main carbon impurities presence in the CNT fibre (a) non-graphitic carbon, covering the CNT and (b) graphitic layers encapsulating an inactive catalyst particle.

As it is shown in the figures 4.26.a-b, the mass loss between 100-500ºC is assigned to the non-graphitic carbon and volatile hydrocarbons adsorbed on the surface of CNTs [204], because the graphitic sp^2 carbon is degraded over 550ºC. The remaining material after 650ºC corresponds to the residual catalyst including most likely to a small proportion of sulphur that in turn decomposes to leave only Fe_2O_3 at 800ºC (figure 3.3).

The fraction iron catalyst particles is decreasing with and increasing thiophene concentration from 23% to 3.5% (Figure 4.26.a). As it was observed in the figure 4.9.a, the mass proportion in MWCNT compared to SWCNT is around 14 times heavier. This effect shows that iron catalyst-graphitic carbon ratio decreases significantly due to the formation of more graphitic layers.

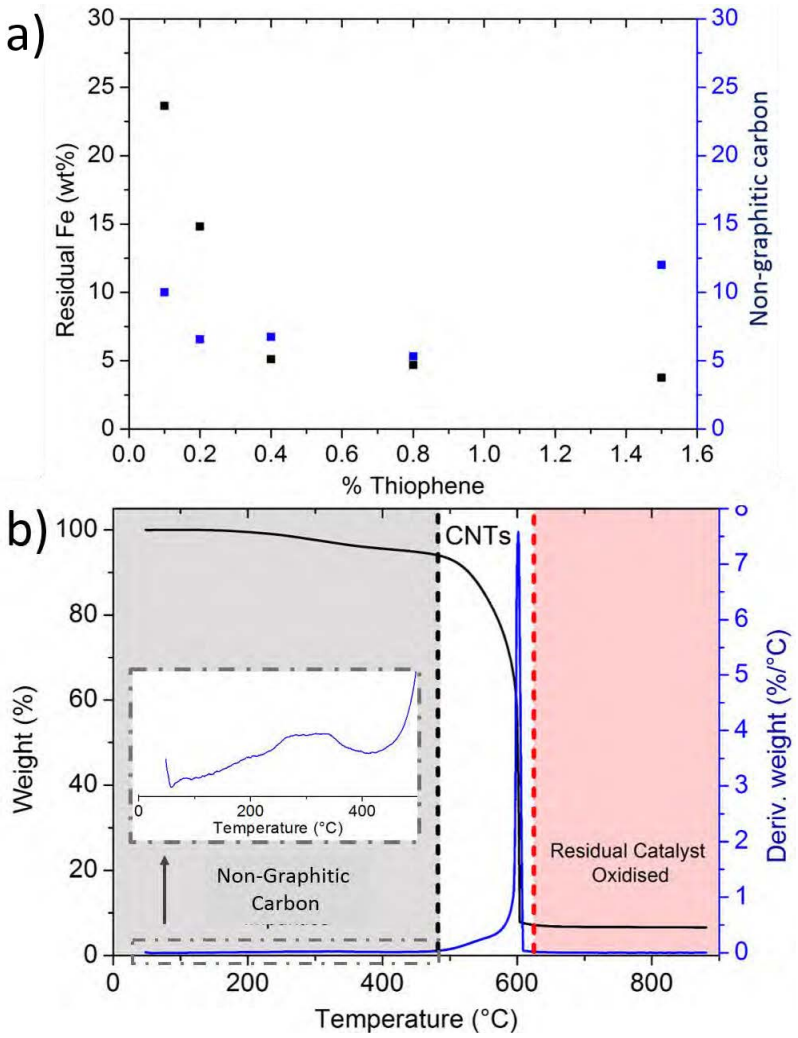

Figure 4.26. (a) Typical TGA plot of mass loss and derivative mass lost against the temperature showing the evidence of non-graphitic carbon and residual catalyst. (b) Amount of residual iron and non-graphitic carbon present in CNT fibres produced with different amounts of thiophene. The data are obtained from TGA.

4.6.2. Silicon-based impurities

SiC and SiO_x are clearly observed by various characterization methods used (eg: EDS, XPS and XRD), particularly when analysing bulk fibre samples collected over several minutes. The recurrent presence of Si in the EDS

Spectra of CNT was figure 4.29 presents an example. In order to analyse these impurities in more detail they were separated from the CNTs by extensive sonication in acetone solvent. The inorganic impurities rapidly precipitate.

Silicon peak is coupled with the presence of oxygen and carbon peaks, when the isolated particles are analysed (figure 4.27.a). Figure 4.27.b presents examples of a SEM micrograph of a silicon particles in the CNT fibre. Which are removed from the fibre with ultrasounds. The particles have a wide range of shapes (circular or cylindrical) and sizes.

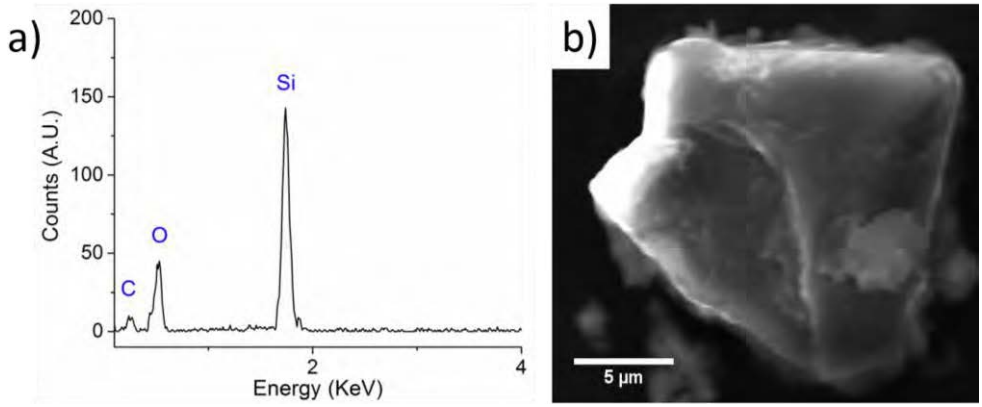

Figure 4.27. (a) EDS spectra showing the presence of silicon particles over the fibre, coupled with the presence of O and C. (b) SEM micrograph showing different silicon particles with different shapes and sizes.

The observation of Si2p XPS spectra (figure 4.28.a) provides further confirmation of silicon compounds. It is evidenced the presence of two peaks at 102eV and 103.5 eV, which correspond to the SiC and SiO_x energy position respectively[205].

XRD confirms the results (figure 4.28.b), a typical diffraction pattern reveals the main peaks related from SiC (111; 200; 220; 222; 400) and SiO (111; 220; 333; 222; 331 and 442).

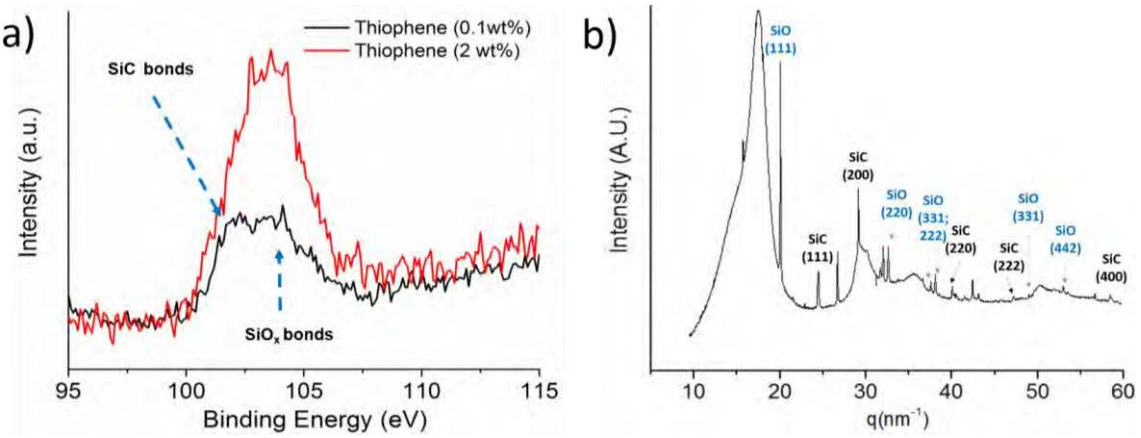

Figure 4.28. (a) XPS spectra showing two peak related with SiO_x compound, (b) Radial integration from a WAXS pattern, showing the peaks related to SiO_x and SiC.

The combination of reducing atmosphere and high temperature (1250ºC) provides the perfect condition to the reaction between silicon oxide and hydrogen. The reactor is made of mullite (62.5% Al_2O_3; 35.2% SiO_2; and impurities). Silicon oxides react with hydrogen forming silicon monoxide or silicon. Figure 2.10.a shows a comparison of mass loss per area against time at 1400ºC for different silicon sources. The kinetic constant is extracted experimentally through the figure 2.10.b. Therefore, it is possible to calculate the amount of silicon in the reaction area, knowing the silicon source, the surface area exposes to the hydrogen and the temperature (figure 2.10.c). The presence of silicon in the reaction was ignored in the traditional growth models, consequently the interaction of the silicon with the other elements needs to be further researched[118]. Secondary effect related to the SiO_2 reduction is the release of oxygen atoms to the reaction area, which can provide the effects discussed in the oxygen section.

$SiO_2(s) + H_2(g) \rightarrow SiO(g) + H_2O$ & $SiO(g) + H_2(g) \rightarrow Si(g) + H_2O(g)$ [118].

Taking into account our reaction conditions. At 1250ºC the available area is 0.17m^2, extrapolated from figure 2.10.b it is extracted the reaction rate; r = $3x10^5$g/h.cm^2 and finally, it is calculated the silicon mass loss from the mullite tube around ≈ 0.05 g/h.

Due to mullite is not a homogenous material, kinetic studies are complicated to carry on. Nevertheless, it is possible to make a predictions, measuring the mass

loss over the time in this conditions. It is noteworthy that Al_2O_3 does not react with H_2[118]. Furthermore the presence of carbon can carry on the following reaction.

$$SiO(g) + 2C(g) \rightarrow SiC(s) + CO(g)$$ [206]

SiO is difficult to synthesise and it is unstable under ambient conditions. However it was found for example at the interface between charcoal and silica when SiO_2 is reduced[45]. SiO can be quenched from the gaseous phase[207].

The role of silicon oxides in chemical reaction is mainly using for supporting heterogeneous catalyst reaction. Furthermore, silicon carbides are also catalyst support. It is possible to produce SiC under the CNT growth conditions from the SiO_2 and the concentrated carbon presents in reduced atmosphere at 1250ºC[208].

Final evidence of the importance of silicon was experimental. Same parameters was utilised to reproduce the typical reaction condition with the exception of changing the tube from mullite (SiO_2-Al2O_3) to alumina (Al_2O_3). Observing the absence of a continuous fibre production, even modifying the parameters as hydrogen rate, precursors feed rate, concentration of reactants or carbon sources.

4.7. Current limitations of the growth model

The synthesis of CNT fibres are performed by direct spinning from the gas-phase (aerogel) during the CNT growth in hydrogen atmosphere at 1250ºC. Gas-phase is controlled not only by the injection feed rate and hydrogen flow but also the precursors. Modifying these parameters is possible to change the type of CNTs, density and shape in the aerogel. However, due to the high temperature, it is difficult to make experiments in the point of the reaction experiment, which are measured in post-synthesis conditions.

4.7.1. Kinetic of decompositions

The different decomposition temperature is critical for the reaction understanding, providing the location information; where iron, sulphur and carbon become available for producing CNTs. Temperature profile is important because it is going to determine, where the precursors are decomposed.

However, there is a significant challenge to analyse, as determine the decomposition route for the reactants in presence of metal catalyst, which can determine important synthesis information. CVD Reactor has a gradient of temperature, thus in this specific location the reactants are injected and they are decomposed at different positions. Temperature profile is determined under the main synthesis condition. Figure 4.29 shows the temperature profile inside of the furnace. Slope is sharp until 1100ºC and smoother until 1250ºC.

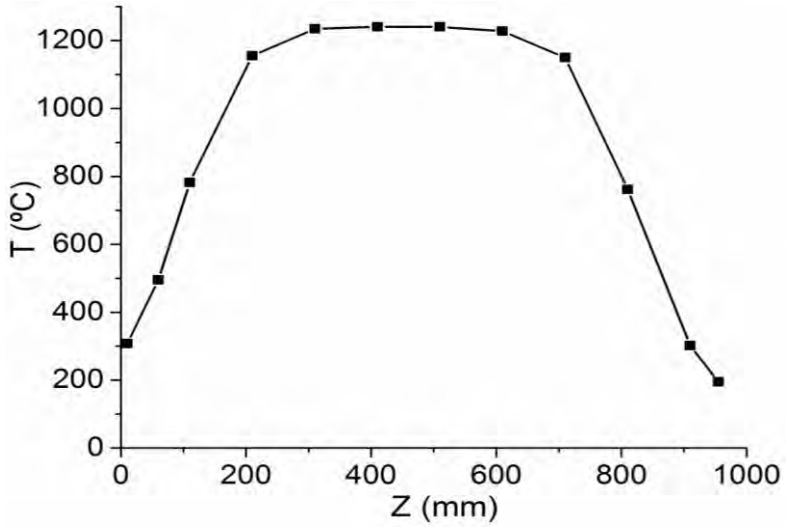

Figure 4.29. Temperature profile in the reactor 0mm represents the top; 1000 mm corresponds to the exit.

Ferrocene decomposition route starts at ≈ 400ºC[209] according to the following reaction:

$$Fe\ (\ C_5H_5)_2 \rightarrow Fe + 2(\ C_5H_5)\ \ [210]$$

Iron atoms after 400ºC are available to interact between them producing nanoparticles. Thiophene starts the decomposition ≈ 850ºC (in absence of Fe), assuming the sulphur becomes available. Firstly the reaction is given more than 15 products in different amounts and is practically complete at 1050ºC[211].

Due to the large numbers of carbon-containing molecules. It is possible to use carbon source as a variable, in terms of decomposition temperature in order to understand how the influence of the availability position into the CNT growth is.

Aliphatic alcohols start to decompose at 400-500ºC and finish around 800ºC[93][94], carbon availability is between iron and sulphur availability. However, aromatic compounds break the aromatic ring over 950ºC[95][212], which means that ferrocene and thiophene are already decomposed. Figures

4.30.a-b show the availability of iron, sulphur and carbon using as a carbon source butanol and toluene respectively.

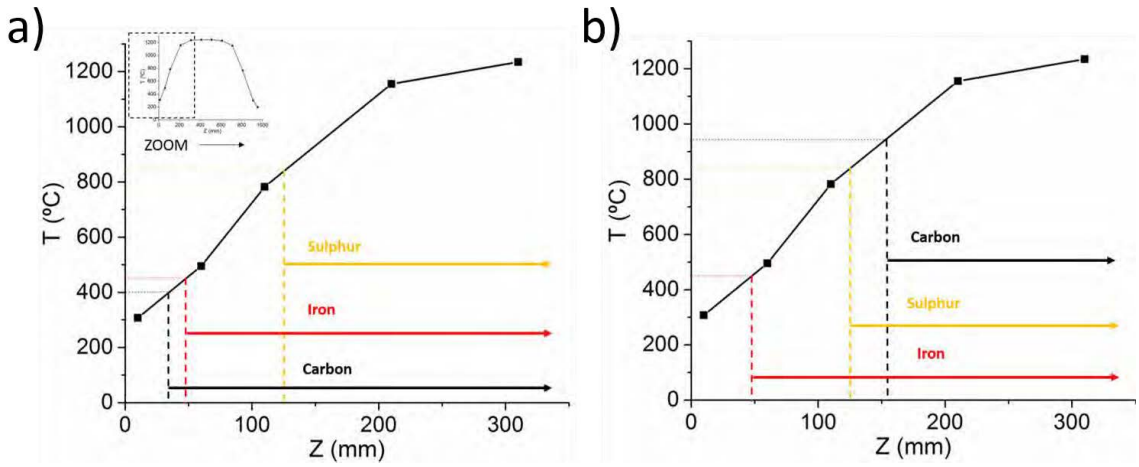

Figure 4.30. Overlay of the availability of iron, sulphur along with (a) aliphatic alcohol or (b) aromatic compound over the reactor length.

Using aliphatic carbon (e.g. butanol), the distance from carbon ≈ iron to sulphur availability is approximately 10 cm, taking into account normal hydrogen flow (e.g. 1.3 l/min), the difference in time is ≈ 10 seconds. On the other hand, synthesising with an aromatic compound, iron is available 7 and 10 cm before than sulphur and carbon respectively. Ideally, as it is discussed in section 4.4, the sequence for growing long CNTs is iron-sulphur-carbon. An importance result, which can support this theory is the fact that it is possible to spin at 0.02 wt.% of thiophene concentration with toluene as a carbon source. However, the lower limit of thiophene concentration to produce a CNT fibre with butanol is 0.1 wt.%. This result is likely to increase number of CNTs, therefore, the number of active catalyst particles. Moreover, temperature is the other critical factor. Thus injected aromatic compounds allows to spare catalyst over 950ºC, when the kinetic promotes the synthesis of longer CNTs[213].

This discussion enable to explain why the reaction yield increases from 5-9% with butanol to 20% with toluene, in term of carbon injected/carbon in CNTs, even though the CNT tube is not identical synthesised with different carbon source in terms of diameter.

Different temperature in the reaction does not evidence any change in the type of the tube (figure 4.31.a). It was measured the lineal density and reaction yield decreasing the temperature of the furnace from 1250ºC until 1100ºC (figure

4.31.b), in order to confirm the discussion about the carbon source importance. Decreasing temperature leads to less lineal density from 0.58 to 0.18 at 1250ºC and 1100ºC respectively and in terms of injected carbon/output carbon goes from 7% to 2%. Raman spectra 2D peak position (figure 4.31.c) confirms that the changes in the tube (in terms of number of layers) are negligible because it is dominated by the ratio S/C. Consequently, it is affecting to the reaction kinetic, in other words the length of the CNTs.

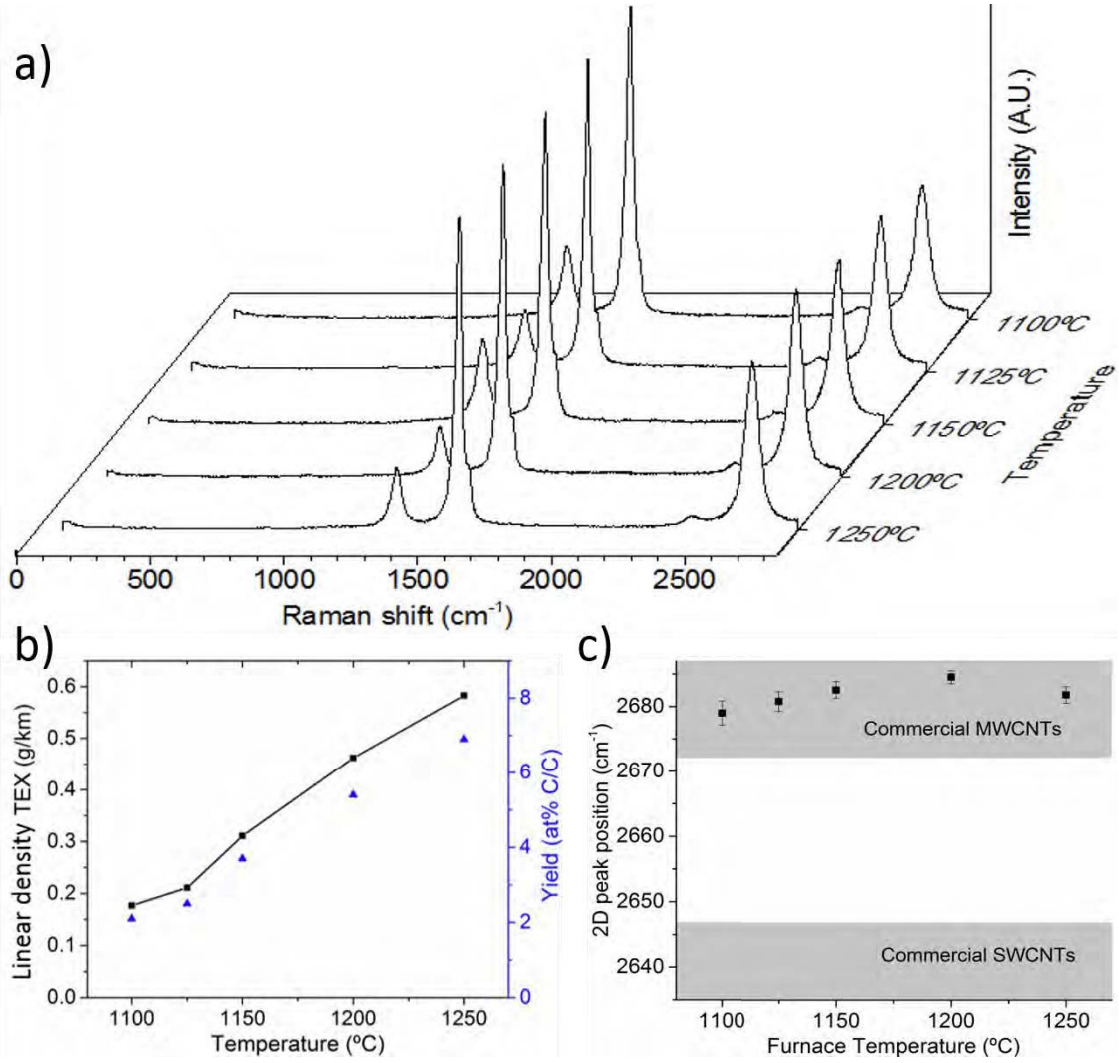

Figure 4.31. (a) Normalised raman spectroscopy data at different reaction temperature from 1100 to 1250ºC (b) Plot of the effect of increasing temperature on fibre linear density and reaction yield. (c) Plot of Raman 2D (G´) peak position for samples produced at different furnace temperature.

4.7.2. Suggested experiments

High temperature and hydrogen atmosphere are two limiting factors responsible for complex characterization and study of the reaction in-situ. Reaction are influenced by interconnected parameters as concentration and decomposition of

reactants, temperature profile, reaction atmosphere and role of the secondary elements. The following section describes new experiments or reactor design, to obtain new results and evidences in the context of CNT reaction.

To understand better the decomposition route of the reactant under synthesis parameters, it is possible to extract a ceramic pipe directly from the upper part of the reactor, where the reaction is ongoing. The stream components will be measured by gas chromatography (GC) almost in-situ. Nevertheless, the gas could be react along the ceramic pipe. This equipment would provide more information to identify the compounds, which are presented in the reactor along the reactor. Allowing to determine the decomposition route from the different precursors. Some apparatus are already designed[214], providing some information from the reaction. However, the gas recombination from the furnace to the analyser, it is a difficult challenge that it is not already solved.

The decomposition sequence is critical in order to obtain active catalyst. Ternary diagram recommended introducing the precursors, which leads to Fe-S-C sequence. All the precursors are introduced by the injection system in the upper part simultaneously. Designing a new configuration, carbon source would be injected, thought an independent inlet stream, after the interaction between iron and sulphur, avoiding carbon saturation into the catalyst before sulphur reach to the surface.

Figure 4.32 shows the schematic representation of the injection system. Fe and S are introduced though a sublimation system, independently from carbon. Which is injected by a ceramic pipe in the reaction area, after Fe-S interaction. Outlet stream is connected with a CG equipment for analysing the gases produced during the decomposition stage.

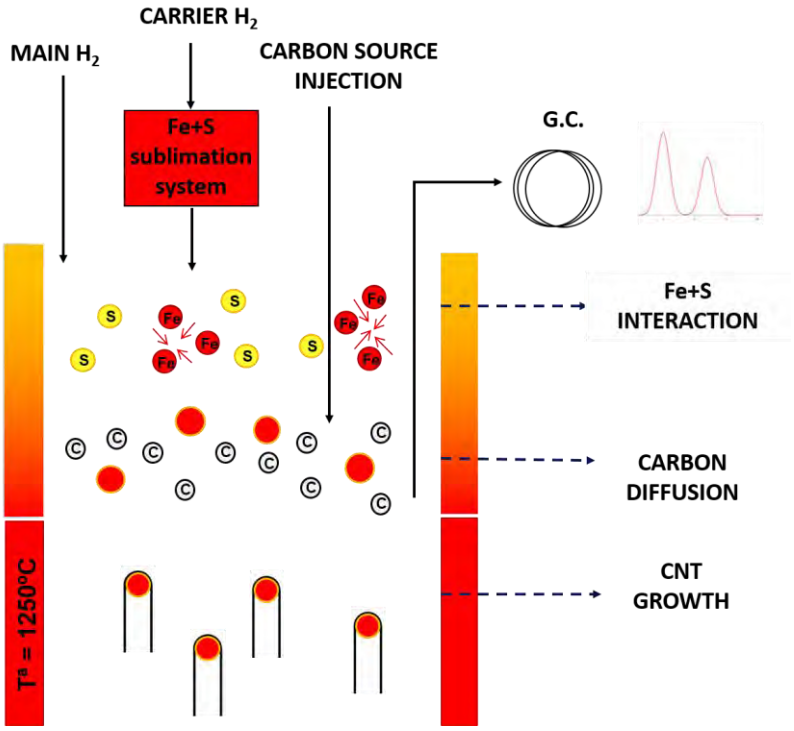

Figure 4.32. Schematic representation of the injection system, introducing the configuration suggested.

Using a range of aromatic compounds could improve the understanding of reaction. The main similarity is the aromatic ring, which is very stable. Benzene could be the base reactant and compare with toluene or benzyl-alcohol which differ in the radical bounded with the aromatic ring. Toluene has a methyl group (- CH_3) and benzyl alcohol will add a hydroxyl group (-OH) compare to toluene (figure 4.33). Allowing to evaluate the importance of radicals attached to phenyl as the role of oxygen.

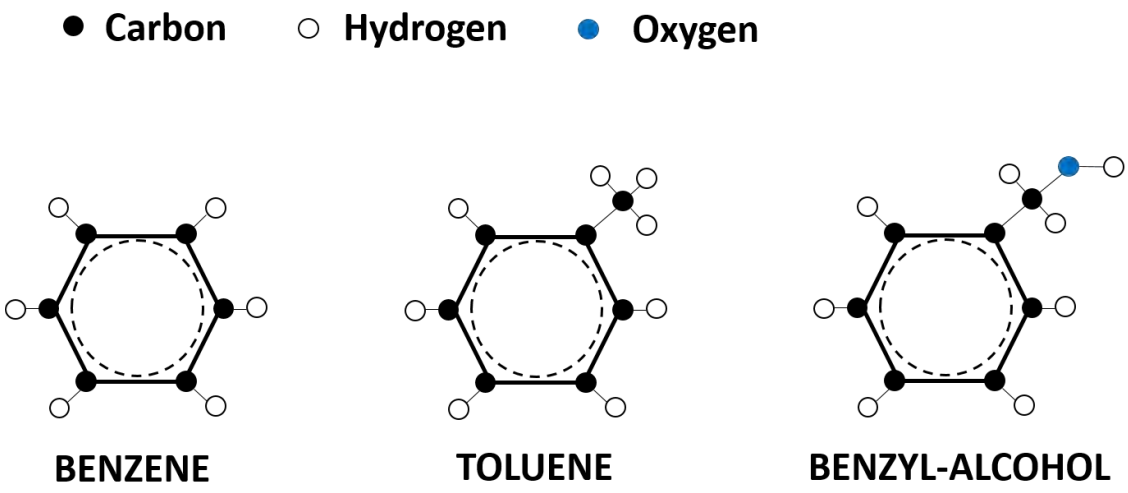

Figure 4.33. Benzene, toluene and benzyl- alcohol formulae.

4.8. Summary

In this chapter, it is studied the reaction from the gas-phase. Representing the direct CNT fibre process showing the aerogel formation and the shape of the fibre.

It is possible to synthesised continuous CNT fibres on a kilometre scale with control of the CNTs in terms on number of layers from SWCNT to MWCNT by adjusting the concentration of S precursor in the reaction. At low S concentration CNTs are predominantly SW of approximately 1 nm diameter. Increasing S makes catalyst particles larger and increases inner diameter and number of layers of CNTs, producing at medium sulphur DWCNT and collapsed CNTs and at higher S, MWCNTs. This transition from SW to MW is clearly seen in Raman, particularly as an upshift in the 2D band due to the increase in number of adjacent layers, similar to observation in graphene. Sulphur effect is independent of the choice of C precursor (Butanol, Toluene or Benzyl alcohol) used for the CVD growth of CNTs.

Analysing SWCNTs fibre is found the inherent predominance of metallic and high chiral angle CNTs. It is observed in the G band, with a Breit-Wigner-Fano line shape with an asymmetric factor q with values between -0.14 and -0.4, which correspond with Metallic-SWCNTs values. Thought XRD, 390 CNTs were measured, shows that the 80% of the CNTs present chiral angles between 20º and 30º.

Through a combination of TGA, XPS, OEA and HRTEM, it is estimated the compositions of catalyst particles and found that inactive particles, which represent over 99.9% of those produced in the reactor and aggregated in the fibre, are encapsulated due to their high C content.

Encapsulation occurs because at high C contents the catalyst is in equilibrium with solid C, i.e. graphite. In contrast, active particles have an earlier arrival of sulphur that limits carbon solubility. Upon C arrival and saturation the catalyst particle is not in thermodynamic equilibrium with solid C, thus, instead of forming an encapsulating layer C gets extruded as a CNT and the particle remains active.

Liquid catalyst particles are synthesised the CNTs and post-spinning catalyst particles are analysed. Catalyst structure suggests a Fe FCC core surrounded by a liquid Fe-S shell, according to thermodynamic calculations. The presence of sulphur in the catalyst is critical. Controlling the carbon diffusion in the catalyst, stabilized the edge of the nascent CNT and rejected the carbon from the catalyst forming the graphitic layers.

At higher S concentrations the amount of active catalyst in the gas-phase increases, enlarging particles through collisions and coalescence. As a result, the inner and outer diameter and number of layers of the CNTs increase too. The increase in CNT number of layers an inner diameter is responsible for a higher fibre linear density and reaction yields.

In this process, it is possible to control the availability of the elements throw the decomposition temperature of the precursors. Butanol started the decomposition route at 400ºC before Fe (450ºC) and S (850ºC) elements, but phenyl group present in toluene, it starts to decompose over 950ºC. Growth temperature controls the range of CNT lengths in the fibre, directly related with the properties. Several experiment are suggested in order to obtain more information about kinetic and secondary reactants.

Finally, the combination of reducing atmosphere and high temperature (1250ºC) provide the perfect condition to the reaction between silicon oxide and hydrogen, forming SiO, SiC or silicon. Silicon effect is critical for the reaction, without Si was not possible to obtain a continuous fibre.

5 Fibre orientation: Strong CNT fibres by drawing inspiration from polymer fibre spinning

5.1. Introduction

In this chapter, it is presented a method to spin highly oriented continuous fibre of adjustable CNT type, with mechanical properties in the high-performance range. By lowering the concentration of nanotubes in the gas phase, through either reduction of the precursor feed rate or increase in carrier gas flow rate, the density of entanglements is reduced and the CNT aerogel can thus be drown up to 17 draw ratio (times more than the carrier gas speed) and wound at fast rates over 50m/min.

Increasing CNT bundle orientation is achieved without affecting the synthesis process, as demonstrated by Raman spectroscopy and confirmed by TEM micrographs. This fact implies that the parameters controlling composition in terms CNT diameter and number of layers, are decoupled from those fixing CNT orientation.

Applying these principles then, high-performance fibre is produced under dilute conditions and high draw ratios with mechanical properties in the range of 60 GPa/SG and 1.1GPa/SG in tensile modulus and strength, respectively. Degree of orientation is demonstrated by wide and small angle X-ray scattering. As it was discussed in the chapter 4, controlling S/C ratio is possible to tune the CNT from single to multiple layers. Properties of CNT fibres consisting in SW and MWCNT was measured, which surprisingly have very similar tensile properties. These results demonstrated a route to control CNT assembly and reinforce their potential as a new high-performance fibre.

5.2. Assembly stage in the direct spinning method.

In the reaction area, the CNTs are assembled into a fibre through creating links, crystal between tubes and entanglements between bundles. This fibre is then drawn through and out of the reactor tube and continuously spun onto a winder.

Two effects occurs during the action of drawing the aerogel. Firstly, fibre densifies from aerogel, obtaining a denser fibre and orients the CNTs and its bundles to each other and preferentially parallel to the fibre axis. The aerogel is drawn several times faster (draw ratio ≈ 17 ≈ 55 m/min) than the carrier gas velocity, typically ≈ 3 m/min. Consequently, when pulling the aerogel out of the reaction it is dragged against the gas molecules. This leads to frictional forces that orient the CNTs parallel to the drawn direction, i.e. to the fibre axis.

The challenge is in defining a draw ratio since the process require a minimum drawn to extract the material. In this work, it is assume that DR is 1 correspond to the gas velocity along the reactor. Since drawing is expected to orient the CNTs, it is them interest to the maximum draw ratio for different synthesis conditions.

The maximum draw ratio (D_R) is a good parameter of how much an aerogel can be drawn during the spinning process and thus a good figure of merit of orientability when exploring the spinning parameter space. Figure 5.1 shows a 3D plot of D_R, against precursors feed rate and the H_2 gas flow. Varying the amount of thiophene, it does not affect tendency and converges to higher winding rates by decreasing the feed rate and/or high H_2 flow rate. It is worth mentioning that the window of orientable fibres shown belongs to the parameter under which is possible to spin kilometres of continuous CNT fibre can be spun. However the intrinsic windows just taking into account the aerogel properties are probably bigger once the specific details of the spinning reactor design are factored out. There was injection limitation with the equipment below 1.5ml/h, whereas increasing the hydrogen flow rate created difficulties for extracting the wide aerogel continuously CNT fibre from the reactor.

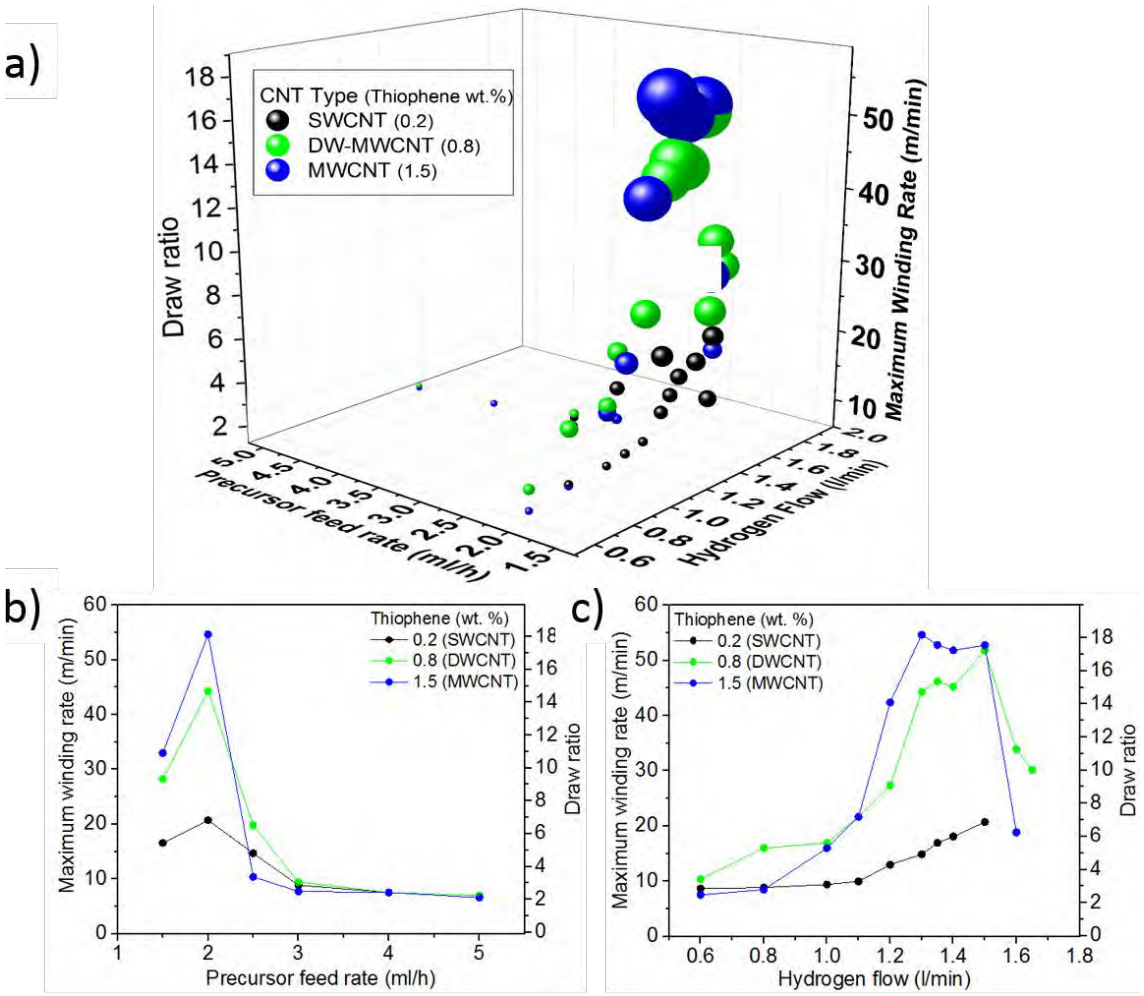

Figure 5.1. (a) Dependence of the maximum winding rate with precursor feed rate an hydrogen flow, showing that faster rates are obtained in dilute conditions when the concentration of CNTs in the gas phase is lower and therefore the possibility to draw the aerogel and orient the CNTs is higher. (a) Surface plot of parameters space for different aerogel compositions. Constant hydrogen flow (b) and constant feed rate (c) section of parameter space showing the equivalent role of these two parameters in diluting the aerogel.

Figure 5.1.b and 5.1.c represent a section of the 3D plot at constant hydrogen flow and constant feed rate, respectively. Keeping one of the factor constant, it is possible to evaluate better the degree of influence over the aerogel. Both parameters play equivalent role in providing dilute conditions in the reactor and leading to higher values of $W_{Max.}$ Consequently, whether the CNT aerogel is more diluted, the concentration of CNTs in the aerogel is also low, leading to lower density of entanglements. Allowing to spin faster the macroscopic fibre. In the figure 5.1.a, it was included a new axis *Draw ratio*, for the corresponding winding rate maxima.

One of the most promising and important aspect of controlling the CNT orientation and assembly in aerogel is modified the reactor condition, without affect the reaction leading to control at the same time both aspect orientation with the type of CNT in terms of number of the layers and chirality.

Raman spectroscopy spectra confirm that modifying the feed rate and hydrogen flow rates in the reaction ranges does not affect significantly to the type of the CNTs. Figure 5.2 shows the 2D peak position, evidencing the similar values, therefore, the same type of tube in terms of number of layers.

The values were constant when the precursor feed rate (figure 5.2.a) and the hydrogen flow rate (figure 5.2.b) in this range. This again confirms in passing that increasing the precursor feed rate does not affect to the diameter or number of layers though coarsening of catalyst particles. TEM micrographs for the different conditions confirmed no mayor compositional differences.

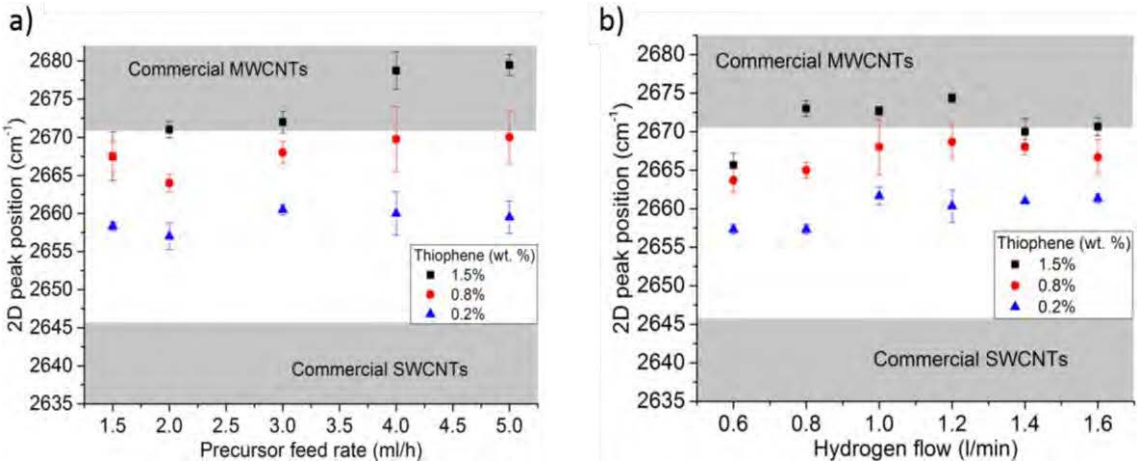

Figure 5.2. (a) 2D Raman band position dependence with (a) precursor feed rate and (b) hydrogen flow for three types of CNT fibres showing that the CNT fibre composition is not significantly altered when controlling the assembly through the dilution.

These results also confirm that within the parameters of this work, the type of CNT in terms of diameter and number of the layer is controlled by the precursor mixture, particularly the ratio of S/C [215]. Furthermore, precursor feed rate and hydrogen gas flow, while enabling the catalytic reaction, also have secondary role fixing the aerogel concentration and thus the possibility of CNT assembly into a macroscopic fibre.

Though SEM micrographs (figure 5.3.a-b). It is possible to observe the different density of CNT in the aerogel modifying the precursor feed rate from 5ml to 2ml. Which also affect the number of entanglements per CNT.

Figure 5.3. As-spun macroscopic fibre at two different precursor feed rates (a) 5ml/h and (b) 2ml/h at zero draw ratio.

There is a transition from non-stretchable to stretchable. A direct indication of aerogel area is obtained by visual inspection of the reaction. The shape of the aerogel is an inverted hollow cone, converging in the centre to form the fibre. Figure 5.4.a shows photographs of the aerogel at constant hydrogen flow. The precursor feed is decreased from 5ml/h until 2ml/h going from a concentrated aerogel, which can be spun at $D_R = 2.5$, to more diluted aerogel that it is possible to spin until $D_R = 17.5$ and produce oriented fibre.

An aerogel diameter is calculated by image analysis of the intensity profile across the diameter of the ceramic tube. This requires using inner tube diameter as a reference. The photographs used in this study were taken from a video during stable reaction conditions. Figure 5.4.b shows the aerogel diameter by about 20% increasing, when the precursor feed rate is decreased from 5ml/h until 2ml/h. These results are in agreement with the results obtained increasing the hydrogen flow rate in a similar macroscopic fibre reactor[84].

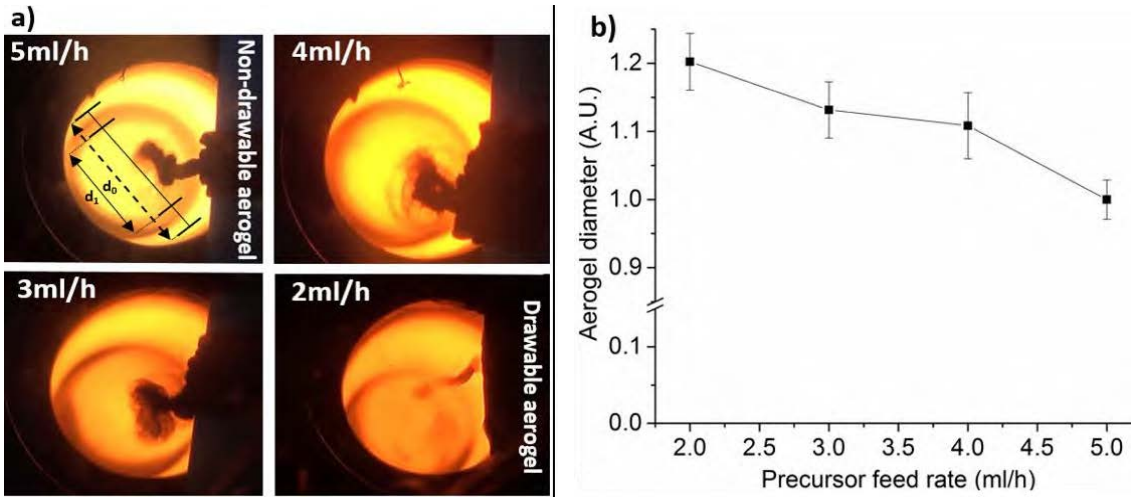

Figure 5.4. (a) Optical images showing the aerogel expanding as feed rates is decreasing while diluting. (b) Comparison of aerogel diameter from image analysis showing 20% increment.

Furthermore, it is worth mentioning that the reaction yield is in similar ranges in terms of carbon conversion:

The conversion rate is calculated as $\%_{conv} = {}^{m_{carbon\ in\ fiber}}/_{m_{carbon\ injected}}$

The conversion is not significantly affected and remained at around 8.5%. Variations between samples were below 10%.

It was spinning stable CNT fibre during a certain time period. The sample was weight and compared with the amount of carbon introduced in the injection. Table 5.1 below lists the fibre mass obtained by thermogravimetric analysis technique and the mass of precursors injected. Comparing the results obtained synthesising stretchable and non-stretchable fibre.

Table 5.1 Carbon and catalyst input in precursors and in the CNT fibre.

	Carbon injected		**Fibre mass**	
	5ml/h	**2ml/h**	**5ml/h**	**2ml/h**
Carbon (g)	2.64	1.06	0.244	0.087
Catalyst (Fe+S) (g)	0.033	0.0013	0.01	0.004
% carbon conversion			**9.2%**	**8.2%**

5.3. Entanglements in aerogel fibre spinning.

Figure 5.5 shows the scheme of the process, representing the two different conditions. Concentrated aerogel can only be spun from the reactor but due to the entanglements, it is not possible to spin over D_R 2.5, precluding the orientation. On the other side, one enable the orientation due to reduction of entanglements, increasing the spinning speed up to D_R 17.5.

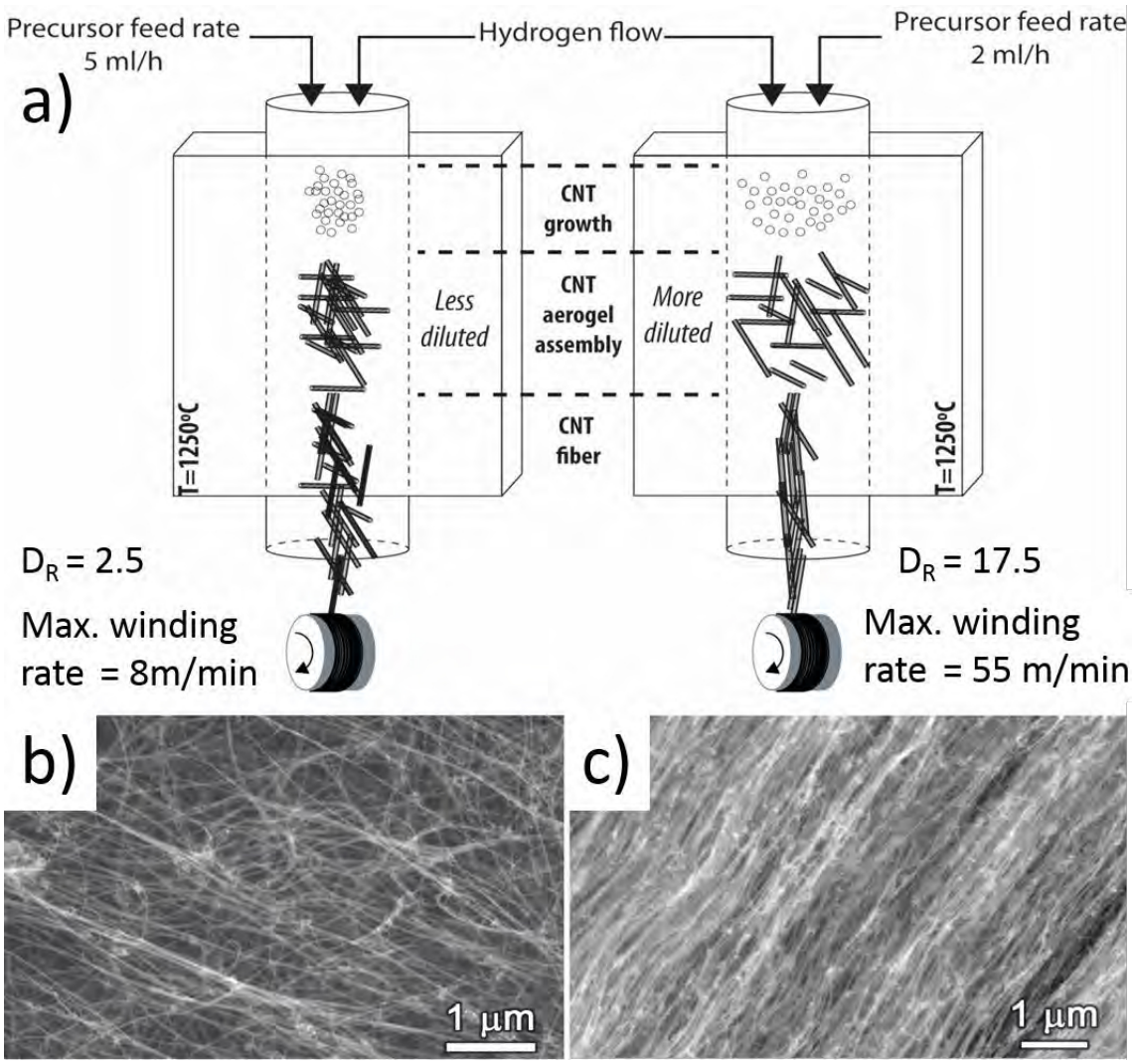

Figure 5.5. (a) Schematic representation of the direct CNT fibre spinning process showing the effect of aerogel dilution on the orientability of the final fibres. SEM micrographs of (b) non-oriented and (c) oriented fibres.

Due to the dilution of the aerogel, the entanglements per CNT were reduced. The possibility to draw faster a more dilute CNT aerogel occurs because of the reduction in the number of CNT entanglements. This is supported by the fact that although the SWCNT material (0.2wt% thiophene) has a mass linear density that is about 5 times lower than the MWCNTs, i.e. that the SWCNT aerogel is roughly 5 times less dense than the MWCNT aerogel, both show very similar trends in figure.5.1.

The implication is that maximum drawing rate does not scale with the density of the material in the gas phase, but with the numbers of particles in the gas phase. Thus, the dilution through adjustment of feed rate or hydrogen flow rate represents a reduction in the number of CNT contacts points in the gas phase.

The window for drawing, then represents conditions under which the aerogel has sufficient CNT association to withstand the frictional stresses associated with dragging it against the gas, but few enough to enable CNT rearrangement during the process.

The mechanism proposed is inspired to polymer fibre spinning, especially close to the case of polyethylene (PE). Previous studies with PE fibre spinning from the melt or cold/hot drawing produced fibres with mechanical properties around 1GPa -70GPa for tensile strength and modulus respectively. These values are sharply lower than the expectation created by the individual PE crystal measurements. Pennings ground breaking work synthesized a ultra-high molecular weight PE fibre spectra and Dyneema by dilute the solutions[216], increasing substantively the mechanical properties[217]. It was possible to reduce the number of entanglements in the gel fibre, decreasing the concentration of polymer in paraffin oil. Less entanglements lead to higher drawing ratio to produce more degree of orientation and crystallinity. Improving the mechanical properties until 6GPa - 160GPa for tensile strength and modulus respectively[218].

Although, there are different length between the polymer chains and the CNTs (around 10 Å[219] compared to 0.1-1mm), the comparison of gel and aerogel spinning follows the same principle of reducing association of building blocks by decreasing the concentration in the reaction, allowing to the CNTs in the fibre be rearrangement and assembly into a more oriented structure upon drawing.

5.4. Orientation and properties

The expected in the degree of orientation upon faster drawing of the CNT fibre is confirmed by SAXS/WAXS, as shown in the SAXS patterns in figure 5.6.a from fibres produced under dilute conditions and spun at D_R = 0.47 and D_R = 12.6, respectively. SAXS reflection in the equator reflect the alignment of CNT bundles parallel to the fibre axis, with the FWHM from azimuthal integration decreasing from 53 to 25 (figure 5.6.b), confirming the bundle orientation. This is a first approximation related to the XRD interpretation. Along the chapter 6, a detail study of the fibre structure is presented.

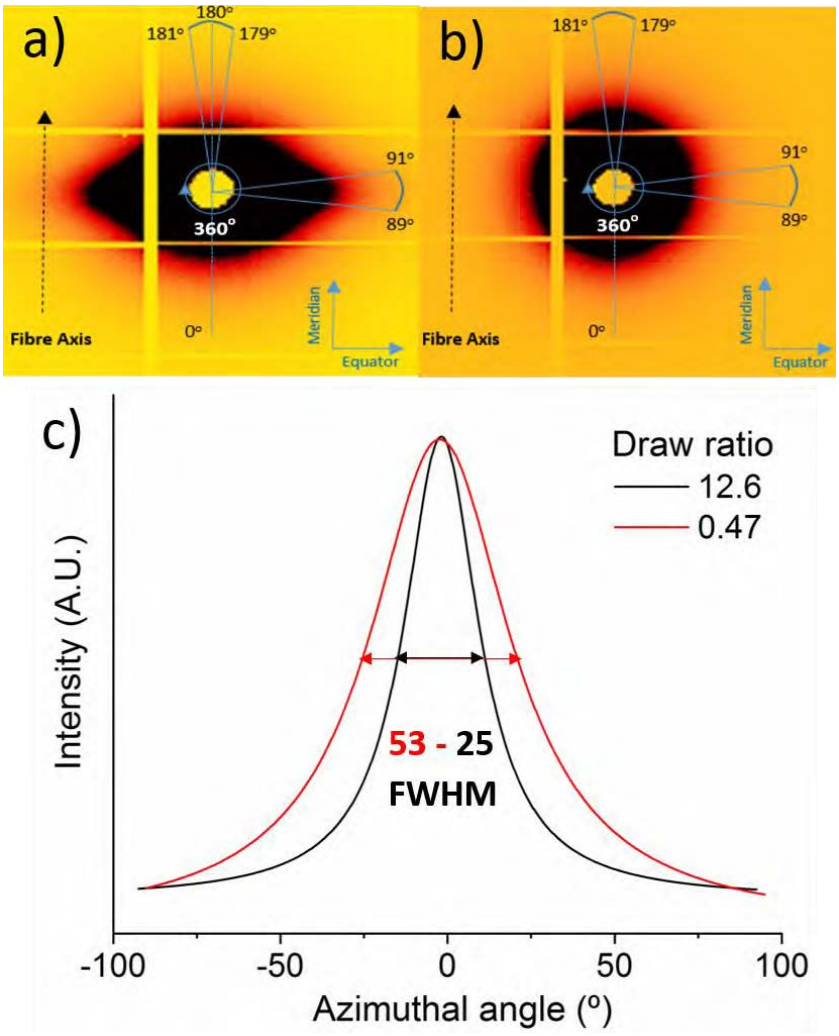

Figure 5.6. Typical SAXS pattern of an (a) oriented and (b) non-oriented fibre. (c) Comparison between azimuthal integration.

It is worth emphasising that the measurements were done in macroscopic fibre consist of arrays of > 10-100 and 500 CNT filaments. Figure 5.7 shows the effect of decreasing the number of filaments in the samples 10/100/5000 filaments, spinning in the same conditions. It is evidenced the importance of the number of filaments. In non-oriented fibre (0.47 draw ratio), FWHM decreases from 77º to 43º and in the oriented fibre (12.6 draw ratio), FWHM goes from 36º to 23º. The conclusion is that the perfect scenario to interpret the results is measuring a single filament in order to reject the artefacts related to the filament misalign.

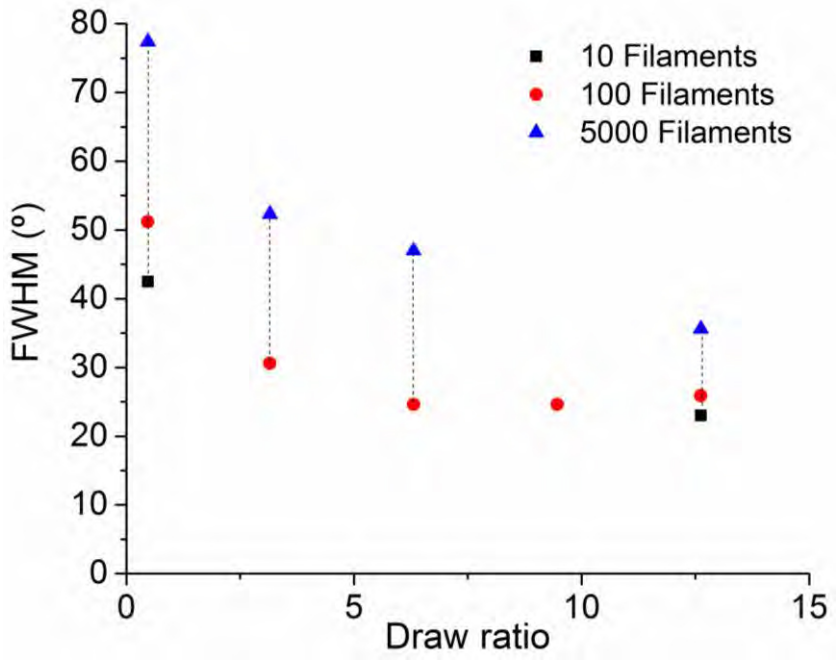

Figure 5.7. FWHM of the azimuthal profile measure from sample with different number of filaments 10-100 and 5000, spinning at different draw ratio.

Due to the size of the sample the orientation distribution might be significantly broadened by fibre misalignment and thus give an overestimates of the FWHM compared with an individual filament. Further confirmation about the orientation is presented in the chapter 6.

A brief summary from conclusions extracted along the chapter 6, which is useful in order to interpret mechanical properties, are the following:

- Volumetric density increases with draw ratio. However, densification process affects dramatically to volumetric density but it is negligible in terms of mechanical properties.
- Increasing draw ratio leads to more oriented bundle and CNTs and the pores are more elongated.

Figure 5.8 shows two typical stress/strain curves from high and low oriented CNT fibre. Indicating the highlights that can be extracted from the curves (Young's modulus, specific tensile strength, toughness and strain) for better understanding of the results.

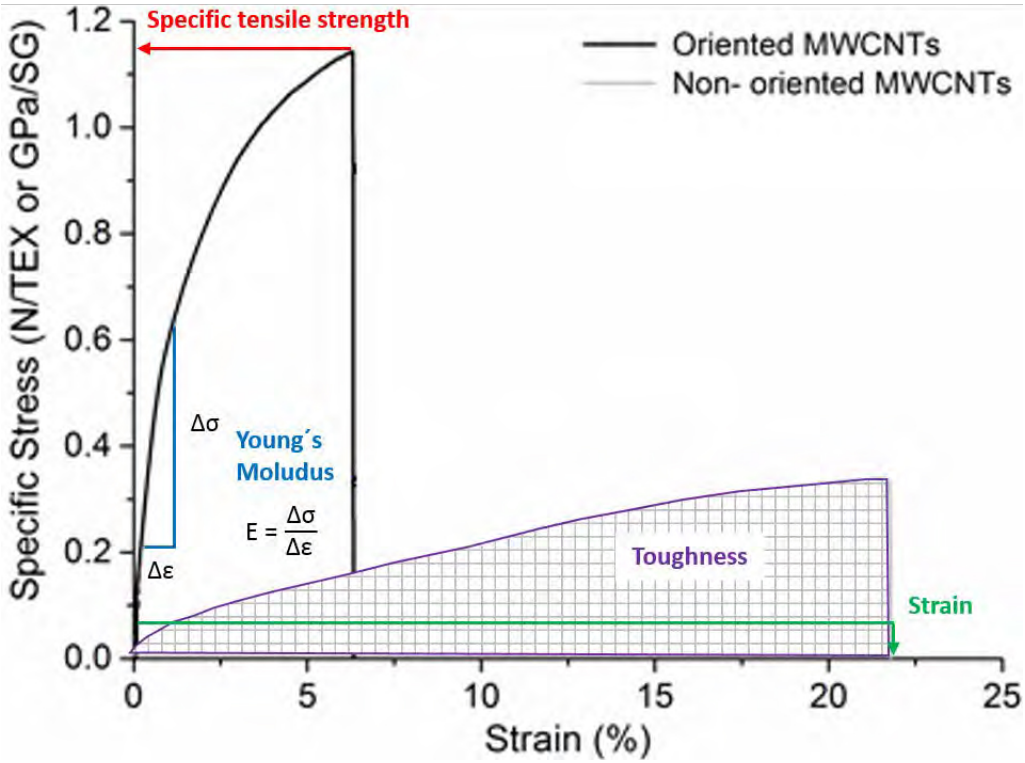

Figure 5.8. Strain-stress curves for highly and poorly oriented CNT fibres.

Figure 5.9.a shows the young´s modulus and toughness against draw ratio. Figure 5.9.b are shown the maximum specific stress and strain of densified single filaments spun at different draw ratios from 0.47 to 15.8.

Increasing the draw ratio indicates that young´s modulus and maximum specific stress increase significantly. Young´s modulus goes from 3 to over 60 GPa/SG and maximum specific stress from 0.2 until 1.1 N/TEX. These effects are clearly related to the bundle orientation along the fibre. The increase of the alignment of the bundle leads to more load paths participating, effectively along the direction of the load applied.

Strain reduction from 20% until 8% is an expected consequence of increasing the orientation. It is worth mentioning that the maximum draw ratio for this specific aerogel is 17.3 and the best properties are achieved at the 75% of the maximum draw ratio (12.6). Increasing draw ratio over a limit leads to decrease the density of links between CNTs in the bundles, worsening their properties.

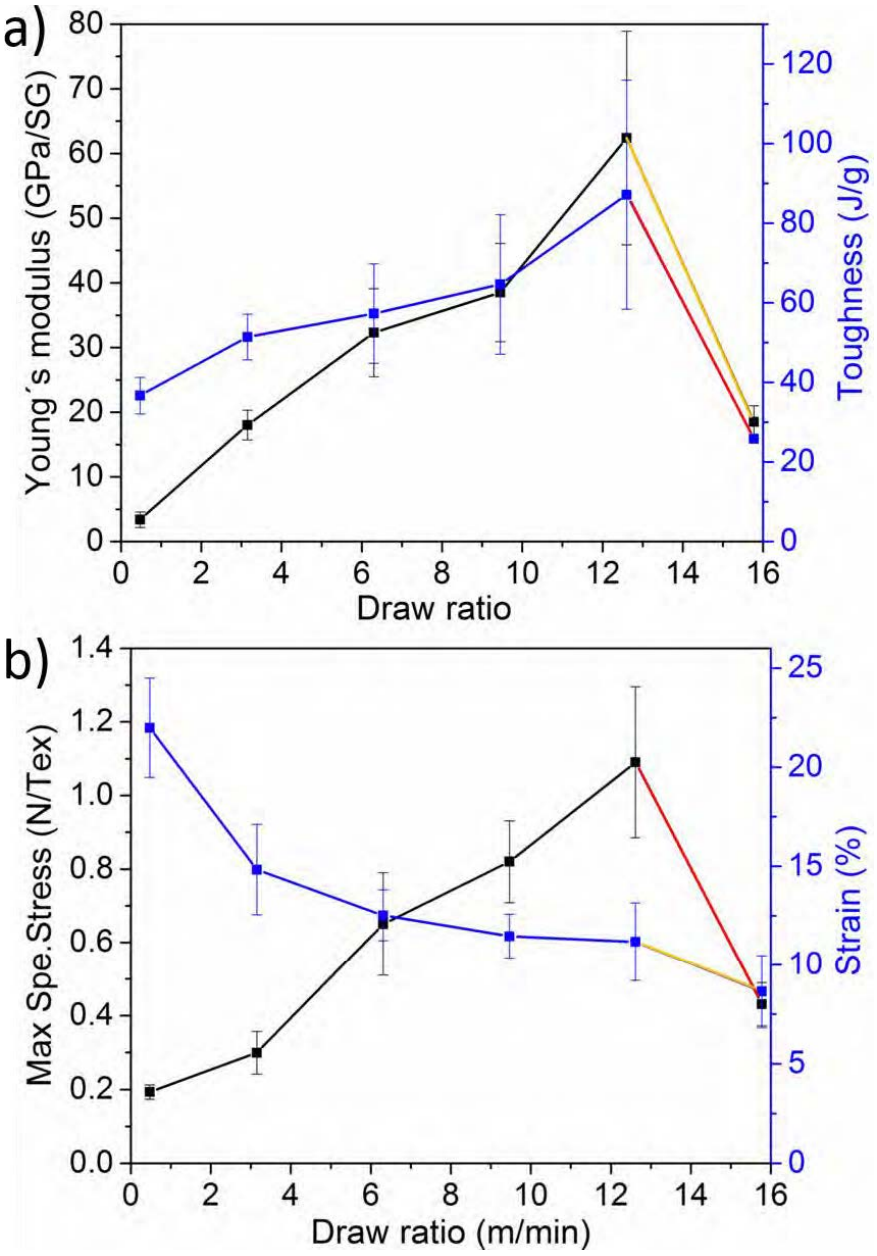

Figure 5.9. Mechanical properties of single filaments (a) Young´s modulus, toughness, (b) specific stress, and strain against draw ratio, samples length is 20mm.

While a modulus increase is expected as a consequence of improved CNT orientation, the increment in toughness, reaching values 3 times that Kevlar is surprising. Work is in progress to evaluate the different mechanism, taking part in the deformation of the CNT fibres. Such studied are possible due to the contribution of this work in reproducibility, making uniform samples of fixed composition and controlled microstructure. Several of these samples were tested by J.C Fernández.

To summarise, toughness is dominated by the bundle packing and CNTs orientation and the number of links are created during the reaction stage. Even after densification, it is not possible to affect this value decreasing the volume in two orders of magnitude. Thus, the reaction stage modifications or increasing the alignment are the options for changing dramatically the mechanical properties of the material.

Furthermore, mechanical properties are evaluated depending on the type of CNT in terms of number of the layers, showing that the dependence is secondary. Figure 5.10 present a typical strain-stress curves from oriented and non-oriented fibre made of SWCNT and MWCNT.

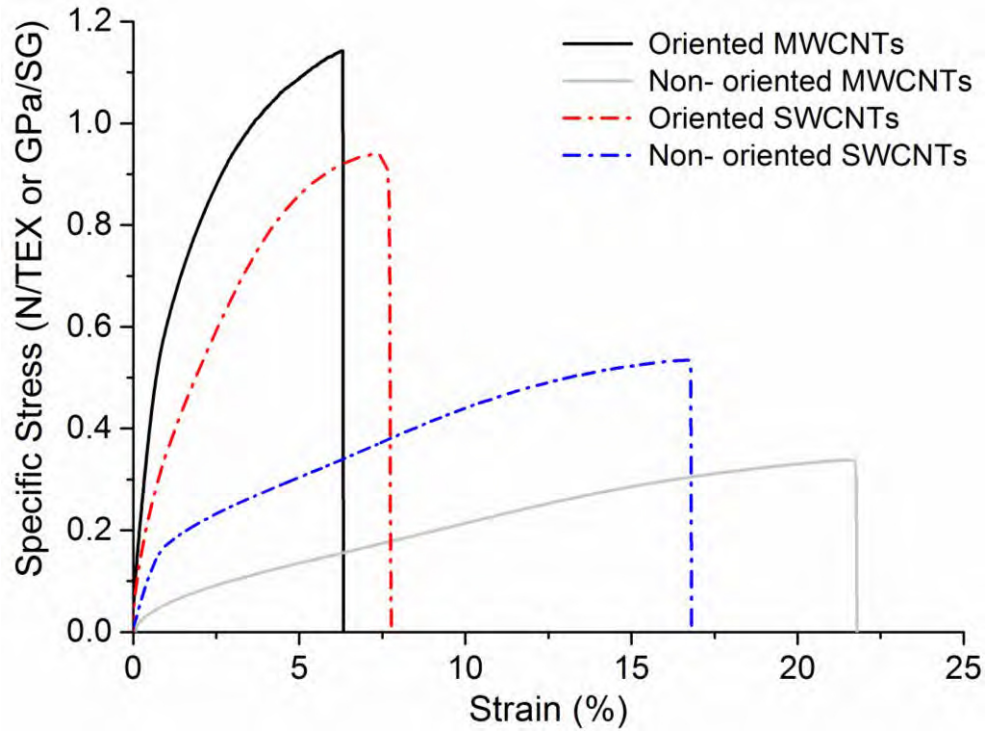

Figure 5.10. Strain-stress curves for highly and poorly oriented CNT fibres made of SWCNTs or MWCNTs, showing that the degree of orientation dominates over composition in establishing the final mechanical of the fibre.

Similarly, it is possible to study the effect of CNT type on tensile properties. Preliminary results have shown small dependence on number of CNT layers in the range (1-5). Oriented fibres have specific tensile strength around 1.1 GPa/SG and modulus close to 60 GPa. However, non-oriented fibre have specific tensile strength around 0.3-0.5 GPa/SG and modulus between 5 to 20 GPa. As might be

expected, the strain increases also from 10% to 20%. Average results are shown in the table 5.2.

Table 5.2. Table with average tensile properties of CNT fibre produced under different spinning conditions.

Spinning conditions	Specific tensile strength (GPa/SG or N/TEX)	Specific tensile modulus (GPa/SG or N/TEX)
Oriented (MWCNT)	1.1	62
Non-oriented (MWCNT)	0.29	6.1
Oriented (SWCNT)	0.85	37.4
Non-oriented (SWCNT)	0.47	15.5

These results present the importance of the microstructure in the CNT fibre, in order to obtain high properties at macroscopic scale. Chapter 6 shows a deeper studies in the fibre structure from the interaction between tube until between fibril[158], showing the potential of high-performance mechanical and electrical properties in CNT fibres. Which are established early in the pre-assembly in the aerogel (gas phase).

5.5. Summary

It was demonstrated in this chapter that direct spinning process the association of CNTs in the gas-phase is critical in determining the possibility to draw the CNT aerogel and thus produce oriented CNT fibres. There are two possibilities, which allows to spin under diluted conditions, obtaining thought low feed rate of precursors or increasing high carrier gas flow rate. Under dilute conditions the fibre can be taken from the aerogel and it is pulled against the gas in the reactor up to 17 draw ratio and due to the friction against the carrier gas. It is possible to align the CNTs preferentially parallel to each other and to the fibre axis.

Decreasing the CNT concentration leads to have less entanglements so as to allow the rearrangement of CNTs, yet enough of them to withstand drawing. Direct spinning process has similarities to wet spinning of high performance polymer fibres, particularly polyethylene, where is critical the density of entanglements in the solution and the properties of the gel fibre are seen as key stages of the spinning process.

It is very important to remark the importance of separating the orientation effect from the CNT composition (in terms of type of tubes). Through raman spectroscopy measurements, it is shown that the dilution of CNT in the aerogel does not affect the type of the tube, controlling as it was discussed in the chapter 4. Decoupling of synthesis of building block from their assembly. Consequently, it is possible to produced oriented or non-oriented fibre in the range of SWCNTs to MWCNTs.

Though the orientation, it is possible to tune the mechanical properties of the fibre. Oriented over non-oriented fibres increases modulus and tensile strength from 4 to 62 GPa and from 0.2 to 1.1 GPa, respectively. However the strain values decrease from 20% until 10%. The effect of the type of CNT (SW or MWCNT) is negligible compared to the orientation. Accurate evaluation of the role of outer CNT layers in inter-tube stress transfer, and in general, establishing a quantitative relation between draw ratio, nanotube alignment and mechanical performance, requires precise measurements of orientation on individual CNT fibre filaments using synchrotron radiation. This effect will be the further discuss in the chapter 6.

6 Fibre structure

6.1. Introduction

A CNT fibre is composed of a millions of individual CNT building blocks, forming a complex hierarchical structure, comprising filaments on different length scales, and preferentially oriented parallel to each other along the fibre axis. CNT fibre has an excellent combination of properties. Mechanical properties similar as Kevlar and electrical conductivity reached until $3.5x10^5$ S/m. Such combination of properties derives from their unusual structure. They have properties typical of a solid monolithic material, such as high strength and stiffness, but these coexist with a large porosity, similar to that of an activated carbon. In terms of transport, they can also be treated as network of conductive elements. The previous chapter introduced evidences that the degree of orientation can be adjusted during the drawing stage of fibre spinning.

CNT fibre is a hierarchical structure mainly divided in three level. Every level correspond with an architecture at different scales; carbon nanotube, bundles of CNT and filaments. Figure 6.1 summarises the different levels in the CNT fibre.

CNTs are the first level. There are one dimension structures, the aspect ratios along the axis as on the order of 10^5 -10^6. The differences between the tubes are several; the number of the layers from SW to MW, affecting to the diameter; the chirality of the tubes defined by the direction of rolling (zig-zag - chiral and armchair) and the ratio between number of layers / diameter promoted the self-collapse. The CNT diameters are in the range from 0.9 nm to 30nm.

Bundles are the second level, several parallel CNTs are stacked forming bigger architectures. CNTs are connected between crystal or entanglements but not perfectly stack along the fibre axis, promoting elongated nano-porous between the CNTs. The dimension of bundles are in the range of 5nm to 200nm.

Finally, filament is the third level, bundles are entangled forming a microporous structure. Several filaments create ropes or cables.

Control of the different fibre levels lead to synthesised the best CNT fibre for each individual application.

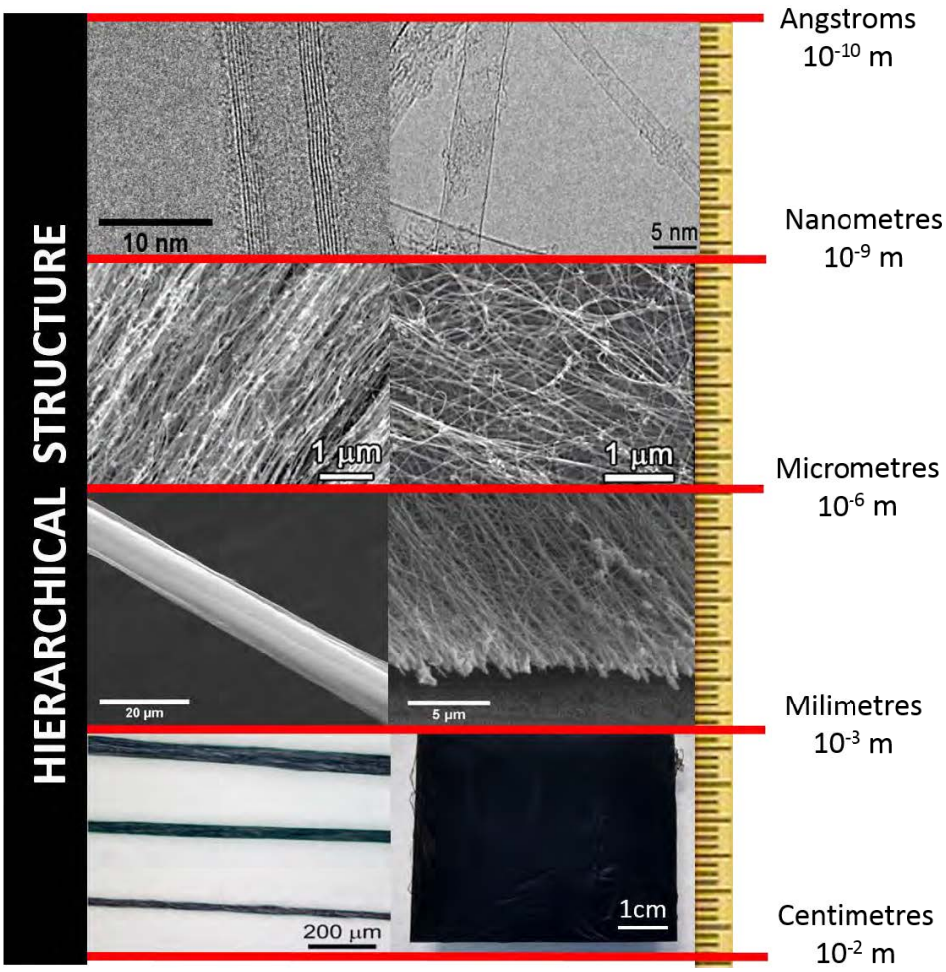

Figure 6.1. Hierarchical structure of CNT fibre at different scales from angstrom to centimetres.

This chapter provides an in-depth study of the fibre structure at different length scales using a wide range of techniques: gas adsorption, small and wide angle X-ray scattering, electron microscopy and ellipsometry, with special emphasis on orientation and densification imparted during assembly, and their effect on bulk properties.

CNTs form bundles, where CNTs are packed in close proximity (< 0.4nm) and forming crystal by means of overlapping along the CNT axis. High magnification electron micrographs show that the pore structure is a reflection of a wide distribution of interbundle separation (Figure 6.2.a). Which has dimension one or two orders of magnitude higher than a single CNT, but then diversify forming the mesoporous structure (Figure 6.2.b). WAXS and SAXS enable determination of the association of CNTs and orientation.

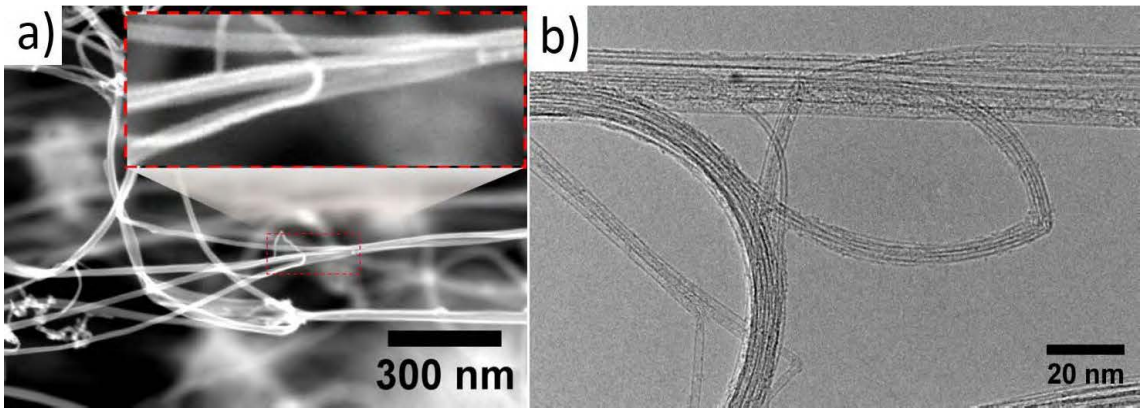

Figure 6.2. (a) SEM and (b) TEM images of the typical CNT structure between bundles and CNTs, providing to the macroscopic CNT fibre a fractal architecture.

6.2. Pore structure from gas-adsorption (isotropic porous material)

In the view of the effect of drawing on CNT orientation, it is of interest to see if better alignment comes at the expense of a resolution in specific surface area and changes in pore structure. Samples fabrication in this chapter requires an absolutely control over reaction to reproduce exactly the same conditions with the exception of the drawing ratio. Furthermore, BET and BJH measurements require a high amount of fibre, around 70 mg. The material necessary to obtain these values is extracted during hours. Showing the big challenge of controlling the synthesis conditions to be reproducible along the time, producing kilometres of fibre. It is possible to control the fibre orientation, aligning the bundle along fibre axis. This bundle rearrangement allows to tune the fibre structure, changing the fibre architecture. Figure 6.3 shows SEM micrograph of and non-oriented (draw ratio = 0.47) and oriented (draw ratio = 12.6) fibre structure.

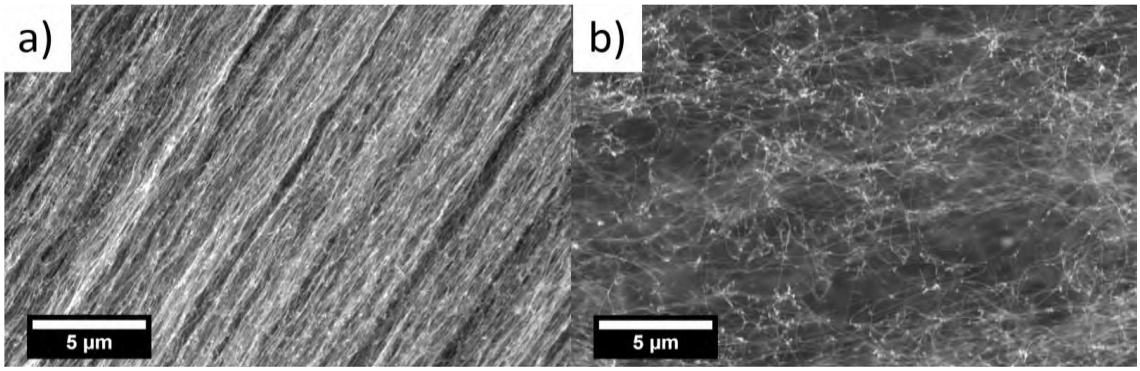

Figure 6.3. SEM images of the CNT with different orientation. (a) CNTs oriented along the fibre axis showing predominance of elongated porous. (b) CNTs randomly distributed with ellipse shape porous.

6.2.1. BET surface area

Macroscopic fibre is a porous material and it is possible to extract information about the structure by BET technique: surface area and pore size distribution. These samples were subjected to gas adsorption measurements and analysing by E. Senokos. Figure 6.4.a shows the adsorption and desorption plot of nitrogen at 77K after degassing the samples. According to the IUPAC classification of adsorption isotherms, the hysteresis loop between the adsorption and desorption corresponds to the type IV isotherm. This isotherm is associated with capillary densification that it occurs in mesopores and limits adsorption at high values of $P/P^o > 0.7$.

Surface area is calculated according to the BET model (section 3.1), using the data points of the adsorption branch in the relative pressure (P/P^o) range <0.3. Below 0.3 the values in the isotherm are related to monolayer coverage of nitrogen molecules on the fibre surface (figure 6.4.b) and thus, pressure can be related to the adsorption surface.

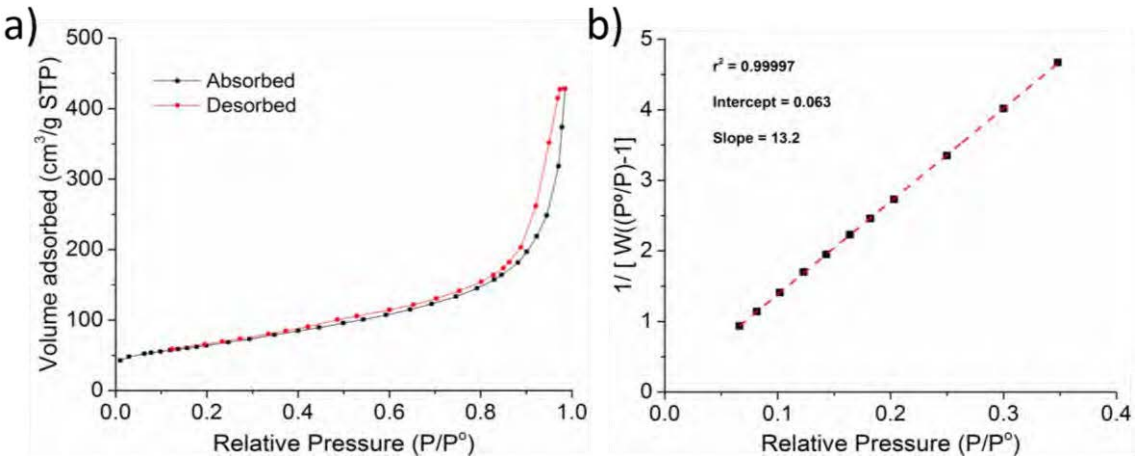

Figure 6.4. (a) N_2 adsorption/desorption isotherms and (b) a linear regression on the multi point BET plot.

The resulting specific surface area (S_{BET}) is ≈ 260m^2/g. It is independent of the draw ratio, at least in the accessible under the synthesis conditions used from 0.47 (1.5m/min) to 12.6 (40m/min) (figure 6.5.a).This is interesting considering that the fibre produced at higher draw ratio has much higher degree of CNT orientation (described in section 6.3) and which therefore have different degrees of alignment. The unexpected increase in specific surface area at higher draw ratios is attributed to the amount of amorphous carbon in the sample. Due to the

higher resident time inside of the reactor, which leads to increase the exposition to the amorphous carbon present in the reaction atmosphere. Increasing drawing ratio leads to less amount of amorphous carbon in the CNT fibre (Figure 6.5.b), as a results of less amorphous carbon, the surface of CNT are available, and thus an increase in specific surface area.

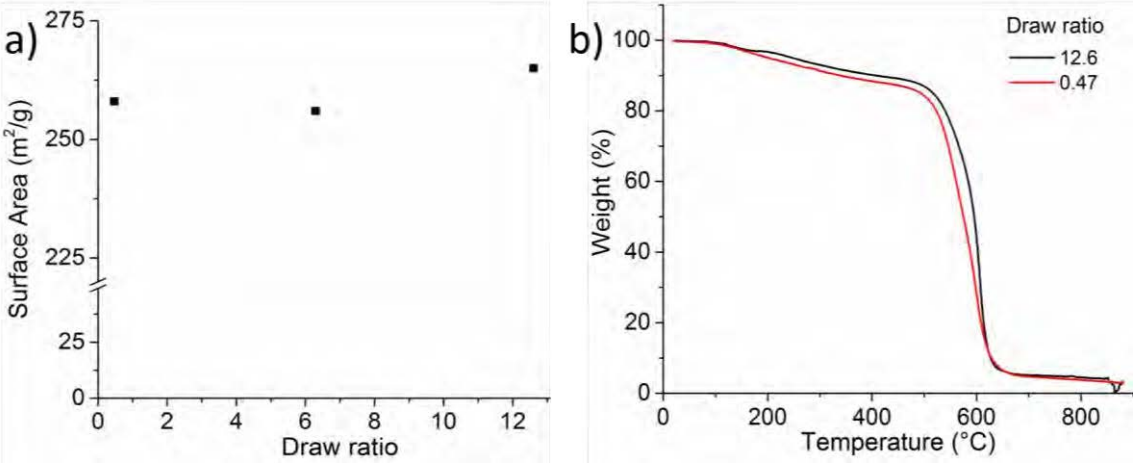

Figure 6.5. (a) Specific surface area measured at different draw ratios (different CNT orientation). (b) TGA measurements at different draw ratio are showing small increase in amorphous carbon at low speed.

6.2.2. Pore size distribution

The pore size distribution is determined by BJH analysis of N_2 desorption isotherm data. Figure 6.6 shows the pore size distribution for CNT fibre produced with different draw ratios. All the samples have a wide range of sizes from 2nm until 120nm, centred around 50-60nm, in the mesopore range[191]. The width of distribution depends on the draw ratio. Increasing the draw ratio decreases the FWHM in the pore size distribution peak. 33 for draw ratio = 12.6 compared with 44 for draw ratio = 0.47.

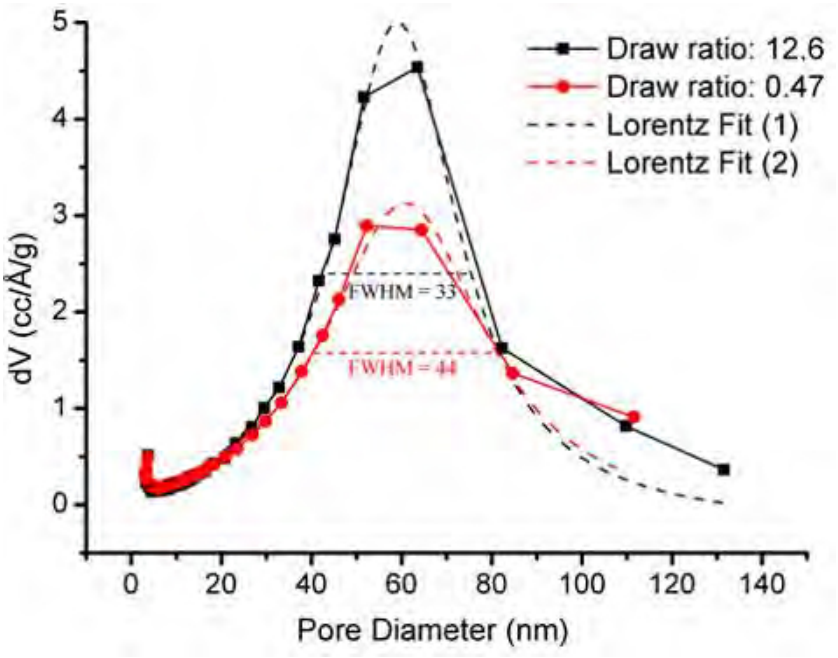

Figure 6.6. Pore size distribution calculated by BJH method at different draw ratio.

6.2.3. Fractal structure though gas-adsorption

Based on adsorption isotherms, it is possible to calculate surface fractal dimension. Which describes the geometry of the surface and its periodicity at different scales. Thus, it can be determined through gas adsorption isotherms on the surface of porous materials. Fractal structure is formulated by the following equation:

$$n = C \,.\, a^{-Ds} \qquad Equation(6.1)$$

Where, the number *n* is the number of molecules of size *a* over a range of lengths, which is covering the surface of the fractal structure with a monolayer; *C* is a constant and D_s is the surface fractal dimension. D_s =3 represent an irregular surface. Thus, D_s = 2 is related to the smooth surface[220].

A fractal dimension can be determined from adsorption isotherms using modified Frenkel-Halsey-Hill (FHH) theory, according to the equation[221].

$$\ln(V/V_{\mathrm{m}}) = \mathrm{Cte} + (D_{\mathrm{FHH}} - 3)[\ln(\ln(P_0/P))] \qquad Equation\ (6.2)$$

Where V is the volume of adsorbed gas at the relative pressure of P/P_0, V_m the volume of monolayer coverage. Figure 6.7 shows a representative plot of $\ln(V/V_{\mathrm{m}})$ against $\ln(\ln(P_0/P))$ of a CNT fibre. It is fairly linear over the entire adsorption range, although with two distinct regimes.

The first one (regime I) is in the range -0.21 $\leq \ln(\ln(P_0/P)) \leq$ 0.3 and corresponds to the Langmuir monolayer coverage of the CNTs by adsorbent gas molecules. The second (regime II) below $\ln(\ln(P_0/P)) \approx$ - 0.21 corresponds to multilayer adsorption capillary densification. Only the monolayer coverage section of the adsorption isotherm provides accurate values for the dimensionality of the surface.

Taking the slope in this regime, the resulting surface fractal dimension comes out as 2.55. It is in agreement with the values reported by gas adsorption 2.49-2.53[222] [223] and the results by SAXS. The value of D_s of 2.5 - 2.6 obtained is comparable to those reported for CNT membranes studied by SEM (2.43-2.86)[148], gas-adsorption alone (≈2.6)[225] and dynamic light scattering (2.24-2.58)[226].

Figure 6.7. Fractal dimension analysis of CNT fibres. Plot of nitrogen adsorption isotherm showing the linear best-fit at regime where Langmuir monolayer adsorptions (Insert schematics) are dominant before the capillary densification.

6.3. Hierarchical structure (anisotropic porous material)

Gas adsorption measurements are useful to characterize porous solids, but fail to recognize the shape of the pores. The first evidence of the anisotropic structure of CNT fibres is by electron micrographs. Such structure can be readily studied by WAXS/SAXS. Figure 6.8 shows a schematic of CNT fibre and the information that is possible to extract from typical SAXS and WAXS measurements.

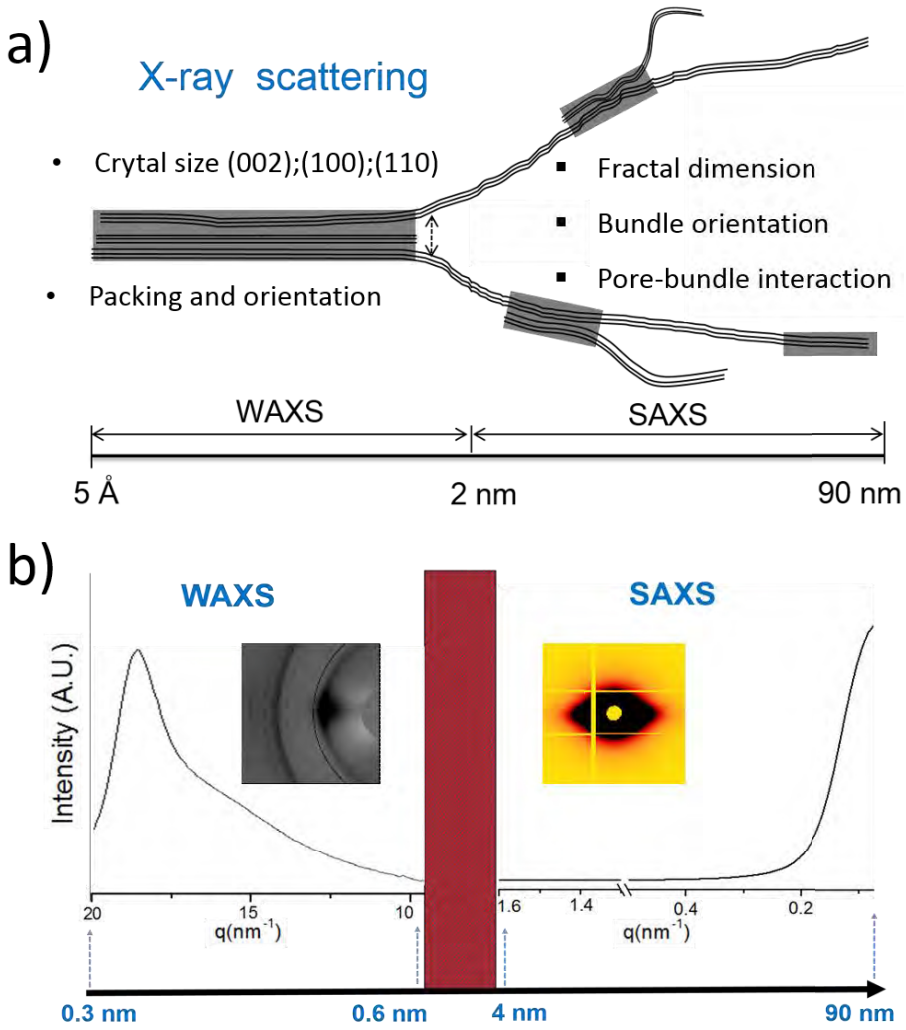

Figure 6.8. (a) Schematic of a CNT fibre with the information that it is possible to extract from (b) typical SAXS and WAXS pattern and their integration.

WAXS patterns provide information in distances between angstroms and 1nm, correspond to the crystal structure and intertube stacking and orientation. SAXS provides information about the pore structure in the range 4-90nm for the measurements presented in this work. The degree of orientation in this fibres can be obtained by either WAXS/SAXS as they are approximately equivalent[114]. Finally, it is noted that, having an unknown gap between SAXS and WAXS, the

equatorial component of SAXS, the fibre streak, extends all the way up to the WAXS region. To assist in the interpretation of WAXS/SAXS results, fibre produced at different draw ratio and therefore with different degree of orientation, are analysed.

6.3.1. SAXS: Fractal structure and bundle interaction

The sample, consists of 100 filaments, is oriented vertically. The oblong shape of the pattern with stronger equatorial reflections, is due to the preferential alignment of CNTs in the fibre axis. The interpretation of SAXS data for diffuse systems is a challenge, and when they are anisotropic this become even more complex.

Figure 6.9 presents a plot of SAXS scattering intensity against log q, obtained from 360º azimuthal integration. The graph shows predominantly a smooth drop in intensity. In the Porod region towards higher q values (q = 0.2 – 0.9 nm^{-1}, d-spacing about 7 to 30 nm) the power law $I(q) \propto q^{-X}$ gives a slope of X = 3.4. Materials with a uniform smooth surface are characterized by Porod slopes of 4, whereas values of X < 4 are typical of porous media, such as particle aggregates, colloidal systems, activated carbons and porous ceramics [224], which are better described as fractal structures. For 3 < X < 4, as it is the case for CNT fibres, the material corresponds to a surface fractal, instead of a mass fractal for which X is < 3). For a surface fractal $I(q) \propto q^{-(6-D_s)}$ and thus the surface fractal dimension, D_s is 2.59 [146]. This ignore sample anisotropy.

Figure 6.9. Fractal dimension analysis of CNT fibres. Plot of SAXS intensity against scattering vector. Insert (SEM image) is used for visual guide.

It is also in the range of values for activated carbon (2.8-3)[227] studied by the same techniques, nuclear graphite measured by small angle neutron scattering (2.8)[228].

The results in the figure 6.10 correspond to fibre made up of MWCNTs. Fibres of predominant SWCNTs produced by reducing the concentration of sulphur promotor obtain values of D_s = 2.8 from 360º SAXS integration. The diameter and number of layers of CNT determine their flexural rigidity and thus influence their ability to bend and reshape to maximise contact with adjacent tube, producing bigger bundles and increase the Porod slope.

It is then of interest to analyse how D_s is affected by the degree of CNT orientation. Thus, synchrotron SAXS measurements performed on a multifilament samples produced spinning at different draw ratio.

Different integration are performed in the SAXS pattern, equatorial, median and 360º, in order to obtain a complete information related with the changes in the pattern intensity; dash blue lines indicate the integration area. In figure 6.10 fractal dimensions are plotted against draw ratio, converging towards value of 2.55-2.6 and remaining constant with draw ratio. Nevertheless, Equatorial and meridian fractal surface obtain different values 2.75 and 2.45, respectively. This indicates that fibres are rougher radially than longitudinally.

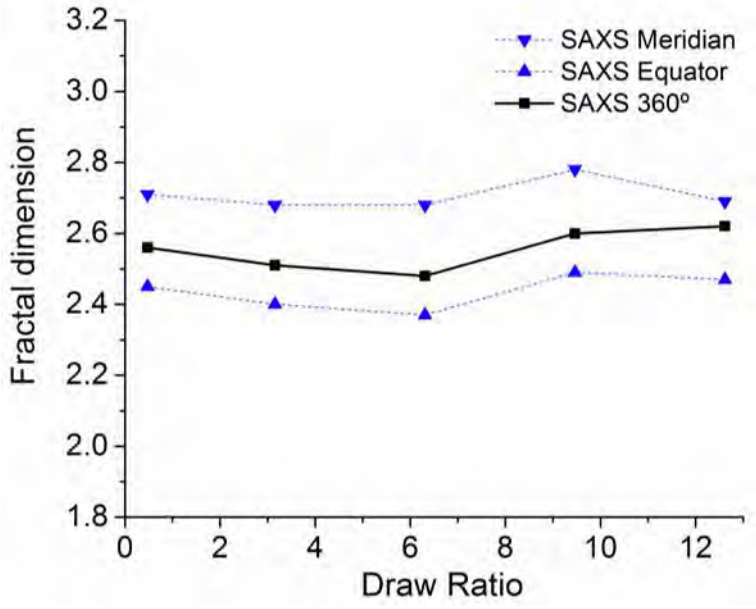

Figure 6.10. Plot of fractal dimension against draw ratio for equatorial, meridian and 360º. Result suggests that Porod slope remains constant with bundle alignment.

Anisotropic pore structure

Further information about the pore structure can be extracted from SAXS data. In this work is assumed that the system can be treated as two phases separated by a sharp interface, with an arrangement similar to that is shown in figure 6.11.

All the values are calculated through the following mathematical equations;

The average lateral size of pore can be calculated from the Porod chord length, l_P, and the porosity, P: $\langle l_{pores} \rangle = \frac{l_P}{1-P}$ $Equation\ (6.3)$

The Porod chord length is given by $l_P = \frac{Q}{K_P}$ $Equation\ (6.4)$

Where Q is the invariant: $Q = \int_0^\infty q^2\, I(q) dq$ $Equation\ (6.5)$

K_P is the Porod constant: $K_P = \lim_{q \to \infty} q^{-4} I(q)$ $Equation\ (6.6)$

The length of scattering elements in the longitudinal fibre direction, L_3, can be obtained from intercept slope of the linear plot of q x B_{obs} against q.

$$B_{obs} = \frac{2\pi}{L_3} + qB_\phi \quad Equation\ (6.7)$$

B_ϕ is the orientation distribution. This equation can be applied when the azimuthal profiles can be fitted by Lorentzians. The pore structure drawn in figure 6.11a, it can be described by parameters, L_3, L_p and B_ϕ

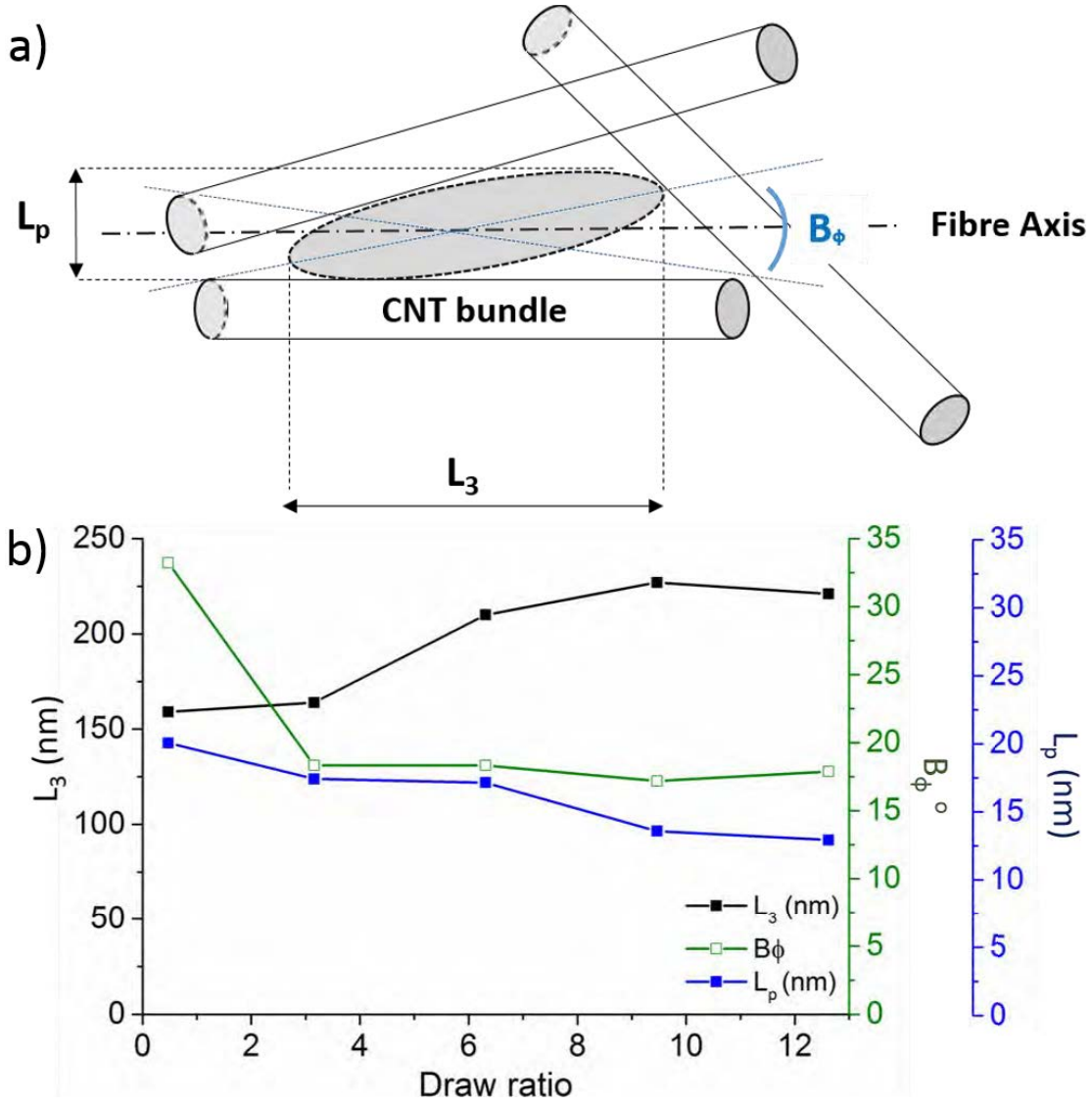

Figure 6.11. (a) Schematic representation from the L_3, L_p and B_ϕ. (b) L_3 and B_ϕ and(c) L_c and L_p against draw ratio, showing how the parameters change, when the draw ratio increase orienting CNT fibre.

Figure 6.11.b presents values of L_3, B_ϕ and L_p, for fibres produced with draw ratio from 0.5 to 12.5. L_3 goes from 159 to 227nm, indicating that the pores in the meanwhile L_p decreasing 40%. L_3 and L_p are parameters related to the average length the structural unit in the fibre axis and perpendicular direction, respectively. B_ϕ decreases significantly when draw ratio increases, the change is more accused in the range from 0.5 to 3 in draw ratio; orientation values goes from 33º until 17º. This parameter is directly related with the bundle orientation along the fibre. Consequently, it is possible to confirm that the alignment of bundles increases from draw ratio between 0.3 - 3. However, the change is smoother when the draw ratio raise 3 until 12.5. Changing bundle orientation in the CNT

fibre affects directly to the pores structure. Due to the orientation, inter-bundle pores have more elongated structure along the fibre axis. To sum up, table 6.1 presents all the structural parameter extracted from fibre structure.

Table 6.1. List of structural parameters, extracted from SAXS pattern (L_3, L_p, B_ϕ, BET and BJH).

	Draw ratio				
Parameters	**0.47**	**3.15**	**6.3**	**9.5**	**12.6**
Orientation Distribution B_ϕ(degree)	33.2	18.3	18.3	17.2	17.9
Average lateral size of the pore L_p(nm)	20.3	17.6	17.3	13.8	13.1
Average length of the pore L_3(nm)	159	164	210	227	221
Inter-bundle elongation ratio L_3/L_p	7.8	9.3	12.1	16.4	16.9
BET (m^2/g)	258	-	256	-	265
BJH (Range (nm) & FWHM)	61 & 44	-	-	-	56 & 33

Figure 6.12.a shows the real dimension of a pore, synthesised at draw ratio = 12.6. It is possible to observe that the dimensions are in agreement, compare to the electron micrographs.

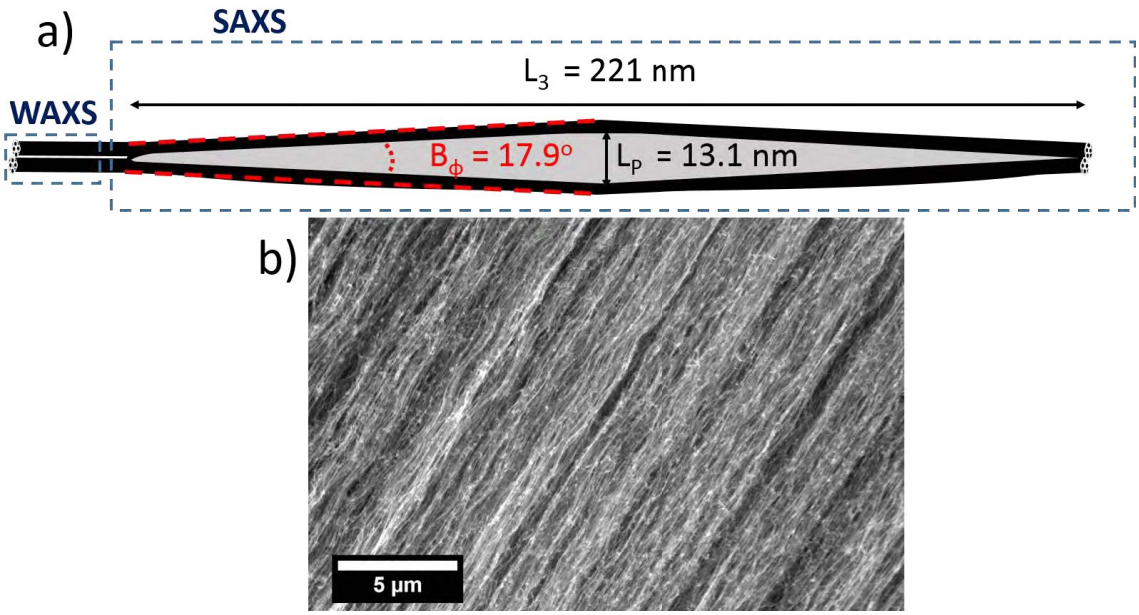

Figure 6.12. (a) Schematic representation from the L_3, L_p and B_ϕ in a realistic mesopore between bundles and (b) SEM micrograph at draw ratio = 12.6.

Although the SAXS data correspond generally to a diffuse system as a consequence of the range of interbundle spacing, there is a small feature at low

q values (0.9 – 1.2) on the equator. This effect is more accused in oriented fibre. Figure 6.13.a presents a SAXS integration from a align fibre (draw ratio = 12.6, in equatorial and meridian, observing that the effect is more accused in oriented fibre and it is not noticeable in meridian integration. Comparing the result with non-align fibre (draw ratio = 0.47) the effect is less predominant (figure 6.13.b).

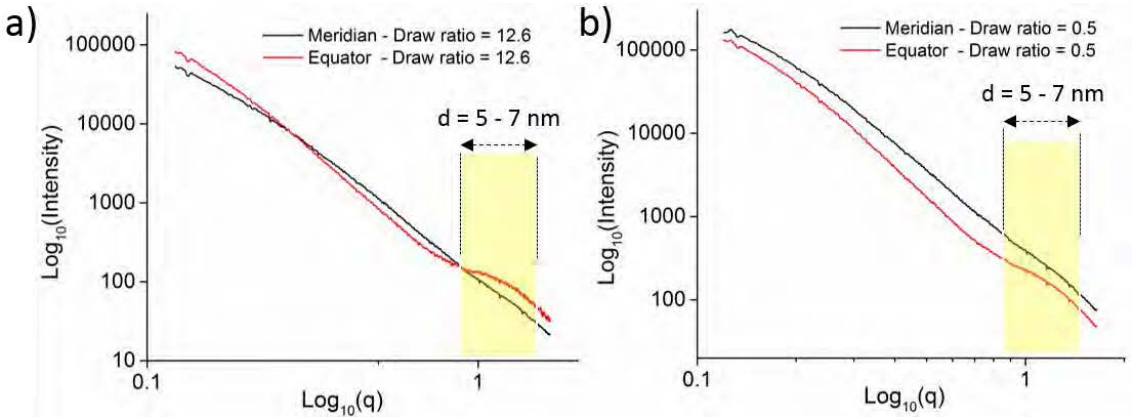

Figure 6.13. Fibre intensity against q in logarithmic scale with different draw ratios (a) 12.6 and (b) 0.5. Significant changes appear in the slope in the q range from 0.9 to 1.2 nm^{-1}, represented with yellow background.

It is clear that SAXS and WAXS probe the same entities, but at different length-scales. This is confined by comparison of the FWHM at different q. Taken as FWHM of the azimuthal profile at different distance, it is evidence that the degree of orientation has a smooth slope in the range from q = 0.07 to 18 nm^{-1} (figure 6.14). Which is a confirmation that CNT fibre is a fractal structure, remains the structure almost constant at different scales.

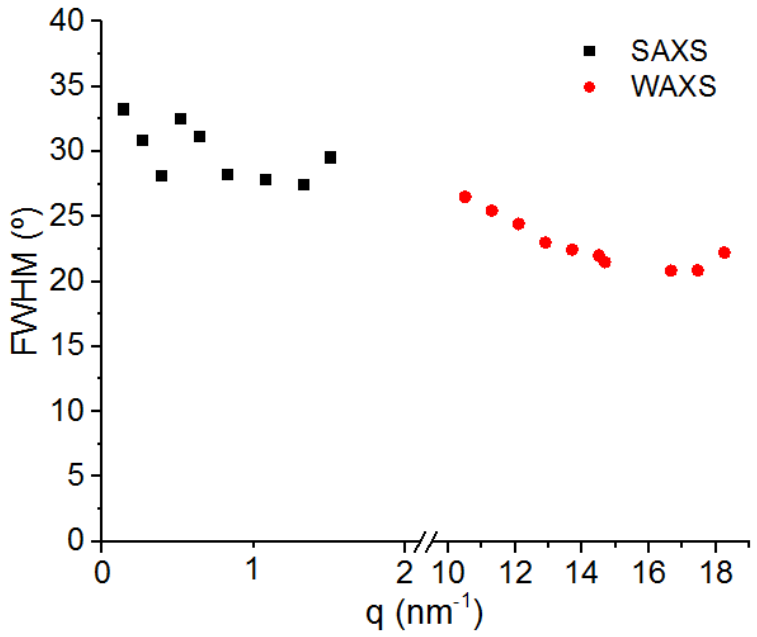

Figure 6.14. FWHM of the azimuthal profile at different distance from q = 0.07 to 18 nm^{-1}, related to SAXS and WAXS patterns.

The degree of orientation is almost constant at different scales: between CNTs and bundles. This data evidences the link between SAXS and WAXS patterns in the interpretation of the CNT fibre. E.g. Evaluation of this SAXS region, together with the azimuthal integration 002 reflection in WAXS pattern, could provide structural information from the fibre. Nevertheless, because stress and charge transfer between CNTs occurs over distance below 1 nm, it is of interest to inspect more closely to WAXS.

6.3.2. WAXS: Orientation, packing and crystal size

Figure 6.15.a shows a typical 2D WAXS pattern for a multifilament sample of CNT fibre. The pattern is divided due to the detector limitations to obtain whole information. Figure 6.15.b shows the fibre in the direction related to the pattern. White dash lines are represented the two possible integration direction (figure 6.15.c).

Integrating along q, it is possible to extract CNT crystal sizes (002); (100); (110) and packing of the CNTs in the bundle. Thus, azimuthal integration permits to complete the information (together with azimuthal integration in SAXS) about orientation of the CNTs along the fibre. Figure 6.15.d shows the position of the CNT crystal reflections. Which will be further evaluated along this section.

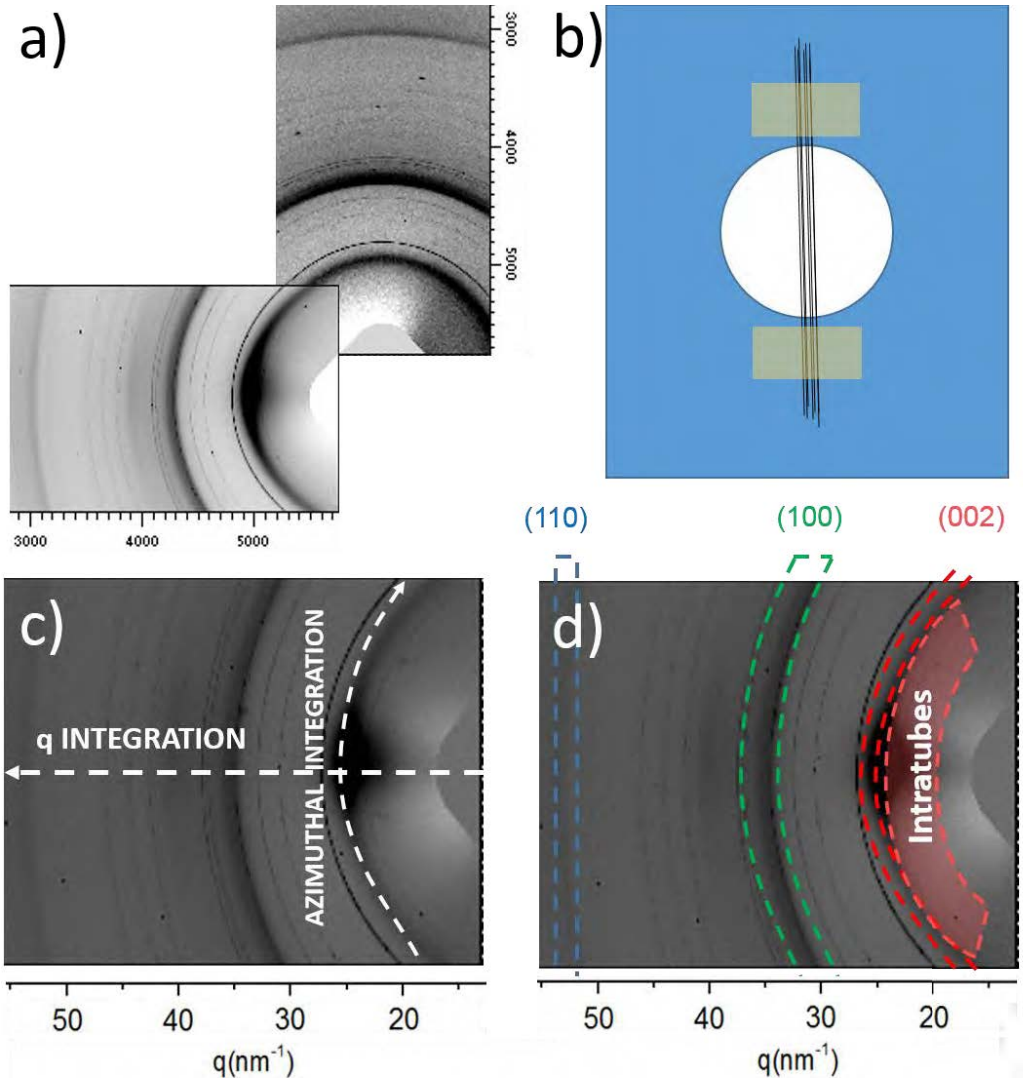

Figure 6.15. (a) Typical 2D SAXS diffraction pattern from an oriented CNT fibre(b) located perpendicular to the 002 reflection.(c) Integration direction: azimuthal and radial (q) and (d) the CNT crystal positions in the pattern.

Figure 6.16 represents a radial integration along the equator direction from a CNT fibre wound at draw ratio 12.6. There is an overlap between the intratube and the intertube effect. It is a challenge distinguish the contribution in the peak in the range of q from 10 to 20 nm^{-1}.

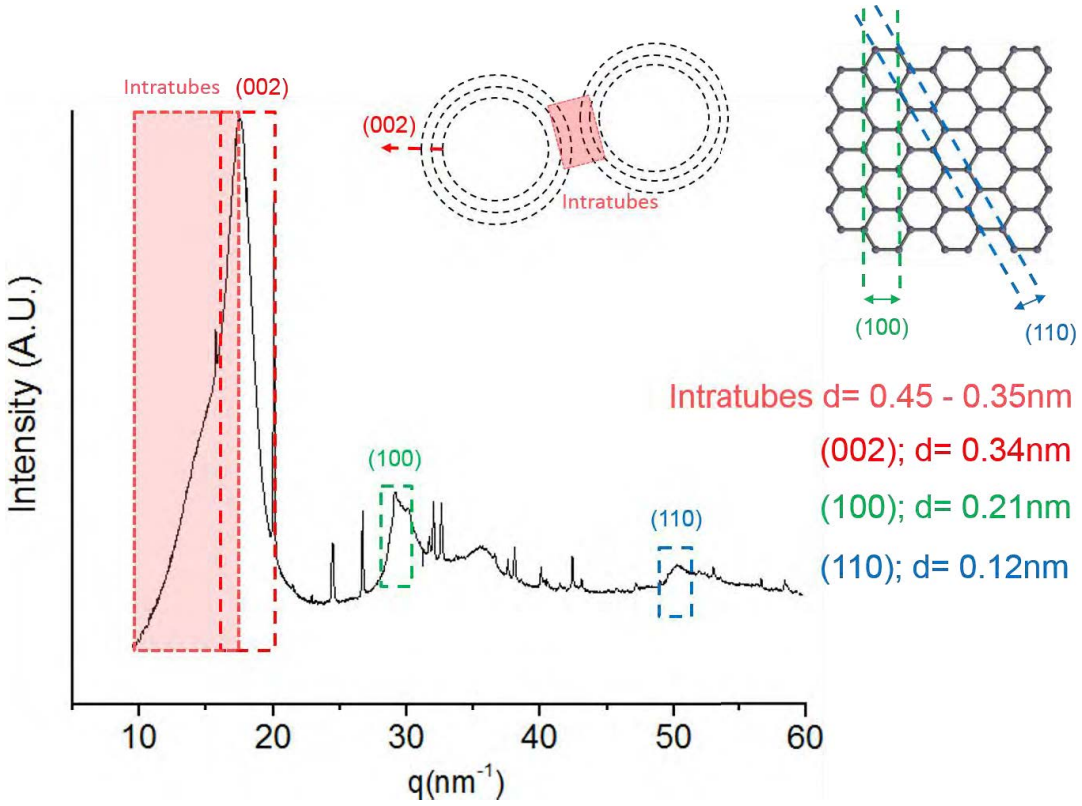

Figure 6.16. Typical radial integration from a 2D patterns in the equatorial direction from an oriented fibre. CNT reflections are represented with dash lines: red (002); green (100); and blue (110), which are related with 0.34-0.21 and 0.12nm, respectively.

Intratube corresponds with almost the maximum intensity and it is centred in 0.345nm, which is the distance between two turbostratic graphitic layers in the nanotube (002) [229]. (002) reflection is concentrated in the equator due to the preferential orientation of the CNTs along the fibre axis. Furthermore, the shoulder at higher distances, over 0.355nm, represents the relative position of the CNTs to each other and it is related with the packing of the CNT into the bundle.

Figure 6.17 shows the 002 reflection integrated in the range of 80º, comparing the intensities at different draw ratios, normalised by the invariant (Q) and smooth. Which are indicative of the fraction of graphitic planes in coherent stacking, which are taking part in stress transfer. Integration of the peaks provides an estimate of the fraction of coherent graphitic domains. Figure 6.17b presents a 002 integration with a cut-off interlayer separation of 0.4nm, which is assumed to be close to the limit for interlayers stress transfer. This effect is important in order to understand the effect of the orientation related to the mechanical properties (section 5.4).

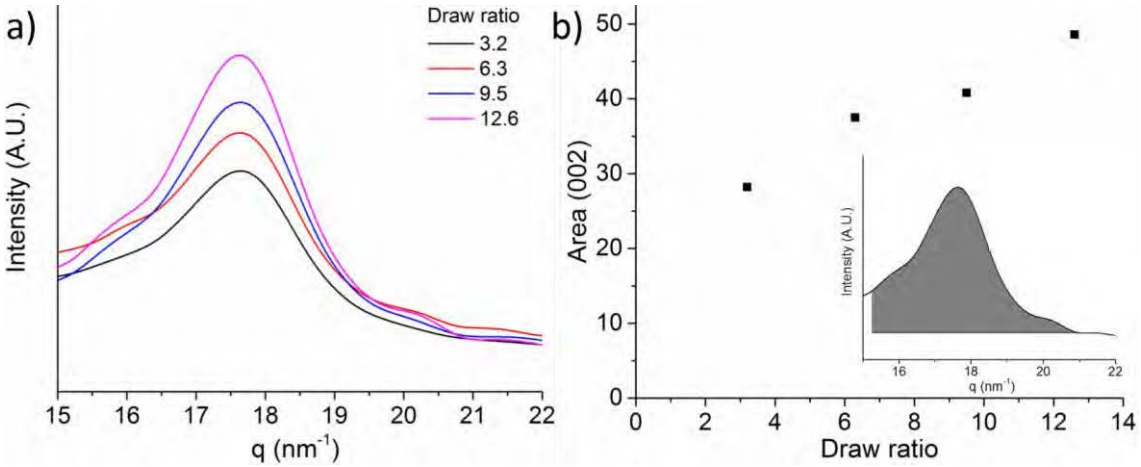

Figure 6.17. (a) Radial integration in the range between q = 15 to 22 nm^{-1}, 002 refection at different draw ratio are compared normalised by the invariant. (b) 002 integration area at different draw ratio until 0.4nm.

In the previous figure, the three main CNT reflections are emphasised with dash lines: red (002); green (100); blue (110) and its physical representation in the structure. Though Scherrer equation is possible to calculate the crystal size from the FWHM of the (110) peak.

$$d_{002} = \frac{K\,\lambda}{\beta \cos\theta} \qquad Equation\ (6.8)$$

Where K is the shape factor (0.9 is the typical value), β is the FWHM in radians, λ is the wavelength and θ is the Bragg angle. Table 6.2 presents all the structural parameter extracted from WAXS integration:

Table 6.2. Parameter extracted from WAXS pattern: Crystal sizes and azimuthal angle.

	Draw ratio				
Parameters	**0.47**	**3.15**	**6.3**	**9.5**	**12.6**
Crystal size (110) Equatorial (nm)	4.6	4.3	4	4.1	3.6
Crystal size (110) Meridian (nm)	4.6	4.7	4.6	5.3	4.6
Azimuthal Angle (002) (Degrees)	35.1	21	21	19.3	18.3

In the SAXS section, it is also discussed the results in terms of orientation though the pore-opening angle and relative orientation. Utilising the azimuthal integration to raise until these results. Furthermore, it is possible to calculate the orientation in WAXS, integrating the pattern in the azimuthal direction in the (002) region. FWHM is calculated, fitted by a lorentzian peak (figure 6.18.a). As in SAXS,

narrower peak distribution means more orientation of CNTs along the fibre. However, this is for multifilaments.

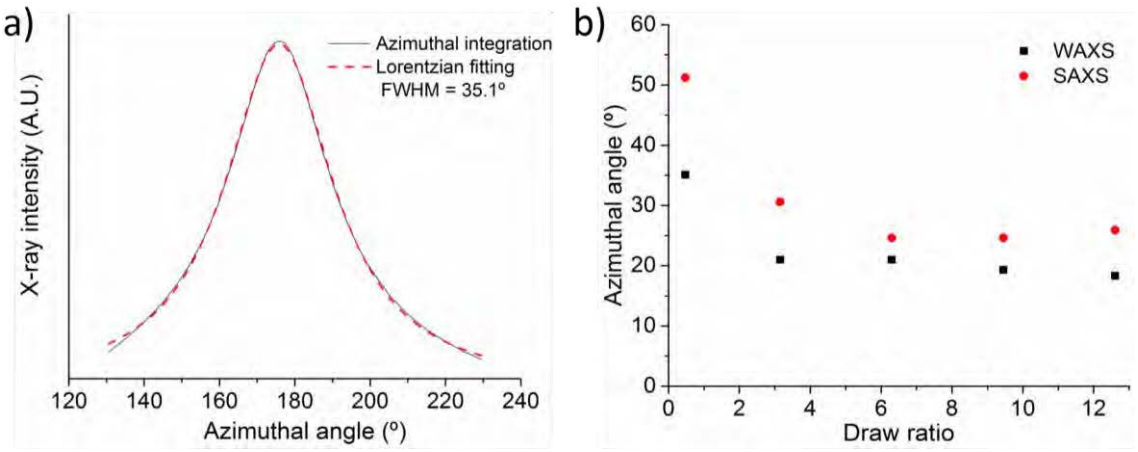

Figure 6.18. (a) Azimuthal integration from 002 reflection in WAXS pattern from non-oriented CNT fibre, fitted by a Lorentzian peak. (b) Comparative of orientation though FWHM between samples spun at different draw ratio.

Figure 6.18.b shows that the orientation in the fibre of the azimuthal profile has the same tendency in WAXS and SAXS, increasing the orientation very sharply in the range from 0.47 to 3. In spite of the bundle orientation is not modified from 6 to 12.6, the CNT shows a little improve when the draw ratio is increased. Therefore, the overall similarity between SAXS and WAXS indicates the equivalent orientation between bundles and CNTs.

It is worth mentioning that CNT fibre has approximately 10-15 wt% of carbon materials, which are not CNTs, predominantly graphitic material. Therefore, (002) reflection, which is not in the equatorial direction, is related to different graphitic material in addition to non-align CNTs.

Continuing along the radial integration in the WAXS pattern, (100) is the following reflection at 29.6 nm^{-1}. However, it is very difficult to extract information from this reflection. The (100) distance is 0.21nm and it matches with other 5 reflection, which are related with the catalyst mainly Fe FCC (111), martensite (101) and (110). In this range from q = 28 to 35nm^{-1} is extracted more information from the catalyst structure. Therefore, it is further discussed in section4.4.

Finally, the reflection (110) is located in q = 53nm^{-1}, on one hand the peak is detected isolated in the pattern and it can be analysing properly. On the other hand it is the less intense peak and it is necessary enough material to obtain

intensity in order to provide trustable information. (110) reflection is commonly used for analysing isolated CNTs by electron diffraction due to it is possible to extract the chirality of the tube[85], directly related with optical and electrical properties [230].

However, bundles have several connections between CNTs, creating junctions analogous to crystals. Especially, collapse CNTs, due to the less curvature, produce better connexions between the CNTs.

This structure is observed frequently in the bundles. TEM micrographs shows two different bundle from different points of view (figure 6.19.a-b). First micrograph shows the lateral part of the bundle, observing the graphitic layers stacked to each other. The distances between layers correspond with approximately turbostratic distance 0.345nm and view from above, finding Moiré patterns, which is created when two layers are displaced or rotated, separated by a small distance. Figure 6.19.c shows the deconvolution of the 110 peak.

(110) crystal sizes are plotted in figure 6.19.d at different draw ratios in order to observe the effect of the CNT orientation in the bundle structure. Radial integration in equatorial and meridian direction are analysed. The changes in the dimensions are minimum. The dimensions are between 4 and 5 nm in both directions. Nevertheless, small effect can be observed, increasing the draw ration goes to increase the difference between the two crystal dimensions. Consequently, the crystal is more extended along the fibre axis coming from the CNT rearrangement during the CNT orientation.

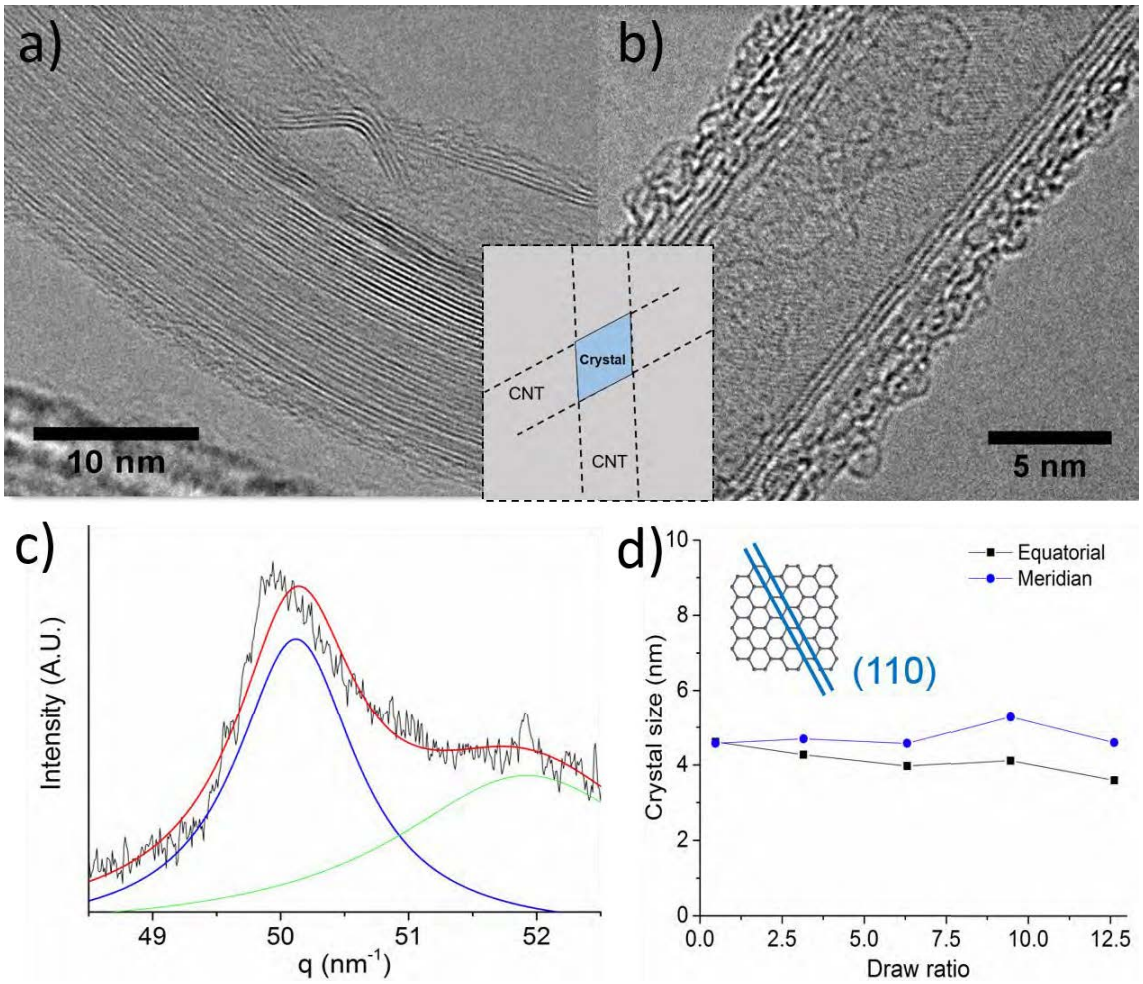

Figure 6.19. (a) CNT bundle formed by around 40 collapse CNTs. (b) CNT bundle constituted by CNTs. Schematic of two CNTs in the fibre, forming a crystal junction (inset). Overlapping of graphene layers create Moiré pattern, confirming the presence of collapse CNTs. (c) 110 peak deconvolution. (d) Crystal size extracted from 110 reflection.

6.3.3. Volumetric density

The macroscopic effect of the reduction in pore size is to increase apparent volumetric density. Figure 6.6 presents values of volumetric density determined from gravimetric linear density and average fibre diameter measured by 10 SEM micrographs.

Figures 6.20 presents the plots of volumetric densities against draw ratio. As the winding rate approaches the gas-flow rate in the reactor; volumetric fibre density increases at higher winding rates as the higher degree of alignment improves packing from 320 to 460kg/m^3.

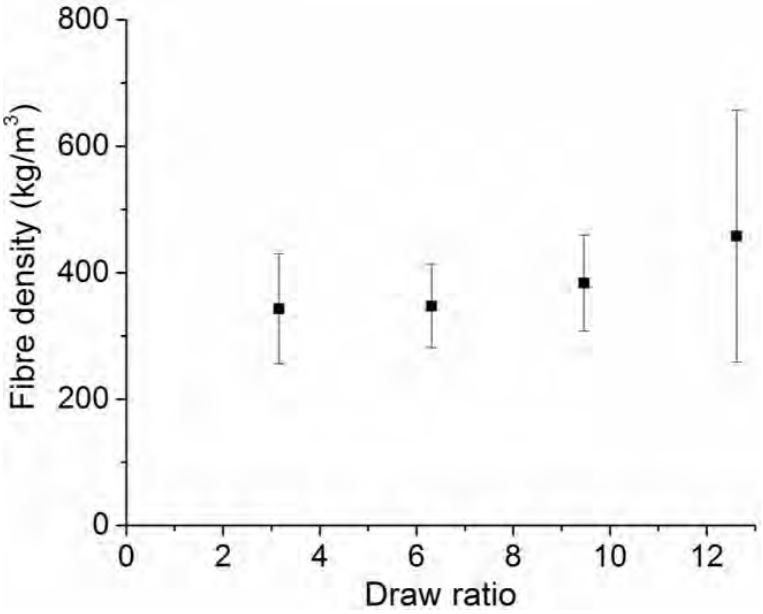

Figure 6.20. Dependence of fibre volumetric density on the draw ratio.

Overall, CNT fibre has a predominantly mesoscale distribution and it is possible to tune the fibre structure in terms of pore size and shape distribution. Modifying draw ratio, CNT alignment is increased. Although the increase in CNT alignment is expected to improve their packing (volumetric density) and thus reduce some of the porosity, specific surface area is not substantially affected.

6.4. Effect of densification in the CNT structure.

In this chapter, it is described the importance of the structure. However, it is worth mentioning that the CNT filaments used in the measurements or the macroscopic fibre or film involved in devices, have to be densified in order to decrease the porosity and create architecture manageable. Otherwise, structure of the architecture will be damaged during manipulation process. On average, the porosity of the CNT fibre as-spun is over than 99%. Figure 6.21.a-b show a schematic illustration of the densification process. Capillarity force acts into the CNT bundles, bringing together with a volatile liquid (acetone in this samples). Non-supported CNT fibre leads to produce fibres, using as a cables or sensors. Other possibility is densify the fibre onto a substrate, creating a densification perpendicular to the surface. Densification process is instantaneous.

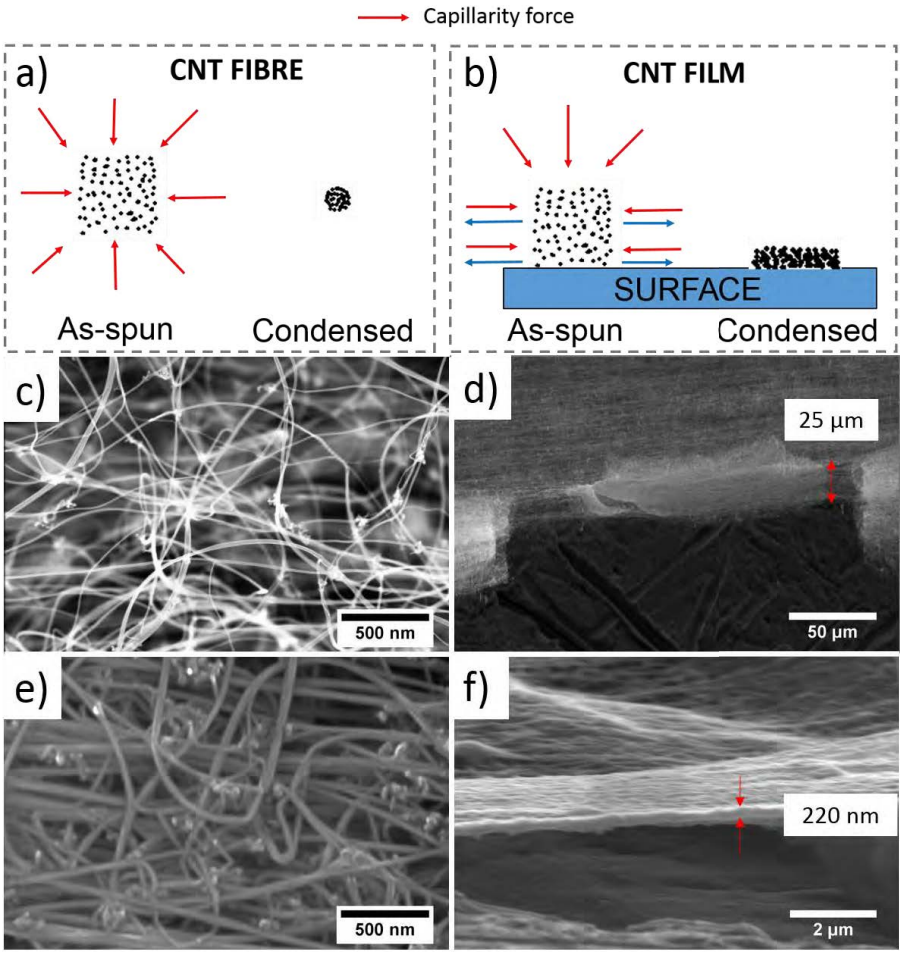

Figure 6.21. Schematic illustration of the densification process in a (a) CNT fibre and (b) film. (c)-(f) SEM micrographs show the effect of densification in the fibre and film structure. Decreasing the porosity and dimensions two orders of magnitudes.

Figure 6.21.c&e present a surface imagen from a single filament as-spun and after densification, respectively. It is clearly observed that the macroscopic pores are closed and the bundles are dramatic decreased the distances to each other. Figure 6.21.d&f show the effect of densifying the fibre over a substrate. The thickness of the CNT film decrease two orders of magnitude from 25µm to 220nm, stabilized the structure in order to be manipulated.

There is no technique, which allows to the calculated the pore size distribution of an as-spun CNT fibre. BET require at least 25mg to obtain a trustable results that in volume it hundred time high than the BET container, and mercury porosimetry would deform the structure after applying pressure. Actually, direct measurement from SEM micrograph is the best option. It is not the most accurate method, however it could be provide an insight about the pore size distribution. It is assumed that the pores are ellipses. Pore area is calculated as an average of two

main distances d_1 and d_2. Figure 6.22 shows the results of pore size distribution from an as-spun fibre and it is compared with densified fibre. The main area is related with pores bigger that 1µm (>55%), whereas in densified fibre 100% of the pores are below 100nm.

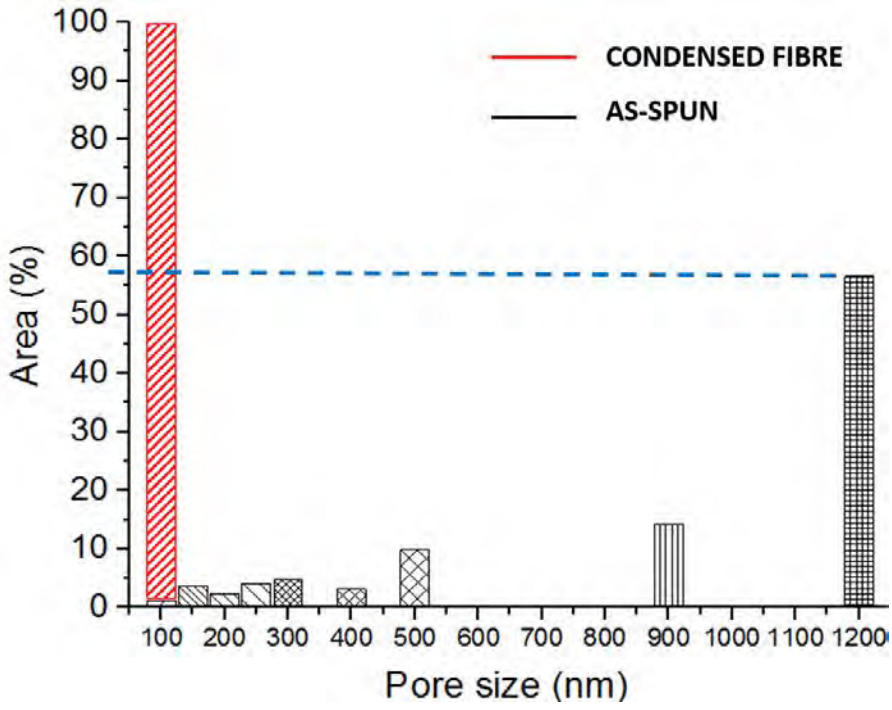

Figure 6.22. Histogram of pore size distribution, showing the macropores densification the dimension to mesopores.

Analysing specific stress - strain curves for densified and as-spun fibre, it is possible to extract information about the densification effect in the fibre structure.

Figure 6.23.a shows optical micrographs of a CNT fibre as-spun and after densification, the diameter is more decreasing from more than 110µm (as-spun) until 10µm (densified) and taking this values into account the density increase by 120. However, this big macroscopic modification in the fibre structure is not affect to the nanostructure structure of the fibre.

WAXS/SAXS patterns (figure 6.23.b) from as-spun and densified fibre were measured, observing nearly identical results, with the equatorial radial profile showing minor differences (figure 6.23.c). This suggest that the distance between CNT and the packing between bundles remains unchanged (<2nm). However, these measurements correspond to multiple filaments.

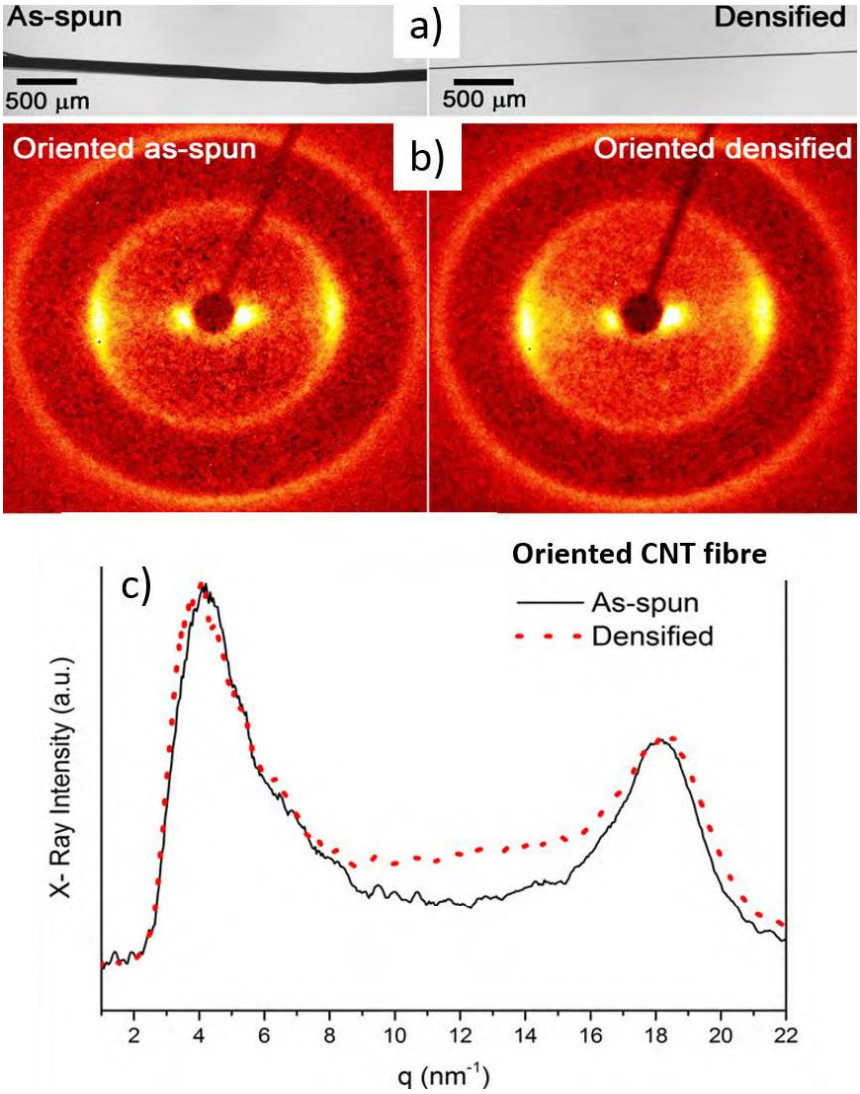

Figure 6.23. Effect of post-spin capillary densification on fibre structure and properties. (a) Optical micrographs of a CNT fibre before and after densification. (b) SAXS/WAXS patterns showing no changes in orientation after post-spin densification, and (c) equatorial radial profile confirming that CNT and bundle packing at small separations (<2nm) remain mostly unaltered.

After this analysis, it is not surprise that the post-spin densification neither affect CNT fibre properties, taking in consideration that there is no change in the structure. Continuous electrical measurement were perform to evaluate the different behaviour between as-spun and densified fibre (figure 6.24.a). It presents that aside from a transient change upon liquid exposure due to the slight swelling[136], the resistance after acetone evaporation recovers the same value and remains constant the conductivity per unit mass after decreasing the diameter one order of magnitude. Figure 6.24.b shows a mechanical test comparing also as-spun and densified CNT fibre, presenting similar modulus and

not very different tensile strength, being the effect of the densification negligible compared to the orientation effect.

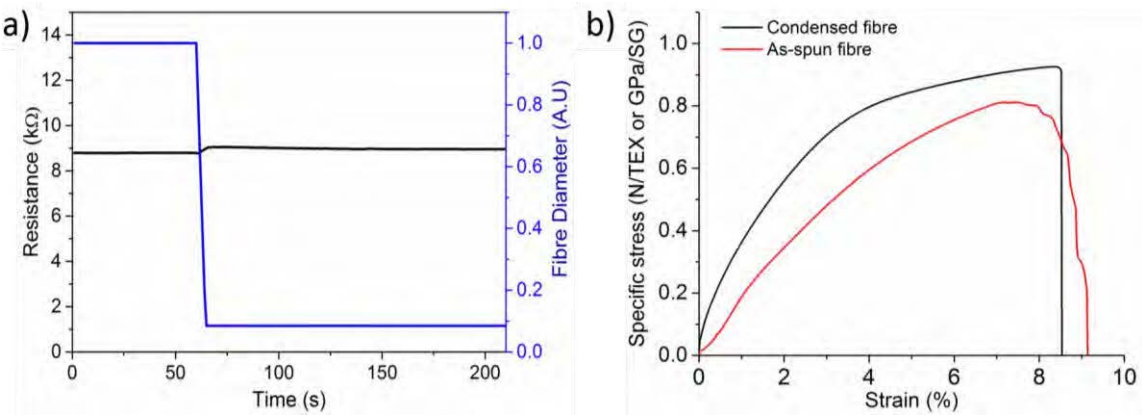

Figure 6.24. (a) Continuous measurement of electrical resistance during the densification process also shows no substantial change in spite of a diameter reduction of an order of magnitude. (b) Stress-strain curves of as-spun and densified fibres with minor differences in strength, modulus and ductility.

After these results is demonstrate that the densification does not affect the important links in the fibre, related to the CNT distance and bundle packing, which are the important parameters to change and load transfer processes. The densification impact is related with the reduction of macroscopic porous, providing to the CNT an increase in the density an order of magnitude.

6.5. Thin films (optical effects)

In direct spinning method, the most common CNT macroscopic architecture is the fibre, exploiting axial properties over long lengths for many applications. However, in many applications is required the exploitation of the properties over large area, synthesising CNT films; as electrodes or transistors. Thin-film interference is other observable phenomenon related to nanometre films.

This section is motivated by the observation that when CNT films are deposited onto reflective substrates, thin films of CNT develop colour, ranging from blue to red. Thin films of CNTs are produced by controlling an aerogel and careful deposited onto a substrate. In this specific application, it has chosen reaction parameters to produce translucent CNT film. Which essentially consists in dilute reaction conditions which therefore produce a low-density aerogel[231].

The big challenge is control the film characteristics in terms of type of the CNT, orientation, thickness and being homogeneous over large areas. It is reported CNT films by filtration of isolated CNTs[232] or directly dropped from vertical array[233], creating aligned buckypapers and over a specific substrate[234].

Figure 6.25 shows a schematic of the aerogel formation and optical micrographs of it at the top and bottom regions of the CVD reactor tube. As a consequence of catalyst particle dynamics and thermophoresis effects [235][236], the CNTs are concentrated in a thin annular region in the reactor tube (figure 6.25.a). This hollow structure is typical of the direct spinning process, and often referred to as a “sock”[84] [83] as it is mentioned in chapter 4. The frictional forces that arise from dragging it against the gas reduce the aerogel diameter, producing an inverse hollow cone (figure 6.25.b).

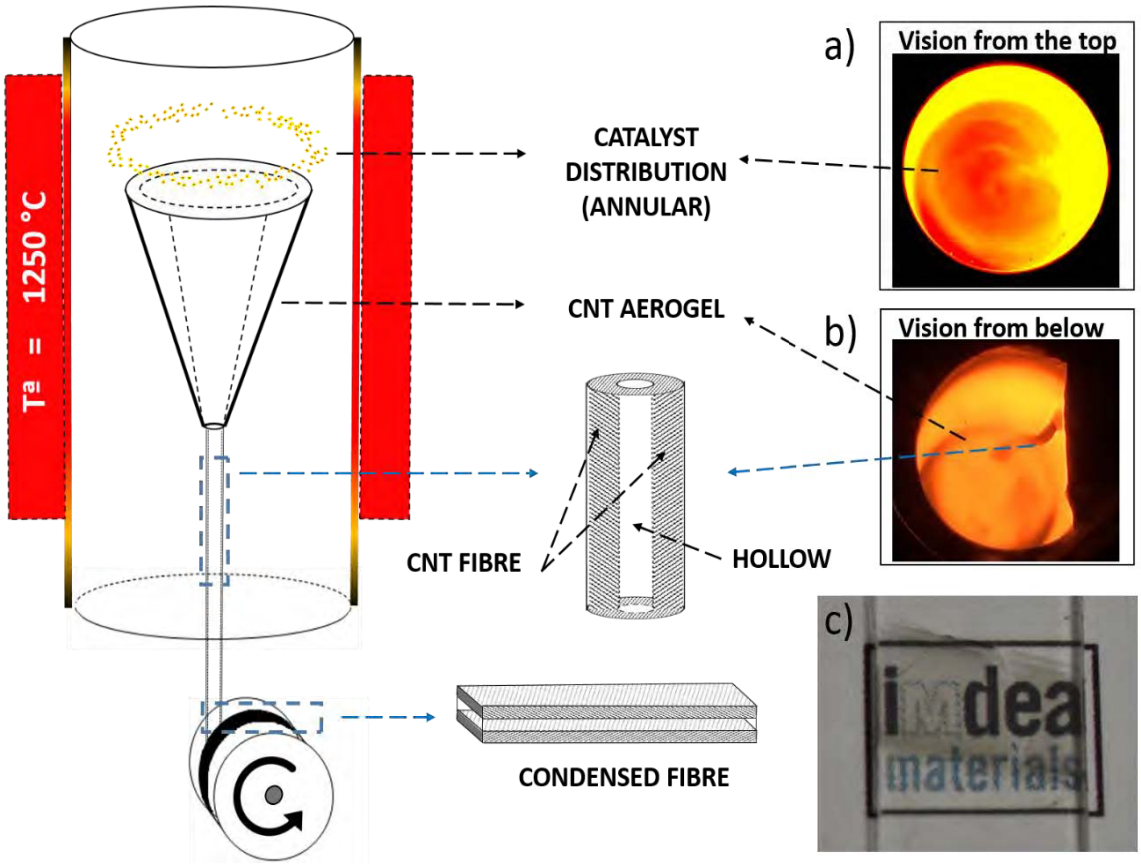

Figure 6.25. Schematic representation of the direct CNT fibre process showing the aerogel formation and the shape of the fibre as-spun and after densification. Inset optical images show (a) CNTs distributed in the annular region and (b) producing an inverse hollow cone architecture. (c) Photograph of a CNT monolayer film supported in quartz, showing its transparency.

At the end of the reactor, the material consists of a diaphanous cylindrical veil composed of a network of CNTs. As this material is deposited onto a substrate it flattens and forms a thin film, which under appropriate synthesis conditions can be transparent and conductive (Figure 6.25.c). Films of different thickness can be produced by overlapping more layers of aerogel material. Evidently, depositing additional layers reduces both transparency and sheet conductance[237].

Interestingly, when deposited onto a reflective surface the dense CNT fibre film shows the development of colour. The optical micrograph in figure 6.26.a shows and example of a sample of CNTs on aluminium with marked blue, green, yellow and reddish colour fringes. A film consisting of an individual CNT fibre layer has a thickness around 40nm, depending on synthesis and drawing conditions. Hence, samples with a few layers (<20) have a thickness in the visible range, as shown in the example in figure 6.26.b, and this, it can lead to thin-film optical interface in reflection mode. It is worth mentioning that colour in these films develop only after CNT films have been densified through capillary forces upon contact with a volatile liquid. This confirms that colour has a structural origin, as in a photonic crystal.

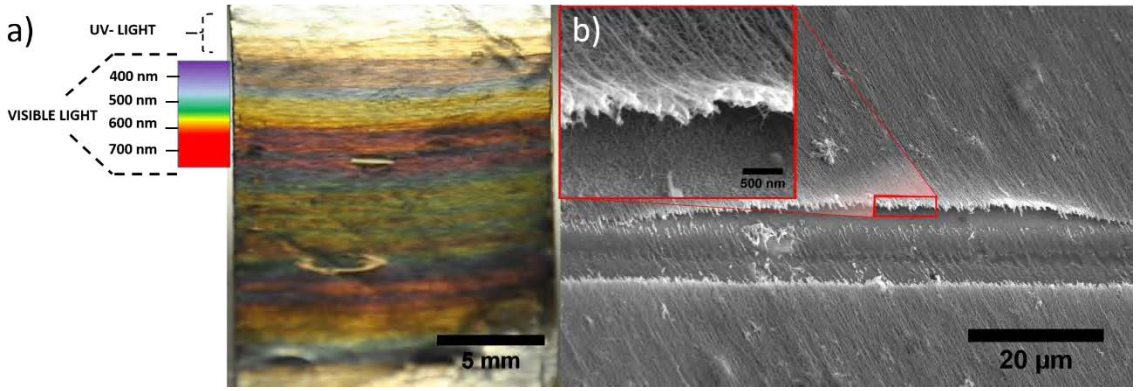

Figure 6.26. (a) Camera picture of CNT film showing the effect of increasing thickness of the film. Different colours appear in the sample related to the film reflection from 350 to 800nm. (b) SEM micrographs of the analysed surface, in the inset it shows a higher magnification and reported a film made it by tens of CNT layers.

The different colours are visible only when the photonic crystal structure is around 150nm (violet) until 400nm (nm). Which corresponds with the half the wavelength from colours observed in the sample. Below, the thickness are in the UV range and upper in the IR range. Therefore, it is possible to control the thickness of CNT

film by evaluating the colour through a simple UV-Vis spectroscopy measurements.

The correlation between observed colour and sample thickness is presented in Figure 6.27. Here, thickness was determined by atomic force macroscopy on samples that were previously milled with a focused ion beam SEM so as to produce cross sections with minimum damage.

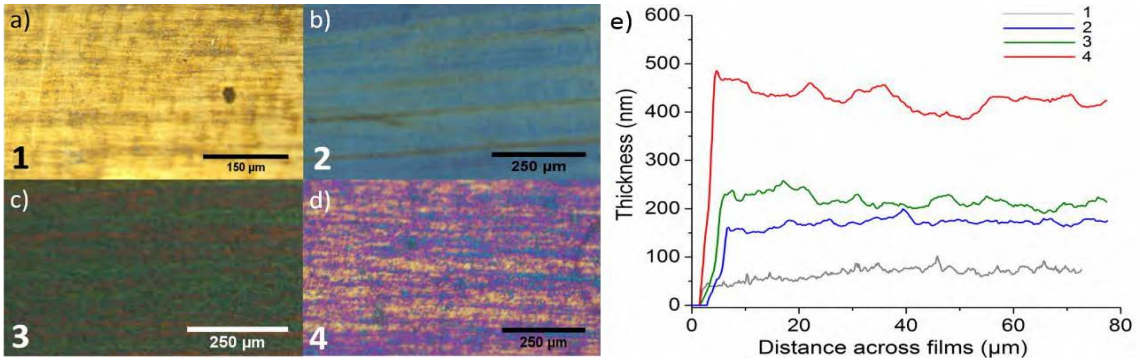

Figure 6.27. Correlation between observed sample colour and CNT fibre film thickness. Optical micrographs showing different colours: (a) Brown-colour, (b) blue, (c) green, (d) reddish. (e) CNT fibre thickness in different regions related with brown-no colour, blue, green and red colour respectively, measured by AFM microscope. Analysing the thickness is λ/2 compare to the colour wavelength.

CNT film creates a 2D structure through the repetition of layers with different refractive index (n_a and n_b) and thickness (d_a and d_b). The film produce an interference of light reflected from the different layers of dielectric stack. Figure 6.28 represents a diagram of single layer CNT film, forming a dielectric mirror. *Layer a* is made of CNTs structure and *layer b* is air.

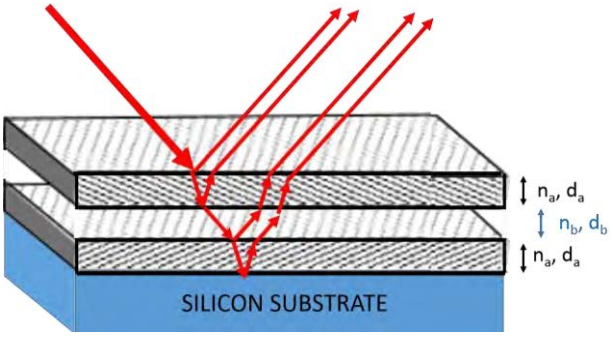

Figure 6.28. Diagram of a dielectric mirror, forming by three thin film, two are made with CNTs and the other is air. Red lines show the path length, the different distance leads to interferences.

The sequence of stacking layers and the intrinsic structure of the CNT fibre extracted from the furnace behaves as a dielectric mirror. Dielectric mirror is

composed of multiple thin layers of dielectric material. Controlling the type and the thickness of the dielectric layers, it is possible to design optical structures with different reflectivity by varying the wavelength.

The optical properties of thin films of CNTs fibre were studied by ellipsometry measurements in collaboration with C. Pecharroman from ICMM-CSIC.

Dielectric mirror has values close to 100% in reflectance over a narrow range of wavelength. The effect of increasing the number of layers in a dielectric mirror in presented in figure 6.29. In this particular example the reflection has the maximum at 1000nm. The wave frequency in the annex peaks depend on the number of layers. On the edges of the maximum, secondary waves are observed. Increasing the number of layers leads to more frequency on the waves. Increasing the number of layers leads to decrease the maximum of absorbance in the sample.

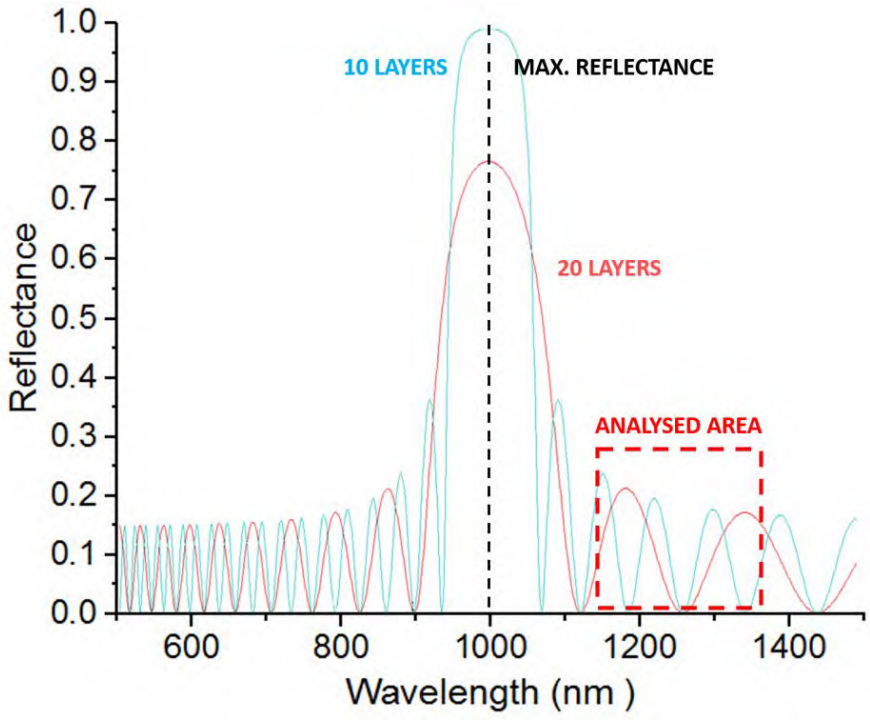

Figure 6.29. Typical reflectance of a dielectric mirror when the maximum reflectance is localised in 1000nm. Dash red line limited the analysed area observed in the CNT films.

In our particular case, single CNT layer is around 40nm thick. Therefore, the optical path is notable thinner compare to the visible wavelength (one order of magnitude). The maximum reflectance is shifted around 80nm. In visible range the curves correspond with secondary waves.

In the initial oscillations, the phase is drawn by the following equation:

$$\varphi = \frac{2\pi}{\lambda} N\,(n_a\, d_a cos\theta_a + n_b\, d_b\, cos\theta_b) \quad Equation\,(6.9)$$

From the equation, it is possible to extract that the reflectance scale with 1/N (nº of layers).Therefore, to compare the frequency the wavelength is normalised by the number of the layers.

Figure 6.30.a shows the secondary waves for different number of CNT layers; 7-10-12 and 20. The minimum is proportional to the number of layers and centred in 0.05nm^{-1}. These minimums correspond with the parallel polarisation at this wavelength, which is also in agreement with the maximum in perpendicular direction. The Dash red lined empathised the region observed in the CNT films.

Finally, theoretical simulations are performed, assuming n_a=2, n_b=1 and layer thickness = 18 nm (double layer is 36nm) at reflectance angle 75º , in order to compare with the experimental results.

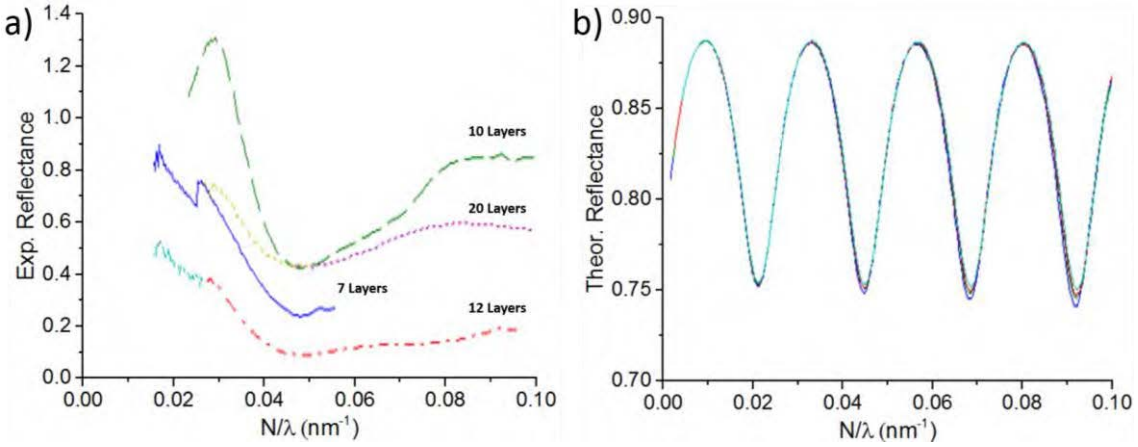

Figure 6.30. (a) Reflectance intensity related with the samples produced. Inverse of the wavelength is normalised though number of layers.

Introducing the number of layer produced 7-10-12 and 20, the minimums and the maximums are proportional to the number of periods (figure 6.30.b). Consequently, duplicating the number of layers, the minimum and maximum shift to the double of the wavelength.

6.6. Summary

CNT fibre is composed of a millions of individual CNT, which are considered as a nanostructure building blocks, forming a hierarchical structure. Fibre structure is studied from two different points of view, analysing structure as isotropic by gas

adsorption and considered as anisotropic, using SAXS/WAXS measurements to extract the structural information.

Isotropic properties of CNT fibre are analysed by gas adsorption method. The surface area is ≈ 260m^2/g for samples with different draw ratios, ranging from 0.47 (1.5m/min) to 12.6 (40m/min). The pore size distribution is determined by BJH analysis of N_2 desorption isotherm data. Meso-scale distribution of porous size is independent of the draw ratio. However, increasing the draw ratio leads to narrower pore size distribution, centred between 50 and 60nm, compared with low draw ratio in which are more spread. CNT fibre is a fractal structure and it is possible to obtain fractal dimension from gas adsorption ≈ 2.55, which is nearly identical to the SAXS values.

Anisotropic properties of CNT fibre are analysed by SAXS/WAXS, confirmed by electron microscopy. SAXS/WAXS measurements cover a wide range of distance from few angstrom to tens of nanometres. Integrating the patterns in the azimuthal direction, it is possible to obtain the degree of orientation. The orientation increase very sharply in the range from 0.47 to 3 from 50 to 24 in SAXS integration and from 35 to 17 in WAXS integration. In spite of the bundle orientation is not modified from 6 to 12.6, the CNT fibre increases the mechanical properties. Radial integration of 002 leads to confirm better packing in the bundle, however crystal size remain constant. SAXS parameters L_3 and L_p confirm that changing bundle orientation in the CNT fibre affects directly to the pores structure. Due to the orientation, inter-bundle pores have more elongated structure along the fibre axis.

Post-spin densification was evaluated through 2D WAXS/SAXS measurements. Acetone was used as a solvent due to high volatilization. Capillarity forces are responsible to densify the CNT fibre, decreasing the diameter one order of magnitude. However, this effect is not modified the fibre structure in the nanoscale, links of CNTs or packing of bundles. Consequently, the electrical and mechanical properties are not affected or the change is negligible compared with the orientation. This fact conclude that the CNT assembly occurs during the reaction in the gas phase. The real challenge is control the synthesis parameters in the reactor, which allows to modify the CNT association in the aerogel without sacrificing control of chemistry and morphology. Through decomposition

temperature is possible to affect the sequence of elements (Fe-S-C) and the kinetic, modifying the catalyst and therefore the CNT links. Otherwise it will require innovative manipulation methods that can act on the aerogel as it is reaction over 1200ºC in a fraction of seconds.

Finally, CNT films stacked create a 2D structure through the repetition of layers with different refractive index (n_a and n_b) and thickness (d_a and d_b). Though the ellipsometry, it is possible to confirm that CNT films behave as a dielectric mirror. Tuning the colour of the film is possible, weather the thickness is around 150nm the film is violet and at 400nm is red. Which corresponds with the half the wavelength from colours observed in the sample. Below, the thickness are in the UV range and upper in the IR range.

7 CNT fibre industrial aspects

7.1. Introduction

Direct spinning from CVD reaction is one of the most promising process for a large-scale production of CNT materials. Namely, it is possible to produce a large amount of material continuously in different architectures. Along this work, it was shown important progress in controlling the nanostructure and the microstructure of the fibre, controlling the CNT type in macroscopic fibre as well as improving the alignment of the bundles throw the fibre. These improvements lead to obtain high performance carbon nanotube fibres. However, the mass production is relatively low, between 1 to 3 CNT mg/min. Therefore, it is necessary a scalability study in order to transfer all the knowledge from the laboratory to the industry. CNT characterisation is performed at different feedstock to scale-up the process, analysing important parameters as reproducibility, indispensable for industrial production.

The production of CNT fibre using a cradle to gate life cycle assessment (LCA) is examined. The LCA study has been carried out considering two type of reactors: a semi-industrial (lab-scale) and industrial, comparing two different carbon sources, butanol and toluene. This method combines technical, economic and environmental criteria covering the life cycle of a CNT fibre production in order to assess the substitution potential of CNT fibre for different application compare with the traditional materials or other carbon materials.

Finally, CNT fibres have already a broad variety of application. The multifunctional nanocomposites group investigates tailoring the structure of these hierarchical materials through combination with polymers, hybridisation with semiconductors and fine control of the building blocks at a molecular scale. CNT fibre can be an electrode in a supercapacitor or other energy storage devices. Moreover, it can be used as a sensor to control the polymer infusion or monitor the stress of a structural piece, creating heterojunction in combination with semiconductors or composites with polymers. Several devices and applications manufactured by our CNT fibre, it is presented in this chapter.

7.2. Scalability

In order to progress from the lab scale samples to the commercial devices. It is necessary to increase the CNT production from mg/min to g/min. As it is discussed along this work, it is possible to tune the CNT fibre from single wall to multiwall and also modify the aerogel, producing stretchable fibre with CNT oriented along the fibre axis. Therefore, it is necessary to evaluate whether these parameters can be scaled-up, remaining constant the quality of the sample.

According to the geometry of the reactor, the synthesis of CNT fibre is performed at two different flow rates 2ml/h and 5ml/h. In order to evaluate the scalability of the process the injected solution remains constant; butanol 97.7%, ferrocene 0.8% and thiophene 1.5%.

Briefly, it is worth mentioning the concept of stretchable fibre and non-s stretchable. As it is discussed in chapter 5, the aerogel can be modifying in order to allow to stretch the aerogel and oriented the CNT fibre. This effect is also observable directly in the fibre appearance. Figure 7.1.a shows a single filament from CNT fibre non-stretchable, the high density of CNT provide to the fibre black colour and higher linear density. In figure 7.1.b is observed a stretchable fibre, more homogeneous and transparency in its appearance.

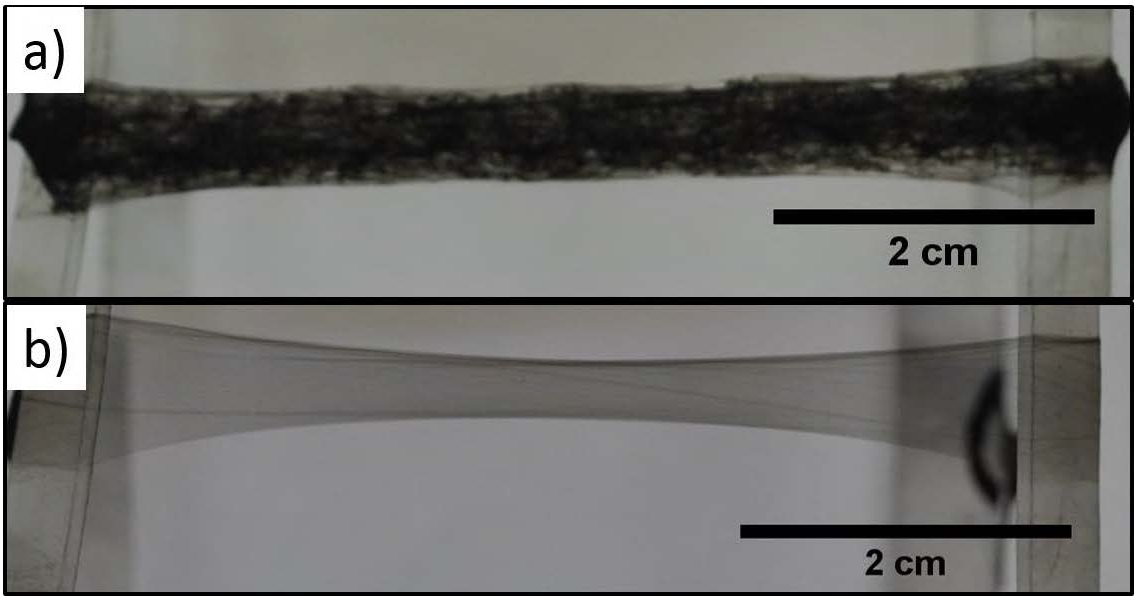

Figure 7.1. Optical micrographs show the appearance from (a) non-stretchable and (b) stretchable fibre.

The transition between two fibre configurations occurs in a short range. Furthermore, the fibre has to be homogeneous in order to increase the spinning speed. This inflexion point could be defined as straightness point.

Tuning hydrogen, it is possible to define another important points: lower spin limit and high spin limit. Outside of this range, it is not able to spin continuously.

Firstly, the fibre is evaluated at injection feed rate of 2ml/h. The hydrogen flow rate is varied every 0.2l/min, from 0.6 until 1.8l/min. The ratio of the reactant in the reaction area changes, when hydrogen flow is modified.

Figure 7.2.a shows the element ratio in all the scenarios. Straightness point is situated at 1.4 l/min. Furthermore the lower and high spin limit is evidenced at 0.8 and 1.8 l/min respectively. To distinguish oxygen, iron and sulphur ratio the plot is zoom in figure 7.2.b.

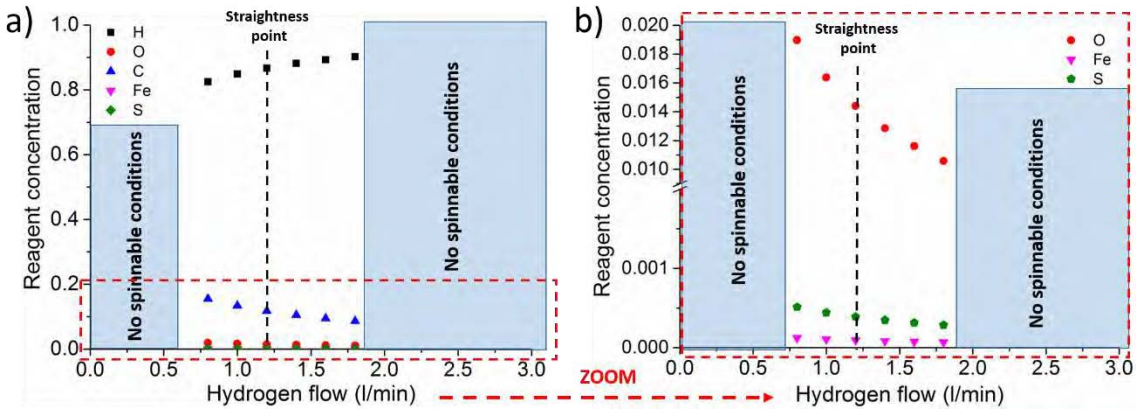

Figure 7.2. (a) Element ratio presents in the reaction area, defining the lower and high spin limit at 2ml/h. (b) Zoom mode from the oxygen, iron and sulphur ratio.

The fibre characterisation is very well-known at conventional hydrogen flows, explained in previous chapters. Therefore, the extremes (samples at lowest and highest hydrogen) are analysed in detail and discussed to clarify why it is not possible to spin beyond the limits.

Figure 7.3.a-d shows raman spectra and TEM images from fibre that was spun at 0.8 and 1.8, respectively. The graphitisation of CNTs is optimal in both cases as well as its homogeneity along the sample. At higher hydrogen in the upper limit, CNT concentration in the reaction area is not enough to spin a continuous fibre after 1.8l/min. At low hydrogen, the problem could be related to the saturation of catalyst particles with carbon. Thus, reducing the hydrogen flow

leads to higher carbon concentration. Implying that less number of catalyst are active and therefore low amount of CNT are synthesised. TEM micrograph reported an increment in the ratio between the inactive particles and the long CNT at low hydrogen.

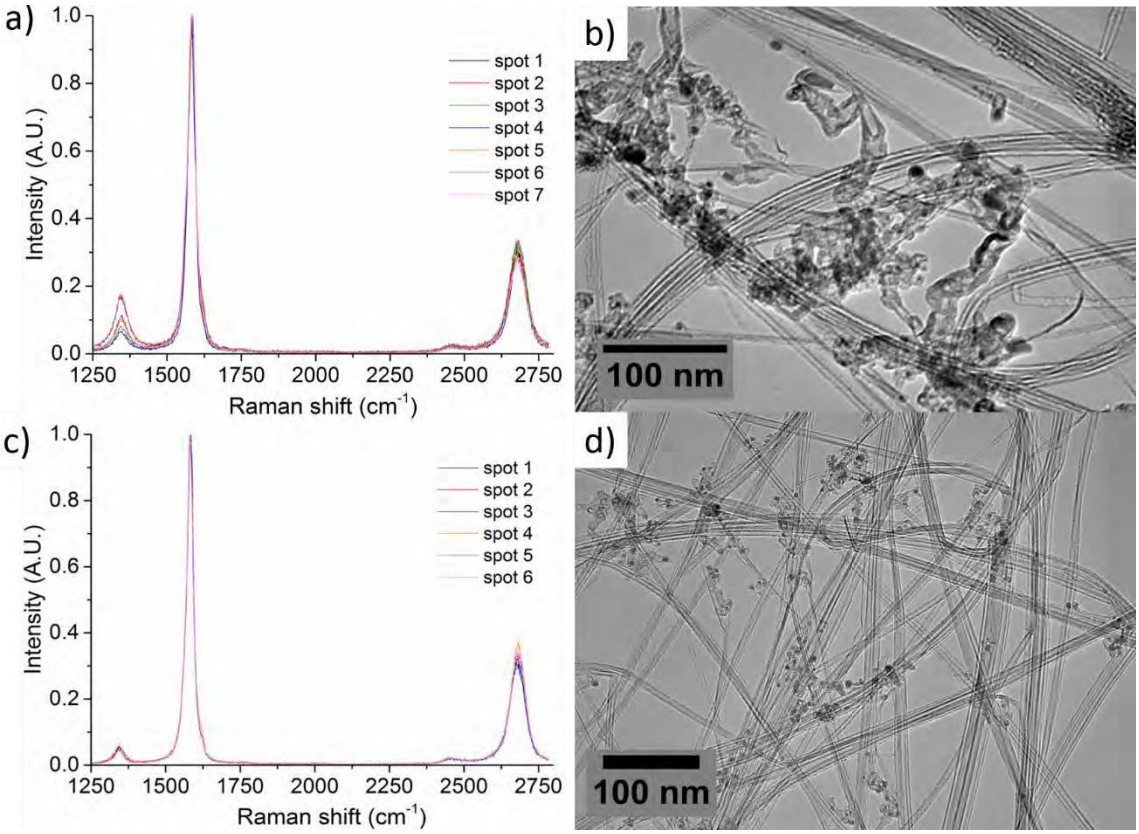

Figure 7.3. (a) Normalised Raman spectroscopy data spun (a) 0.8 and (c) 1.8l/min. Results are confirmed by TEM electron micrographs at 2ml/h.

To scale-up the process the precursor feed rate was incremented in 2.5 times, injecting 5ml/h. The procedure used were identical to compare key parameter of the reaction at high feed rate.

At feed rate 5ml/h, it was possible to synthesised continuous fibre from 0.6 until 2.8l/min. This increment in the range was expected, because the concentration of CNTs in the reaction area are higher and it is necessary further dilution to find the reaction limits.

Figure 7.4.a shows the element ratios present in the reaction area, against the hydrogen flow rate. Straightness point appear at 2.6 l/min. In order to distinguish oxygen, iron and sulphur ratios, the plot is also zoom in figure 7.4.b.

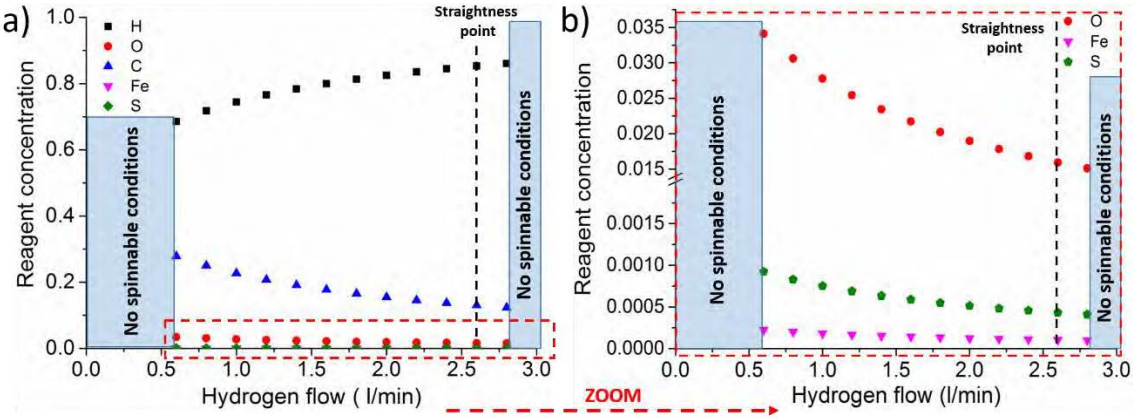

Figure 7.4. (a) Element ratios present in the reaction area, defining the lower and high spin limit at 5ml/h. (b) Zoom mode from the oxygen, iron and sulphur ratios.

Analysing the sample at highest hydrogen, the results are analogous than at 2ml/h. The limiting factor to spin continuously at is the extremely dilution of CNTs in the reaction area caused by the hydrogen. The quality and homogeneity of CNTs present in this sample pretty good

Analysing the characterisation obtained from the sample synthesised at 0.6l/min confirms the previous explanation. Catalyst particles are saturated with carbon at low hydrogen rates. As it is shown in the figure 7.5a-b, the sample is poorly graphitised, the intensity of raman spectra are very low and the peaks very broad.

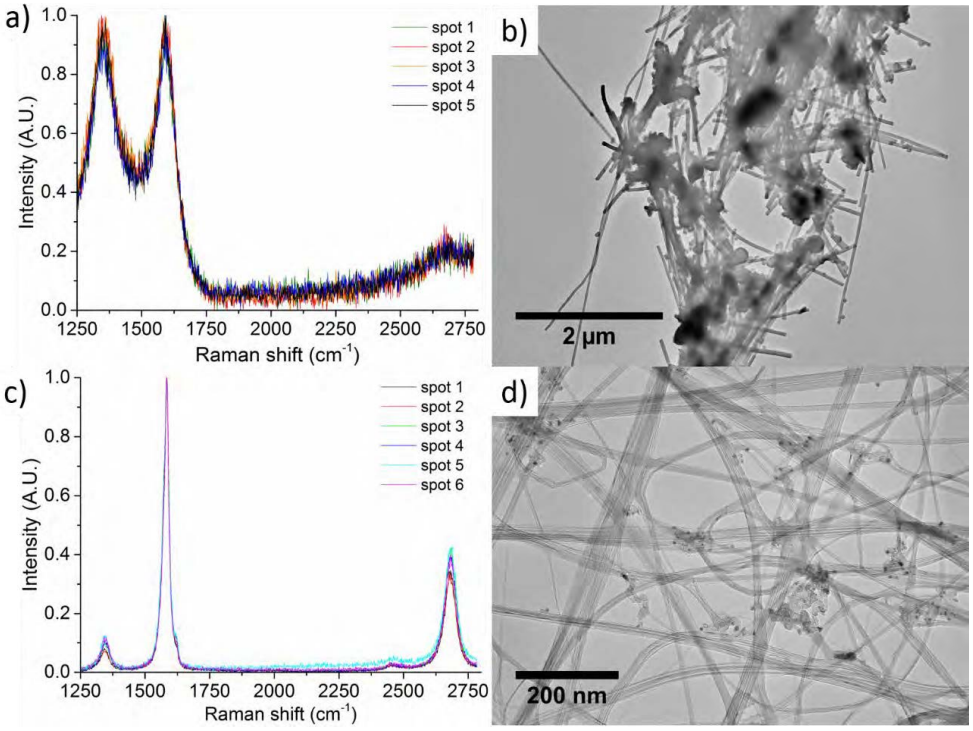

Figure 7.5. (a) Normalised Raman spectroscopy and TEM micrographs from samples synthesised at 0.6 (a) and 2.8l/min, at 5ml/h.

Finally, figure 7.6 shows a summary, comparing different precursor feed rate (2 and 5ml/h). It is shown the range in which CNT fibre is stretchable and non-stretchable, emphasising in the straightness points. The different ratio of elements are also compared. The values in the straightness point are similar in both cases. Therefore, it is possible to conclude that ratio of elements are critical in order to stretch the fibre and also is scalable.

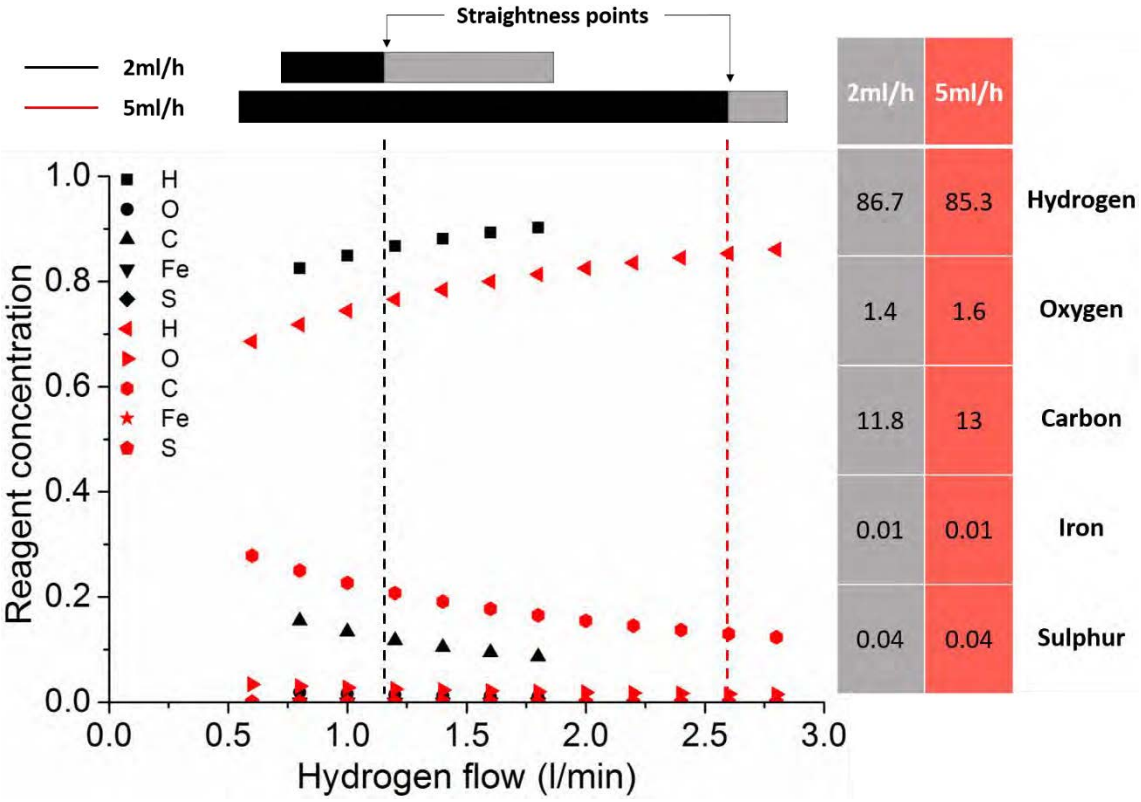

Figure 7.6. Comparison of Element ratio at different precursor feed rate (2 and 5 ml/h) presents in the reaction area. Stretchable and non-stretchable fibre are remark in grey and black colour, respectively.

7.3. Reproducibility

Along the work presented in this manuscript. It was synthesised different fibre under different conditions. This variety allows to use the best fibre per application.

In order to studied the properties of a specific fibre and its implementation in macroscopic device. The most important characteristic is its reproducibility.

To study the fibre reproducibility, the reaction was maintained constant and stable for hours. Figure 7.7.a shows a photograph of a common bobbin with around 1Km of CNT sample material. For each sample it was taken Raman spectra on

different segments of fibre extracted randomly from a bobbin with at least 50m of CNT fibre length. The Raman spectra is shown in figure 7.7.b.Every point include at least 5 measures.

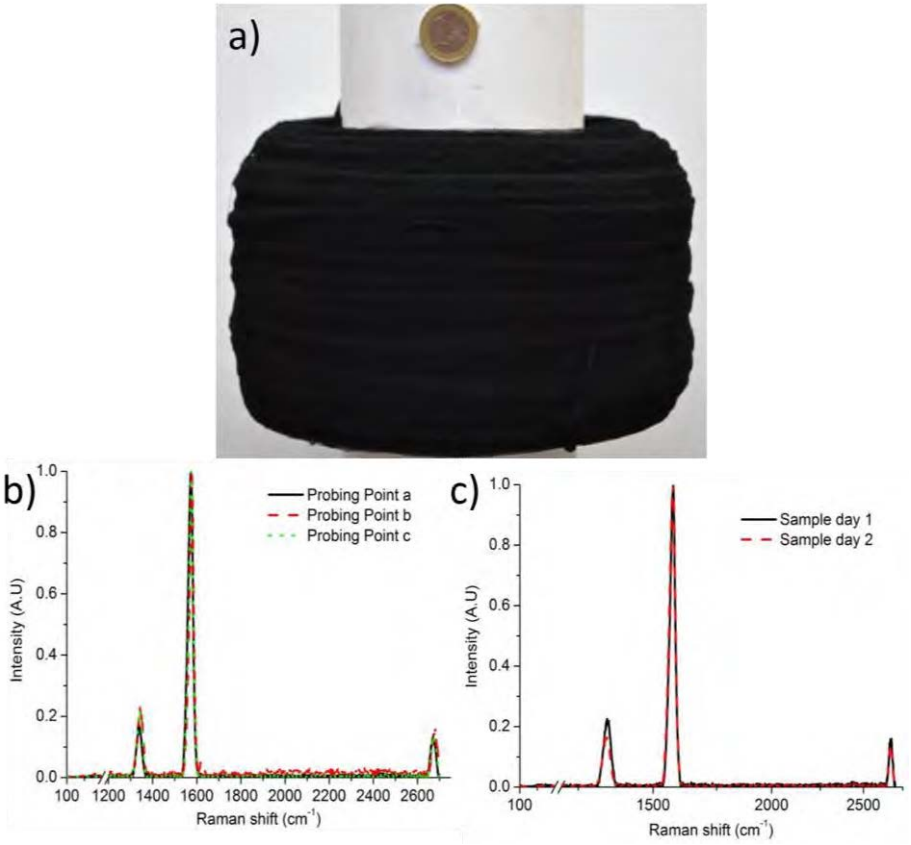

Figure 7.7. (a) Photograph of a bobbin with approximately one kilometre of CNT fibre produced over a couple of hours of continuous spinning. (b) Normalized Raman spectra measured on 3 different spots along the sample of > 150m. (c) Normalized Raman spectra of fibre (1.5 wt% of thiophene) produced on different days.

Furthermore, it was characterised fibre samples produced in different days. The whole thiophene series was synthesised several times, repeating the conditions in the furnace and obtaining the same tendency analysing raman data. Figure 7.7.c do not show significant differences are observed in the spinning process or the fibre produced when reproducing the synthesis conditions.

During the scale-up process, the CNT fibres are measured at different precursors feed rates. Figure 7.8.a-b show 5 raman spectra from different regions in the sample CNT fibre, produced at 5ml/h, 2ml/h. The measurements in the same fibre are identical and comparing the volume injection, the differences are negligible. The measurement are performed in samples bigger than 150m length.

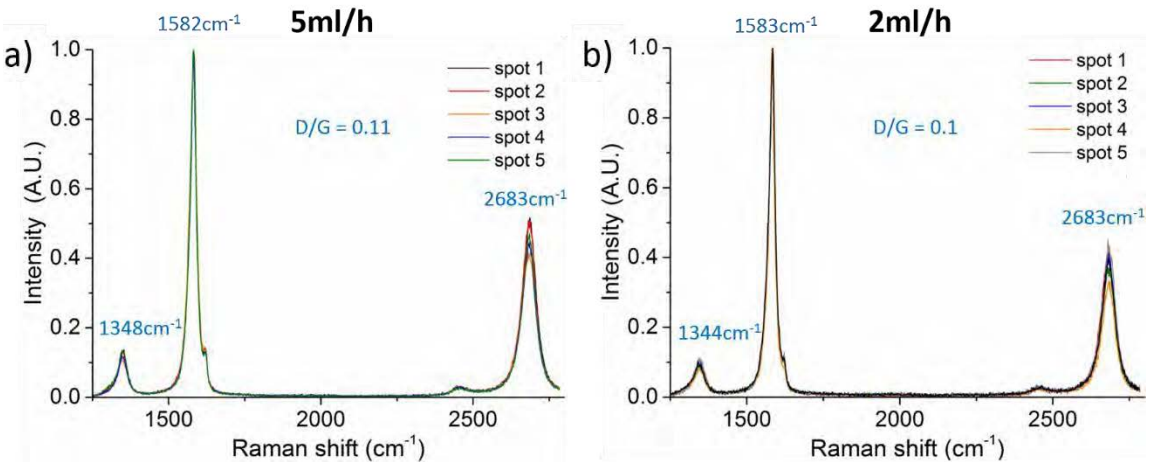

Figure 7.8. Normalized Raman spectra of fibre at (a) 5ml/h and (b) 2ml/h (1.5 wt% of thiophene) measure on different regions spots along the sample of > 150m.

Therefore, it is demonstrated that the CNT fibre produced along this work, it is reproduced, allowing to be used in different new applications in which the CNT fibre are considered as constant parameter, evaluating other components or properties intrinsically related with the specific device.

7.4. Sustainability (Life cycle assessment)

CNT fibre are promising structure which have already a broad variety of application. In this section, the production of CNT fibre by direct spinning for gas phase using a cradle to gate life cycle assessment is examined. The Life-Cycle Assessment (LCA) study has been carried out considering two different configuration: a semi-industrial and industrial. Furthermore, butanol and toluene are examined as a promising carbon sources. The LCA study is carried out by using primary data based on the experimental performance of the CNT production. LCA is a standardised (ISO 14040/44) and established for the assessment of the sustainability. Relevant inputs are compiled, evaluating the potential environmental risks, collected in 17 categories (outputs). Figure 7.9 represents a scheme of LCA, summarising the representative inputs and outputs.

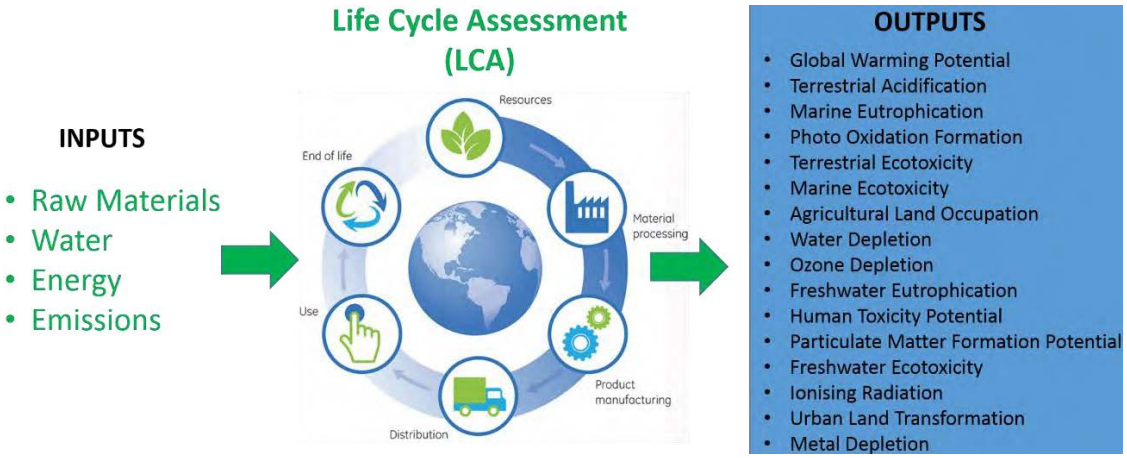

Figure 7.9. Schematic representation of a LCA process[238].

LCA is a comprehensive framework for quantifying ecological and health impact of a product or system over its complete life cycle. Nowadays, it is starting the LCA studies on nanomaterials, mainly due to the previous lack of information related to the inventory data. Despite the uncertainty derived from the assessment of this new type of material, there is a necessity to establish their sustainability. Consequently, the study cannot be as exhaustive compare with other materials, although the study provide a first baseline evaluation for emerging material and technology.

7.4.1. Description of the process

One of the main advantages of the production route by direct spinning from CVD reaction, for producing large-scale CNT fibres, it is the possibility to synthesis in one step. Nevertheless, it is possible to divide the process in 6 different stages as summarised figure 7.10.

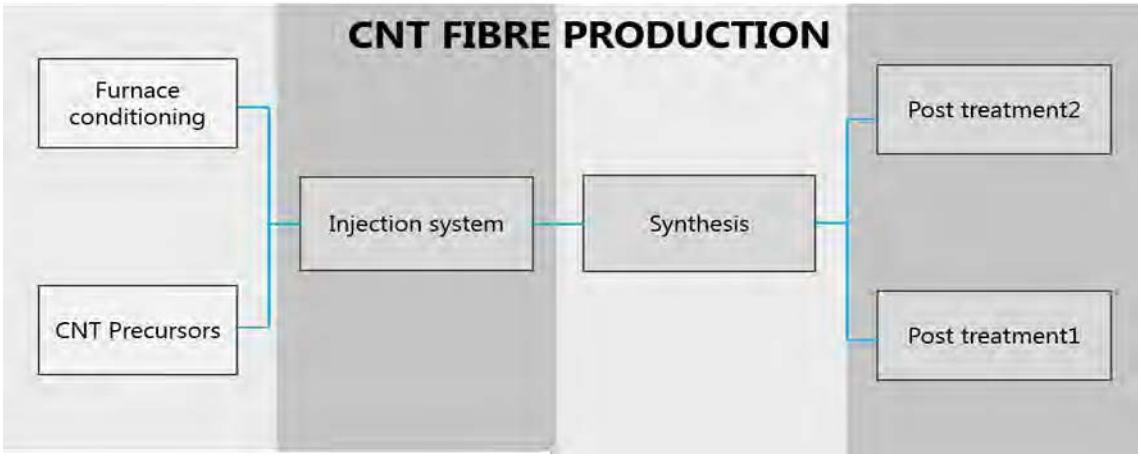

Figure 7.10. Schematic diagram shows the different stages in which the production route can be divided.

The study is focused on two mainly configurations semi-industrial scale and industrial scale (figure 7.11). Furthermore the fibre is synthesised by two carbon sources butanol and toluene and different feed rates 50 -250 -1000 ml/h.

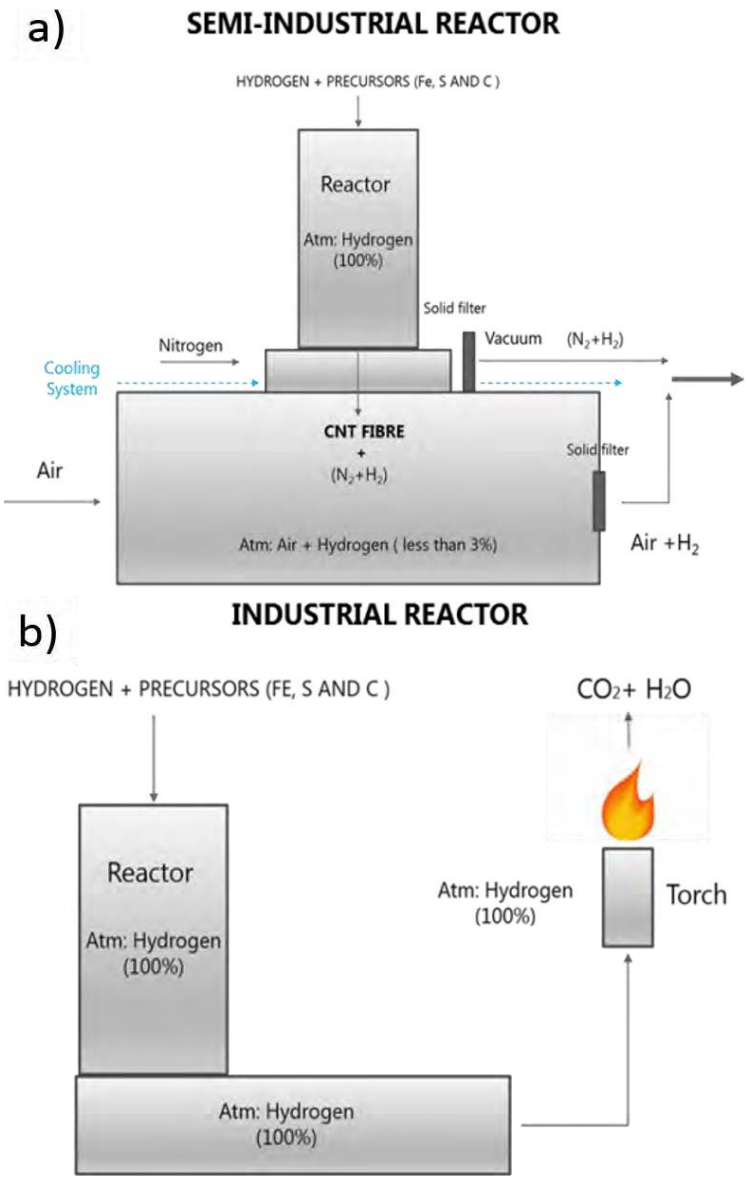

Figure 7.11. Schematic diagram shows the different configuration (a) semi-industrial and (b) industrial.

7.4.2. Environmental performance of CNT fibre production

The aim of this LCA is to assess the environmental performance of the manufacturing of CNT fibre from direct spinning method. In order to calculate all the parameters, it is necessary to introduce the inputs of the process as the source materials and energy consume and its outputs as residues. The LCA was obtained in collaboration to ALCA group in EMPA Institute (Swiss Federal

laboratories for materials science and technology). The inventory data were modelled in SimaPro 8.1, software (PRè Sustainability) and Ecoinvent data 3.1 is used as inventory database.

As functional unit and reference flow “1 kg produced CNT fibre” is used for all the LCA calculation. Impacts are determined dividing in 17, related to the emissions released and the resources consumed during the synthesis process. In details, the following midpoint indicators have been examined here:

Global Warming Potential (GWP)	Ozone Depletion (OD)
Terrestrial Acidification (TA)	Freshwater Eutrophication(FE)
Marine Eutrophication (ME)	Human Toxicity Potential (HT)
Photo Oxidation Formation (POF)	Particulate Matter Formation Potential (PMF)
Terrestrial Ecotoxicity (TE)	Freshwater Ecotoxicity (FE)
Marine Ecotoxicity (ME)	Ionising Radiation, (IR)
Agricultural Land Occupation (ALO)	Urban Land Transformation (ULT)
Water Depletion (WD)	Metal Depletion (MDP)
Fossil Depletion (FD)	

Semi-Industrial Reactor

Firstly, semi-industrial configuration is analysed individually. This reactor was built in IMDEA Materials by the functional nanocomposite group. Figure 7.12 shows the relative contribution from the different stages for the configuration with butanol and feed ratio of 50 ml/h.

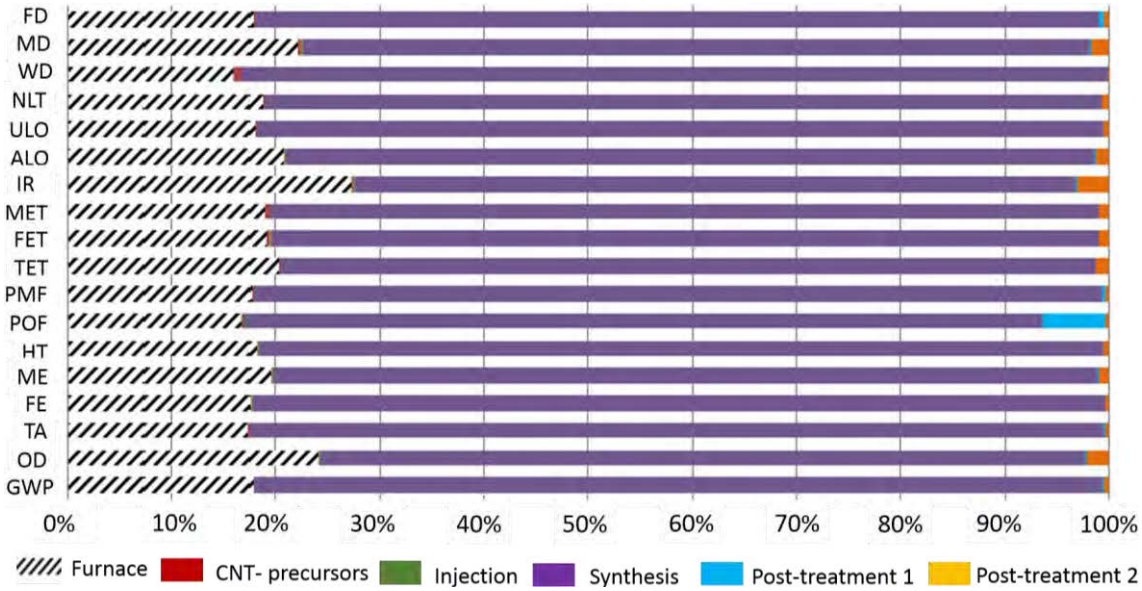

Figure 7.12. Environmental performance of CNT fibre production with butanol with 50ml/h as a feed ratio

In overall environmental impacts, synthesis represents a large part of the impacts. To obtain more information related to this stage, the impact assessment is divided into different categories: Precursor steps, energy, water consumption, chemicals inputs and directs impacts (figure 7.13). Results shows as chemical inputs are the main driver of the environmental performance assesses for the synthesis step. Nitrogen flow is the main contributor around 75% of the environmental impact.

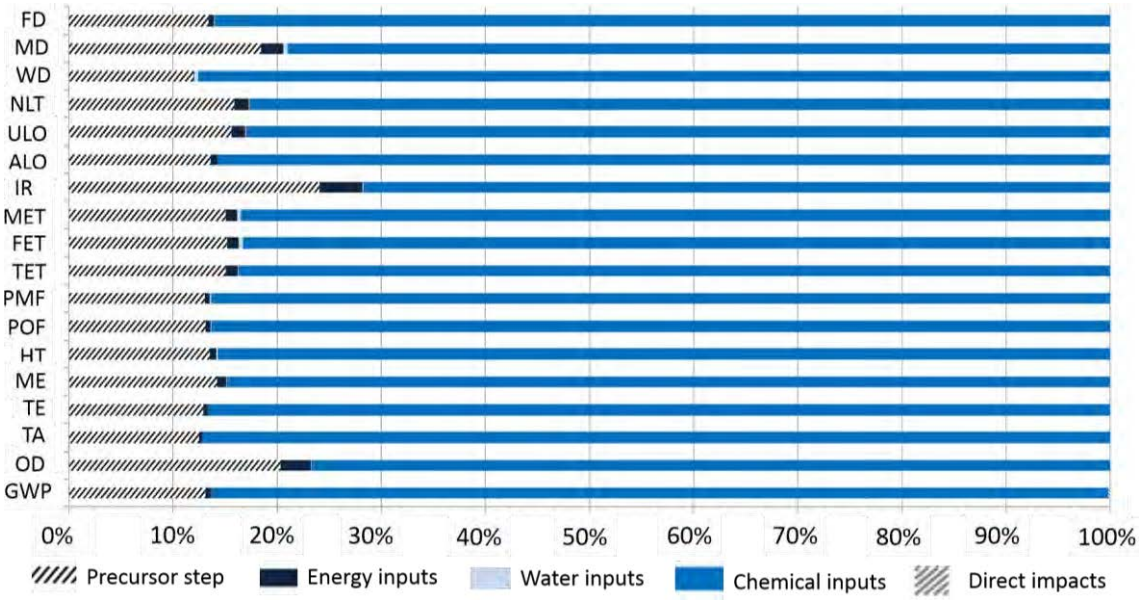

Figure 7.13. Environmental impacts of the synthesis step at 50ml/h.

The same distribution is observed increasing the precursor feed rate from 50ml/h to 1000ml/h. However, the overall impact decreases, increasing the precursor feed rate from 50 to 250ml/h (figure 7.14). These results are not surprising, increases mass production leads to more efficient process. The relative impact of the scenario at feed at 50 ml/h contributes as 50%; whereas the scenario at 250 ml/h and 1000 ml/h contributes to 25% each.

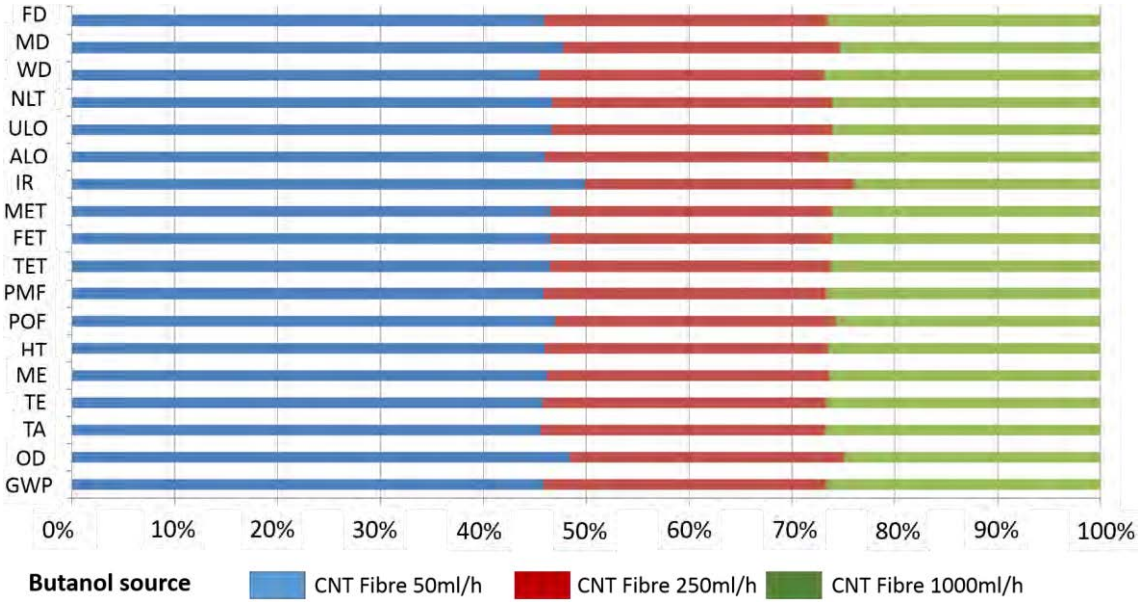

Figure 7.14. Comparison of the environmental impact increasing from 50 to 1000ml/h.

Butanol is analysed more in detail because is the main carbon precursor used during this work. Although, toluene is starting as a carbon source. Toluene as butanol releveled a similar trends when the precursor feed rate increases. However, the conversion is higher under the same reaction parameters. Consequently, it leads to better environmental performance, the reduction is 50% approximately as it is shown in the figure 7.15.

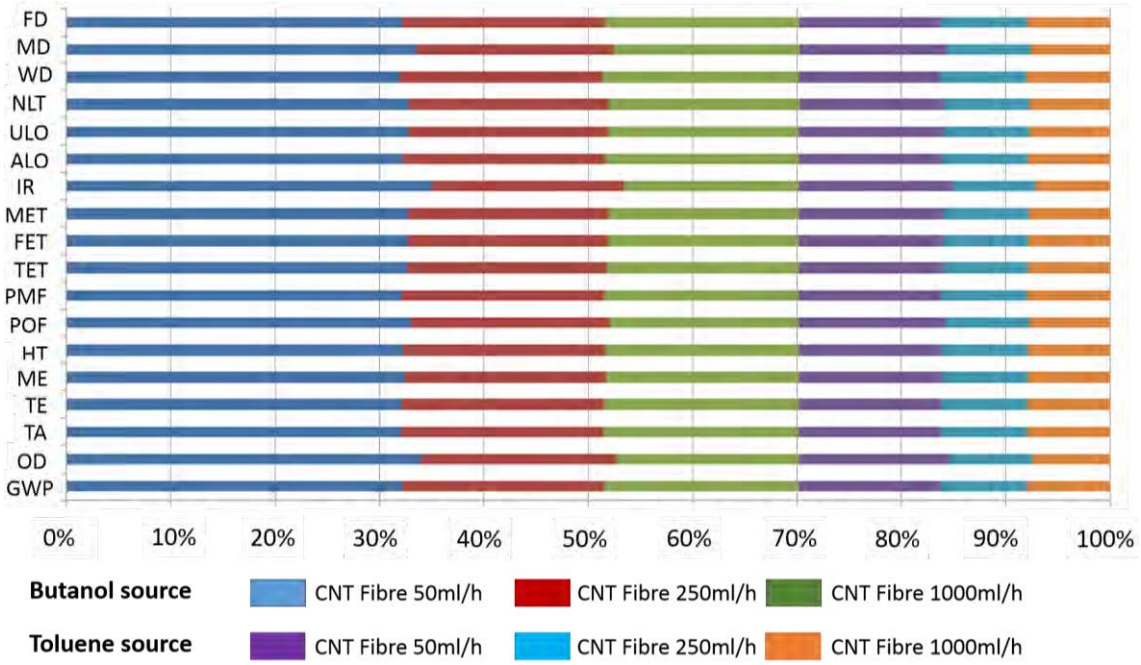

Figure 7.15. Environmental impact comparing different scenario with butanol and toluene as a carbon source and increasing the precursor feed rate from 50ml/h to 1000ml/h.

***Industrial Reactor**:*

One step process is one of the main advantages of this process. Therefore, three companies decided to scale up to industrial factory. *Tortech Nano fibers* in Israel, *Nanocomp Technologies* in United States and *INFRA technology* in Russia are the pioneers in scaling up the process.

The industrial configuration has been simplified (figure7.11.b). The atmosphere is kept in hydrogen along the process, avoiding changing the atmosphere after the synthesis step. Therefore, nitrogen inlet and vacuum stream are not necessary, removing the main contributor of the environmental impact in the semi-industrial process. Fibre is synthesised in the reactor and spun in electrical winders. Hydrogen stream is collected through the system and it is burned in a torch producing the following reaction:

$$2H_2 + O_2 \rightarrow 2H_2O\ (vapour)$$

$$C\ (s) + O_2\ (g) \rightarrow CO_2\ (gas)$$

Investment is higher in the industrial configuration. However, the cost per Kg of CNT is reduced significantly. The environmental impact is analysed for toluene

and butanol as a carbon source. The figure 7.16 shows results obtained for toluene as a carbon source.

In contrast with semi-industrial configuration, the main environmental impact is produced in the furnace conditioning, followed by the step of precursors, synthesis and finally post-treatment 2. All the impact categories follows the same tendency with the exception of POF category, which is dominated by post treatments, up to 55%, governed by the use of acetone.

Furnace conditioning is mainly responsible due to the use of nitrogen and the electrical consumption.

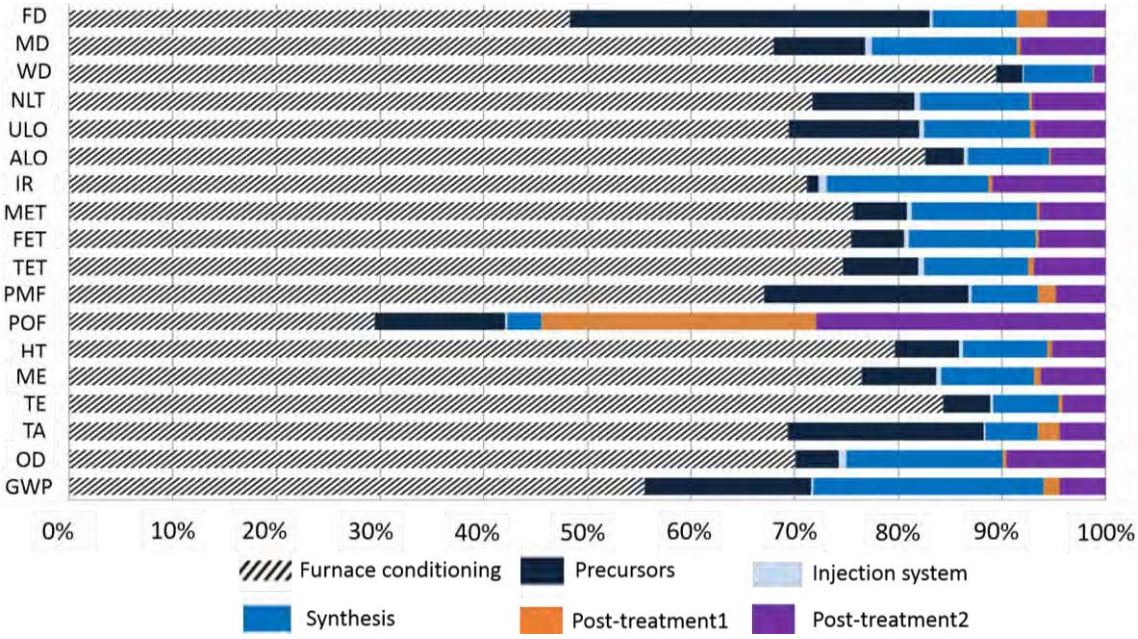

Figure 7.16. Environmental impact of CNT fibre production with a toluene as a carbon source at industrial configuration.

The step of furnace conditioning is highly energy demanding (i.e. electricity input of 22.19kWh). Lower impact would be aspect in case the nitrogen could be reuse within the step of furnace conditioning. Currently, the amount of nitrogen applied in the step of furnace conditioning has been considered as a direct emission into air.

The comparison performed for among the upscale processes of CNT fibre via toluene and butanol as precursors confirms the results obtained at semi industrial configuration. Thus, the scenario with toluene as precursor revelled better environmental performance for the entire impact category (figure 7.17).

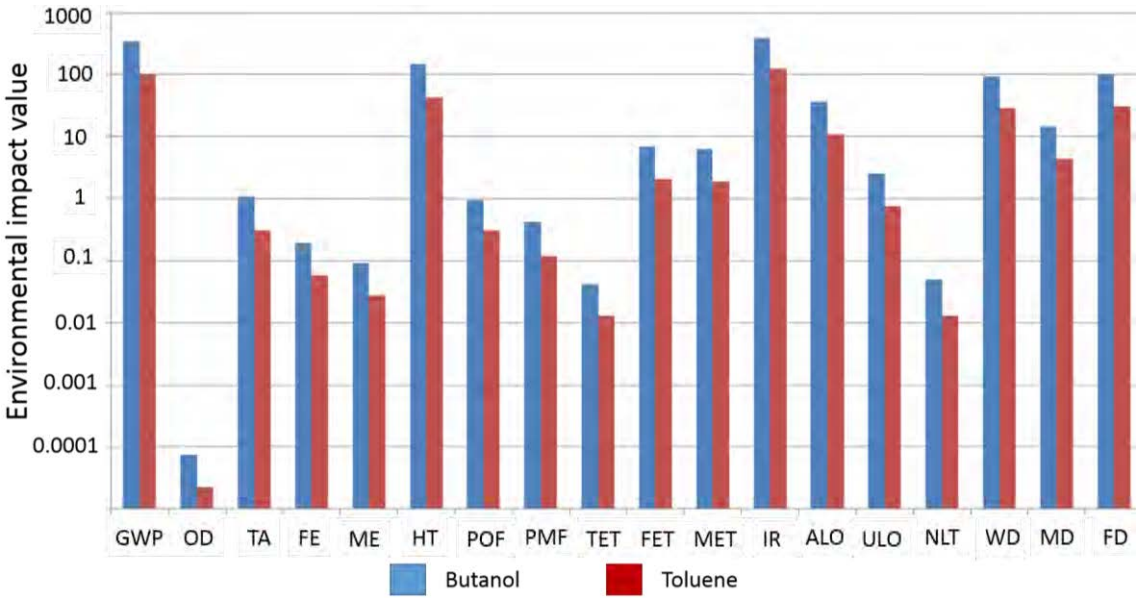

Figure 7.17. Comparison of the environmental performance of the scaled–up processes of CNT fibre (toluene and butanol). The impact score for each impact category is reported in industrial scale.

Finally, it is important to compare the differences between the lab-scale and the industrial process (figure 7.18). Industrial set-up can deal with a big amount of hydrogen, decreasing the impact in two order of magnitude. Consequently, it is possible to conclude that. CNT production, even more accused in the industrial configuration, it has an acceptable environmental impact.

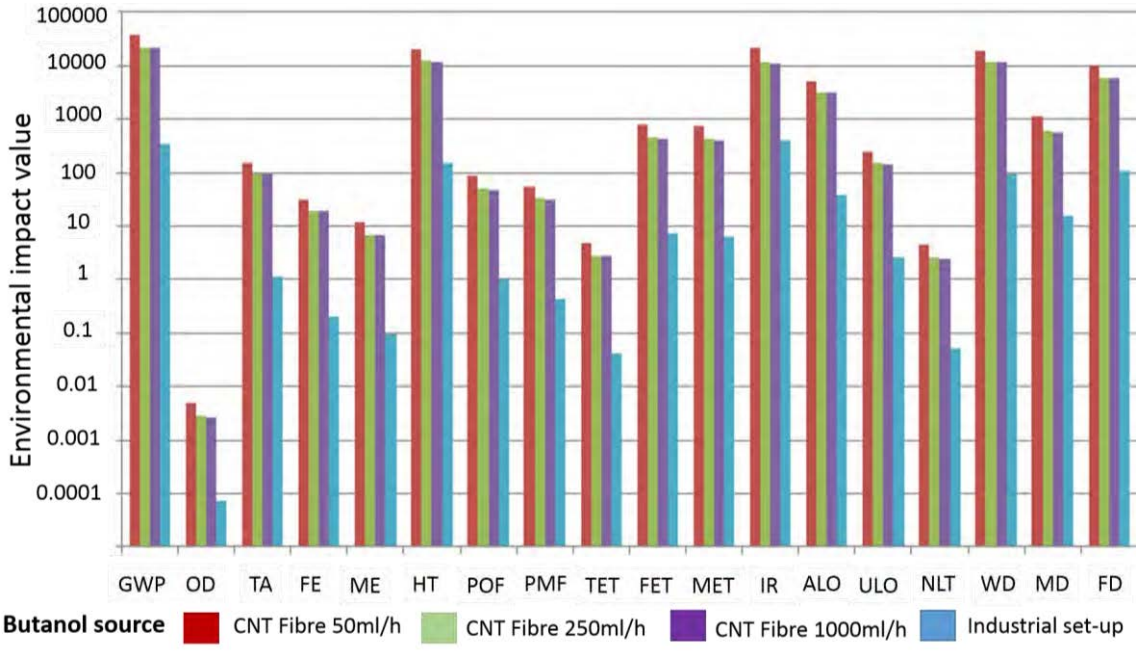

Figure 7.18. Comparison of the environmental performance of the scaled–up processes of CNT fibre (toluene and butanol). The impact score for each impact category is reported in industrial scale.

7.5. Macroscopic applications

During the previous chapter, the discussion was mainly related with the synthesis and CNT fibre characterisation. Thus, different CNT and architectures can be manufactured. Therefore, it is possible to optimise the best type CNT fibre per application. In this section is presented different applications, which are developed by *Multifunctional Nanocomposites Group*.

7.5.1. Flexible Supercapacitors

Mesoporous structure, high surface area, mechanical and electrical properties create an especial combination of qualities, ideal in order to obtain a high-performance electrode in supercapacitor and electrochemical applications[181]. The electrodes perform of pure CNT fibre are assembly into all-solid electric double layer capacitor (EDLC). Furthermore, it is observed the presence of quantum capacitance in the CNTs, exemplifying how the low dimensionality of appropriately synthesised CNT electrodes can lead as a large enhancement in the performance of macroscopic energy storage devices. Charge-discharge measurements show power and energy densities as high 58kW/kg and 14Wh/kg, respectively. Long term experiments demonstrate stable capacitance and energy retention during 10000 cycles of charge-discharge at 3.5V[178]. Figure 7.19.a-b show a CNT as-spun and densified fibre, respectively, which is necessary for preparing a CNT electrode. 100cm^2 laminated device is shown in figure 7.19.c and solid-state SC devices of 4.5 cm^2 in figure 7.19.d, powering a red LED. These are two of the possible architecture for performing the supercapacitor. Furthermore, the supercapacitors could be bent and folded 180º without degradation of their properties, raising the capacitance until 28F/g. Mechanical properties are also performed, obtaining specific strength of 0.4 GPa/SG and a modulus of 18 GPa/SG.

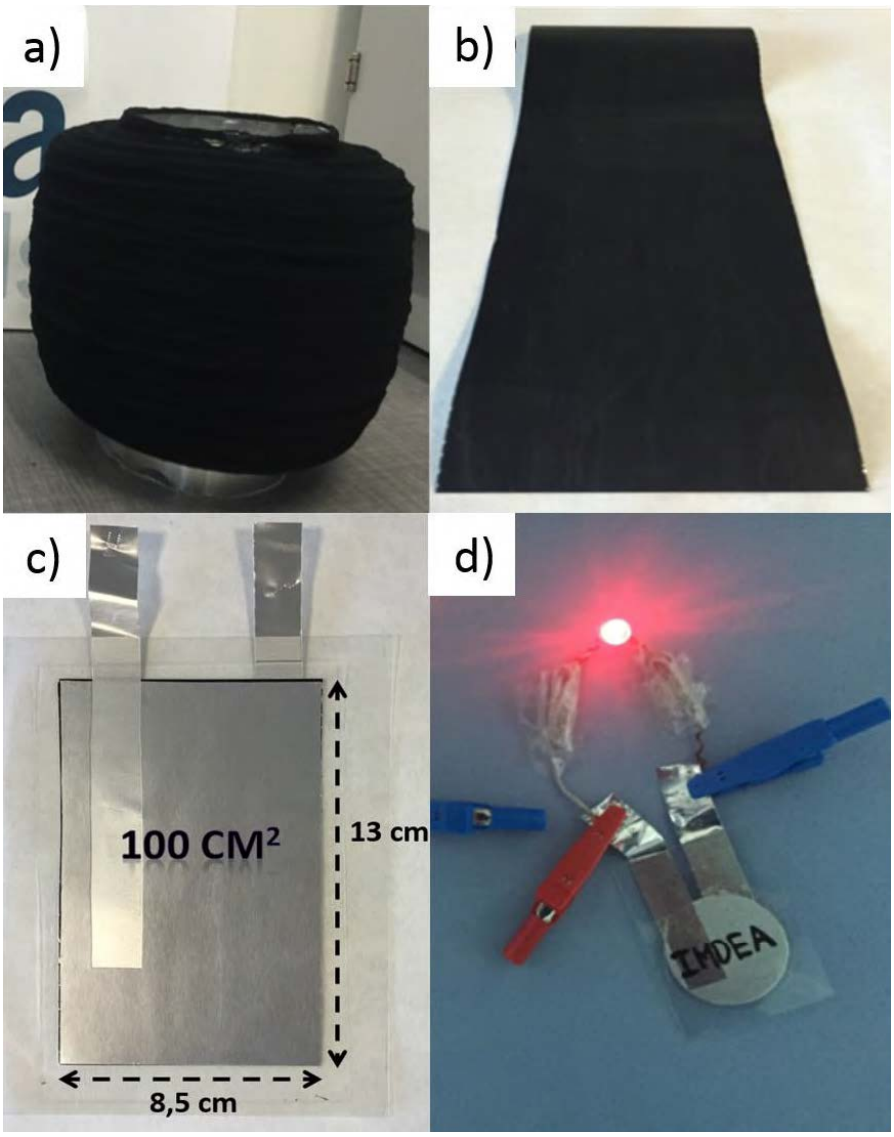

Figure 7.19. Kilometres of fibres directly spun over an aluminium sheet (a) as-spun and (b) after densification with acetone. (c) 100cm^2 laminated device and (d) solid-state SC devices of 4.5 cm^2 based on our CNT produced, powering a red LED [178] [239].

7.5.2. Sensor

The sensing capabilities of CNT fibres arise from the role of inter-tube charge transfer in determining longitudinal transport properties, such as electrical conductivity. Fernández-Toribio et al has actively studied this phenomenon with a particular focus on the application as sensors in composite fabrication. The sensing mechanism is depended on adsorption of liquid/polymer in the pores structure, modifying the longitudinal fibre resistance[183]. Figure 7.20.a shows a typical CNT fibre sensor, which was spun at a draw ratio of 6.3. Sensors are densified by manual densification of 10 individual filaments into a single yarn. The diameter of the yarn is 40μm and the conductivity is 3.5x10^5 S/m. Figure 7.20.b

represents the radial infiltration process along the length of the fibre, introducing molecules in the fibre radially inward. Figure 7.20.c-d show the experimental set-up, which is made of four glass fibre plain and balance woven 1-15 layers. CNT fibre is in the mid-plain, oriented parallel to the direction of the resin flow. Electrical measurements are performed, extracting the contacts to ensure no interferences. Vacuum infusion with CNT yarn as a sensor reflects one of the main propose, using nanostructure materials for macroscopic scale application (industrial processes).

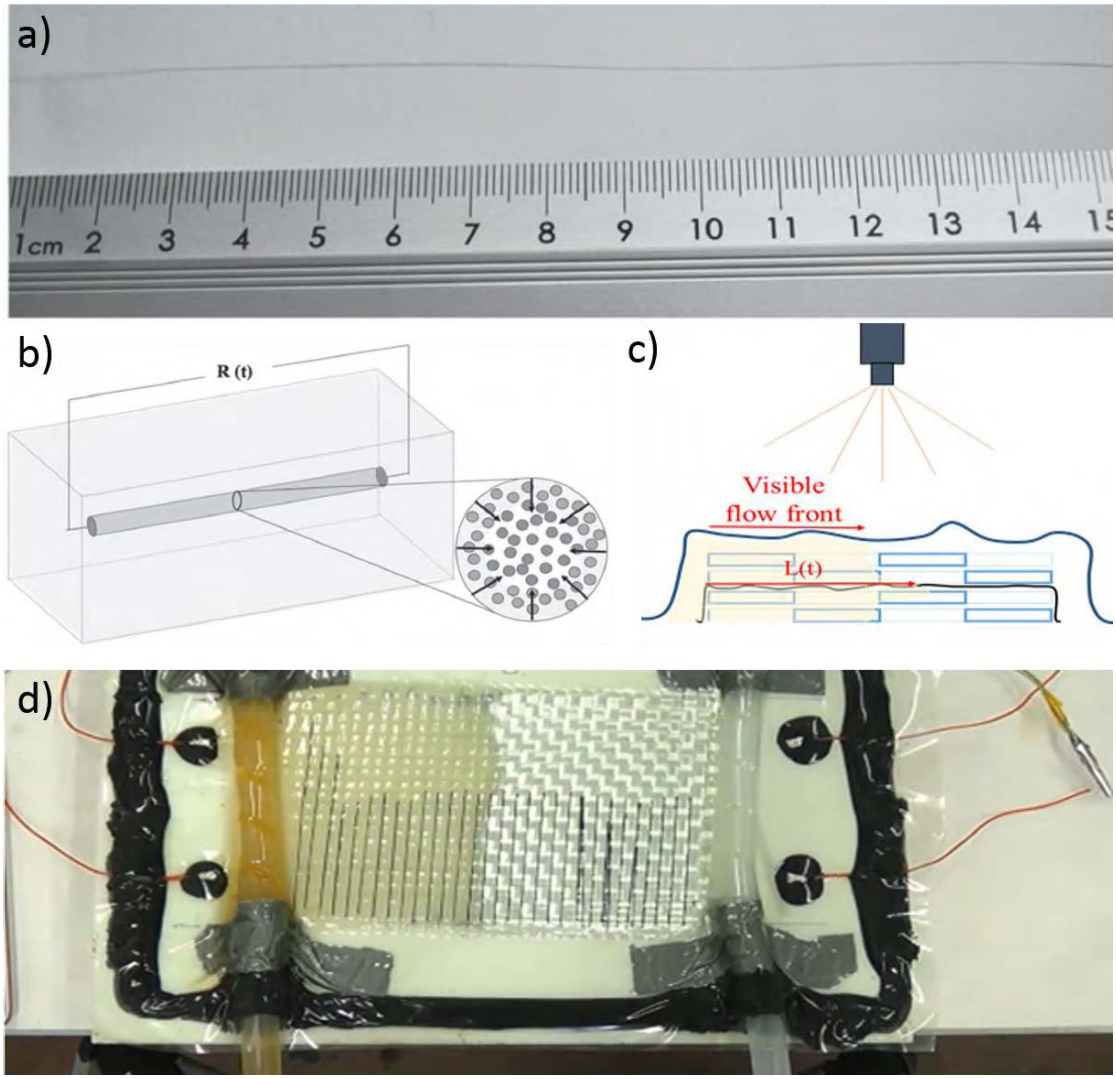

Figure 7.20. (a) Optical micrograph showing the CNT fibre yarn architecture. (b) Schematic representation of the radial infiltration of the fluid across the CNT fibre by capillary forces. (c) CNT fibre is located between two glass fibre fabrics in the flow direction. (d) Vacuum infusion set-up , using the CNT fibre as a sensor[183].

Other macroscopic application is related to the use of CNT fibre yarns as a sensor into a front and rear wings of a formula student car due to its sensitive to

mechanical deformations. The CNT fibre is synthesised from toluene as a carbon source and the length is 1 meter. Measuring the electrical resistance, it is possible to detect wings shape changes and relate to mechanical stresses induced by aerodynamic loads. Figure 7.21.a shows the electrical contact, which is stitched along the front wing (figure 7.21.b-c). Finally, in the figure 7.21.d is presented the UC3M formula student car.

Figure 7.21. (a) Electrical contact for controlling the CNT yarn resistance. (b) Photograph of the F1 spoiler after CNT fibre implementation. (c) Overview of the F1 spoiler with two CNT yarn stitched. (d) Picture of UC3M F1 prototype. [Courtesy J.C Fernandez-Toribio]

7.5.3. Energy harvesting

CNT fibre film in large macroscopic scale 10 cm^2 is utilised to grow ZnO, synthesising heterojunctions between ZnO and CNT film. It results in a bulk heterojunction, creating a 10 μm layer of ZnO crystals with preferential orientation c-axis perpendicular to the CNT film. CNT film provides large surface area, as well as metallic character. In addition to a semiconductor leads to develop a synthetic hybridisation process. Thus, the hybrid CNT/ZnO shows a piezo resistive and piezoelectric behaviour. To summarise, the electronic properties of the heterojunctions are critical in order to produce energy harvesting structural composite structures.

Figure 7.22.a-b show a schematic representation of the electrical set-up to develop the heterojunction hypothesis. Electronic measurements are performed across the ZnO/CNT fibre interface. Figure 7.22.c shows a demonstration of ZnO energy harvesting device with a CNT film flexible electrodes.

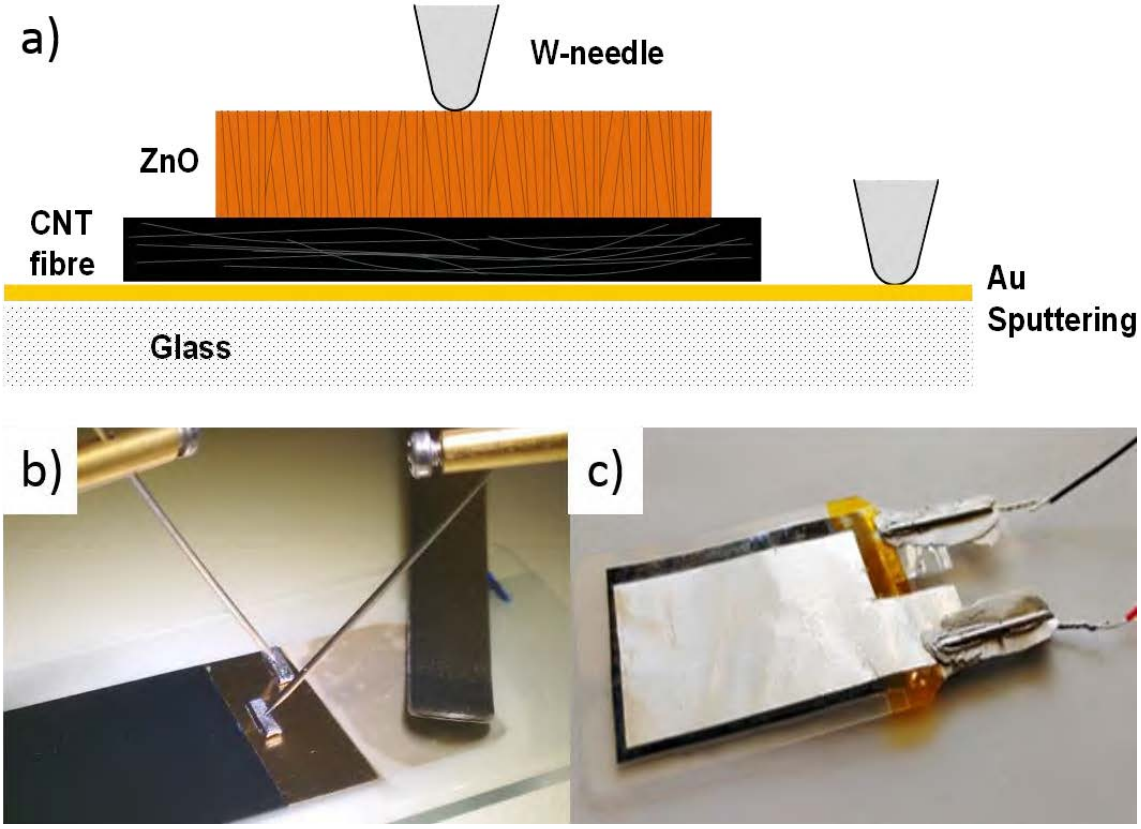

Figure 7.22. Schematic diagram shows the device as a combination of CNT fibre and zinc oxide. (b) Device developed for the electrical measurements. (c) Energy harvesting device. [Courtesy A. Monreal]

7.5.4. Composites

The mesoporous structure of the CNT fibre is a very promising material to integrate into polymer matrices to produce composites. The porosity provides the material accessible to polymer infiltration. Mechanical properties are enhanced through stress transfer between bundles via the infiltrated polymer[154]. Figure 7.23.a shows the schematic diagram of a composites preparation. CNT fibre is collected into a resin substrate and include between carbon fibre prepreg, obtaining a 30x30cm sample in order to be tested (figure 7.23.b).

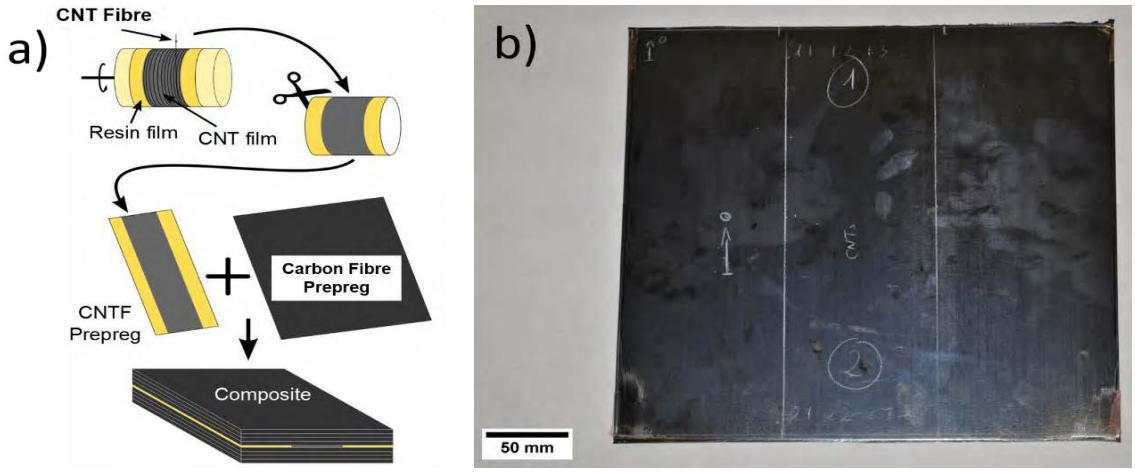

Figure 7.23. (a) Schematic diagram shows a composites preparation, which is made with CNT fibre and carbon fibre prepreg. (b)Optical micrograph of a composites with 30x30 cm dimension. [Courtesy of B.Mas].

CNT fibre is also presented as an active component in the fabrication of small scale unidirectional non-woven CNT fibre composites with thermoplastics or thermoset matrices. CNT fibre is responsible for inducing the nucleation of semi-crystalline polymer perpendicular to the fibre surface as a transcrystalline layer. CNTs adsorb the polymer chains and lead to a soft-epitaxy mechanism. Polymer chains grow perpendicular to the CNT, producing a high degree of undercooling due to the high thermal conductivity of the CNT fibres[130]. Figure 7.24.a-b represent a micrograph of a CNT fibre/iPP composites and graphene fibre composites, respectively. CNT and graphene promote the nucleation of crystal perpendicular to the fibre. The main difference is that CNT produces the high-density nucleation sites compare with graphene, which induces a low density due to the structural defects and the low interaction with the iPP[240].

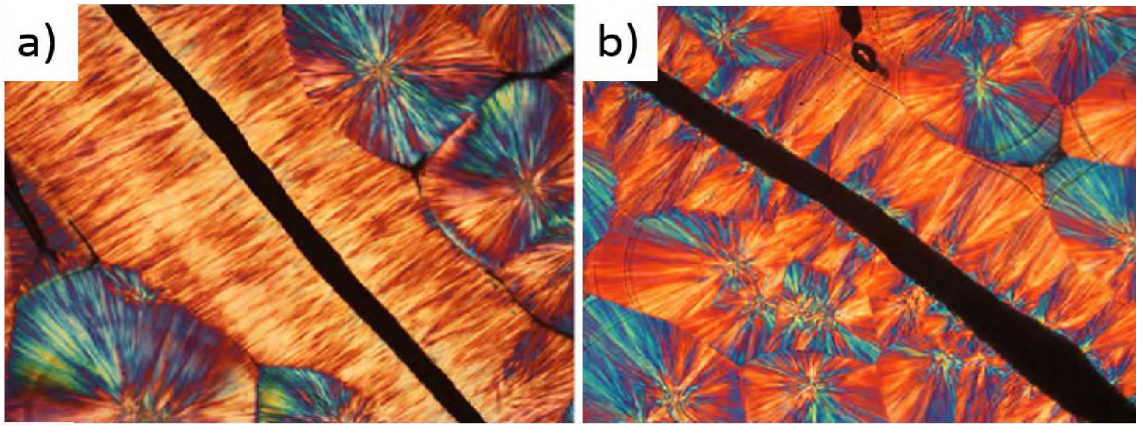

Figure 7.24. Optical micrographs of transcrystallised iPP induced by (a) CNT fibre. The results are compared with graphene fibre, showing different behaviour under the same conditions[240].

7.6. Summary

In this chapter, it was demonstrated that the CNT fibre synthesised by direct spinning is scalable. It is analysed the concentration of reactant in the reaction area, modifying the precursor feed rate in 2.5. Furthermore, the critical points were defined and related with the fibre quality. This inflexion point between stretchable and non-stretchable is defined as straightness point. Furthermore, tuning hydrogen, it is possible to define another important points: lower spin limit and high spin limit. Which are defined as the low and high hydrogen ratio in the in the reaction. The responsible of these limits are the CNT concentration (in the upper limit) and the carbon concentration in the catalyst (in the lower limit), allowing to spin continuously CNT fibre. Besides, it was demonstrate that CNT fibre samples are produced under reproducible and stable reaction conditions that ensure continuous spinning maintainable for hours.

Life cycle assessment is performed in order to reduce the environmental impact for producing CNT fibre by direct spinning method. It was evaluated different precursor feed rate, carbon source and set-up configuration. Increasing the precursor feed rate decrease the impact in 50%. Using toluene instead butanol, it is possible to improve ≈55%. Due to the better control of the process, industrial set-up is not using nitrogen, reducing the synthesis stage impact more than 70%. In overall the industrial configuration decrease in two order of magnitude the environmental impact, comparing to semi-industrial configuration.

CNT fibre have shown perfect properties and structure for many application. Mesoporous structure, high surface area, mechanical and electrical properties create an especial combination of qualities, ideal in order to obtain a high-performance electrode in supercapacitor and electrochemical applications. Vacuum infusion and mechanical deformation sensor is developed with the fibre synthesised in yarn architecture. The sensing capabilities of CNT fibres arise from the role of inter-tube charge transfer in determining longitudinal transport properties, such as electrical conductivity. Using other configuration, CNT film provides large surface area as well as metallic character to perform heterojunctions together with semiconductor as ZnO, which properties are critical in order to produce energy harvesting structural composite structures. Finally,

thanking to mesoporous structure, CNT fibre is a very promising material to integrate into polymer matrices to produce composites. The porosity provides the material accessible to polymer infiltration. Mechanical properties are enhanced through stress transfer and it is determined that CNT fibre are responsible for inducing the nucleation of semi-crystalline polymer perpendicular to the fibre surface as a transcrystalline layer.

8 Conclusions & Future work

8.1. Conclusions

Direct spinning with floating catalyst by CVD is one of the most promising techniques to implement the nanotechnology in macroscopic devices and applications. This method provides the possibility to produce high amount of material in only one step, which is also economically attractive to the industry to scale-up the process. Even though, the knowledge is already limited in several aspects as synthesis, structure, properties and its transference to the industry. This work provides some answers related to the different questions of the CNT fibre.

One of the most valuable aspect of this method is the possibility to tune the final product through the reaction, realising the possibility of synthesising the best fibre per application. It is demonstrate the possibility to produce continuous CNT fibres on a kilometre scale with control of the CNTs in terms on number of layers from SWCNT to MWCNT by adjusting the concentration of S precursor in the reaction. The dimension of the tube are affected, at low S concentration CNTs are predominantly SW of approximately 1 nm diameter. Increasing S coarsening larger catalyst particles and CNT increases inner diameter and number of layers. This transition from SW to MW is clearly distinguished by raman spectra. RBM peaks and G^- disappear, and confirming by the upshift in the 2D band due to the increase in number of adjacent layers, according to the literature related to graphene. Sulphur effects is independent of the choice of C precursor (butanol, toluene or benzyl alcohol) used for the CVD growth of CNTs.

It is calculated the composition of catalyst particles and found that inactive particles, which represent over 99.9% of those produced in the reactor and aggregated in the fibre, are encapsulated due to their high C content. Controlling the carbon diffusion, through sulphur rich layer, the catalyst particle is not in thermodynamic equilibrium with solid C, thus, instead of forming an encapsulating layer C gets extruded as a CNT and the particle remains active.

Entirely SWCNTs fibre can be synthesised, and it is found the inherent predominance of metallic and high chiral angle CNTs. Chiral distribution matches

with theoretical prediction for CNTs produced by molten catalyst. Catalyst structure suggests a Fe FCC core surrounded by a liquid Fe-S shell, according to thermodynamic calculations. The presence of sulphur in the catalyst is also critical, not only controlling the carbon diffusion in the catalyst but also stabilised the edge of the nascent CNT and rejected the carbon from the catalyst forming the graphitic layers.

During the analysis of reaction are analysed in detail the role of Fe, S, C and H_2 and lesser extent the O_2. However, the combination of reducing atmosphere and high temperature (1250ºC) provides the perfect condition to the reaction between silicon oxide and hydrogen, forming SiO, SiC or silicon. Silicon effect could be critical for the reaction, without Si, it was not possible to obtain a continuous fibre.

Microscopic scale and the bundle distribution is the key for synthesised a high-performance fibre. In this work it is found that the association of CNTs in the gas-phase is critical in determining the possibility to increase the speed in the drawn of the CNT aerogel and thus produce oriented CNT fibres. Finding the CNT concentration, which allows to spin under diluted conditions, the fibre can be extracted from the aerogel and it is pulled against the gas in the reactor up to 17 draw ratio. Due to the friction against the carrier gas, CNT bundles are aligned preferentially parallel to each other along the fibre axis. Decreasing the CNT concentration leads to have less entanglements so as to allow the rearrangement of CNTs. It is very important to remark the importance of separating the orientation effect from the CNT composition (in terms of type of tubes), evidenced through raman spectroscopy measurements.

Though the orientation, it is possible to tune the mechanical properties of the fibre. Oriented over non-oriented fibres increases modulus and tensile strength from 4 to 62 GPa and from 0.2 to 1.1 GPa, respectively. Consequently, the strain values decrease from 23% until 8%. The effect of the type of CNT (SW or MWCNT) is negligible compare to the orientation.

Wide range of mechanical properties in the fibre is related to the complex structure from CNT fibre that it was studied in detail. Fibre is composed of a millions of individual CNT, which are considered as a nanostructure building blocks, forming a hierarchical structure. Fibre structure is studied from two

different points of view, analysing structure as isotropic structure by gas adsorption and considered as anisotropic, using SAXS/WAXS measurements to extract the structural information.

Isotropic properties of CNT fibre are analysed by gas adsorption method. The surface area is ≈ 260m^2/g for samples with different draw ratios, ranging from 0.47 (1.5m/min) to 12.6 (40m/min). Meso-scale distribution of porous size is independent of the draw ratio. Observing the micrographs at different scale is concluded that CNT fibre is a fractal structure. The fractal dimension was determined from gas adsorption ≈ 2.55, which is nearly identical to the SAXS value.

Anisotropic properties of CNT fibre are analysed by SAXS/WAXS, measurements cover a wide range of distance from few angstrom to tens of nanometres, obtaining the degree of orientation. Which varies from 50 to 24 in SAXS and from 35 to 17 in WAXS integration. SAXS parameters L_3 and L_p confirm that changing bundle orientation in the CNT fibre affects directly to the pores structure. Due to the orientation, inter-bundle pores have more elongated structure along the fibre axis. Radial integration of 002 leads to confirm better packing in the bundle.

Post-spin densification was evaluated and this effect is not modifying the fibre structure in the nanoscale, links of CNTs or packing of bundles. Consequently, the electrical and mechanical properties are not affected or the change is negligible compare with the orientation. This fact conclude that the CNT assembly occurs during the reaction in the gas phase. The real challenge is control the synthesis parameters in the reactor, which allows to modify the CNT association in the aerogel without sacrificing control of chemistry and morphology.

CNT films stacked create a 2D structure through the repetition of layers with different refractive index (n_a and n_b) and thickness (d_a and d_b). It is possible to confirm that CNT films behave as a dielectric mirror. The colour of the fibre can be tuned only modifying the thickness of the sample. 150nm leads to violet colour whereas at 400nm is red. Which corresponds with the half of the wavelength from colours observed in the sample, corresponded from the visible range. Below 150 nm, emission is in the UV and upper 400nm in the IR range.

Finally, all the knowledge extracted from the reaction was employed to scale-up, modifying the precursor feed rate in 2.5 times. This inflexion point between stretchable and non-stretchable is defined as straightness point. Furthermore, tuning hydrogen, it is possible to define another important points: lower spin limit and high spin limit. Which are defined as the low and high hydrogen ratio in the in the reaction, allowing to spin continuously CNT fibre. Concluding that the possibility to transfer the lab knowledge to the industrial scale is very promising.

Life cycle assessment is performed in order to reduce the environmental impact for producing CNT fibre by direct spinning method. Increasing the precursor feed rate decrease the impact in 50%. Using toluene instead butanol, it is possible to improve ≈55%. And comparing the lab-scale with the industrial configuration, LCA decreases in two order of magnitude the environmental impact.

CNT fibre have shown perfect properties and structure for many application and macroscopic devices have been developed with CNT fibre synthesised by our reactor. Manufacturing a high-performance electrode in supercapacitor for electrochemical applications. Moreover, vacuum infusion and mechanical deformation sensor is developed with the fibre synthesised in yarn architecture.

Using other configuration, CNT film provides large surface area as well as metallic character to perform heterojunctions together with semiconductor as ZnO, which properties are critical in order to produce energy harvesting structural composite structures. Finally, Thanking to mesoporous structure, CNT fibre is a very promising material to integrate into polymer matrices to produce composites. The porosity makes the material accessible to polymer infiltration. Mechanical properties are enhanced through stress transfer and it is determined that CNT fibre are responsible for inducing the nucleation of semi-crystalline polymer perpendicular to the fibre surface as a transcrystalline layer.

8.2. Future work

Despite the continuous knowledge presented by the different groups all over the world during last years, still open questions are concerned to the reaction. As it was discussed in the growth model in chapter 4, it is important the place where the reactants decomposed and start to be available. Therefore, controlling the decomposition of the reactant in the right place at right moment, can increase efficiency of the reaction drastically. Thus, one of the future work is analysed the gases present in reaction, including the intermediate products. Furthermore, it is interesting to study the dissociation mechanism in the surface of the catalyst and its integration in the CNT.

The design of the apparatus will be not very complicated, in fact it is already used in similar reactors. Sample is extracted by a ceramic o quartz pipe directly from the upper part of the reactor, where the reaction is ongoing. The stream components will be measured by gas chromatography (GC) almost in-situ. Nevertheless, the gas could be reacted along the ceramic pipe, therefore, the critical step is maintain the stream with the highest permitted temperature. This equipment would provide more information to identify the compounds, which are presented in the reactor along the reactor. Allowing to determine the decomposition route from the different precursors, even some information related with silicon sub products.

One of the main disadvantages of this CNT method is the hydrogen atmosphere, important security problems and manufacturing costs will be erased removing the hydrogen as a carrier gas, therefore, it is worthy trying to find alternatives. Firstly, it is necessary to studied all the roles related to the hydrogen to find the best substitute. As it was shown in the literature review, the main purpose tasks of the hydrogen are: controlling the carbon concentration; reacts with sulphur producing H_2S; creating a reduced atmosphere and affecting to the reaction temperature through the high thermal conductivity compared with inert gases.

Being only related to the control of carbon concentration, the problem had already be accomplished, because the problem would be just found the appropriate parameters with other gases. The reaction between hydrogen and sulphur can be excluded, concentration of sulphur affects to CNT type. The hydrogen flow is

not modifying the type of CNT that means that the ratio S/C is not affected by increasing hydrogen. Therefore, hydrogen does not react with sulphur.

The critical aspect can be the reduced atmosphere. In this specific case, it will be more difficult to solve and probably it will be not enough just to change hydrogen by an inert gas. It would have to be studied all the possible component reduced and added directly to the reaction, whenever it is reasonably possible. The last option is related to the high thermal conductivity of hydrogen, in this case, it can be helpful to change by helium, which is the closer inert gas and increasing the reactor temperature.

Silicon could be the surprise guest in the reaction. The first evidence of the incorporation of silicon in the fibre was provided by EDS measurements of the fibre and then it was confirmed by WAXS measurements and XPS. Furthermore, it was hidden in the literature from different groups. The role of the silicon is absolutely ignored, the main evidence about its importance is the fact that it is impossible to spin CNT fibre in alumina tube in the same reaction conditions. Therefore, the role of silicon has to be studied in detail, trying to analyse the particles presents in the fibre, crystallinity, shape, size and composition mainly by electron diffraction and confirming through TEM images.

One of the main propose in future works is increased the macroscopic properties. It can be treated from the reaction point of view, because the theoretical values are already order of values higher. The options can be, improving the alignment, increased the packing and the number of tubes per bundle, and promoted the synthesis of collapse, longer tubes without defects. In the big challenge to enhance macroscopic properties from the actual values.

The alternative is improving the properties by post-treatments. Dry or wet-stretched, functionalisation of CNTs, infiltrate or cover with polymers or epoxy resins as well as growth or electrodeposited metals are some good examples of a possible way forward.

The process scale-up, increasing the production one order of magnitude, is accompanied by several chemical engineer challengers. Firstly related to the injection, designing the most appropriate system to provide the necessary amount of precursor feed rate homogenously. Increasing precursor feed rate

leads to increasing the hydrogen flow through the reactor. Manipulate hydrogen is a problem itself, the outlet stream has to be diluted until safety values. This increment means less residence time in the reactor, affecting to the gas temperature, therefore the reaction kinetics. Moreover, increasing flow can induce a change in fluid dynamic, changing from laminar to turbulence. Even though, all this challenges can be solved modifying the parameters, with the knowledge extracted from the reaction step.

9 References

[1] S. Iijima, “Helical microtubules of graphitic carbon,” *Nature*, vol. 354, no. 6348, pp. 56–58, Nov. 1991.

[2] S. Iijima and T. Ichihashi, “Single-shell carbon nanotubes of 1-nm diameter,” *Nature*, vol. 363, no. 6430, pp. 603–605, Jun. 1993.

[3] D. S. Bethune *et al.*, “Cobalt-catalysed growth of carbon nanotubes with single-atomic-layer walls,” *Nature*, vol. 363, no. 6430, pp. 605–607, Jun. 1993.

[4] S. Amelinckx, A. Lucas, and P. Lambin, “Electron diffraction and microscopy of nanotubes,” *Rep. Prog. Phys.*, vol. 62, no. 11, p. 1471, 1999.

[5] C.-H. Kiang, M. Endo, P. M. Ajayan, G. Dresselhaus, and M. S. Dresselhaus, “Size Effects in Carbon Nanotubes,” *Phys Rev Lett*, vol. 81, no. 9, pp. 1869–1872, Aug. 1998.

[6] J. A. Elliott, J. K. W. Sandler, A. H. Windle, R. J. Young, and M. S. P. Shaffer, “Collapse of Single-Wall Carbon Nanotubes is Diameter Dependent,” *Phys Rev Lett*, vol. 92, no. 9, p. 95501, Mar. 2004.

[7] M. He *et al.*, “Precise Determination of the Threshold Diameter for a Single-Walled Carbon Nanotube To Collapse,” *ACS Nano*, vol. 8, no. 9, pp. 9657–9663, Sep. 2014.

[8] B. Mas *et al.*, “Group 16 elements control the synthesis of continuous fibers of carbon nanotubes,” *Carbon*, vol. 101, pp. 458–464, 2016.

[9] X. Meng, M. Li, Z. Kang, X. Zhang, and J. Xiao, “Mechanics of self-folding of single-layer graphene,” *J. Phys. Appl. Phys.*, vol. 46, no. 5, p. 55308, 2013.

[10] K. Hata, D. N. Futaba, K. Mizuno, T. Namai, M. Yumura, and S. Iijima, “Water-Assisted Highly Efficient Synthesis of Impurity-Free Single-Walled Carbon Nanotubes,” *Science*, vol. 306, no. 5700, pp. 1362–1364, 2004.

[11] M. S. Dresselhaus, G. Dresselhaus, and A. Jorio, “UNUSUAL PROPERTIES AND STRUCTURE OF CARBON NANOTUBES,” *Annu. Rev. Mater. Res.*, vol. 34, no. 1, pp. 247–278, 2004.

[12] M. S. Dresselhaus, G. Dresselhaus, and P. C. Eklund, “Preface,” in *Science of Fullerenes and Carbon Nanotubes*, M. S. Dresselhaus, G. Dresselhaus, and P. C. Eklund, Eds. San Diego: Academic Press, 1996, pp. xvii–xviii.

[13] C. Thomsen and S. Reich, “Raman Scattering in Carbon Nanotubes,” in *Light Scattering in Solid IX*, M. Cardona and R. Merlin, Eds. Berlin, Heidelberg: Springer Berlin Heidelberg, 2007, pp. 115–234.

[14] L. Sun, F. Banhart, A. V. Krasheninnikov, J. A. Rodríguez-Manzo, M. Terrones, and P. M. Ajayan, “Carbon Nanotubes as High-Pressure Cylinders and Nanoextruders,” *Science*, vol. 312, no. 5777, pp. 1199–1202, 2006.

[15] A. L. MACKAY and H. TERRONES, “Diamond from graphite,” *Nature*, vol. 352, no. 6338, pp. 762–762, Aug. 1991.

[16] M. Sammalkorpi, A. Krasheninnikov, A. Kuronen, K. Nordlund, and K. Kaski, “Mechanical properties of carbon nanotubes with vacancies and related defects,” *Phys Rev B*, vol. 70, no. 24, p. 245416, Dec. 2004.

[17] M. M. J. Treacy, T. W. Ebbesen, and J. M. Gibson, “Exceptionally high Young’s modulus observed for individual carbon nanotubes,” *Nature*, vol. 381, no. 6584, pp. 678–680, Jun. 1996.

[18] M.-F. Yu, B. S. Files, S. Arepalli, and R. S. Ruoff, “Tensile Loading of Ropes of Single Wall Carbon Nanotubes and their Mechanical Properties,” *Phys Rev Lett*, vol. 84, no. 24, pp. 5552–5555, Jun. 2000.
[19] B. . Demczyk *et al.*, “Direct mechanical measurement of the tensile strength and elastic modulus of multiwalled carbon nanotubes,” *Mater. Sci. Eng. A*, vol. 334, no. 1–2, pp. 173–178, Sep. 2002.
[20] Y. Wu *et al.*, “Determination of the Young’s Modulus of Structurally Defined Carbon Nanotubes,” *Nano Lett.*, vol. 8, no. 12, pp. 4158–4161, 2008.
[21] B. Peng *et al.*, “Measurements of near-ultimate strength for multiwalled carbon nanotubes and irradiation-induced crosslinking improvements,” *Nat Nano*, vol. 3, no. 10, pp. 626–631, Oct. 2008.
[22] M.-F. Yu, O. Lourie, M. J. Dyer, K. Moloni, T. F. Kelly, and R. S. Ruoff, “Strength and Breaking Mechanism of Multiwalled Carbon Nanotubes Under Tensile Load,” *Science*, vol. 287, no. 5453, pp. 637–640, 2000.
[23] B. I. Yakobson, C. J. Brabec, and J. Bernholc, “Nanomechanics of Carbon Tubes: Instabilities beyond Linear Response,” *Phys Rev Lett*, vol. 76, no. 14, pp. 2511–2514, Apr. 1996.
[24] C. Lee, X. Wei, J. W. Kysar, and J. Hone, “Measurement of the Elastic Properties and Intrinsic Strength of Monolayer Graphene,” *Science*, vol. 321, no. 5887, pp. 385–388, 2008.
[25] S. Frank, P. Poncharal, Z. L. Wang, and W. A. de Heer, “Carbon Nanotube Quantum Resistors,” *Science*, vol. 280, no. 5370, pp. 1744–1746, 1998.
[26] P. Lambin, L. Philippe, J. C. Charlier, and J. P. Michenaud, “Electronic band structure of multilayered carbon tubules,” *Comput. Mater. Sci.*, vol. 2, no. 2, pp. 350–356, 1994.
[27] L. X. Benedict, V. H. Crespi, S. G. Louie, and M. L. Cohen, “Static conductivity and superconductivity of carbon nanotubes: Relations between tubes and sheets,” *Phys Rev B*, vol. 52, no. 20, pp. 14935–14940, Nov. 1995.
[28] A. Bachtold *et al.*, “Scanned Probe Microscopy of Electronic Transport in Carbon Nanotubes,” *Phys. Rev. Lett.*, vol. 84, no. 26, pp. 6082–6085, Jun. 2000.
[29] S. Hong and S. Myung, “Nanotube Electronics: A flexible approach to mobility,” *Nat Nano*, vol. 2, no. 4, pp. 207–208, Apr. 2007.
[30] L. Pietronero, S. Strässler, H. R. Zeller, and M. J. Rice, “Electrical conductivity of a graphite layer,” *Phys Rev B*, vol. 22, no. 2, pp. 904–910, Jul. 1980.
[31] I.-K. Hsu, M. T. Pettes, A. Bushmaker, M. Aykol, L. Shi, and S. B. Cronin, “Optical Absorption and Thermal Transport of Individual Suspended Carbon Nanotube Bundles,” *Nano Lett.*, vol. 9, no. 2, pp. 590–594, Feb. 2009.
[32] J. Hone, M. Whitney, C. Piskoti, and A. Zettl, “Thermal conductivity of single-walled carbon nanotubes,” *Phys Rev B*, vol. 59, no. 4, pp. R2514–R2516, Jan. 1999.
[33] A. Bachtold *et al.*, “Scanned Probe Microscopy of Electronic Transport in Carbon Nanotubes,” *Phys Rev Lett*, vol. 84, no. 26, pp. 6082–6085, Jun. 2000.
[34] T. Y. Choi, D. Poulikakos, J. Tharian, and U. Sennhauser, “Measurement of thermal conductivity of individual multiwalled carbon nanotubes by the 3-ω method,” *Appl. Phys. Lett.*, vol. 87, no. 1, 2005.

[35] P. Kim, L. Shi, A. Majumdar, and P. L. McEuen, “Thermal Transport Measurements of Individual Multiwalled Nanotubes,” *Phys Rev Lett*, vol. 87, no. 21, p. 215502, Oct. 2001.
[36] A. A. Balandin *et al.*, “Superior Thermal Conductivity of Single-Layer Graphene,” *Nano Lett.*, vol. 8, no. 3, pp. 902–907, Mar. 2008.
[37] “M. Rodríguez. Biological samples positioning device for irradiations on a radial channel at the nuclear research reactor. Ing Mecánica V13 N2 Habana Mayo-Ago 2010.” .
[38] K. Stano *et al.*, “Direct Spinning of Carbon Nanotube Fibres from Liquid Feedstock,” *Int J Mater Form*, vol. 1, p. 59, 2008.
[39] C. N. Hooker, A. R. Ubbelohde, and D. A. Young, “Thermal Conductance of Graphite in Relation to its Defect Structure,” *Proc. R. Soc. Lond. Math. Phys. Eng. Sci.*, vol. 276, no. 1364, pp. 83–95, 1963.
[40] M. Endo, K. Takeuchi, S. Igarashi, K. Kobori, M. Shiraishi, and H. W. Kroto, “The production and structure of pyrolytic carbon nanotubes (PCNTs),” *J. Phys. Chem. Solids*, vol. 54, no. 12, pp. 1841–1848, 1993.
[41] “Zhang, G.Y., et al., Ultra-High-Yield Growth of Vertical Single-Walled Carbon Nanotubes: Hidden Roles of Hydrogen and Oxygen. Proceedings of the National Academy of Sciences of the United States of America, 2005. 102(45): p. 16141- 16145.”
[42] S. Hofmann, C. Ducati, J. Robertson, and B. Kleinsorge, “Low-temperature growth of carbon nanotubes by plasma-enhanced chemical vapor deposition,” *Appl. Phys. Lett.*, vol. 83, no. 1, pp. 135–137, 2003.
[43] T. Yamada *et al.*, “Revealing the Secret of Water-Assisted Carbon Nanotube Synthesis by Microscopic Observation of the Interaction of Water on the Catalysts,” *Nano Lett.*, vol. 8, no. 12, pp. 4288–4292, 2008.
[44] Y. Xu, E. Dervishi, A. R. Biris, and A. S. Biris, “Chirality-enriched semiconducting carbon nanotubes synthesized on high surface area MgO-supported catalyst,” *Mater. Lett.*, vol. 65, no. 12, pp. 1878–1881, 2011.
[45] V. Jourdain and C. Bichara, “Current understanding of the growth of carbon nanotubes in catalytic chemical vapour deposition,” *Carbon*, vol. 58, pp. 2–39, 2013.
[46] M. Motta, I. Kinloch, A. Moisala, V. Premnath, M. Pick, and A. Windle, “The parameter space for the direct spinning of fibres and films of carbon nanotubes,” *Proc. E-MRS 2006 Symp. E Sci. Technol. Nanotub. Nanowires*, vol. 37, no. 1–2, pp. 40–43, Mar. 2007.
[47] S. Zhang *et al.*, “Solid-state spun fibers and yarns from 1-mm long carbon nanotube forests synthesized by water-assisted chemical vapor deposition,” *J. Mater. Sci.*, vol. 43, no. 13, pp. 4356–4362, 2008.
[48] S. Hofmann, G. Csányi, A. C. Ferrari, M. C. Payne, and J. Robertson, “Surface Diffusion: The Low Activation Energy Path for Nanotube Growth,” *Phys Rev Lett*, vol. 95, no. 3, p. 36101, Jul. 2005.
[49] M. Kumar, “Carbon Nanotube Synthesis and Growth Mechanism,” *Intech*, 2011.
[50] D. Teschner *et al.*, “The Roles of Subsurface Carbon and Hydrogen in Palladium-Catalyzed Alkyne Hydrogenation,” *Science*, vol. 320, no. 5872, pp. 86–89, 2008.
[51] L. Durrer, T. Helbling, C. Zenger, A. Jungen, C. Stampfer, and C. Hierold, “{SWNT} growth by {CVD} on Ferritin-based iron catalyst nanoparticles

towards {CNT} sensors," *Sens. Actuators B Chem.*, vol. 132, no. 2, pp. 485–490, 2008.
[52] O. V. Yazyev and A. Pasquarello, "Effect of Metal Elements in Catalytic Growth of Carbon Nanotubes," *Phys Rev Lett*, vol. 100, no. 15, p. 156102, Apr. 2008.
[53] C. P. Deck and K. Vecchio, "Prediction of carbon nanotube growth success by the analysis of carbon–catalyst binary phase diagrams," *Carbon*, vol. 44, no. 2, pp. 267–275, Feb. 2006.
[54] E. A. Sutter and P. W. Sutter, "Giant carbon solubility in Au nanoparticles," *J. Mater. Sci.*, vol. 46, no. 22, p. 7090, 2011.
[55] A. L. Borisova and O. V. Evtushenko, "Diffusional processes in the welding of some refractory carbides to metals," *Sov. Powder Metall. Met. Ceram.*, vol. 18, no. 7, pp. 481–487, 1979.
[56] "Nanometric size effect on Ge diffusion in polycrystalline Si," *J. Appl. Phys.*, vol. 104, no. 10, p. 104910, Nov. 2008.
[57] D. Bolton, Kim Feng, "Size dependence of the coalescence and melting of iron clusters: A molecular-dynamics study," *Phys. Rev. B*, vol. 70, 2004.
[58] F. Benissad, P. Gadelle, M. Coulon, and L. Bonnetain, "Formation de fibres de carbone a partir du methane II: Germination du carbone et fusion des particules catalytiques," *Carbon*, vol. 26, no. 4, pp. 425–432, 1988.
[59] C. L. Cheung, A. Kurtz, H. Park, and C. M. Lieber, "Diameter-Controlled Synthesis of Carbon Nanotubes," *J. Phys. Chem. B*, vol. 106, no. 10, pp. 2429–2433, 2002.
[60] F. Schäffel *et al.*, "Tailoring the diameter, density and number of walls of carbon nanotubes through predefined catalyst particles," *Phys. Status Solidi A*, vol. 205, no. 6, pp. 1382–1385, 2008.
[61] H. Yoshida, T. Shimizu, T. Uchiyama, H. Kohno, Y. Homma, and S. Takeda, "Atomic-Scale Analysis on the Role of Molybdenum in Iron-Catalyzed Carbon Nanotube Growth," *Nano Lett.*, vol. 9, no. 11, pp. 3810–3815, Nov. 2009.
[62] M. He *et al.*, "Key roles of carbon solubility in single-walled carbon nanotube nucleation and growth," *Nanoscale*, vol. 7, no. 47, pp. 20284–20289, 2015.
[63] W. L. Wang, X. D. Bai, Z. Xu, S. Liu, and E. G. Wang, "Low temperature growth of single-walled carbon nanotubes: Small diameters with narrow distribution," *Chem. Phys. Lett.*, vol. 419, no. 1–3, pp. 81–85, 2006.
[64] Y. Yao *et al.*, "Temperature-mediated growth of single-walled carbon-nanotube intramolecular junctions," *Nat Mater*, vol. 6, no. 4, pp. 283–286, Apr. 2007.
[65] M. H. Rümmeli *et al.*, "Catalyst Volume to Surface Area Constraints for Nucleating Carbon Nanotubes," *J. Phys. Chem. B*, vol. 111, no. 28, pp. 8234–8241, Jul. 2007.
[66] A. Gamalski, E. S. Moore, M. M. J. Treacy, R. Sharma, and P. Rez, "Diffusion-gradient-induced length instabilities in the catalytic growth of carbon nanotubes," *Appl. Phys. Lett.*, vol. 95, no. 23, p. 233109, 2009.
[67] M. Paillet *et al.*, "Growth and physical properties of individual single-walled carbon nanotubes," *Diam. Relat. Mater.*, vol. 14, no. 9, pp. 1426–1431, 2005.
[68] E. Einarsson, Y. Murakami, M. Kadowaki, and S. Maruyama, "Growth dynamics of vertically aligned single-walled carbon nanotubes from in situ measurements," *Carbon*, vol. 46, no. 6, pp. 923–930, 2008.

[69] R. Rao, D. Liptak, T. Cherukuri, B. I. Yakobson, and B. Maruyama, “In situ evidence for chirality-dependent growth rates of individual carbon nanotubes,” *Nat Mater*, vol. 11, no. 3, pp. 213–216, Mar. 2012.
[70] R. T. K. Baker, J. J. Chludzinski, N. S. Dudash, and A. J. Simoens, “The formation of filamentous carbon from decomposition of acetylene over vanadium and molybdenum,” *Carbon*, vol. 21, no. 5, pp. 463–468, 1983.
[71] E. R. Meshot, D. L. Plata, S. Tawfick, Y. Zhang, E. A. Verploegen, and A. J. Hart, “Engineering Vertically Aligned Carbon Nanotube Growth by Decoupled Thermal Treatment of Precursor and Catalyst,” *ACS Nano*, vol. 3, no. 9, pp. 2477–2486, Sep. 2009.
[72] “On the diffusion-controlled growth of multiwalled carbon nanotubes,” *J. Appl. Phys.*, vol. 97, no. 11, p. 114301, May 2005.
[73] Z. P. Huang, D. Z. Wang, J. G. Wen, M. Sennett, H. Gibson, and Z. F. Ren, “Effect of nickel, iron and cobalt on growth of aligned carbon nanotubes,” *Appl. Phys. A*, vol. 74, no. 3, pp. 387–391, 2002.
[74] W.-H. Chiang and R. M. Sankaran, “Relating carbon nanotube growth parameters to the size and composition of nanocatalysts,” *Diam. Relat. Mater.*, vol. 18, no. 5–8, pp. 946–952, 2009.
[75] M. Picher, E. Anglaret, R. Arenal, and V. Jourdain, “Self-Deactivation of Single-Walled Carbon Nanotube Growth Studied by in Situ Raman Measurements,” *Nano Lett.*, vol. 9, no. 2, pp. 542–547, Feb. 2009.
[76] D. N. Futaba, K. Hata, T. Yamada, K. Mizuno, M. Yumura, and S. Iijima, “Kinetics of Water-Assisted Single-Walled Carbon Nanotube Synthesis Revealed by a Time-Evolution Analysis,” *Phys Rev Lett*, vol. 95, no. 5, p. 56104, Jul. 2005.
[77] B. Zhao, D. N. Futaba, S. Yasuda, M. Akoshima, T. Yamada, and K. Hata, “Exploring Advantages of Diverse Carbon Nanotube Forests with Tailored Structures Synthesized by Supergrowth from Engineered Catalysts,” *ACS Nano*, vol. 3, no. 1, pp. 108–114, Jan. 2009.
[78] H. Zhang, G. Cao, Z. Wang, Y. Yang, Z. Shi, and Z. Gu, “Influence of Ethylene and Hydrogen Flow Rates on the Wall Number, Crystallinity, and Length of Millimeter-Long Carbon Nanotube Array,” *J. Phys. Chem. C*, vol. 112, no. 33, pp. 12706–12709, 2008.
[79] S. C. Hawkins, J. M. Poole, and C. P. Huynh, “Catalyst Distribution and Carbon Nanotube Morphology in Multilayer Forests by Mixed CVD Processes,” *J. Phys. Chem. C*, vol. 113, no. 30, pp. 12976–12982, 2009.
[80] Y.-L. Li, I. A. Kinloch, and A. H. Windle, “Direct Spinning of Carbon Nanotube Fibers from Chemical Vapor Deposition Synthesis,” *Science*, vol. 304, no. 5668, pp. 276–278, Apr. 2004.
[81] R. Andrews *et al.*, “Continuous production of aligned carbon nanotubes: a step closer to commercial realization,” *Chem. Phys. Lett.*, vol. 303, no. 5–6, pp. 467–474, 1999.
[82] Y. Jung, J. Song, W. Huh, D. Cho, and Y. Jeong, “Controlling the crystalline quality of carbon nanotubes with processing parameters from chemical vapor deposition synthesis,” *Chem. Eng. J.*, vol. 228, no. 0, pp. 1050–1056, 2013.
[83] Zhong XH, Li YL, Liu YK, Qiao XH, Feng Y, Liang J, Jin J, Zhu L, Hou F, Li JY, “Continuous multilayered carbon nanotube yarns.,” *Adv Mater. 2010 Feb 9;22(6):692-6*.

[84] D. Conroy, A. Moisala, S. Cardoso, A. Windle, and J. Davidson, “Carbon nanotube reactor: Ferrocene decomposition, iron particle growth, nanotube aggregation and scale-up,” *Chem. Eng. Sci.*, vol. 65, no. 10, pp. 2965–2977, 2010.
[85] R. M. Sundaram, K. K. K. Koziol, and A. H. Windle, “Continuous Direct Spinning of Fibers of Single-Walled Carbon Nanotubes with Metallic Chirality,” *Adv. Mater.*, vol. 23, no. 43, pp. 5064–5068, 2011.
[86] D. Janas, A. Cabrero-Vilatela, J. Bulmer, L. Kurzepa, and K. K. Koziol, “Carbon nanotube wires for high-temperature performance,” *Carbon*, vol. 64, pp. 305–314, 2013.
[87] S.-H. Lee *et al.*, “Synthesis of carbon nanotube fibers using the direct spinning process based on Design of Experiment (DOE),” *Carbon*, vol. 100, pp. 647–655, 2016.
[88] C. Hoecker, F. Smail, M. Pick, and A. Boies, “The influence of carbon source and catalyst nanoparticles on {CVD} synthesis of {CNT} aerogel,” *Chem. Eng. J.*, p. , 2016.
[89] T. S. Gspann *et al.*, “High thermal conductivities of carbon nanotube films and micro-fibres and their dependence on morphology,” *Carbon*, vol. 114, pp. 160–168, 2017.
[90] S.-H. Lee, J. Park, H.-R. Kim, J. Lee, and K.-H. Lee, “Synthesis of high-quality carbon nanotube fibers by controlling the effects of sulfur on the catalyst agglomeration during the direct spinning process,” *RSC Adv*, vol. 5, no. 52, pp. 41894–41900, 2015.
[91] J. Song, S. Kim, S. Yoon, D. Cho, and Y. Jeong, “Enhanced spinnability of carbon nanotube fibers by surfactant addition,” *Fibers Polym.*, vol. 15, no. 4, pp. 762–766, 2014.
[92] T. S. Gspann, F. R. Smail, and A. H. Windle, “Spinning of carbon nanotube fibres using the floating catalyst high temperature route: purity issues and the critical role of sulphur,” *Faraday Discuss*, vol. 173, no. 0, pp. 47–65, 2014.
[93] J. A. Barnard and H. W. D. Hughes, “The pyrolysis of ethanol,” *Trans Faraday Soc*, vol. 56, no. 0, pp. 55–63, 1960.
[94] J. A. Barnard, “The pyrolysis of n-butanol,” *Trans Faraday Soc*, vol. 53, no. 0, pp. 1423–1430, 1957.
[95] D. He, A. Dichiara, H. Li, and J. Bai, “Thermal Decomposition of Xylene for the Synthesis of Carbon Nanomaterials,” in *Xylenes: Synthesis, Characterization and Physicochemical Properties*, 2013, pp. 127–154.
[96] R. A. Couttenye, M. H. De Vila, and S. L. Suib, “Decomposition of methane with an autocatalytically reduced nickel catalyst,” *J. Catal.*, vol. 233, no. 2, pp. 317–326, Jul. 2005.
[97] A. Shaikjee and N. J. Coville, “The role of the hydrocarbon source on the growth of carbon materials,” *Carbon*, vol. 50, no. 10, pp. 3376–3398, 2012.
[98] Sundaram, Rajyashree M. and Windle, Alan H, “Effect of Carbon Precursors on the Structure and Properties of Continuously Spun Carbon Nanotube Fibers,” *Science of Advanced Materials*, vol. 7, no. 4, pp. 643–653, 2015.
[99] R. Z. Fei WEi, “Chapter 4 Systhesis and Properties of Ultralong Carbon Nanotubes,” in *Nanotube Superfiber Materials*, .
[100] A. K. Chatterjee, M. Sharon, R. Banerjee, and M. Neumann-Spallart, “{CVD} synthesis of carbon nanotubes using a finely dispersed cobalt catalyst

and their use in double layer electrochemical capacitors," *Electrochimica Acta*, vol. 48, no. 23, pp. 3439–3446, 2003.
[101] S. Hofmann *et al.*, "In situ Observations of Catalyst Dynamics during Surface-Bound Carbon Nanotube Nucleation," *Nano Lett.*, vol. 7, no. 3, pp. 602–608, 2007.
[102] C. T. Wirth *et al.*, "The Phase of Iron Catalyst Nanoparticles during Carbon Nanotube Growth," *Chem. Mater.*, vol. 24, no. 24, pp. 4633–4640, 2012.
[103] R. Rao *et al.*, "Revealing the Impact of Catalyst Phase Transition on Carbon Nanotube Growth by in Situ Raman Spectroscopy," *ACS Nano*, vol. 7, no. 2, pp. 1100–1107, 2013.
[104] Motta, M. S., Moisala, A., Kinloch, I. A., and Windle, A. H., "The Role of Sulphur in the Synthesis of Carbon Nanotubes by Chemical Vapour Deposition at High Temperatures," *J. Nanosci. Nanotechnol.*, vol. 8, pp. 2442–2449, 2008.
[105] *R.M. Sundaram. Production, Characterisation and Properties of Carbon Nanotube fibres. Chapter 6 p127-162*. .
[106] Rao, Rahul and Pierce, Neal and Zhang, Xianfeng and Wheeler, Robert and Maruyama, Benji and Talapatra, Saikat, "Understanding the Role of Sulfur in Tuning the Diameter and Morphology in the Chemical Vapor Deposition Growth of Carbon Nanotubes," *Materials Express*, vol. 1, no. 2, pp. 160–166, 2011.
[107] J. N. Wang, X. G. Luo, T. Wu, and Y. Chen, "High-strength carbon nanotube fibre-like ribbon with high ductility and high electrical conductivity," *Nat. Commun.*, vol. 5, p. 3848, Jun. 2014.
[108] F. Guo *et al.*, "Fabrication of highly conductive carbon nanotube fibers for electrical application," *Mater. Res. Express*, vol. 2, no. 9, p. 95604, 2015.
[109] G. Hou *et al.*, "The effect of a convection vortex on sock formation in the floating catalyst method for carbon nanotube synthesis," *Carbon*, vol. 102, pp. 513–519, 2016.
[110] Y. Jung, J. Song, W. Huh, D. Cho, and Y. Jeong, "Controlling the crystalline quality of carbon nanotubes with processing parameters from chemical vapor deposition synthesis," *Chem. Eng. J.*, vol. 228, pp. 1050–1056, 2013.
[111] B. Yu, P.-X. Hou, F. Li, B. Liu, C. Liu, and H.-M. Cheng, "Selective removal of metallic single-walled carbon nanotubes by combined in situ and post-synthesis oxidation," *Carbon*, vol. 48, no. 10, pp. 2941–2947, 2010.
[112] Rajyashree M. Sundaram, *Production, characterisation and properties of carbon nanotube fibres*, vol. 3. 2012.
[113] Juan J. Vilatela, *Structure, properties and treatments of carbon nanotube fibres*, vol. 6. 2009.
[114] R. J. Davies, C. Riekel, K. K. Koziol, J. J. Vilatela, and A. H. Windle, "Structural studies on carbon nanotube fibres by synchrotron radiation microdiffraction and microfluorescence," *J. Appl. Crystallogr.*, vol. 42, no. 6, pp. 1122–1128, Dec. 2009.
[115] M. Motta, A. Moisala, I. A. Kinloch, and A. H. Windle, "High Performance Fibres from 'Dog Bone' Carbon Nanotubes," *Adv. Mater.*, vol. 19, no. 21, pp. 3721–3726, 2007.
[116] Q. Fu and T. Wagner, "Interaction of nanostructured metal overlayers with oxide surfaces," *Surf. Sci. Rep.*, vol. 62, no. 11, pp. 431–498, 2007.

[117] M. J. Bronikowski, “Longer Nanotubes at Lower Temperatures: The Influence of Effective Activation Energies on Carbon Nanotube Growth by Thermal Chemical Vapor Deposition,” *J. Phys. Chem. C*, vol. 111, no. 48, pp. 17705–17712, Dec. 2007.
[118] Tso, S and Pask, J, “Reaction of Silicate Glasses and Mullite with Hydrogen Gas,” *J. Am. Ceram. Soc.*, vol. 65, no. 8, pp. 383–387, 1982.
[119] B. Vigolo *et al.*, “Macroscopic Fibers and Ribbons of Oriented Carbon Nanotubes,” *Science*, vol. 290, no. 5495, pp. 1331–1334, 2000.
[120] A. B. Dalton *et al.*, “Super-tough carbon-nanotube fibres,” *Nature*, vol. 423, no. 6941, pp. 703–703, Jun. 2003.
[121] P. Miaudet *et al.*, “Hot-Drawing of Single and Multiwall Carbon Nanotube Fibers for High Toughness and Alignment,” *Nano Lett.*, vol. 5, no. 11, pp. 2212–2215, 2005.
[122] V. A. Davis *et al.*, “Phase Behavior and Rheology of SWNTs in Superacids,” *Macromolecules*, vol. 37, no. 1, pp. 154–160, 2004.
[123] L. M. Ericson *et al.*, “Macroscopic, Neat, Single-Walled Carbon Nanotube Fibers,” *Science*, vol. 305, no. 5689, pp. 1447–1450, 2004.
[124] N. Behabtu *et al.*, “Strong, Light, Multifunctional Fibers of Carbon Nanotubes with Ultrahigh Conductivity,” *Science*, vol. 339, no. 6116, pp. 182–186, 2013.
[125] M. Zhang, K. R. Atkinson, and R. H. Baughman, “Multifunctional Carbon Nanotube Yarns by Downsizing an Ancient Technology,” *Science*, vol. 306, no. 5700, pp. 1358–1361, 2004.
[126] X. Zhang *et al.*, “Ultrastrong, Stiff, and Lightweight Carbon-Nanotube Fibers,” *Adv. Mater.*, vol. 19, no. 23, pp. 4198–4201, 2007.
[127] X. Zhang *et al.*, “Strong Carbon-Nanotube Fibers Spun from Long Carbon-Nanotube Arrays,” *Small*, vol. 3, no. 2, pp. 244–248, 2007.
[128] A. E. Aliev *et al.*, “Thermal transport in {MWCNT} sheets and yarns,” *Carbon*, vol. 45, no. 15, pp. 2880–2888, 2007.
[129] “Macroscopic fibers of well-aligned carbon nanotubes by wet spinning.Zhang S, Koziol KK, Kinloch IA, Windle AH. Small. 2008 Aug;4(8):1217-22.”
[130] H.Yue, “Polymer interaction with macroscopic CNT fibres and fabrication of nanostructured composites,” UPM, 2015.
[131] *Staudinger, H. Die Hochmolekularen Organischen Verbindungen - Kautschuk und Cellulose -. (Springer Berlin Heidelberg, 1932).* .
[132] J. W. Hill and W. H. Carothers, “Studies of Polymerization and Ring Formation. XIX.1 Many-Membered Cyclic Anhydrides,” *J. Am. Chem. Soc.*, vol. 55, no. 12, pp. 5023–5031, 1933.
[133] K. Koziol *et al.*, “High-Performance Carbon Nanotube Fiber,” *Science*, vol. 318, no. 5858, pp. 1892–1895, 2007.
[134] A. G. Rinzler *et al.*, “Large-scale purification of single-wall carbon nanotubes: process, product, and characterization,” *Appl. Phys. A*, vol. 67, no. 1, pp. 29–37, 1998.
[135] J. J. Vilatela and D. Eder, “Nanocarbon Composites and Hybrids in Sustainability: A Review,” *ChemSusChem*, vol. 5, no. 3, pp. 456–478, 2012.
[136] J. Qiu, J. Terrones, J. J. Vilatela, M. E. Vickers, J. A. Elliott, and A. H. Windle, “Liquid Infiltration into Carbon Nanotube Fibers: Effect on Structure and Electrical Properties,” *ACS Nano*, vol. 7, no. 10, pp. 8412–8422, 2013.

[137] A. V. Neimark *et al.*, “Hierarchical Pore Structure and Wetting Properties of Single-Wall Carbon Nanotube Fibers,” *Nano Lett.*, vol. 3, no. 3, pp. 419–423, 2003.
[138] H. Yue, A. Monreal-Bernal, J. P. Fernández-Blázquez, J. Llorca, and J. J. Vilatela, “Macroscopic CNT fibres inducing non-epitaxial nucleation and orientation of semicrystalline polymers,” *Sci. Rep.*, vol. 5, p. 16729, 2015.
[139] X.-H. Zhong *et al.*, “Continuous Multilayered Carbon Nanotube Yarns,” *Adv. Mater.*, vol. 22, no. 6, pp. 692–696, 2010.
[140] A. Gupta, I. R. Harrison, and J. Lahijani, “Small-angle X-ray scattering in carbon fibers,” *J. Appl. Crystallogr.*, vol. 27, no. 4, pp. 627–636, Aug. 1994.
[141] M. G. Dobb, D. J. Johnson, A. Majeed, and B. P. Saville, “Microvoids in aramid-type fibrous polymers,” *Polymer*, vol. 20, no. 10, pp. 1284–1288, 1979.
[142] S. Ran *et al.*, “In-Situ Synchrotron WAXD/SAXS Studies of Structural Development during PBO/PPA Solution Spinning,” *Macromolecules*, vol. 35, no. 2, pp. 433–439, 2002.
[143] W. O. Statton, “Crystallite regularity and void content in cellulose fibers as shown by small-angle x-ray scattering,” *J. Polym. Sci.*, vol. 22, no. 102, pp. 385–397, 1956.
[144] O. Kratky and G. Porod, “Diffuse small-angle scattering of x-rays in colloid systems,” *J. Colloid Sci.*, vol. 4, no. 1, pp. 35–70, 1949.
[145] J. Qui, *Ingress of liquid into carbon nanotube materials*. 2012.
[146] Bale, Harold D. and Schmidt, Paul W., “Small-Angle X-Ray-Scattering Investigation of Submicroscopic Porosity with Fractal Properties,” *Phys. Rev. Lett.*, vol. 53, no. 6, pp. 596–599, 1984.
[147] D. Avnir, D. Farin, and P. Pfeifer, “Molecular fractal surfaces,” *Nature*, vol. 308, no. 5956, pp. 261–263, Mar. 1984.
[148] F. De Nicola, P. Castrucci, M. Scarselli, F. Nanni, I. Cacciotti, and M. De Crescenzi, “Multi-Fractal Hierarchy of Single-Walled Carbon Nanotube Hydrophobic Coatings,” *Sci. Rep.*, vol. 5, p. 8583, Feb. 2015.
[149] B. N. Wang, R. D. Bennett, E. Verploegen, A. J. Hart, and R. E. Cohen, “Quantitative Characterization of the Morphology of Multiwall Carbon Nanotube Films by Small-Angle X-ray Scattering,” *J. Phys. Chem. C*, vol. 111, no. 16, pp. 5859–5865, 2007.
[150] Das NCh, Yang K, Liu Y, Sokol PE, Wang Z, Wang H, “Quantitative characterization of vertically aligned multi-walled carbon nanotube arrays using small angle X-ray scattering,” *J Nanosci Nanotechnol.*, vol. 6, pp. 4995–5000, 2011.
[151] T. Belin and F. Epron, “Characterization methods of carbon nanotubes: a review,” *Mater. Sci. Eng. B*, vol. 119, no. 2, pp. 105–118, 2005.
[152] M. Motta, Li, I. Kinloch, and A. Windle, “Mechanical Properties of Continuously Spun Fibers of Carbon Nanotubes,” *Nano Lett.*, vol. 5, no. 8, pp. 1529–1533, 2005.
[153] A. M. Beese *et al.*, “Key Factors Limiting Carbon Nanotube Yarn Strength: Exploring Processing-Structure-Property Relationships,” *ACS Nano*, vol. 8, no. 11, pp. 11454–11466, Nov. 2014.
[154] J. J. Vilatela and A. H. Windle, “Yarn-Like Carbon Nanotube Fibers,” *Adv. Mater.*, vol. 22, no. 44, pp. 4959–4963, 2010.

[155] T. S. Gspann, N. Montinaro, A. Pantano, J. A. Elliott, and A. H. Windle, “Mechanical properties of carbon nanotube fibres: St Venant’s principle at the limit and the role of imperfections,” *Carbon*, vol. 93, pp. 1021–1033, 2015.
[156] K. E. Perepelkin, “Some mechanisms for the elasticproperties of orientated fibre-forming polymers and fibres.,” *Mekhan. Polim.*, pp. 34–42, 1966.
[157] S. Boncel, R. M. Sundaram, A. H. Windle, and K. K. K. Koziol, “Enhancement of the Mechanical Properties of Directly Spun CNT Fibers by Chemical Treatment,” *ACS Nano*, vol. 5, no. 12, pp. 9339–9344, 2011.
[158] J. J. Vilatela, J. A. Elliott, and A. H. Windle, “A Model for the Strength of Yarn-like Carbon Nanotube Fibers,” *ACS Nano*, vol. 5, no. 3, pp. 1921–1927, Mar. 2011.
[159] R. M. Sundaram, K. K. K. Koziol, and A. H. Windle, “Continuous Direct Spinning of Fibers of Single-Walled Carbon Nanotubes with Metallic Chirality,” *Adv. Mater.*, vol. 23, no. 43, pp. 5064–5068, 2011.
[160] A. Lekawa-Raus, K. Walczak, G. Kozlowski, M. Wozniak, S. C. Hopkins, and K. K. Koziol, “Resistance–temperature dependence in carbon nanotube fibres,” *Carbon*, vol. 84, pp. 118–123, 2015.
[161] M. Miao, “Electrical conductivity of pure carbon nanotube yarns,” *Carbon*, vol. 49, no. 12, pp. 3755–3761, 2011.
[162] M. B. Jakubinek *et al.*, “Thermal and electrical conductivity of array-spun multi-walled carbon nanotube yarns,” *Carbon*, vol. 50, no. 1, pp. 244–248, 2012.
[163] A. Lekawa-Raus *et al.*, “Influence of atmospheric water vapour on electrical performance of carbon nanotube fibres,” *Carbon*, vol. 87, pp. 18–28, 2015.
[164] “Correlation of properties with preferred orientation in coagulated and stretch-aligned single-wall carbon nanotubes,” *J. Appl. Phys.*, vol. 96, no. 12, pp. 7509–7513, Dec. 2004.
[165] L. M. Ericson *et al.*, “Macroscopic, Neat, Single-Walled Carbon Nanotube Fibers,” *Science*, vol. 5689, p. 1447, 2004.
[166] M. Motta, Li, I. Kinloch, and A. Windle, “Mechanical Properties of Continuously Spun Fibers of Carbon Nanotubes,” *Nano Lett.*, vol. 5, no. 8, pp. 1529–1533, 2005.
[167] K. Koziol *et al.*, “High-Performance Carbon Nanotube Fiber,” *Science*, vol. 318, no. 5858, pp. 1892–1895, Dec. 2007.
[168] A. Lekawa-Raus, K. K. K. Koziol, and A. H. Windle, “Piezoresistive Effect in Carbon Nanotube Fibers,” *ACS Nano*, vol. 8, no. 11, pp. 11214–11224, Nov. 2014.
[169] D. Janas, A. C. Vilatela, and K. K. K. Koziol, “Performance of carbon nanotube wires in extreme conditions,” *Carbon*, vol. 62, pp. 438–446, 2013.
[170] D. Janas and K. K. Koziol, “Rapid electrothermal response of high-temperature carbon nanotube film heaters,” *Carbon*, vol. 59, pp. 457–463, 2013.
[171] L. Kurzepa, A. Lekawa-Raus, J. Patmore, and K. Koziol, “Replacing Copper Wires with Carbon Nanotube Wires in Electrical Transformers,” *Adv. Funct. Mater.*, vol. 24, no. 5, pp. 619–624, 2014.
[172] A. Lekawa-Raus, L. Kurzepa, X. Peng, and K. Koziol, “Towards the development of carbon nanotube based wires,” *Carbon*, vol. 68, pp. 597–609, 2014.

[173] "http://www.plasan-na.com/tortech-carbon-nano-tube-technologies/," 2017.
[174] "http://www.nanocomptech.com/," 2017.
[175] Mary Ann Curran Walter Klöpffer, annette koehler, and Reinout Heijungs, "Nanotechnology and Life Cycle Assessment: A Systems Approach to Nanotechnology and the Environment." Mar-2007.
[176] D. Janas and K. K. Koziol, "Carbon nanotube fibers and films: synthesis, applications and perspectives of the direct-spinning method," *Nanoscale*, vol. 8, no. 47, pp. 19475–19490, 2016.
[177] D. D. L. Chung, "Materials for thermal conduction," *Appl. Therm. Eng.*, vol. 21, no. 16, pp. 1593–1605, 2001.
[178] E. Senokos, V. Reguero, J. Palma, J. J. Vilatela, and R. Marcilla, "Macroscopic fibres of CNTs as electrodes for multifunctional electric double layer capacitors: from quantum capacitance to device performance," *Nanoscale*, vol. 8, no. 6, pp. 3620–3628, 2016.
[179] B. E. Conway, *Electrochemical Supercapacitors: Scientific Fundamentals and Technological Applications*. Plenum Pub Corp, 2013.
[180] A. G. Pandolfo and A. F. Hollenkamp, "Carbon properties and their role in supercapacitors," *J. Power Sources*, vol. 157, no. 1, pp. 11–27, 2006.
[181] J. J. Vilatela and R. Marcilla, "Tough Electrodes: Carbon Nanotube Fibers as the Ultimate Current Collectors/Active Material for Energy Management Devices," *Chem. Mater.*, vol. 27, no. 20, pp. 6901–6917, 2015.
[182] V. V. N. Obreja, "On the performance of supercapacitors with electrodes based on carbon nanotubes and carbon activated material—A review," *Phys. E Low-Dimens. Syst. Nanostructures*, vol. 40, no. 7, pp. 2596–2605, 2008.
[183] J. C. Fernández-Toribio, A. Íñiguez-Rábago, J. Vilà, C. González, Á. Ridruejo, and J. J. Vilatela, "A Composite Fabrication Sensor Based on Electrochemical Doping of Carbon Nanotube Yarns," *Adv. Funct. Mater.*, vol. 26, no. 39, pp. 7139–7147, 2016.
[184] C. J. Shearer, A. Cherevan, and D. Eder, "Application and Future Challenges of Functional Nanocarbon Hybrids," *Adv. Mater.*, vol. 26, no. 15, pp. 2295–2318, 2014.
[185] A. Moya *et al.*, "Oxygen vacancies and interfaces enhancing photocatalytic hydrogen production in mesoporous CNT/TiO2 hybrids," *Appl. Catal. B Environ.*, vol. 179, pp. 574–582, 2015.
[186] R. J. Mora, J. J. Vilatela, and A. H. Windle, "Properties of composites of carbon nanotube fibres," *Compos. Sci. Technol.*, vol. 69, no. 10, pp. 1558–1563, 2009.
[187] P. Liu, A. Lam, Z. Fan, T. Q. Tran, and H. M. Duong, "Advanced multifunctional properties of aligned carbon nanotube-epoxy thin film composites," *Mater. Des.*, vol. 87, pp. 600–605, 2015.
[188] P.-M. Hannula *et al.*, "Carbon nanotube-copper composites by electrodeposition on carbon nanotube fibers," *Carbon*, vol. 107, pp. 281–287, 2016.
[189] S. Brunauer, P. H. Emmett, and E. Teller, "Adsorption of Gases in Multimolecular Layers," *J. Am. Chem. Soc.*, vol. 60, no. 2, pp. 309–319, Feb. 1938.
[190] E. P. Barrett, L. G. Joyner, and P. P. Halenda, "The Determination of Pore Volume and Area Distributions in Porous Substances. I. Computations from Nitrogen Isotherms," *J. Am. Chem. Soc.*, vol. 73, no. 1, pp. 373–380, 1951.

[191] Sing K.S., “Reporting physisorption data for gas/solid systems with special reference to the determination of surface area and porosity. Pure and Applied Chemistry, 57, 603–619.(1985).”
[192] S.-H. Shim and T. S. Duffy, “Raman spectroscopy of Fe2O3 to 62 GPa,” *Am. Mineral.*, vol. 87, no. 2–3, pp. 318–326, 2002.
[193] A. C. Ferrari *et al.*, “Raman Spectrum of Graphene and Graphene Layers,” *Phys Rev Lett*, vol. 97, no. 18, p. 187401, Oct. 2006.
[194] A. Moisala, A. G. Nasibulin, D. P. Brown, H. Jiang, L. Khriachtchev, and E. I. Kauppinen, “Single-walled carbon nanotube synthesis using ferrocene and iron pentacarbonyl in a laminar flow reactor,” *Chem. Eng. Sci.*, vol. 61, no. 13, pp. 4393–4402, 2006.
[195] V. I. Artyukhov, E. S. Penev, and B. I. Yakobson, “Why nanotubes grow chiral,” *Nat. Commun.*, vol. 5, p. 4892, Sep. 2014.
[196] Don N. Futaba *et al.*, “84% Catalyst Activity of Water-Assisted Growth of Single Walled Carbon Nanotube Forest Characterization by a Statistical and Macroscopic Approach,” *J. Phys. Chem. B*, vol. 110, no. 15, pp. 8035–8038, 2006.
[197] M. Descostes, F. Mercier, N. Thromat, C. Beaucaire, and M. Gautier-Soyer, “Use of {XPS} in the determination of chemical environment and oxidation state of iron and sulfur samples: constitution of a data basis in binding energies for Fe and S reference compounds and applications to the evidence of surface species of an oxidized pyrite in a carbonate medium,” *Appl. Surf. Sci.*, vol. 165, no. 4, pp. 288–302, 2000.
[198] N. J. Saikia *et al.*, “Plasma Fluorination of Vertically Aligned Carbon Nanotubes,” *J. Phys. Chem. C*, vol. 117, no. 28, pp. 14635–14641, 2013.
[199] † Feng Ding *, † Arne Rosén, † Eleanor E. B. Campbell, ‡ Lena K. L. Falk, and § and Kim Bolton†, “Graphitic Encapsulation of Catalyst Particles in Carbon Nanotube Production,” *J. Phys. Chem. B*, vol. 110, no. 15, pp. 7666–7670, 2006.
[200] B. Aleman *et al.*, “Inherent predominance of high chiral angle metallic carbon nanotubes in continuous fibers grown from a molten catalyst,” *Nanoscale*, vol. 8, no. 7, pp. 4236–4244, 2016.
[201] *Bhadeshia, H., and Honeycombe, R. Steels: microstructure and properties: microstructure and properties. Butterworth-Heinemann, 2011.* .
[202] Delmon, B, “Catalyst Deactivation 1980 International Symposium Proceedings.,” *Elsevier Science: Burlington,* 1980.
[203] C. Wu and V. Sahajwalla, “Influence of melt carbon and sulfur on the wetting of solid graphite by Fe-C-S melts,” *Metall. Mater. Trans. B*, vol. 29, no. 2, pp. 471–477, 1998.
[204] M. Naraghi, T. Filleter, A. Moravsky, M. Locascio, R. O. Loutfy, and H. D. Espinosa, “A Multiscale Study of High Performance Double-Walled Nanotube−Polymer Fibers,” *ACS Nano*, vol. 4, no. 11, pp. 6463–6476, 2010.
[205] Z. Wang *et al.*, “Synthesis, characterization and electrical properties of silicon-doped graphene films,” *J Mater Chem C*, vol. 3, no. 24, pp. 6301–6306, 2015.
[206] M. J. Ledoux and C. Pham-Huu, “Silicon Carbide: A Novel Catalyst Support for Heterogeneous Catalysis,” *CATTECH*, vol. 5, no. 4, pp. 226–246, 2001.
[207] J. M. Haschke, “Specialty chemicals. An identity problem,” *J. Chem. Educ.*, vol. 52, no. 3, p. 157, Mar. 1975.

[208] Y.-M. Chiang, R. P. Messner, C. D. Terwilliger, and D. R. Behrendt, “Reaction-formed silicon carbide,” *Mater. Sci. Eng. A*, vol. 144, no. 1, pp. 63–74, 1991.
[209] A. Leonhardt *et al.*, “Synthesis, Properties, and Applications of Ferromagnetic-Filled Carbon Nanotubes,” *Chem. Vap. Depos.*, vol. 12, no. 6, pp. 380–387, 2006.
[210] K. Kuwana and K. Saito, “Modeling {CVD} synthesis of carbon nanotubes: Nanoparticle formation from ferrocene,” *Carbon*, vol. 43, no. 10, pp. 2088–2095, 2005.
[211] J. K. Winkler, W. Karow, and P. Rademacher, “Gas-phase pyrolysis of heterocyclic compounds, part 1 and 2: flow pyrolysis and annulation reactions of some sulfur heterocycles: thiophene, benzo[b]thiophene, and dibenzothiophene. A product-oriented study1,” *J. Anal. Appl. Pyrolysis*, vol. 62, no. 1, pp. 123–141, 2002.
[212] K. C. Hou and H. B. Palmer, “The Kinetics of Thermal Decomposition of Benzene in a Flow System,” *J. Phys. Chem.*, vol. 69, no. 3, pp. 863–868, 1965.
[213] J. B. In, C. P. Grigoropoulos, A. A. Chernov, and A. Noy, “Growth Kinetics of Vertically Aligned Carbon Nanotube Arrays in Clean Oxygen-free Conditions,” *ACS Nano*, vol. 5, no. 12, pp. 9602–9610, 2011.
[214] S. S. Meysami, L. C. Snoek, and N. Grobert, “Versatile in Situ Gas Analysis Apparatus for Nanomaterials Reactors,” *Anal. Chem.*, vol. 86, no. 17, pp. 8850–8856, 2014.
[215] V. Reguero, B. Alemán, B. Mas, and J. J. Vilatela, “Controlling Carbon Nanotube Type in Macroscopic Fibers Synthesized by the Direct Spinning Process,” *Chem. Mater.*, vol. 26, no. 11, pp. 3550–3557, 2014.
[216] L. Smith, P, “Ultrahigh-Strength Polyethylene Filaments by Solution Spinning and Hot Drawing,” *Polym. Bull.*, vol. 1, 1979.
[217] W. W. Adams and R. K. Eby, “High-Performance Polymer Fibers,” *MRS Bull.*, vol. 12, no. 8, pp. 22–26, 1987.
[218] W. Hoogsteen, H. Kormelink, G. Eshuis, G. ten Brinke, and A. J. Pennings, “Gel-spun polyethylene fibres,” *J. Mater. Sci.*, vol. 23, no. 10, pp. 3467–3474, 1988.
[219] Flory, P. J., *Statistical Mechanics of Chain Molecules*. Interscience Publishers, 1969.
[220] P. Pfeifer and D. Avnir, “Chemistry in noninteger dimensions between two and three. I. Fractal theory of heterogeneous surfaces,” *J. Chem. Phys.*, vol. 79, no. 7, pp. 3558–3565, 1983.
[221] P. Pfeifer, Y. J. Wu, M. W. Cole, and J. Krim, “Multilayer adsorption on a fractally rough surface,” *Phys Rev Lett*, vol. 62, no. 17, pp. 1997–2000, Apr. 1989.
[222] T. Kanyó, Z. Kónya, Á. Kukovecz, F. Berger, I. Dékány, and I. Kiricsi, “Quantitative Characterization of Hydrophilic−Hydrophobic Properties of MWNTs Surfaces,” *Langmuir*, vol. 20, no. 5, pp. 1656–1661, 2004.
[223] R. Smajda, Á. Kukovecz, Z. Kónya, and I. Kiricsi, “Structure and gas permeability of multi-wall carbon nanotube buckypapers,” *Carbon*, vol. 45, no. 6, pp. 1176–1184, 2007.
[224] *J.Brinker, G. W. Scherer. Sol-Gel Science The Physics and Chemistry of Sol-Gel Processing. C. Academic Press, INC. 1990.* .

[225] C.-H. Sun, F. Li, Z. Ying, C. Liu, and H.-M. Cheng, “Surface fractal dimension of single-walled carbon nanotubes,” *Phys. Rev. B*, vol. 69, no. 3, Jan. 2004.
[226] I. A. Khan *et al.*, “Fractal structures of single-walled carbon nanotubes in biologically relevant conditions: Role of chirality vs. media conditions,” *Chemosphere*, vol. 93, no. 9, pp. 1997–2003, 2013.
[227] P. Pfeifer *et al.*, “Nearly Space-Filling Fractal Networks of Carbon Nanopores,” *Phys Rev Lett*, vol. 88, no. 11, p. 115502, Feb. 2002.
[228] Z. Mileeva, D. K. Ross, and S. M. King, “A study of the porosity of nuclear graphite using small-angle neutron scattering,” *Carbon*, vol. 64, pp. 20–26, Nov. 2013.
[229] B. McENANEY, “{CHAPTER} 1 - Structure and Bonding in Carbon Materials,” in *Carbon Materials for Advanced Technologies*, T. D. Burchell, Ed. Oxford: Elsevier Science Ltd, 1999, pp. 1–33.
[230] R. Zhang, Y. Zhang, and F. Wei, “Chapter 4 - Synthesis and Properties of Ultralong Carbon Nanotubes,” in *Nanotube Superfiber Materials*, M. J. Schulz, V. N. Shanov, and Z. Yin, Eds. Boston: William Andrew Publishing, 2014, pp. 87–136.
[231] B. Alemán, V. Reguero, B. Mas, and J. J. Vilatela, “Strong Carbon Nanotube Fibers by Drawing Inspiration from Polymer Fiber Spinning,” *ACS Nano*, vol. 9, no. 7, pp. 7392–7398, 2015.
[232] S. Sakurai, F. Kamada, D. N. Futaba, M. Yumura, and K. Hata, “Influence of lengths of millimeter-scale single-walled carbon nanotube on electrical and mechanical properties of buckypaper,” *Nanoscale Res. Lett.*, vol. 8, no. 1, pp. 546–546, 2013.
[233] Y. Inoue *et al.*, “Anisotropic carbon nanotube papers fabricated from multiwalled carbon nanotube webs,” *Carbon*, vol. 49, no. 7, pp. 2437–2443, 2011.
[234] K. K. S. Lau *et al.*, “Superhydrophobic Carbon Nanotube Forests,” *Nano Lett.*, vol. 3, no. 12, pp. 1701–1705, 2003.
[235] G. SEGRE and A. SILBERBERG, “Radial Particle Displacements in Poiseuille Flow of Suspensions,” *Nature*, vol. 189, no. 4760, pp. 209–210, Jan. 1961.
[236] J.-P. MATAS, J. F. MORRIS, and ÉLISABETH GUAZZELLI, “Inertial migration of rigid spherical particles in Poiseuille flow,” *J. Fluid Mech.*, vol. 515, pp. 171–195, 2004.
[237] I. S. Fraser, M. S. Motta, R. K. Schmidt, and A. H. Windle, “Continuous production of flexible carbon nanotube-based transparent conductive films,” *Sci. Technol. Adv. Mater.*, vol. 11, no. 4, p. 45004, 2010.
[238] “http://www.project-sas.com/life-cycle-assessment---lca.html.”
[239] “Large-area, all-solid and flexible electric double layer capacitors based on CNT fibre electrodes and polymer electrolytes. E.Senokos, V. Reguero, L.Cabana, J. Palma, R. Marcilla, J.J. Vilatela. Advanced Technology Materials. Submitted. 2017.”
[240] J. P. Abdou *et al.*, “Interfacial crystallization of isotactic polypropylene surrounding macroscopic carbon nanotube and graphene fibers,” *Polymer*, vol. 91, pp. 136–145, 2016.